# REPORT DOCUMENTATION PAGE

AFRL-SR-AR-TR-05-



0161

| 1. AGENCY USE ONLY *(Leave blank)* | 2. REPORT DATE | 3. REPORT TYPE |
|---|---|---|
| | | |

**4. TITLE AND SUBTITLE**
Multidisciplinary Analysis and Control of High Performance Air Vehicles

**5. FUNDING NUMBERS**
F49620-01-1-0489

**6. AUTHOR(S)**
Dr. Majdedin Mirmirani

**7. PERFORMING ORGANIZATION NAME(S) AND ADDRESS(ES)**
California State University
Los Angeles
5151 State University Drive
Los Angeles, CA 90032-8253

**8. PERFORMING ORGANIZATION REPORT NUMBER**

**9. SPONSORING/MONITORING AGENCY NAME(S) AND ADDRESS(ES)**
Air Force Office of Scientific Research
875 North Randolph Street
Suite 325, Room 3112
Arlington, VA 22203 NM

**10. SPONSORING/MONITORING AGENCY REPORT NUMBER**

**11. SUPPLEMENTARY NOTES**

**12a. DISTRIBUTION AVAILABILITY STATEMENT**

Approved for public release,
distribution unlimited

**12b. DISTRIBUTION CODE**

**13. ABSTRACT** *(Maximum 200 words)*

Funds provided through the DoD infrastructure Support for HBCU/MI grant awarded to California State University, Los Angeles (Cal State LA) by the Air Force Office of Scientific Research (AFSOR) Dynamic Systems and Control on August 2001 were used for development of significant infrastructure of research, competency and capabilities in multidisciplinary modeling and control design of high-performance air vehicles. The investigators established a state-of-the-art research facility at CSULA-the Multidisciplinary Flight Dynamic and Control Laboratory (MFDCLab, www.calstatela.edu/centers/mfdclab) where novel methodologies and tools for accurate modeling, simulation, and control system design for high-performance air vehicles were developed. The accomplishments of this project include: The Rapid Conceptual Design Testbed. Nonlinear Adaptive Flight Control Laws. Aeroservoelasticity Hypersonic Vehicles. Human Resource Development. Integration of Research into Curriculum. Collaboration and Synergies. Leveraging the Grant.

| 14. SUBJECT TERMS | | | 15. NUMBER OF PAGES |
|---|---|---|---|
| | | | 16. PRICE CODE |
| 17. SECURITY CLASSIFICATION OF REPORT | 18. SECURITY CLASSIFICATION OF THIS PAGE | 19. SECURITY CLASSIFICATION OF ABSTRACT | 20. LIMITATION OF ABSTRACT |

# "MULTIDISCIPLINARY ANALYSIS AND CONTROL OF HIGH-PERFORMANCE AIR VEHICLES"

GRANT F49620-01-1-0489

# FINAL REPORT

Submitted to

Lt. Colonel Sharon Heise
Air Force Office of Scientific Research
Dynamics and Control

Principal Investigator: Professor Maj Dean Mirmirani
California State University, Los Angeles
Multidisciplinary Flight Dynamics and Control Laboratory

E-mail: mmirmir@calstatela.edu
Tel: (323) 343 4492
Fax: (323)343-5004

Co-Investigators:
Professors Chivey Wu and Helen Boussalis

Subcontractor: Univesity of Southern California
Principal Investigator: Professor Petros Ioannou

MAY 6, 2005

## EXACUTIVE SUMMARY

Funds provided through the DoD Infrastructure Support for HBCU/MI grant awarded to California State University, Los Angeles (Cal State LA) by the Air Force Office of Scientific Research (AFOSR) Dynamic Systems and Control on August 2001 were used for development of significant infrastructure of research, competency and capabilities in multidisciplinary modeling and control design of high-performance air vehicles. The investigators established a state-of-the-art research facility at CSULA– the Multidisciplinary Flight Dynamics and Control Laboratory (MFDCLab, www.calstatela.edu/centers/mfdclab) where novel methodologies and tools for accurate modeling, simulation, and control system design for high-performance air vehicles were developed. The accomplishments of this project include:

1. **The Rapid Conceptual Design Testbed**: The grant was used to build infrastructure, expertise, competency, and tools for modeling, control, and simulation of complex multidisciplinary aerospace systems. Specifically a "Virtual Testbed" consisting of a cluster of PCs, a rack of dedicated processors and discipline-oriented software linked to create a fully integrated computational environment for air vehicle rapid conceptual design and simulation has been developed.
2. **Nonlinear Adaptive Flight Control Laws**: Nonlinear adaptive control laws for fighter type aircraft and hypersonic flight vehicles have been developed. Algorithms to identify, measure, and isolate failure through a failure identification scheme to maintain attitude stability and reestablish guidance command following performance have been designed. Adaptive guidance laws capable of recognizing the inner-loop performance degradation and maintaining flight path stability have been developed. Design of an onboard algorithm to modify mission/retarget trajectory to maximize chance of survival is underway.
3. **Aeroservoelasticity**: Novel methods for identification and control of aeroelastic instabilities including ARMA and NARMA and neural network models and a linear quadratic Gaussian algorithm have developed.
4. **Airbreathing Hypersonic Vehicles**: Comprehensive literature survey on airbreathing hypersonic vehicle control was conducted. Mathematical models for two generic hypersonic vehicles (GHV) have been developed. An effort to develop a high-fidelity model of an in-house designed full-scale airbreathing GHV with an integrated airframe propulsion system is underway. This model will be used to quantify the coupling between various dynamics that makes control of this class of vehicles very challenging.
5. **Human Resource Development:** The grant was used to attract underrepresented student populations to the study of engineering; provide them the opportunity to be exposed to cutting edge research and development related to NASA missions; encourage them to work for DoD, NASA, and aerospace industry and/or undertake graduate work. Over the three and a half years eleven undergraduate and eighteen graduate CSULA and USC students and numerous college, high School, and international interns, many of them minorities have been supported by the grant. Many have transitioned to MS and PhD programs or have taken employment at aerospace related jobs.

6. **Integration of Research into Curriculum:** The grant became a vehicle for innovative courses and integration of research into the Mechanical Engineering curriculum. The investigators were able to integrate their research into their courses and gain support for development and offering of new courses such as flight dynamics and control, computational flight dynamics, UAV conceptual design and combustion.
7. **Collaboration and Synergies:** As the result of this grant the investigators at Cal State LA established collaboration and synergetic research with USC, University of Kansas, Oklahoma State University, Air Force Research Laboratory at Wright Patterson Air Force Base at Dayton Ohio, Boeing Huntington Beach, and Lockheed Martin at Lancaster California.
8. **Leveraging the Grant:** The track record established by the Air Force grant was crucial in serving the investigators to obtain a major NASA research grant – a five-year six million dollar University Research Center in 2003

The results of the endeavor in each of the technical areas addressed by this project are presented in a series of reports, conference papers and journal papers which are attached in Appendices I - IV. Below a brief summary of the technical results in each area of research focus is briefly described. Other accomplishments including infrastructure and human resource development, student and budget data are also presented in the following sections.

Table of Contents

PAGE

## 1. The Rapid Conceptual Design Testbed

A testbed for rapid conceptual design, multidisciplinary optimization , and simulation of high-performance air vehicles has been developed. The testbed uses state-of-the-art networking technologies and CAE software to enable "virtual aircraft design," the ability to simulate an entire aircraft via computational capabilities. The testbed enables the user to accomplish the complete design cycle in a fraction of time that is currently feasible. The user can shift seamlessly between discipline-oriented CAE software to accomplish conceptual design, detail structural design, and generate the complete aerodynamic data base. Control-oriented software uses the data to outputs equations of motion. Control laws developed can be used for flight simulation and performance evaluation through the entire flight envelope of the vehicle on full-blown high fidelity models. The current state of the testbed consists of a series of data translation codes and graphical user interfaces (GUIs) linking NASTRAN/PATRAN, I-DEAS, STARS, DATCOM, AeroDynamic, Matlab, and Simulink. Entry to the testbed can be at the very start, or with an already existing model. Proof of concept has been demonstrated through a series of test cases involving the complete design cycle, starting from the initial sizing to controller design for simple configuration such as a simple wing and for more complex geometry such as a GHV.

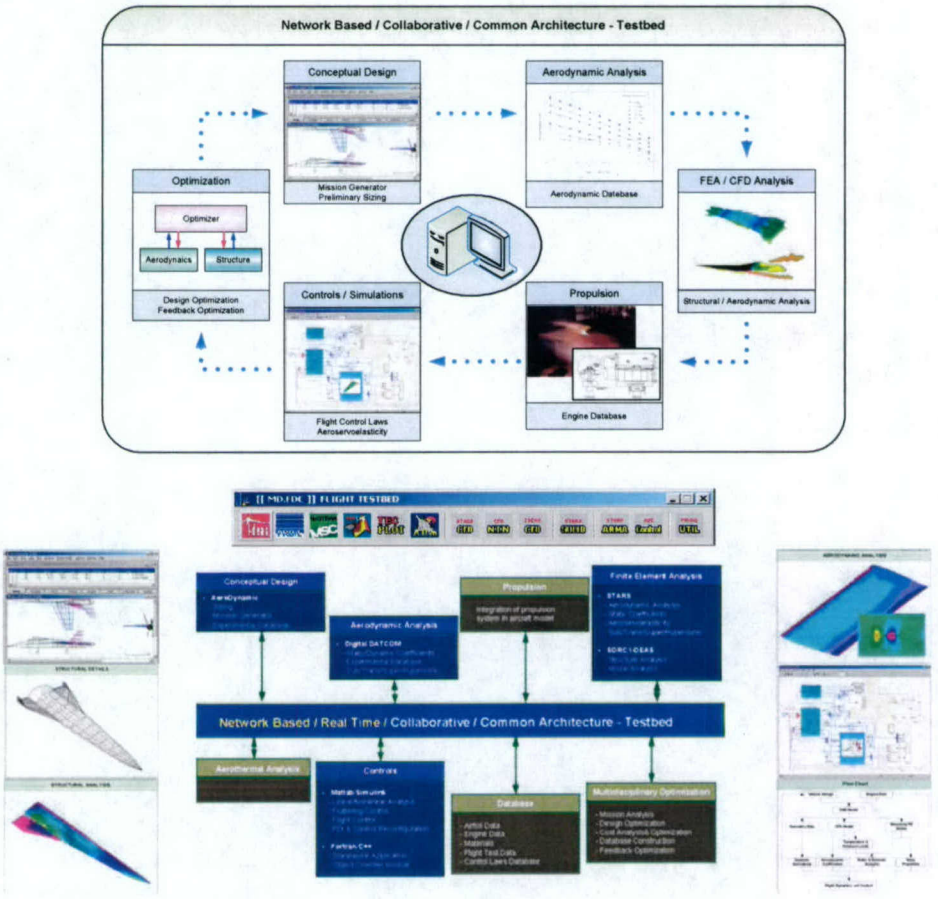


Figure 1 MFDCLab Testbed Configuration

For more detail see Appendix I which includes reprints of the following papers and reports:

1. E. Kemper and C. Wu, "U.S.A.F. DIGITA DATCOM, TEST CASES", California State University, Los Angeles, California, 2001
2. C. Wu and M. Mirmirani, "Development of Multidisciplinary Analysis Software for Teaching and Research", NASA MU-SPIN/MURED Conference, Atlanta, Georgia, September 2000

## 2. Intelligent Flight Control for High-Performance Air Vehicles

Future combat aircraft are expected to operate outside currently achievable flight envelopes pushing their performance closer to possible performance limits. Furthermore, they are expected to maintain their flight control properties in the presence of large uncertainties, classes of subsystem failures and battle damage and large unanticipated disturbances. During aggressive maneuvers the nonlinear nature of the aircraft dynamics becomes crucial. Robust nonlinear adaptive control is a class of intelligent control schemes that has potential for meeting these challenges. In this project the use of advanced adaptive control techniques to deal with uncertainties and nonlinearities high performance air vehicles were exploited. The results are presented in the reports and papers listed below and attached in Appendix II. What was considered in each article is briefly is briefly described below.

In [1] a comprehensive review of failure detection, isolation and control reconfiguration schemes that appear in literature is conducted. The report indicates that the design of such schemes for future high performance aircraft under large uncertainties and nonlinearities is not straightforward and additional research needs to be carried out to meet current and future challenges.

In [2] a class of multi-input multi-output nonlinear systems with unknown nonlinearities is considered. Such systems apply to high performance aircraft especially during unpredictable failures where prior knowledge of aircraft dynamics is no longer valid due to changes in aerodynamics and/or control surface effectiveness due to failure. Nonlinear control schemes using established concepts from robust adaptive control, sliding modes and neural networks were designed which guarantee pre-determined tracking performance. The paper provides a systematic procedure of selecting a number of design parameters so that the tracking error is guaranteed to be within a pre-specified bound in finite time.

In reference [3] the results of the above work are extended to a complex large scale system. In this case the complexity of subsystem interconnections require a decentralized control scheme which is developed using similar elements and techniques used in the work described above. Appropriate bounds are developed for the strengths of the interconnections so that the tracking error for each subsystem converges and stays within pre-specified bounds guaranteed by the choice of certain design parameters.

The results of [2] and [3] are used in reference [4] to design a multi-input/multi-output adaptive sliding controller for the longitudinal dynamics of a generic hypersonic air vehicle. This work is presented in the next paper listed below. In this case the air vehicle is nonlinear, multivariable, and unstable and includes uncertain parameters. Simulation studies are conducted for trimmed cruise conditions of 110,000 ft and Mach 15 where the responses of the vehicle to a step change in altitude and airspeed are evaluated. The controller is evaluated for robustness with respect to parameter uncertainties using simulations. The simulation studies supported by analysis, demonstrate that the proposed controller is robust with respect to parametric as well as nonlinear function uncertainties and meets the performance requirements with relatively low-amplitude control inputs.

In reference [4] longitudinal control of an F-16 aircraft is considered and an adaptive linear quadratic control scheme is designed which meets the performance requirements set by the designer. The control scheme is found to be robust with respect to the parametric uncertainties which could arise during normal operations as well as during failures. The adaptive scheme was shown to be superior to a corresponding gain scheduling scheme from the performance as well as the data storage requirement point of view.

For more detail see Appendix II which includes reprints of the following papers and reports:

1. Y. Huo, P. Ioannou and M. Mirmirani, 'Fault-Tolerant Control and Reconfiguration for High Performance Aircraft: Review', USC CATT Technical Report, Nov 1, 2001,
2. H. Xu and M. Mirmirani, "Robust Adaptive Sliding Mode control Design for a Class of MIMO Nonlinear Systems," Proceedings of the AIAA Guidance, Navigation and Control Conference, Montreal, Canada, August 2002
3. H. Xu, P. Ioannou and M. Mirmirani, 'Adaptive Control For A Class Of Large Scale Nonlinear Systems', accepted in *International Journal of Control,* to appear in 2005
4. H. Xu, M. Mirmirani, and P. A. Ioannou, "Adaptive sliding mode control design for a hypersonic flight vehicle", *AIAA Journal of Guidance, Control, and Dynamics*, Vol. 27, No. 5, September–October 2004 (presented in Appendix D)
5. Y. Huo, M. Mirmirani, P. Ioannou, and R. Colgren, "Adaptive Linear Quadratic Design with Application to F-16 Fighter Aircraft," AIAA Guidance, Navigation, and Control Conference and Exhibit, Providence, Rhode Island, August 2004

## 3. CFD-Based Aeroelasticity and Aeroservoelasticity

Aeroelasticity deals with interaction of aerodynamic, inertia and structural forces during flight. Aeroelastic instabilities such as flutter can potentially be catastrophic and result in destruction of the airframe. In high-performance aircraft such as a full scale hypersonic vehicle, where the airframe and the propulsion system are very tightly integrated the vehicle will experience significant aeroelastic effects. Expensive and time consuming flutter testing is mandatory in certification of all new aircraft to demonstrate that the aircraft can fly safely at all Mach numbers and altitudes within its flight envelope and remains flutter free. CFD-based aeroelasticity offers the potential for developing tools for modeling and rapidly providing valuable preflight data in flight test operations. System identification procedure is used to approximate aerodynamic forces with a set of linear or nonlinear state space formulation. Through this grant significant stride has been made in this direction and methods and tools for identification and control of aeroelastic instabilities have been developed. In reference [1] an LQG control algorithm for an aeroelastic supersonic wing is developed which is written in a code in MATLAB as well as FORTRAN for integration in STARS, the NASA DRFC-developed multidisciplinary software. The aeroservoelastic block diagram shown in Fig. 1 includes aerodynamic, structural and actuator models. The finite element structural model consists of modes that include rigid body, elastic, and control surface motions. The linear state space model for the aeroelastic wing is obtained using ARMA identification technique. The objective is to obtain a controller with limited control authority to suppress flutter. Simulations show that the controller can suppress flutter when it is induced by progressively increasing the dynamic pressure. Neural network-based models also have been employed for the aeroelastic system when the assumption of small structural deformation and quasi static CFD are relaxed. Methods and tools that can be employed for identification of flutter speed in a procedure referred to as "Nonlinear Auto Regressive Moving Average," NARMA have been developed and reported in reference [3]. The method was applied to an aeroelastic wing and simulation studies were conducted. Training data were obtained using STARS steady and unsteady solvers.

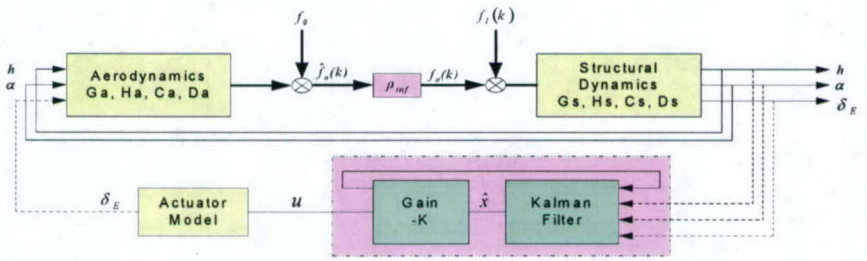


Figure 1 The Block Diagram of Coupled ASE

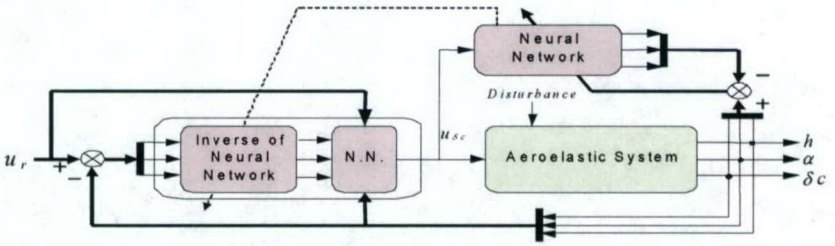


Figure 2 AE Neural Controller Architecture

The behavior of aeroelastic system in transonic regime is of particular interest. A CFD-based study was conducted using STARS, to investigate the flutter boundary prediction in transonic flow regime. STARS Direct Aeroelasticity Analysis Module utilizes Finite Element (FE) methodology for both the CFD solver and the Structural Finite Element solver with modal superposition. A full set of Navier-Stoke governing equations is applied for the steady and unsteady CFD solutions taking advantage of its capability in predicting complex shock induced influence for transonic and supersonic flows. By coupling the solutions from the CFD unsteady solver with the modal vectors from the Structural Finite Element solver, the dynamic equations of aeroelastic system are solved. For the study reported in reference [3] a simple configuration, the AGARD 445.6 Wing for which wind tunnel data are available is used. The results of the flutter analyses are compared with those obtained using the ARMA identification method and wind tunnel testing reported by NASA Dryden (Fig. 5).

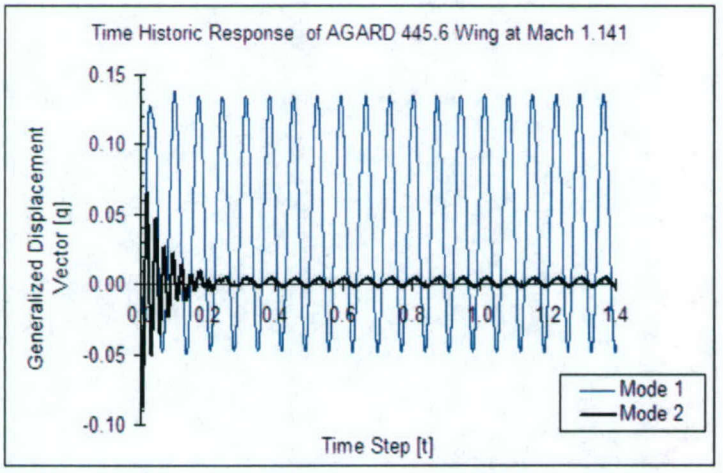


Figure 2 Response of the Generalized Displacement at Critical Flutter Condition

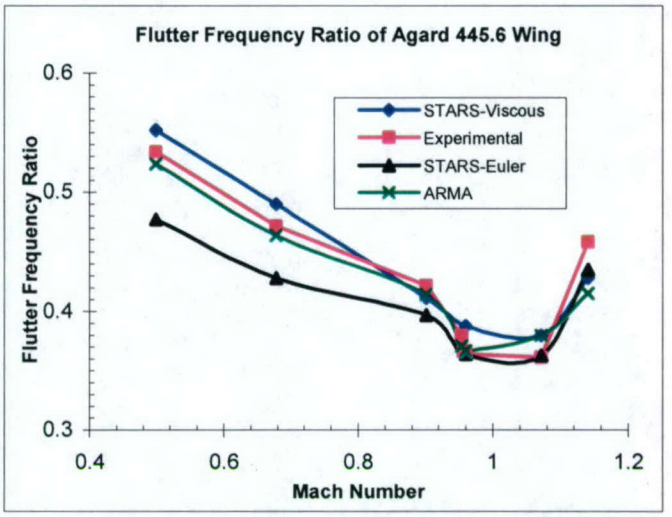


Figure 3 Flutter Frequency Ratio around the Transonic Flow Regime

For more detail see Appendix III which includes reprints of the following papers and reports:

1. S. Choi, H. Xu, and M. Mirmirani, "LQG Control of a CFD-Based Aeroelastic Wing Model,", IEEE Conference on Decision and Control, Maui, Hawaii, December 2003
2. S. Choi, "Nonlinear Dynamics and Control for an Aeroservoelastic System Using Neural Networks", California State University, Los Angeles, California, March 2003
3. C. He, S. Choi, M. Mirmirani, and C. Wu, "CFD-based Aeroelasticity Analysis in Transonic Flow Regime," ASME 2004 International Mechanical Engineering Congress and RD&D Expo, Anaheim, California, November 2004

## 4. Modeling and Control of Air-breathing Hypersonic Flight Vehicles (AHFV)

The unique dynamic characteristics of AHF make modeling and control of AHFVs especially challenging. Due to the strong coupling between the aerodynamics, the airframe, and the propulsion system, the modeling and control techniques used for conventional aircraft are inadequate. Mathematical models incorporating the interactions within the AHFV as well as an integrated airframe-engine control system are needed. Furthermore, the large variations and uncertainties associated with the dynamic characteristics over the flight envelope and the corresponding robustness issues need to be taken into account. Even if dynamic interactions are ignored and parameter variations and modeling uncertainties are assumed to be negligible - an invalid assumption as demonstrated in- the unique aero-thermodynamic characteristics of hypersonic flight need to be considered. Although a number of studies on the control of AHFVs do consider all of the effects described above, most works in the AHF control literature have ignored the coupling effects, have assumed parameter variations and uncertainties to be small, and have considered only some of the aero-thermodynamic characteristics due to hypersonic speed. Even in these cases, significant nonlinearities had to be introduced making them distinctly different from the conventional flight control problems. With renewed interest in air-breathing hypersonic flight for access to space and military applications effort was devoted to develop models and advanced control laws that incorporate the special characteristics of AHFVs. Theses efforts are presented in papers and reports listed below and in section 2. In [1] we conducted a comprehensive review of existing literature on AHFVs identifying the major challenges involved in modeling and control, accomplishments made and issues remaining. In [2] we developed a comprehensive CFD-based model of a GHV, the so-called NASA Langley winged-cone configuration. A complete set of aerodynamic coefficients and stability derivatives, including rate-dependent coefficients using STARS CFD code were obtained. In reference [3], section 2 an adaptive sliding modes control law was developed for a longitudinal model of a GHV reported in open literature.

In addition, the investigators have developed a computer model of an airbreathing hypersonic flight vehicle, the CSULA-GHV, as shown in Figure 5. The configuration and dimensions are developed based on 2-D compressible flow theory, and a set of mission requirements broadly accepted for a hypersonic cruise vehicle intended for both space access and military applications.

Analytical aerodynamic calculation assumes a cruising condition of Mach 10 at an altitude of 100 km. 2-D oblique shock theory predicts shock wave angles, pressure on the frontal surface, and Mach number at the engine inlet. The scramjet engine is simply modeled by a 1-D compressible flow with heating, which predicts the flow rate of hydrogen fuel required for a chosen design Mach number at the engine exit. The exit flow is modeled by 2-D expansion wave theory, which can be used to predict the pressure on the rear surface. Resultant aerodynamic forces and engine thrust are then estimated by the summation of these pressure forces and momentum change of the airflow. Applying moment balance also dictates the center of gravity location of the vehicle for a trimmed flight condition.

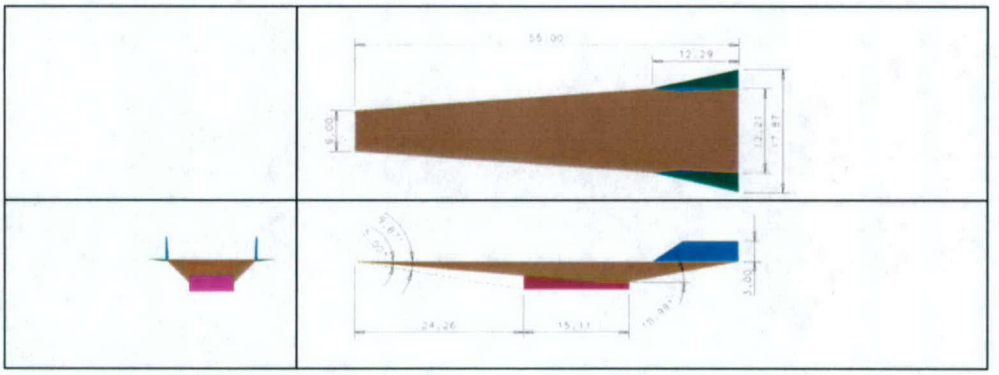

Figure 4 Two side views of a conceptual vehicle design

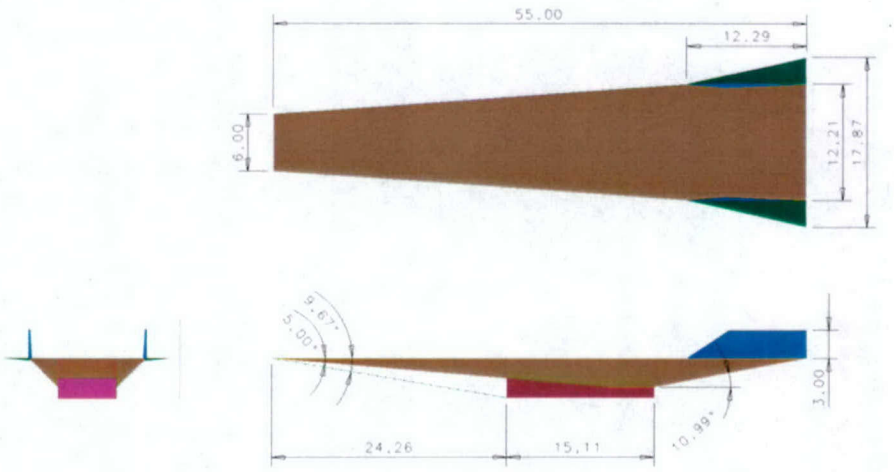


Figure 5 Basic Dimension of CSULA-GHV

Computational Fluid Dynamics (CFD) simulations for a 2-D model of this vehicle have also been conducted using FLUENT, a CFD code capable of simulating compressible flow coupled with combustion. Hydrogen fuel is injected from the upper surface of the scramjet as a boundary condition in this CFD model. Figure 6 shows the CFD results for the shock waves and Mach number contours for coupled aerodynamic propulsion, and H20 produced as a product of the reaction between the free stream air and Hydrogen fuel, both at optimum design condition of zero AoA and the off-design condition of AoA of 5 degrees. The zero AoA simulations are found to agree well with analytical results. In an off-design condition (the three simulations in the second row in Figure 6), the aerodynamic and propulsion performance of the vehicle is clearly reduced. The temperature contours as a result of combustion in the scramjet engine, and the concentration of the H20 product of combustion, are shown in the second and third column of Figure 6, respectively. The product is highly concentrated along the upper walls of the scramjet and nozzle due to the high speed of the air stream, which forbids the fuel to dissipate more uniformly into the scramjet. A more effective fuel injection design

is clearly needed to produce a more uniform reacting flow in the scramjet. This can be expected to be better achieved when full 3-D CFD simulations are conducted, since more design options are possible in a 3-D configuration.

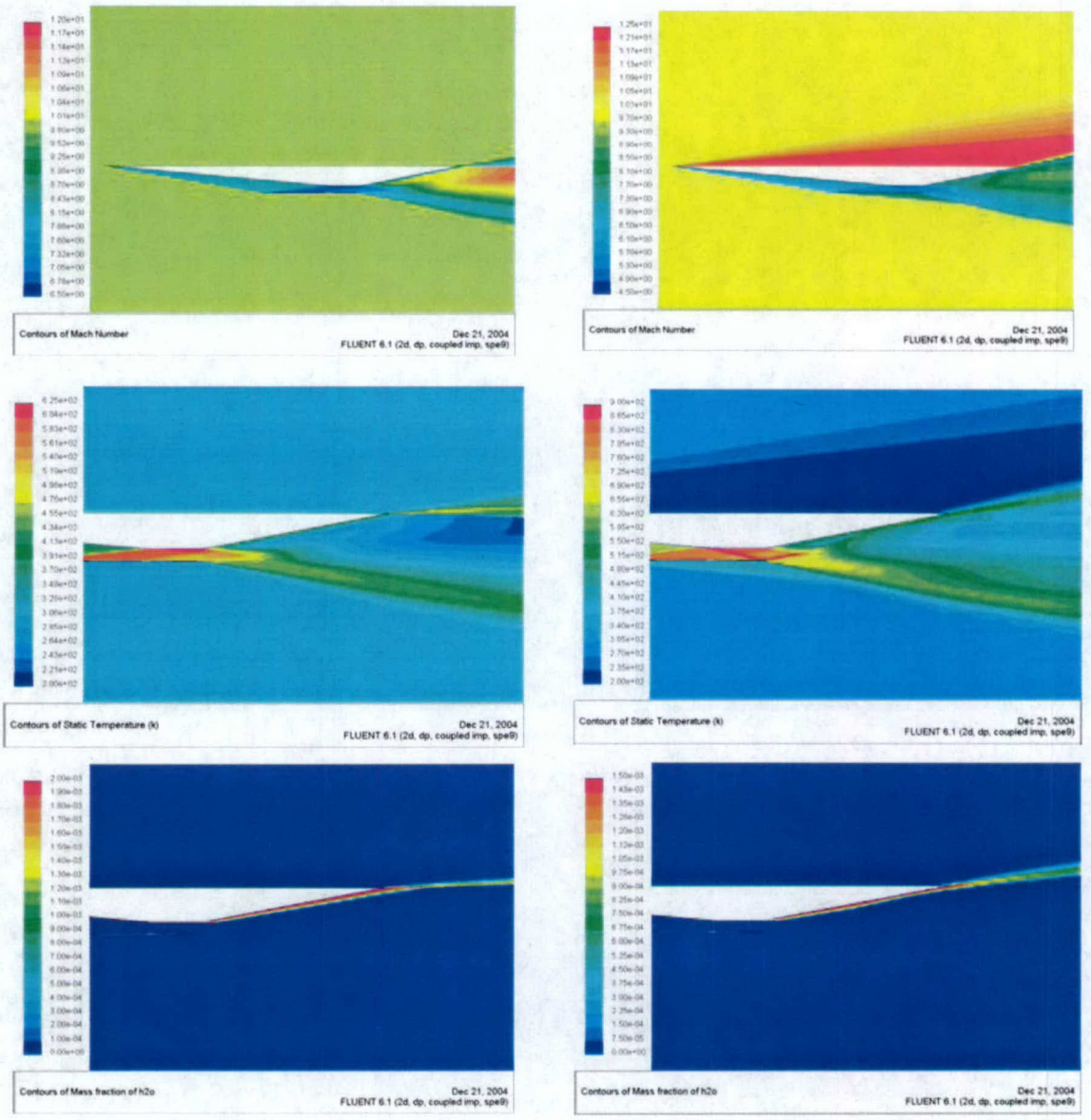


Figure 6: FLUENT Coupled Aero-Propulsion Simulation

To facilitate aeroelastic studies, a finite element model for the CSULA-GHV's airframe has been developed using MSC/NASTRAN, a widely used software program for structural analysis. This structural model consists of 1320 nodes and 1172 elements of fictitious material and shell properties to model actual material and cross sections of the fuselage, tail, and fins. As shown in Figure 7, different element properties are used for different areas to model the real structure. The horizontal and vertical tails are attached to

the fuselage through rigid body connections in this preliminary structural model. Modal analyses for the structure are performed and the mode shapes and corresponding frequencies are obtained. Figure 7 shows the result for the first bending modes.

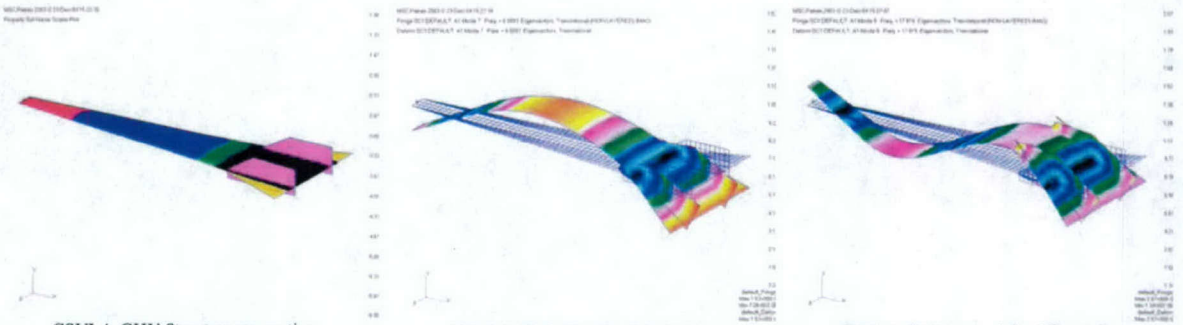

CSULA-GHV Structure properties | CSULA-GHV first flexible mode | CSULA-GHV second flexible mode

Figure 7 NASTRAN Structural Modes Simulation

For more detail see Appendix IV which includes reprints of the following papers and reports:

1. S. Keshmiri, M. Mirmirani, and R. Colgren, "Six-DOF Modeling and Simulation of a Generic Hypersonic Vehicle for Conceptual Design Studies," AIAA Modeling and Simulation Technologies Conference, Providence, Rhode Island, August 2004
2. B. Fidan, M. Mirmirani, and P. Ioannou, "Flight Dynamics and Control of Air-Breathing Hypersonic Vehicles: Review and New Directions," 12th AIAA International Space Planes and Hypersonic Systems and Technologies Conference, Norfolk, Virginia, December 2003

## 5. Human Resource Development

One of the primary objectives of the program was to significantly increase the number of graduate minority engineering students at CSULA. Other major educational goals were the integration of research into the engineering curriculum, enhancement of existing courses, and development of new courses in emerging areas.

During the three years of the AFOSR grant, the investigators have developed a successful model to achieve these goals. Table 1 provides tracking data for students supported by this grant. The collaboration with Ph.D.-granting institutions (USC and the University of Kansas) has been a key to the success of the program. In addition to a natural transition, it provided an opportunity for CSULA students to routinely interact with Ph.D. candidates who served as mentors and role models.

Table 1 Student Participants

| | NAME | Degree Received from CSULA | Current Degree Objective | Institution | Post Graduation Tracking |
|---|---|---|---|---|---|
| 1 | Amir Massoudi | MS | PhD | UCR | Ph.D |
| 2 | Christopher Herwerth | | BS | CSULA | Will Pursue MS at CSULA |
| 3 | Dipak Bhakta | | BS | CSULA | |
| 4 | Hongbing Cheng | | MS | CSULA | |
| 5 | Justinray Rencher | | BS | CSULA | Will Pursue MS at CSULA |
| 6 | Joshua Ward | BS | MS | USC | MS/Lockheed Martin |
| 7 | Micheal Lopez | | BS | CSULA | Lockheed Martin |
| 8 | Mohammed Shamol | | MS | CSULA | Will Pursue PhD |
| 9 | Sangbum Choi | MS | | CSULA | Will Pursue PhD |
| 10 | Shigeru Matsuyama | | MS | CSULA | Will Pursue PhD |
| 11 | Stanley Jacobson | | MS | CSULA | |
| 12 | Uche Ofoma | | MS | CSULA | |
| 13 | Chunlei He | MS | PhD | USC | Ph.D |
| 14 | Moataz Samir | MS | PhD | USC | Ph.D / Boeing |
| 15 | Kamyer Khashayar | MS | | CSULA | Industry |
| 16 | Marisol Avila | BS | MS | CSULA | Industry |
| 17 | Shahriar Keshmiri | | MS | U. of Kansas | Ph.D |
| 18 | Josue Cruz | | MS | CSULA | NASA Langley |
| 19 | Nazli Kahveci | | PhD | USC | |
| 20 | Ying Huo | | PhD | USC | |
| 21 | Jacob Parks | | PhD | USC | |
| 22 | Jianlong Zhang | | PhD | USC | |
| 23 | Baris Fidan | | PhD (graduated) | USC | Post-Doc |
| 24 | Haojian Xu | | PhD (graduated) | USC | Industry |

## 6. Budget Summary

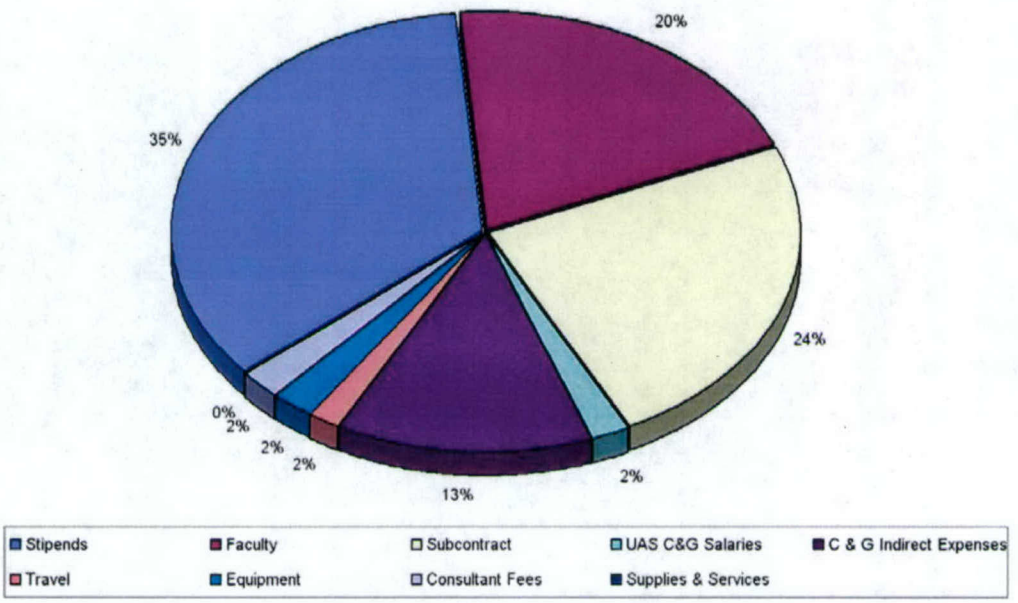


| Description | Amount |
|---|---|
| Stipends | $277,130.98 |
| Faculty | $160,440.82 |
| Subcontract | $190,500.00 |
| UAS C&G Salaries | $15,465.77 |
| C & G Indirect Expenses | $106,637.73 |
| Travel | $13,532.38 |
| Equipment | $19,417.32 |
| Consultant Fees | $16,000.00 |
| Supplies & Services | $875.00 |
| | |
| Total | $800,000.00 |

## 7. Appendices

MULTIDISCIPLINARY FLIGHT DYNAMICS AND
CONTROLS LABORATORY
CALIFORNIA STATE UNIVERSITY AT LOS ANGELES

# U.S.A.F. DIGITAL DATCOM

## TEST CASES

Department of Mechanical Engineering

California State University at Los Angeles

Dr. Chivey Wu and Erik Kemper

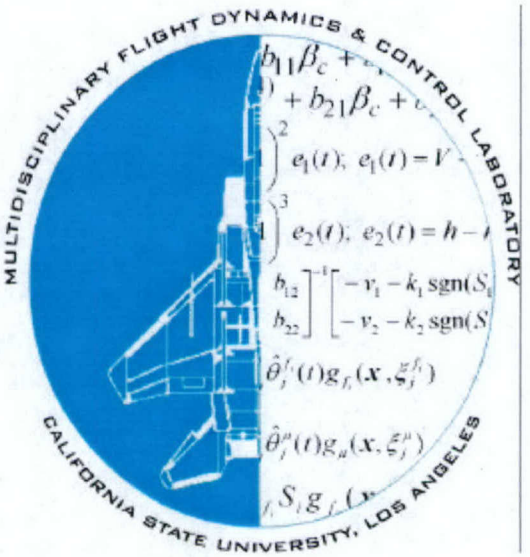

Appendix I


1. E. Kemper and C. Wu, "U.S.A.F. DIGITA DATCOM, TEST CASES", California State University, Los Angeles, California, 2001
2. C. Wu and M. Mirmirani, "Development of Multidisciplinary Analysis Software for Teaching and Research", NASA MU-SPIN/MURED Conference, Atlanta, Georgia, September 2000

## INTRODUCTION

Datcom is a program created by the U.S.A.F. to quickly estimate the aerodynamic stability and control characteristics of an aircraft or component of an aircraft. To examine the capabilities, limitations, and accuracy of Datcom, test cases were conducted for as many configurations and flight regimes as possible. When possible, the data obtained from Datcom was compared with existing data or from results obtained through other methods and software.

## TEST CASES

Test cases were conducted in every flight regime except for transonic flight. Datcom's ability to perform analysis in the transonic region is very limited and produced no results when tested. All test cases were run at normal atmospheric conditions at sea level and the Pitching Moment Coefficients are given with respect to the front of the vehicle.

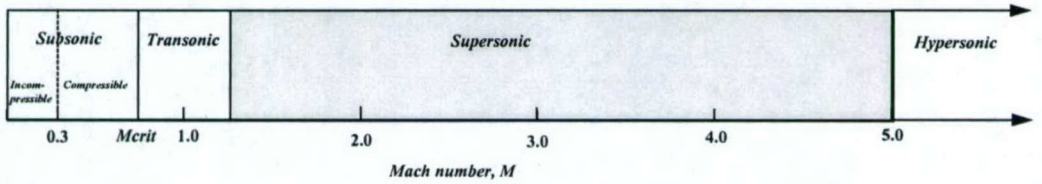


SUBSONIC

- Y-Wing
- Messerschmidt 262
- B-2 Stealth Bomber

SUPERSONIC

- F-16

HYPERSONIC

- X-43
- GHV
- BRV

## SUBSONIC

*Y-Wing*

The Y-Wing is a very simple wing designed for low velocities. It uses a NACA 0012 airfoil, has a wingspan of roughly 2 m, and chord lengths of roughly 1 m.

Assumptions: None

Results: Test case was run at Mach 0.6

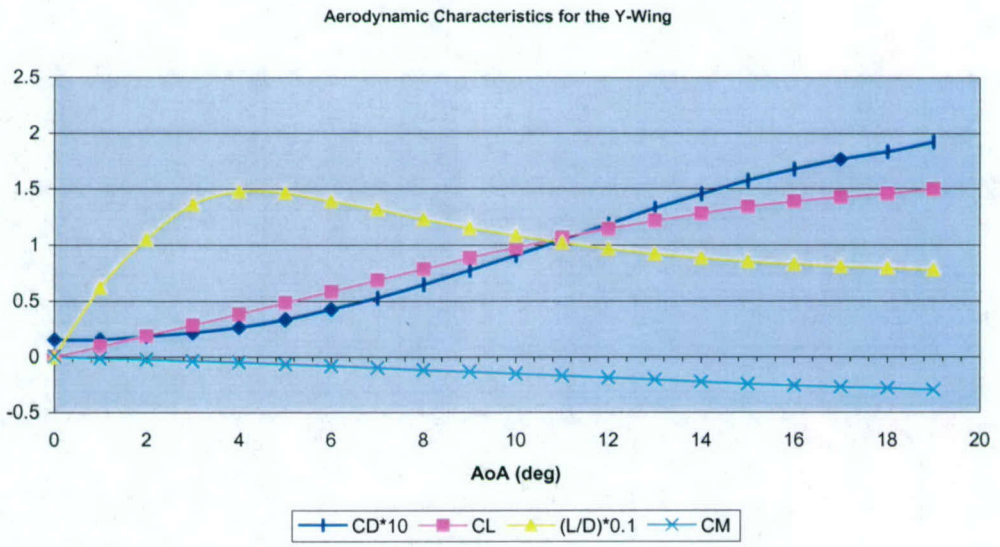

Normal and Axial Force Coefficients for the Y-Wing

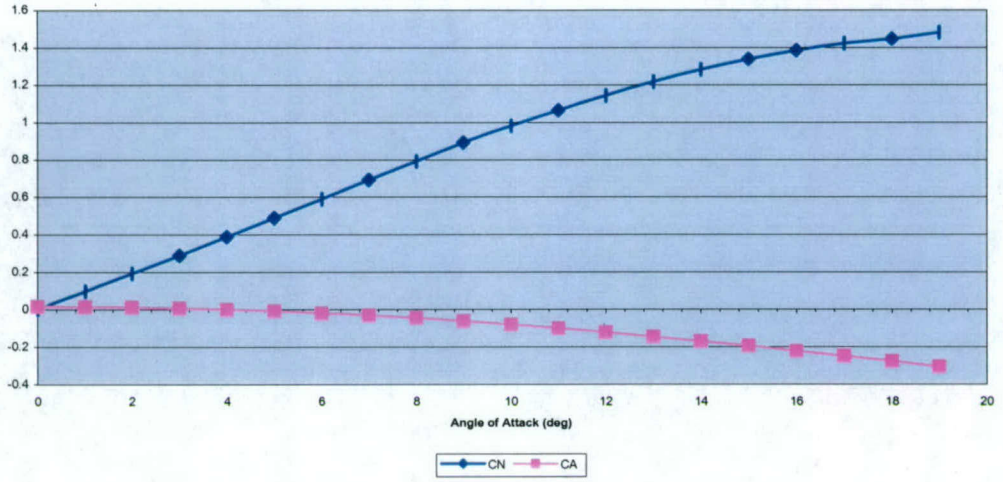


Pitching Angle Stability Derivatives for the Y-Wiing

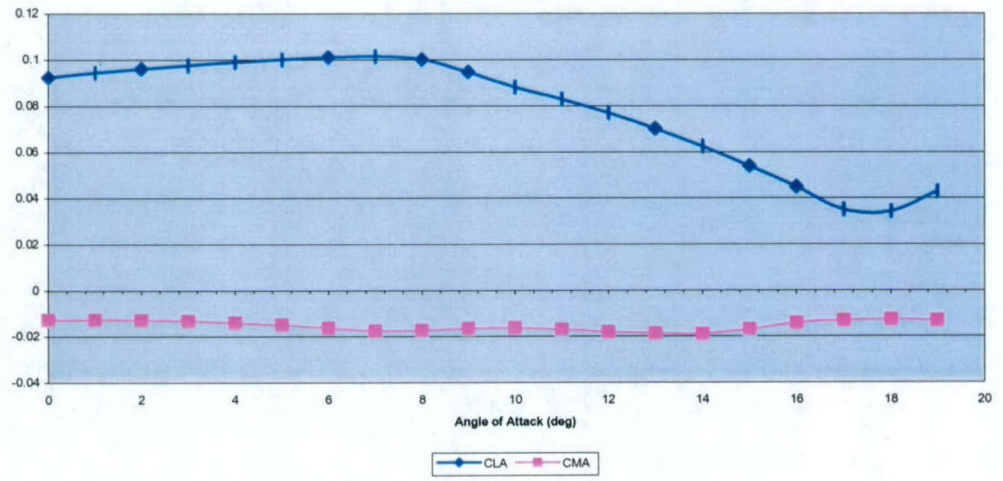

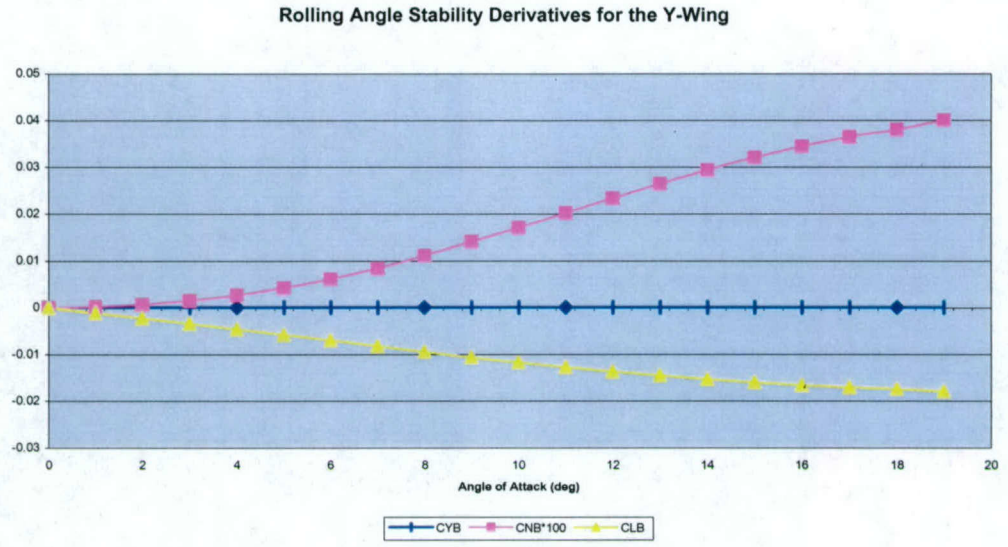


Datcom Analysis for Control Surfaces: Datcom is capable of analyzing the effects of control surfaces at deflected angles. A variety of different control surfaces can be analyzed for symmetrical and asymmetrical deflection angles. The changes in lift, maximum lift, minimum drag, and pitching moment coefficients are calculated for the control surface deflection angles. In addition, the change in induced drag is calculated for each deflection angle at each angle of attack specified. The following graphs are the results for a plain trailing edge flap used on the Y-Wing as shown in the following picture.

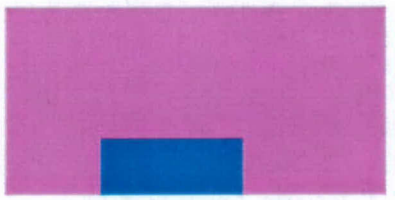

**Planform Geometry for Y-Wing with a plain trailing edge flap**

**Change in Aerodynamic Coefficients Due to Plain Flap Deflection for the Y-Wing**

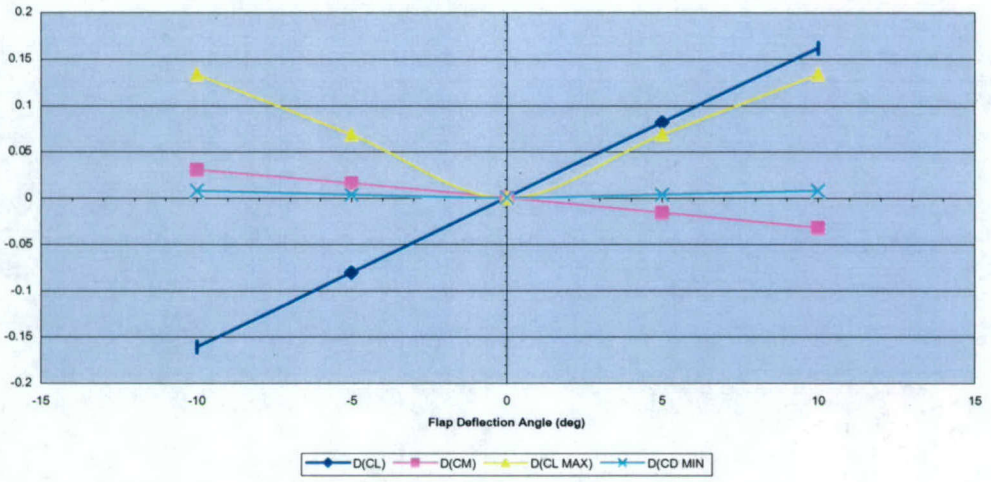


**Induced Drag Coefficient Increment Due to Flap Deflection for the Y-Wing**

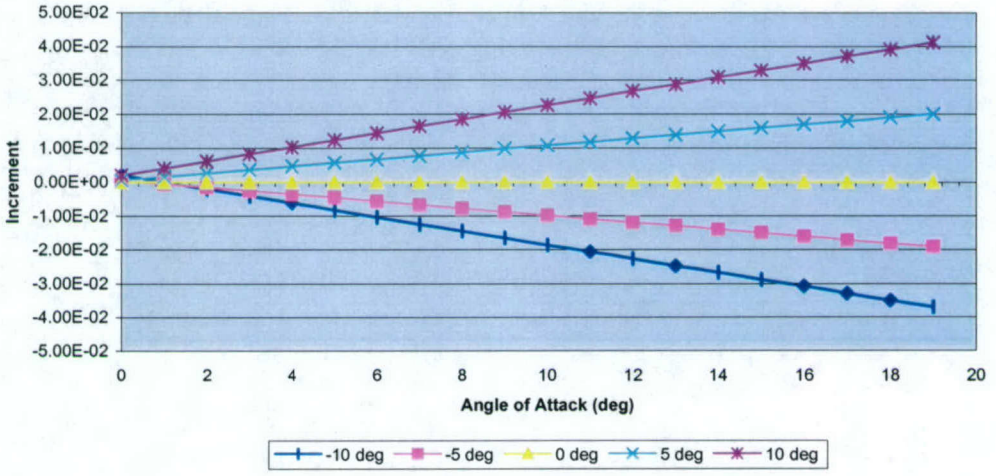

*Messerschmidt 262*

The Messerschmidt 262, or ME 262, is a WWII era jet fighter. It has very simple geometry making it a good test case for Datcom.

Assumptions: NACA 0012 airfoils used for wing, horizontal tail, and vertical fin. Jet engines and cockpit were neglected.

Results: Test case run at Mach 0.8

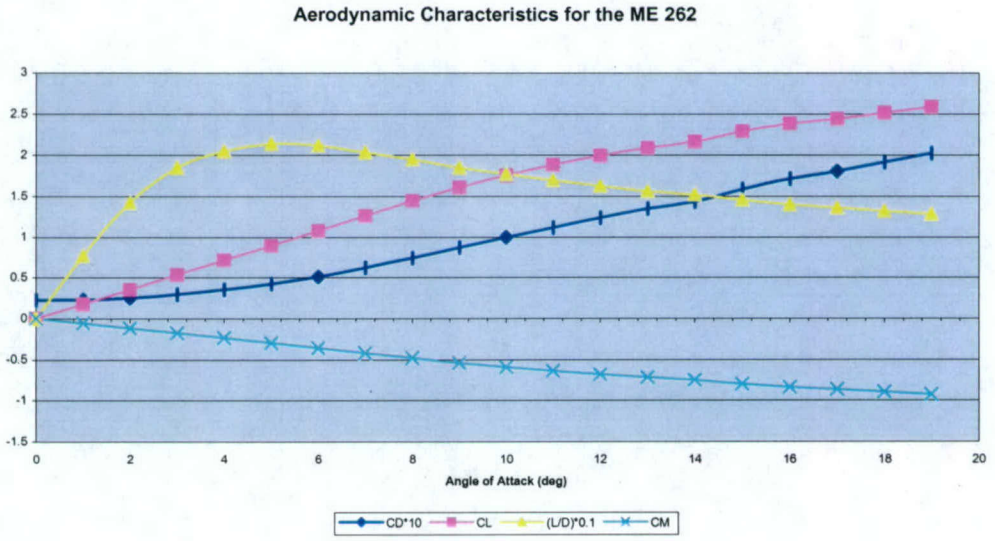

**Normal and Axial Force Coefficients for the ME 262**

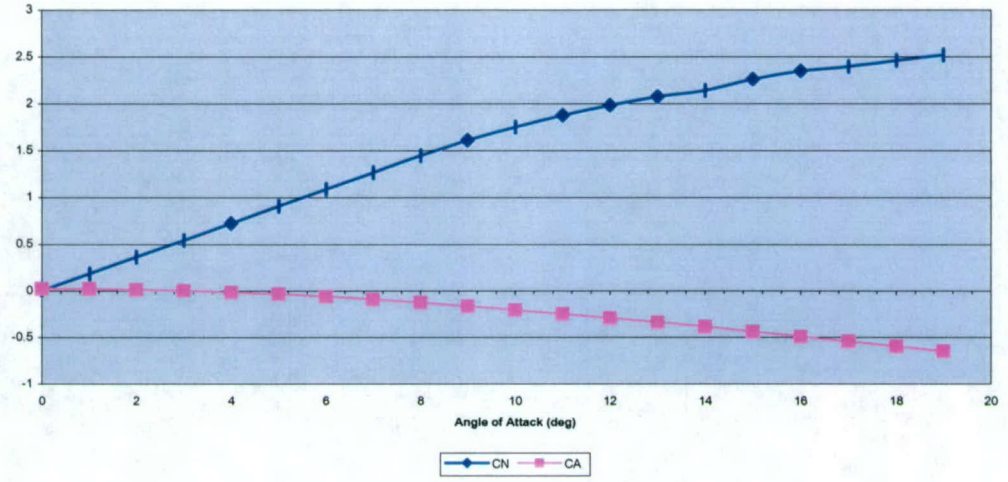


**Pitching Angle Stability Derivatives for the ME 262**

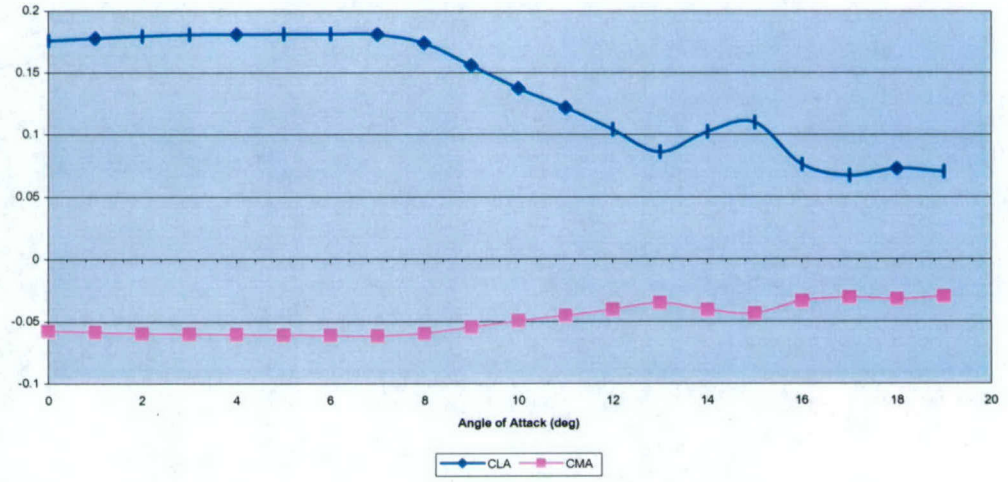

## Rolling Angle Stability Derivatives for the ME 262

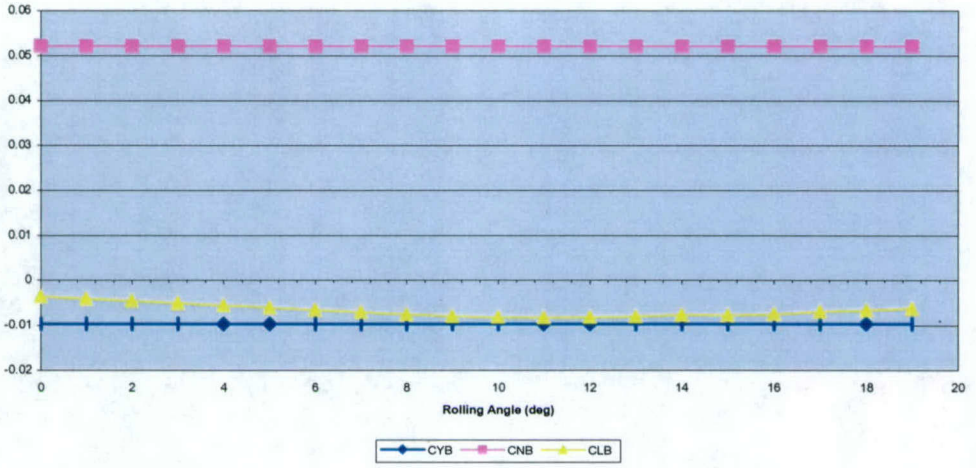

*B-2 Stealth Bomber*

The B-2 is a high subsonic flying wing.

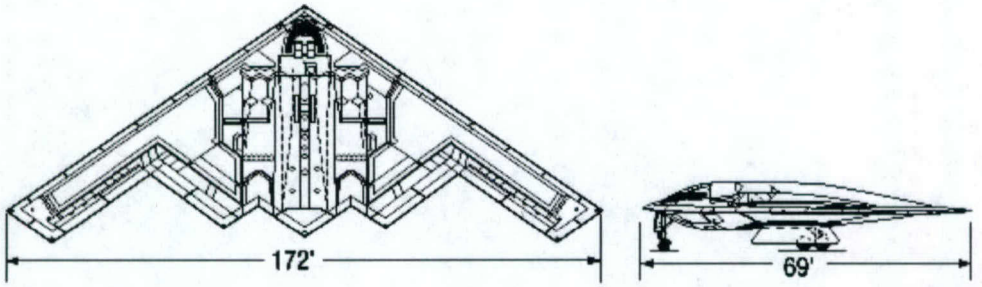


Assumptions: The B-2 was analyzed as a wing (no body) with a NACA 0015 airfoil. The tip chord was assumed to be parallel to the root chord. It is not possible to enter the complexities of the trailing edge of the wing so the B-2 was approximated with the following planform geometries.

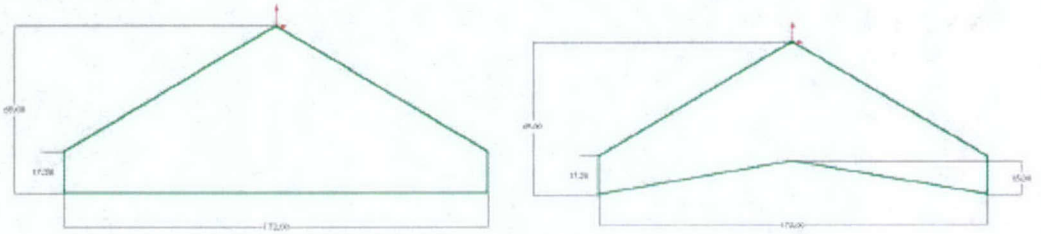

Results: The results for the B-2 with the two different planform geometries were close. The only significant difference was the reduced drag in the second geometry, which gave increased performance over the first geometry. The following two graphs are for the first and second planform geometries respectively.

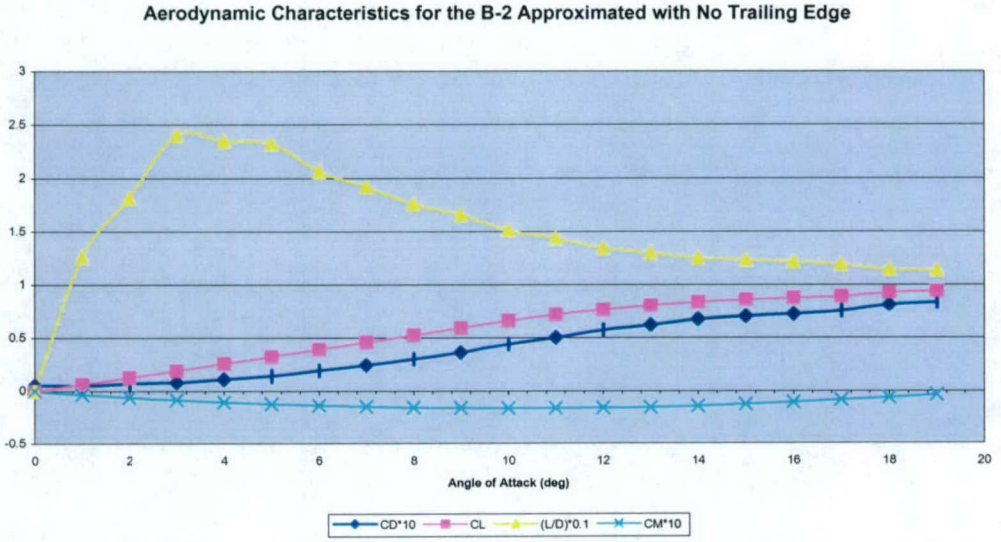

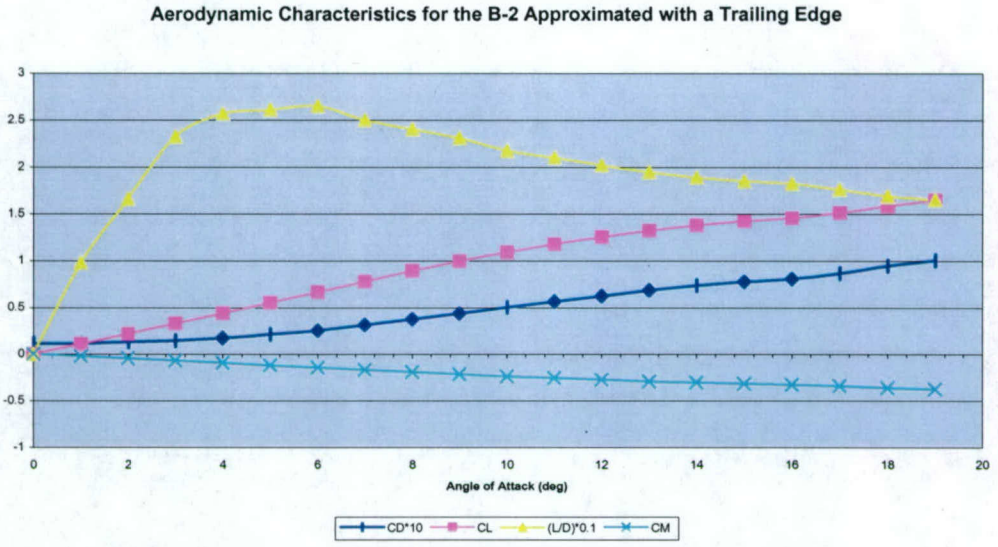


The following graphs are just for the second planform geometry.

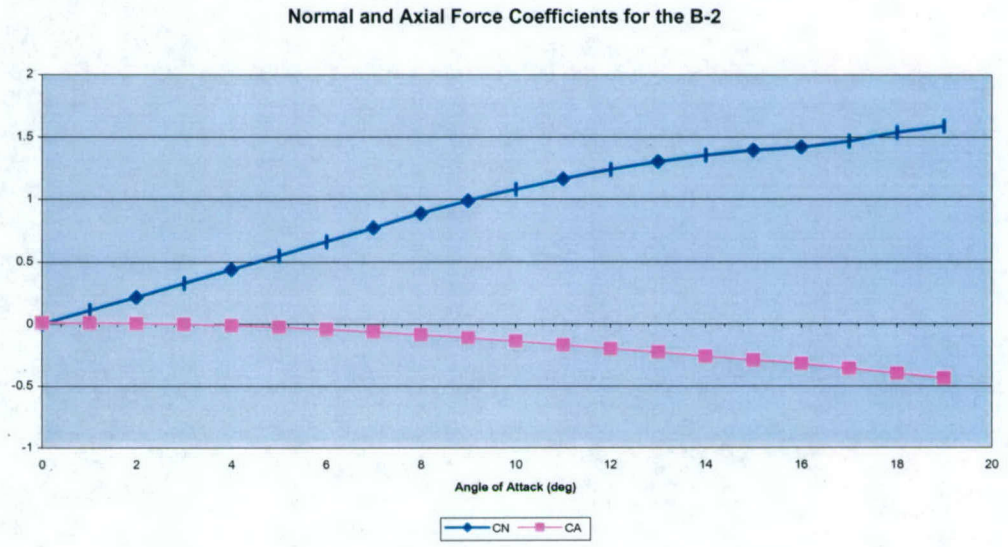

**Pitching Angle Stability Derivatives for the B-2**

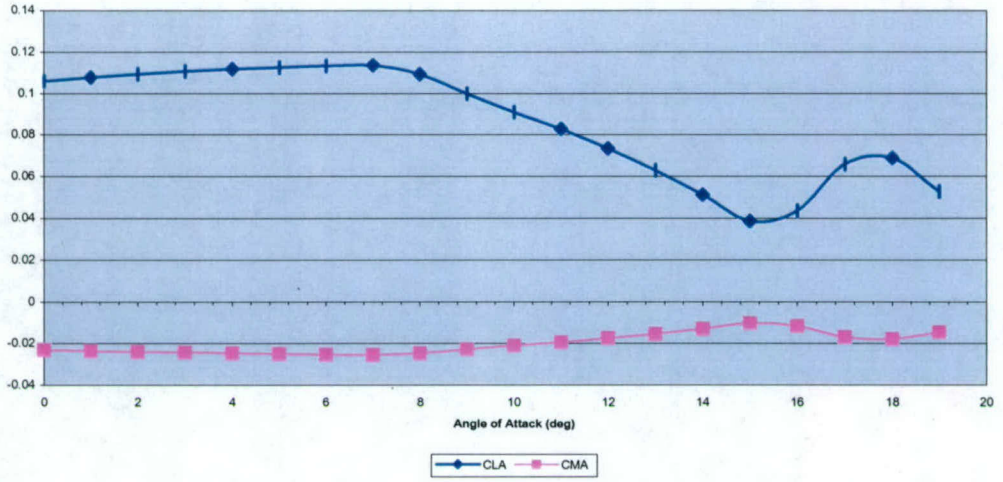


**Rolling Stability Derivatives for the B-2**

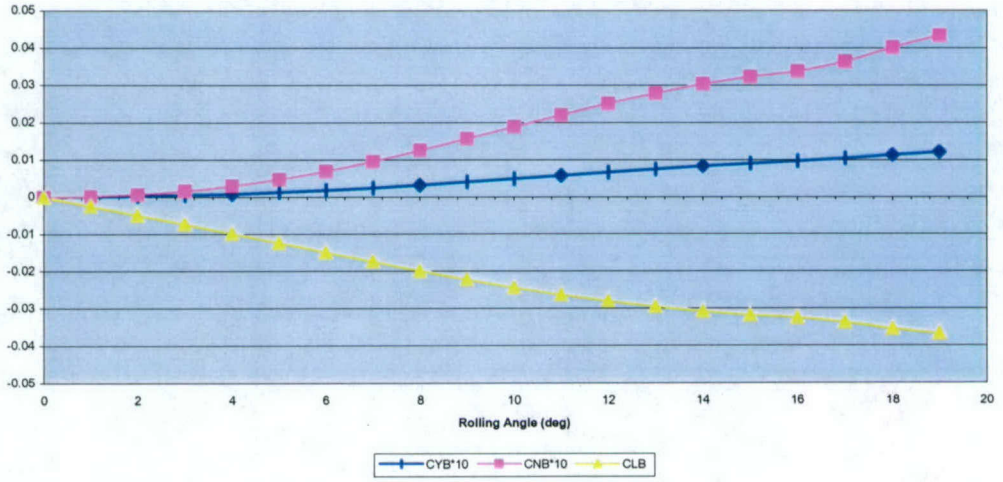

*F-16*

The F-16 is a supersonic jet fighter that typically flies at about Mach 2.0. The basic geometry of the F-16 is relatively simple. But there are some complex features, such as strakes, that cannot be analyzed with Datcom.

Assumptions: Stakes were neglected. The vertical fin, which is actually a series of smaller vertical fins, was analyzed as a single vertical fin. The small fins on the under-body were neglected. The horizontal tail was assumed to be continuous, neglecting the small gap between the rear of the tail and the engine.

Results: Test case was run at Mach 2.0

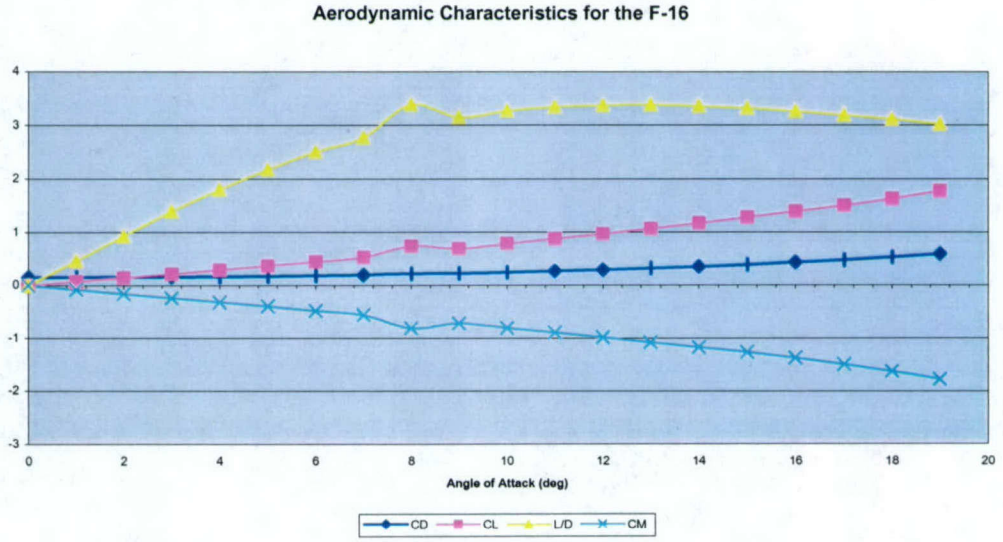

## Normal and Axial Force Coefficients for the F-16

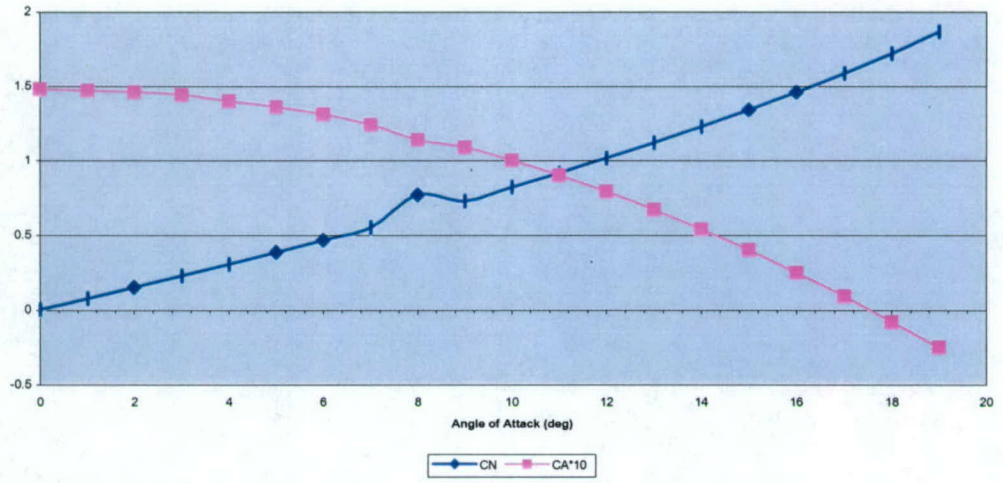


## Pitching Angle Stability Derivatives for the F-16

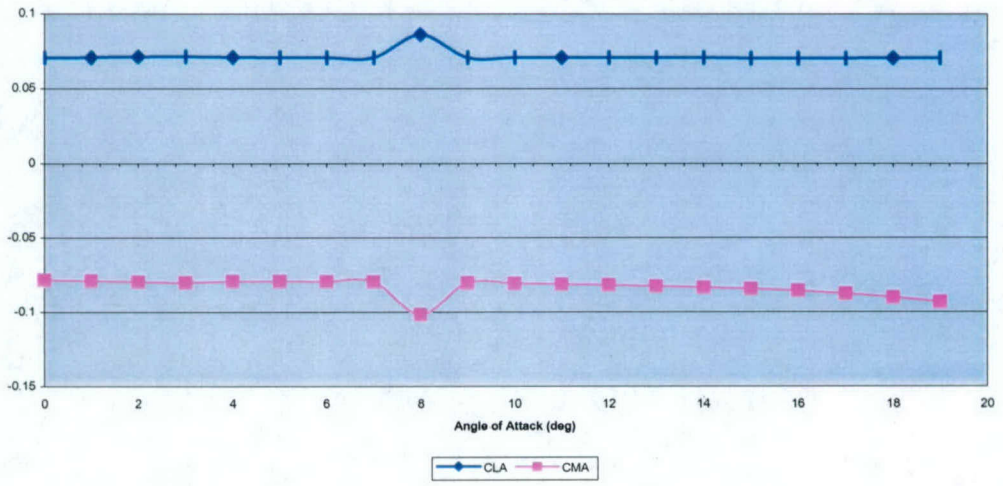

**Rolling Angle Stability Derivatives for the F-16**

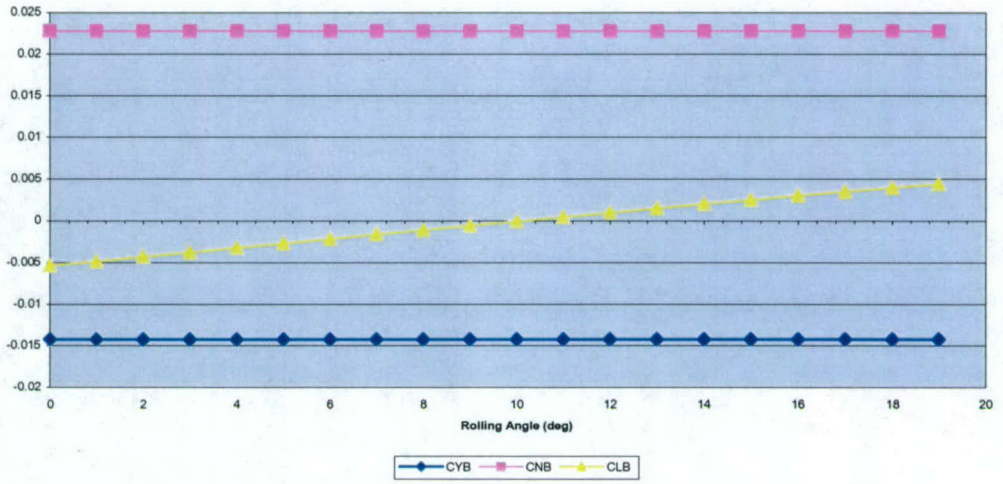

*Hyper X-43*

The X-43 is an experimental aircraft used to test the practicality of using a scramjet engine for hypersonic flight.

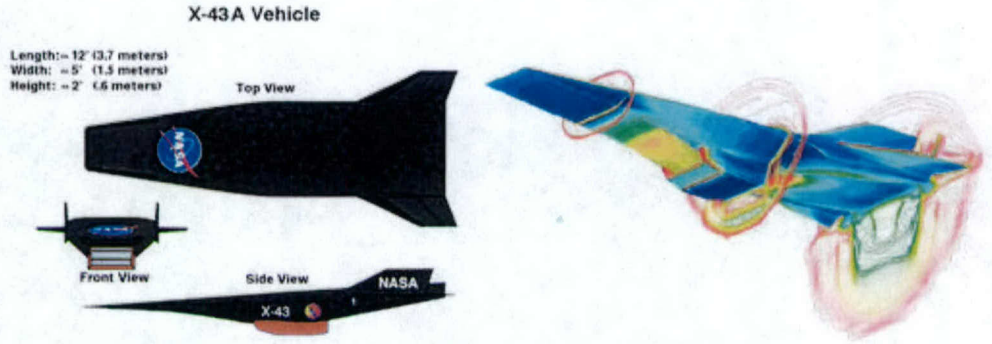


Assumptions: Datcom can only handle bodies of revolution or close approximation. Since the cross sections of the X-43 body are rectangular and trapezoidal they were approximated as elliptical cross-sections. For more information on this test case, see "Aerodynamic Analysis of the X-43 Hypersonic Vehicle using Datcom."

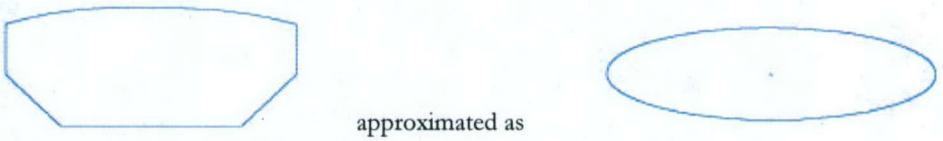


Results: Test case was run at Mach 10.0

## Aerodynamic Characteristics for the X-43

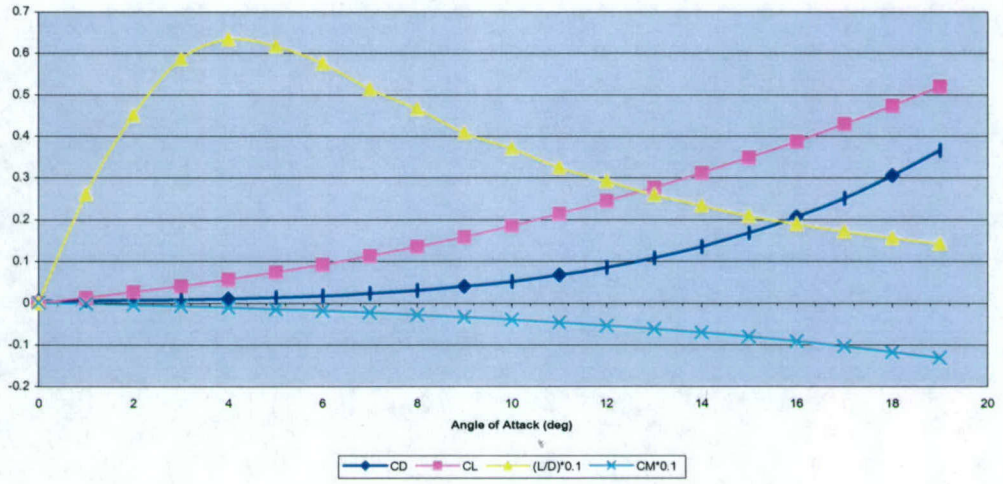


## Normal and Axial Force Coefficients for the X-43

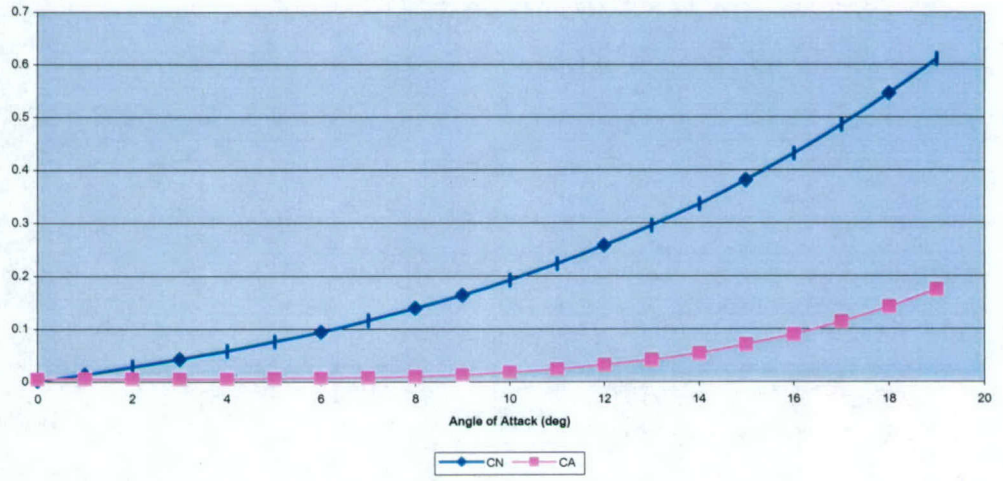

**Pitching Angle Stability Derivatives for the X-43**

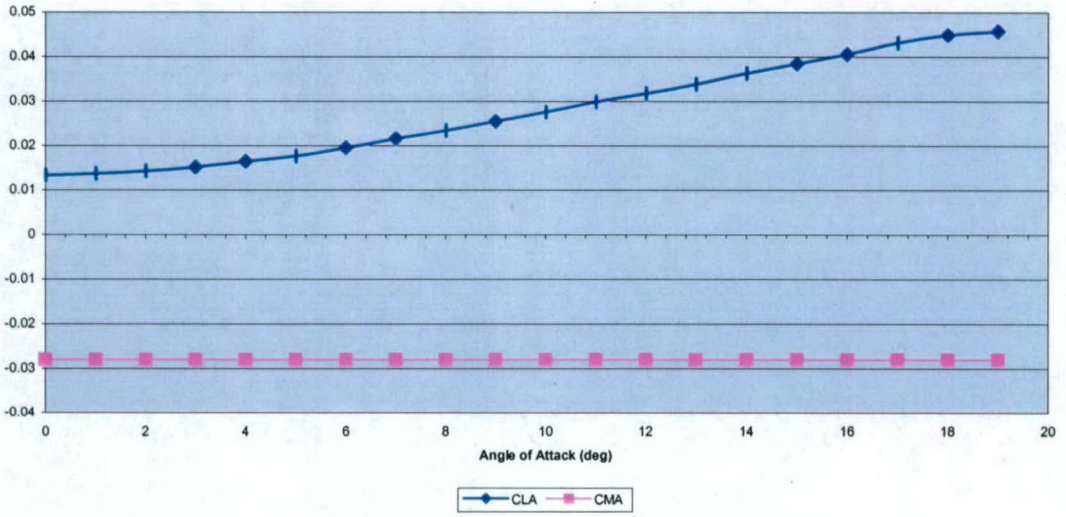


**Rolling Angle Stability Derivatives for the X-43**

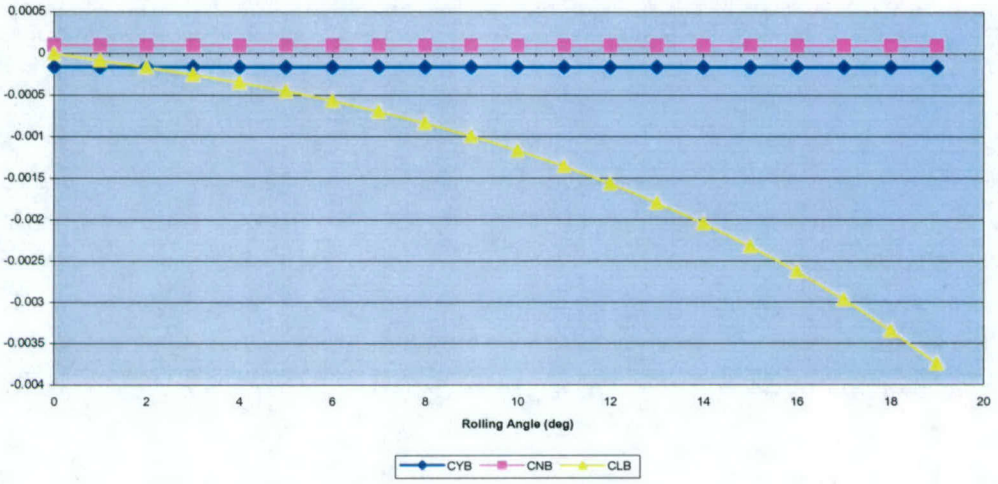

*Generic Hypersonic Vehicle (GHV)*

The GHV is a generic design for hypersonic vehicles. It has that basic properties that a hypersonic vehicle is believed it should possess: small wings at the rear of the vehicle, a relatively flat body, and a continual increase in body cross-section.

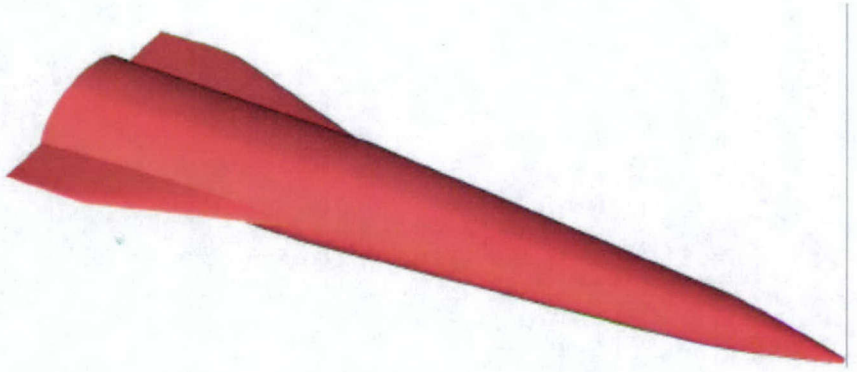

Assumptions: A very thin airfoil was used for the wing.

Results: Test case was run at Mach 10.0

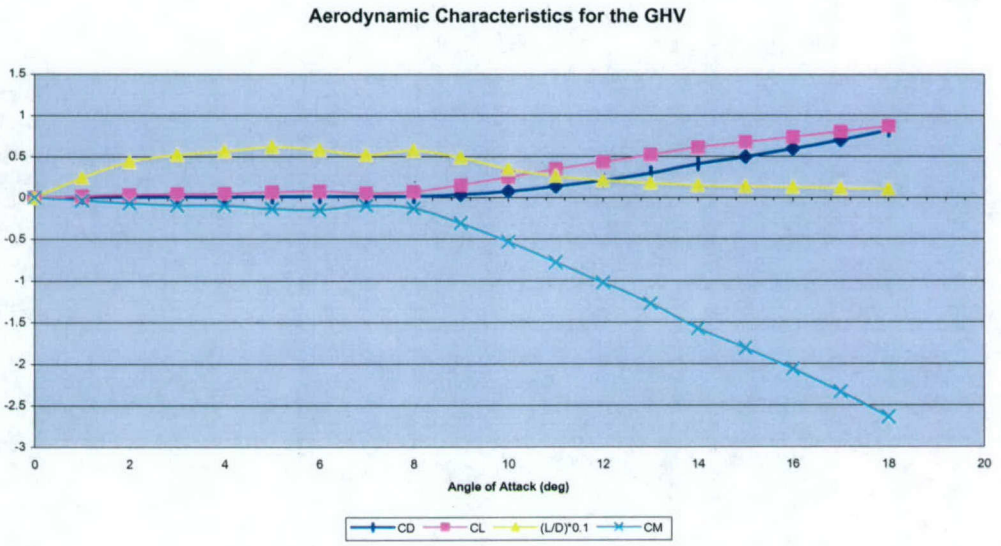

## Normal and Axial Force Coefficients for the GHV

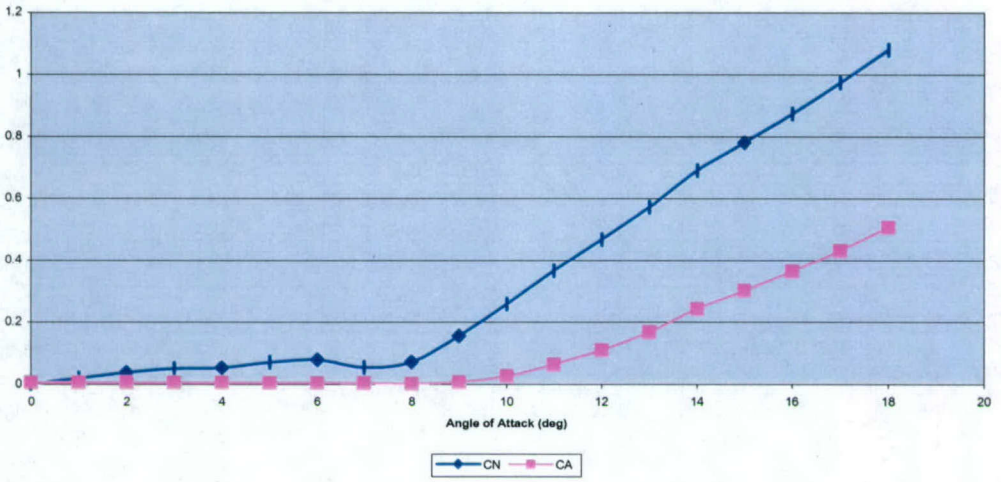


## Pitching Angle Stability Derivatives for the GHV

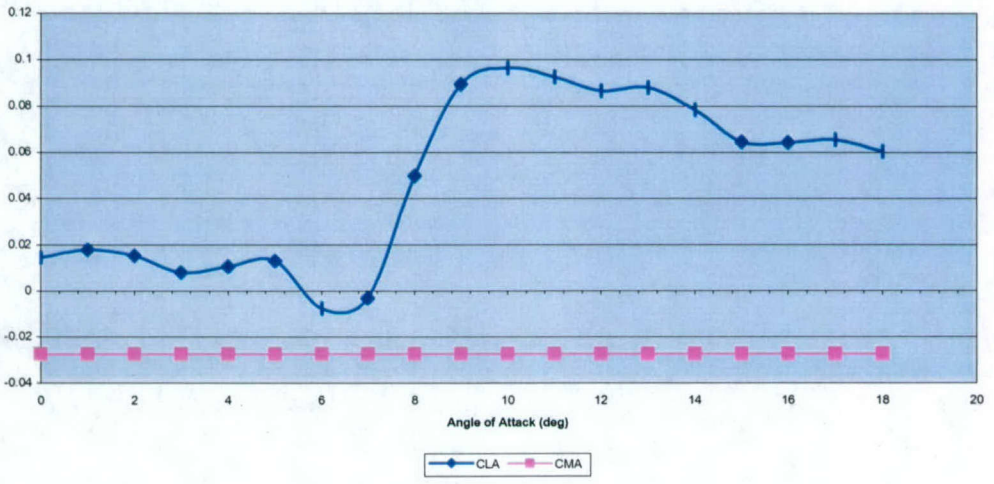

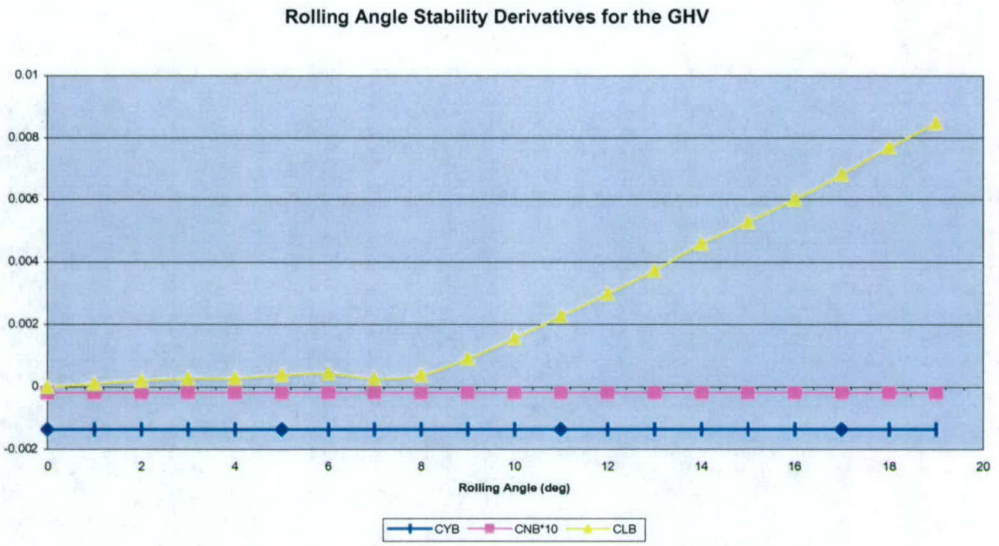


The following is a comparison done between the results obtained from Datcom and I-Newton.

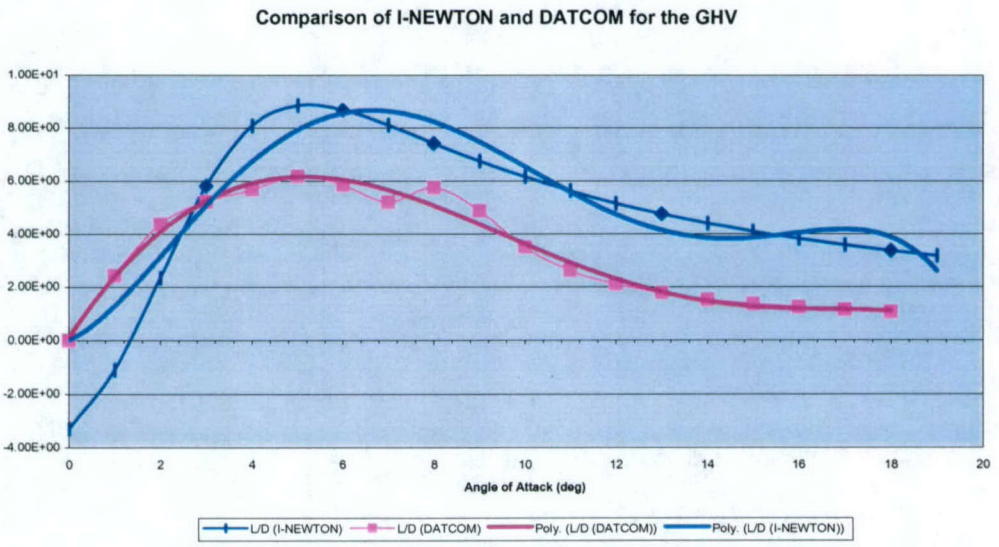

*Biconic Re-Entry Vehicle (BRV)*

The BRV was a concept considered for the entry into Mars' atmosphere to deliver a payload. It is not a vehicle designed for sustained flight.

Assumptions: None

Results: The test case was run at Mach 10.0 and analyzed as a body only.

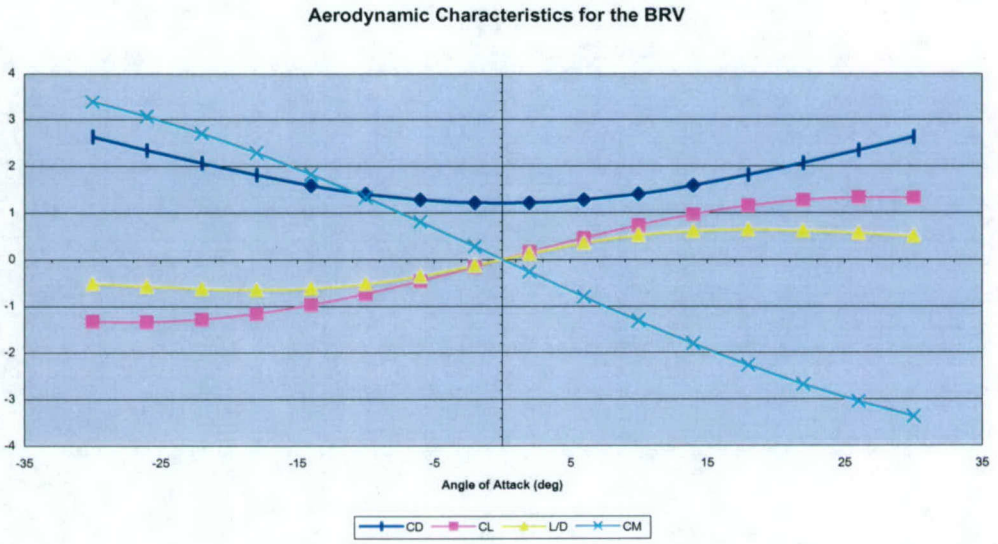

**Normal and Axial Force Coefficients for the BRV**

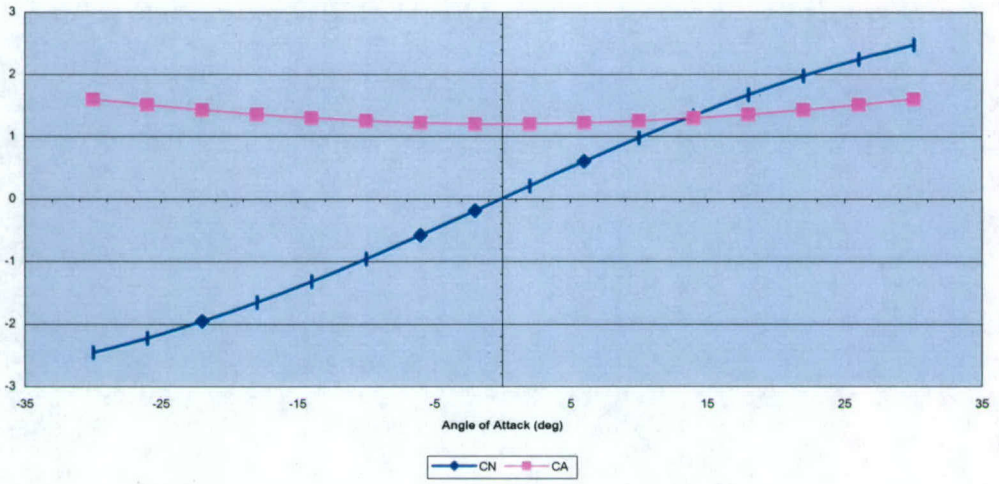


**Pitching Angle Stability Derivatives for the BRV**

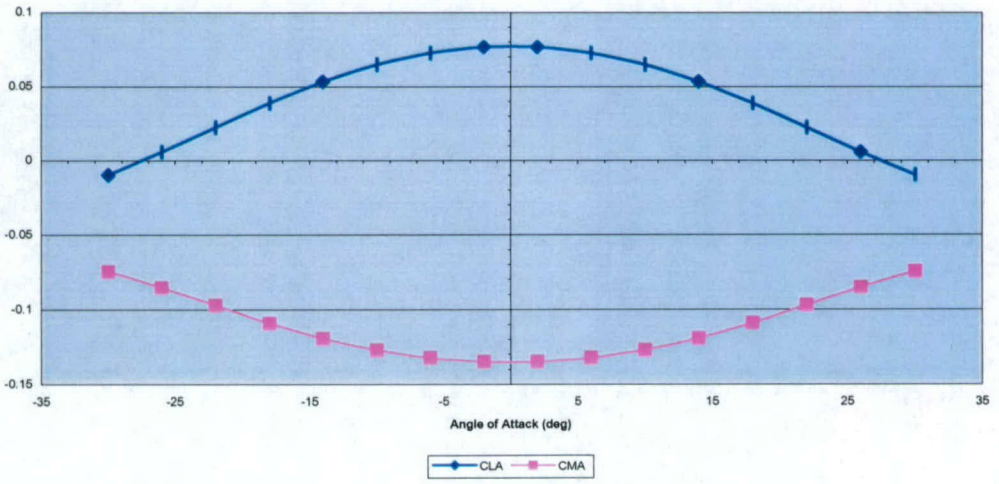

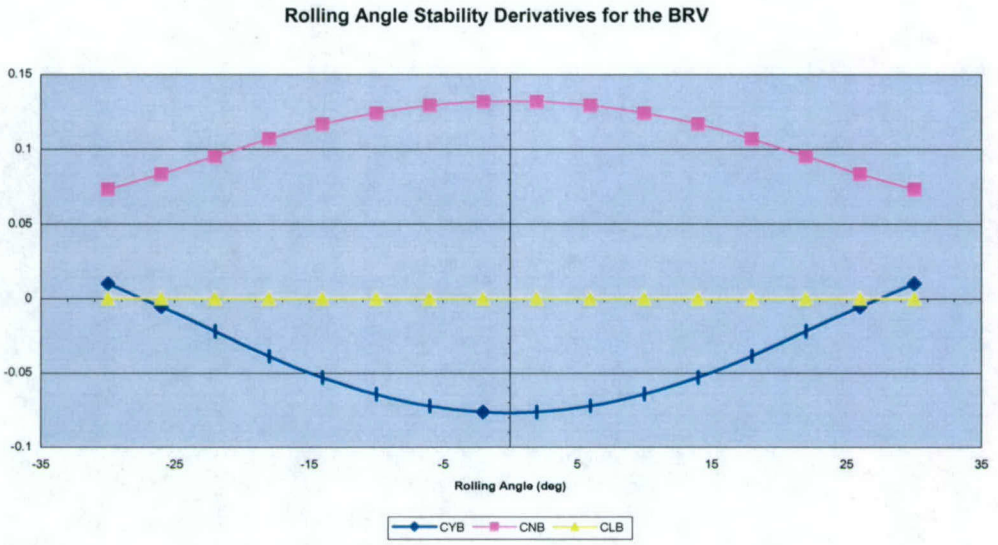


The following is a comparison of Datcom and I-Newton for the lift-to-drag ratios for the GHV. The values obtained from Datcom had to be scaled up by a factor of 10.

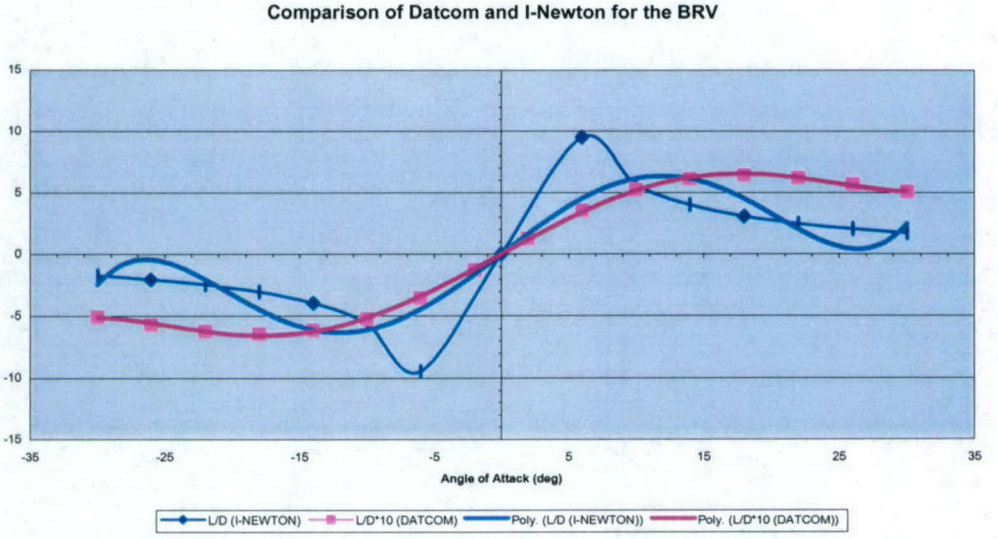

## CONCLUSION

Datcom is a good tool for getting a quick idea about the performance of an air vehicle. However, it is limited in the complexity of vehicle geometry it can analyze. From the results obtained in these test cases it is concluded that Datcom is best suited for subsonic analysis because air vehicles designed for this flight regime tend to have simple geometry. It can be used for supersonic and hypersonic flight regimes too but due to the complexities that vehicles designed for these regimes tend to have, assumptions must be made in most cases. If the number and size of the assumptions are small then Datcom can give reliable results. But if a lot of assumptions are needed to be made the results may become inaccurate and useless.

The translator developed for Datcom, called DatTrans, was used for all of the test cases.
These test cases were conducted as part of a project funded by NASA Dryden Research Center and the U.S. Air Force.

# Development of Multidisciplinary Analysis Software for Teaching and Research

**Chivey C. Wu, and Maj Mirmirani**
Department of Mechanical Engineering
California State University, Los Angeles
Los Angeles, CA 90032

## ABSTRACT

The integration and application of multidisciplinary computer-aided engineering (CAE) software to expedite the configuration and structural designs of aircraft are being attempted. Various interfaces and computer programs have been developed to transfer data between computer aided design (CAD) software, finite element analysis (FEA) codes, computational fluid dynamics (CFD) meshes and control system analysis programs to facilitate multidisciplinary analysis of a vehicle design. The structural, thermal, aerodynamic and control characteristics, and their interactions can be predicted. The computer codes, interfaces and data translators developed, and the modeling and simulation procedures are described herein. The modeling and multidisciplinary analysis of a generic hypersonic vehicle configuration is presented as a test case. The CAE software developed are used to support research projects on air vehicle design and analysis, and to enhance teaching of the emerging field of multidisciplinary engineering analysis.

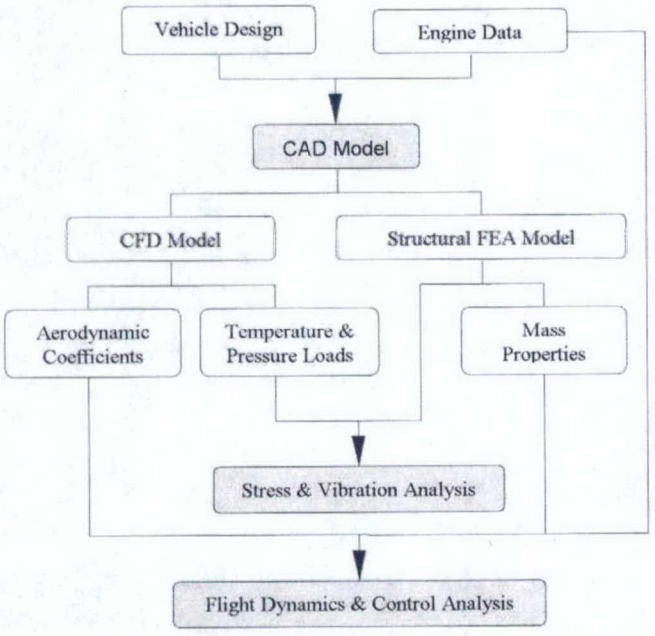


Fig. 1 *I-STARS* Multidisciplinary Analysis System

## INTRODUCTION

A few aircraft design software, such as AAA [1] and RDS [2], are commercially available to assist the design team to come up with a conceptual configuration, starting from a set of flight mission specifications. The methodology used is largely based on empirical data from existing aircraft of similar type. Only crude estimates of vehicle weight, aerodynamic characteristics and flight performance can be made at this stage. Wind tunnel models are subsequently built and tested, or CFD analyses are conducted to verify mainly the aerodynamic characteristics of the design. Then structural design is conducted to create the airframe for the chosen configuration. With modern solid modeling and Finite Element Analysis (FEA) software, structural analysis can then be performed. This cycle of configuration design, CFD analysis, solid modeling, structural design and analysis is often iterated many times before yielding a final design. It is anticipated that if multidisciplinary (CAD/FEA/CFD) analysis can be conducted concurrently once the concept vehicle is designed, the feasibility of the design can be determined at a much earlier stage. Consequently, the final design or comparable options can be determined in a much shorter time before committing expensive wind tunnel testing.

It is the objective of this project to develop and integrate appropriate CAE software to conduct multidisciplinary analysis for a given configuration design. The flow chart in Fig. 1 summarizes the concept and procedure developed for multidisciplinary analysis of flight vehicles.

## DEVELOPMENT OF SOFTWARE & INTERFACE

The first phase of the project has been focused on the development and testing of a graphical user interface (GUI), data translators for selected CAD, FEA, CFD and control simulation software, and specialized computer codes to integrate the design and analysis of flight vehicles. Structural Dynamics Research Corporation's (SDRC) *IDEAS* software was selected as the CAD modeling tool because of its comprehensive capabilities to create complex solid models, generate meshes, perform structural and thermal FEA, and export model data. The primary multidisciplinary FEA software used is *STARS*, developed at NASA Dryden Flight

Research Center by Gupta et. al. [3,4]. Specialized computer codes for estimating aerodynamic forces and stability derivatives on hypersonic vehicles, for interpolating aerodynamic pressure and thermal loads on FEA models, and for flight control simulation have also been developed.

## *IDEAS-STARS* DATA TRANSLATORS

While *IDEAS* is efficient in solid modeling and FEA simulations of structures, it does not have a CFD capability to predict the aerodynamics of the vehicle. On the other hand, *STARS* is capable of simulating interactions between aerodynamics, heat transfer, structure and controls, but lacks a GUI preprocessor for modeling and mesh generation.

In order to take advantage of the features of both software, it is necessary to develop a procedure in *IDEAS* to generate a CFD mesh along with the solid and structural FEA model, and translate both the CFD mesh and FEA model into input data for *STARS*. A computer program package written in C++, called *I-STARS* [5] has been developed to serve this purpose. It consists of the following components:

### CFD Mesh Translator (*I-STARC*)

Once the solid model of a vehicle configuration is created in *IDEAS*, an appropriate "airspace", i.e. the CFD domain, can be created around the model concurrently. Appropriate surface and volume grids for the CFD domain can be obtained by the automatic mesh generation capability in *IDEAS*. A procedure has been developed to write out data files containing the node coordinates, element connectivity and indices specifying the type of boundary conditions, etc. as needed for subsequent CFD analysis. A conversion program call *I-STARC* has been developed to translate these data into *STARS-CFD* input files, so that aerodynamic simulations can be conducted.

### Structural Finite Element Model Translator (*I-START*)

With the *IDEAS* solid model, finite element mesh for the surface and internal structure of the vehicle can be generated interactively. This could be a complex model containing different types of elements (shell, beam, plate, solid, lumped mass, etc.) and materials (isotropic, an-isotropic, laminated, etc.). A procedure has been developed to export information on the nodes, elements, material properties, loads and boundary conditions. A translator called *I-START* has been developed to convert all these data into *STARS* input files for structural FEA. It also imports pressure and temperature distributions, obtained from *STARS-CFD* simulation, as aerodynamic loads on the structural model.

## GRAPHICAL USER INTERFACE (*I-STARS* GUI)

A GUI system, called *I-STARS*, has been developed to link and execute the data translators, CAE software and utility programs interactively and more efficiently. It consists of the following components:

### *STARS-CFD* Virtual Wind Tunnel

This component of the GUI (Fig. 2) enables the user to run *I-STARC* and generate the *STARS-CFD* grid files, specify the free stream condition and CFD control parameters interactively. It executes the *STARS-CFD* code, then the aerodynamic force integration utility program once the solution converges. It provides the options for multi-angle of attack and multi-Mach number simulations. The result is a corresponding set of surface pressure and temperature distributions on the vehicle and overall aerodynamic coefficients.

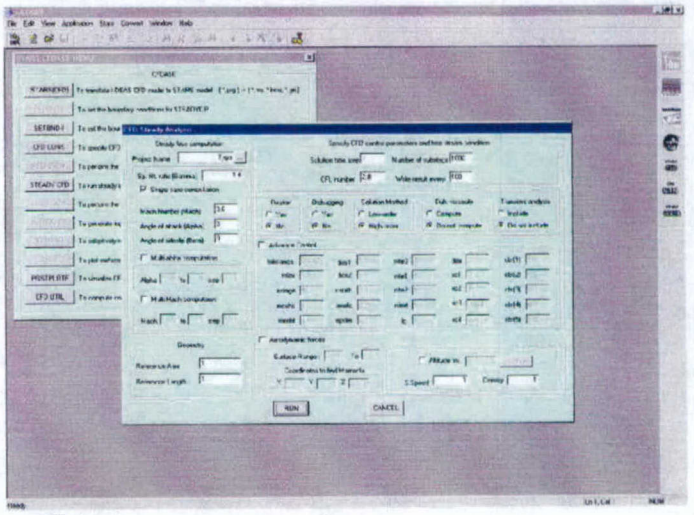

Fig. 2 *I-STARS* GUI – Virtual Wind Tunnel

### Hypersonic Aerodynamics Simulator

A relatively simple code called *I-NEWTON*, based on the modified Newtonian theory for hypersonic flow [6,7], has also been developed to quickly estimate aerodynamic coefficients and stability derivatives. This program employs the surface mesh generated from an *IDEAS* model to predict pressure distributions on the vehicle surface. Consequently, the overall aerodynamic forces can be integrated.

Another component of the GUI has been created to run this hypersonic aerodynamic code for multi-angle of attack and multi-Mach number simulations. A control surface activation sub-panel is also available in this GUI for updating the meshes of the control surfaces at specified deflection angles, so that aerodynamic coefficients and corresponding stability derivatives can be obtained interactively without the need to modify the solid model and regenerate the meshes.

### *STARS-SOLIDS* Structure Analyzer

This component of the GUI provides an interactive environment for executing *I-START* to translate *IDEAS* models into input data files for structural and heat transfer analyses with *STARS*, and import aerodynamic pressure and thermal loads from CFD results needed for static stress and aeroelastic analyses. It consists of several sub-panels designed for different types of analysis (static, vibration, thermal, etc.)

Flight Dynamics and Control Simulator

Longitudinal rigid body equations of motion were used to develop nonlinear control laws for flight vehicles. The equations contain mass and inertia properties, as well as aerodynamic characteristics of the vehicle. Two nonlinear control algorithms, one based on the sliding mode method [8,9], and one based on neural-adaptive techniques have been developed. The approach of the sliding mode control, also called (variable structure systems) is based on its ability to treat nonlinear time-varying, and uncertain systems in a straightforward manner. Equally, adaptive and neural control techniques are known to be the most suitable approach for systems with uncertain and changing dynamics. They are the most effective methods for control design for systems in which distributed dynamics are coupled with other system dynamics. The effects of structural dynamics, aeroelasticity and other unmodeled dynamics were included in the form of uncertainties in the internal and aerodynamic parameters.

A *SIMULINK*-based computer program called *I-CONSIM* has been developed to employ these control algorithms to conduct flight dynamics and control simulations. The top control panel of this simulator is illustrated in Fig. 3. Mass and inertia properties obtained from the FEA model, aerodynamic coefficients and stability derivatives obtained from *STARS-CFD* Virtual Wind Tunnel simulations, and engine data are imported via the plant module. Changes in flight condition are input to the sensor and the controller executes the simulation.

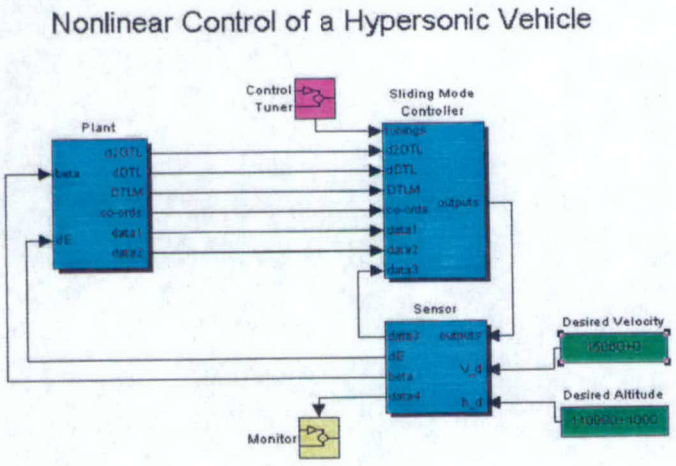


Fig. 3 *I-CONSIM* Flight Control Simulator

## TEST CASE: GENERIC HYPERSONIC VEHICLE

### SOLID MODEL AND STRUCTURE

To verify the software tools developed, multidisciplinary analyses for a generic hypersonic vehicle (GHV) design [5,10] were conducted as a test case. A solid model (Fig. 4) and a FEA model for the structure (Fig. 5) were created with *IDEAS*. The structure consists of thin shells, beams and plates made of various materials. The geometric and mass properties, which are necessary for aerodynamic, structural and flight dynamics control analyses, can be easily obtained from these models.

### CFD GRID & AERODYNAMIC ANALYSIS

A CFD mesh was generated around the solid model, as shown in Fig. 6. The surface pressure distribution on the vehicle obtained from a typical *STARS-CFD* simulation is presented in Fig. 7. Using the *I-STARS* GUI, it is a matter of routine to obtain aerodynamic coefficients at a various angles of attack and/or Mach numbers (Fig. 10). The *I-NEWTON* GUI quickly predicts the effect of control surface deflection at hypersonic speeds, as shown in Fig. 11.

### STRUCTURAL ANALYSIS

*STARS* FEA solution for static stress and deflection due to aerodynamic loading on the structure is given in Fig. 8, and a typical mode shape from vibration analysis is shown in Fig. 9.

### FLIGHT CONTROL SIMULATION

The mass properties and aerodynamic characteristics of the GHV were fed into the *I-CONSIM* flight control simulator, along with performance characteristics of a hypothetical engine. The vehicle response to reach a desired flight speed and altitude can be obtained. For a desired altitude change of 1000 ft, for instance, the corresponding change in elevator deflection angle and engine thrust with time are shown in Fig. 12 and Fig. 13.

## CONCLUSION

A set of computer codes and software interfaces have been developed to integrate design, modeling and analysis for air vehicles. Once a solid model of the design is created, corresponding finite element models for structural analysis and meshing for aerodynamic simulation can be generated. Multidisciplinary analysis involving interactions of aerodynamics, structure and longitudinal flight controls can then be conducted. It is anticipated that three-dimensional flight control simulator and aircraft design software based on sizing from the flight mission and performance requirements may be incorporated in the future. Refinement and optimization of configuration design can be achieved by iterations of this type of multidisciplinary CAE analysis. These CAE tools are being used to support multidisciplinary research projects and integrated into the engineering curriculum to enhance teaching in this emerging field.

## ACKNOWLEDGMENTS

This project was supported by NASA Dryden Flight Research Center under Grant No. NAG4-130 and NAG4-174.

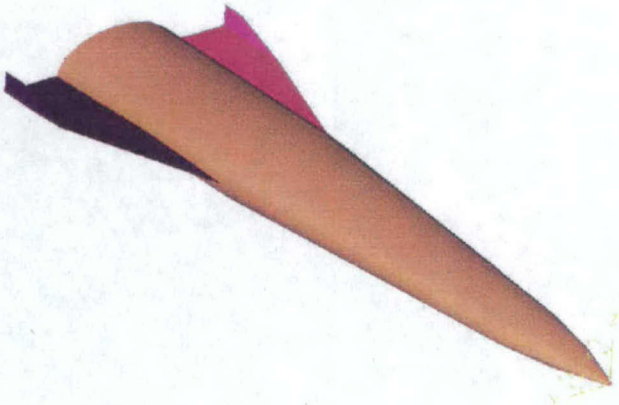

Fig. 4 GHV Solid Model

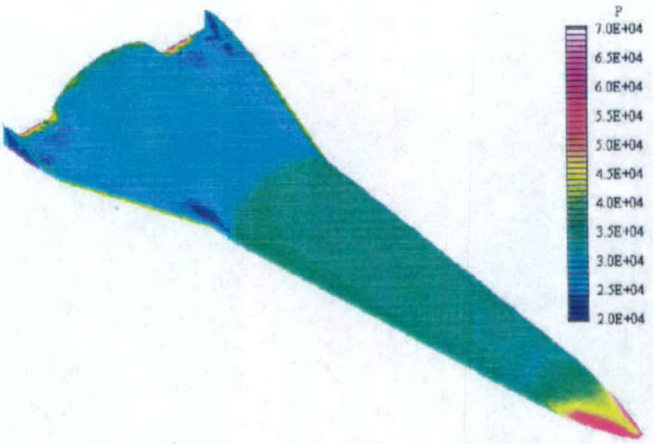


Fig. 7 CFD Results – Surface Pressure

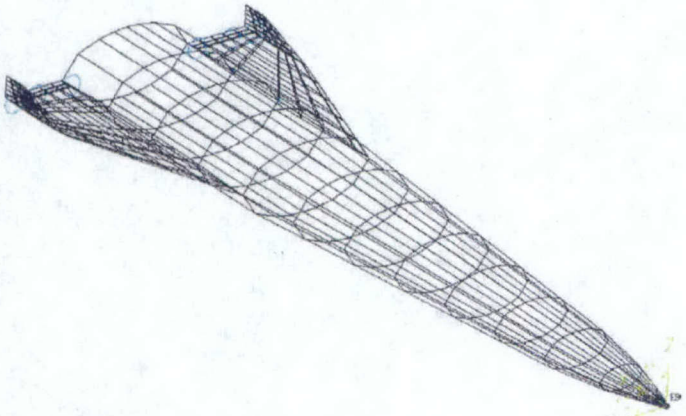

Fig. 5 FEA Structural Model

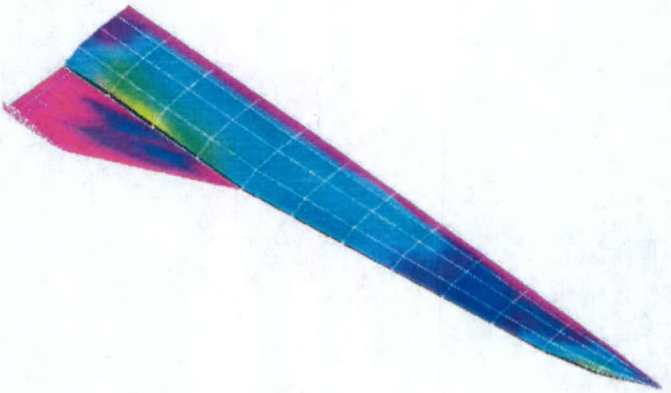

Fig. 8 Static Stress Analysis

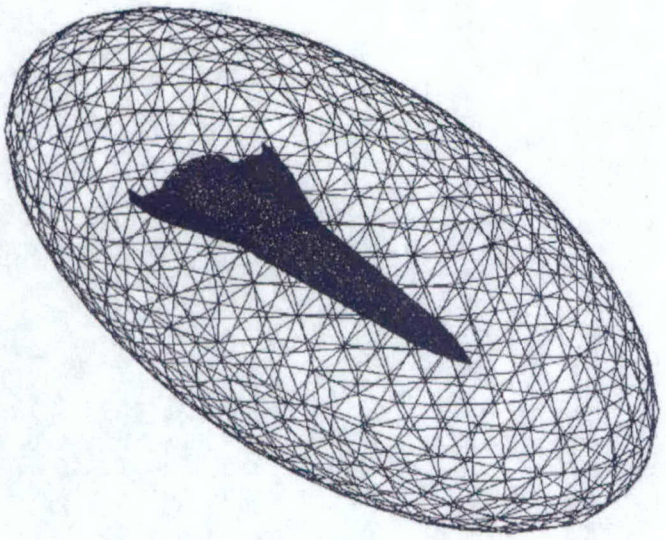

Fig. 6 CFD Mesh

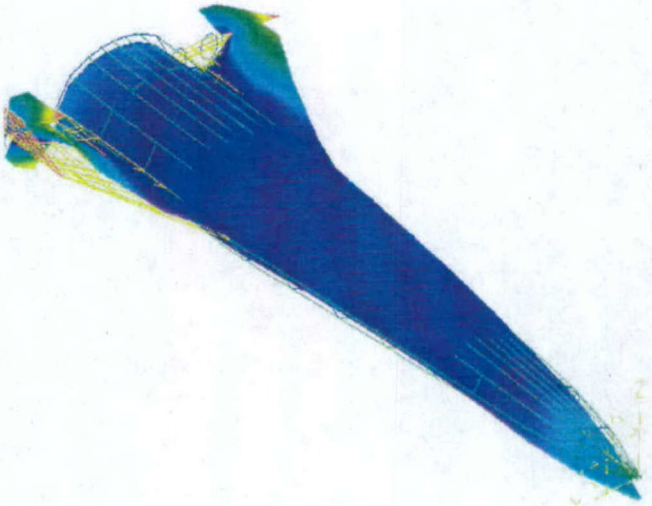

Fig. 9 Aeroelastic Analysis

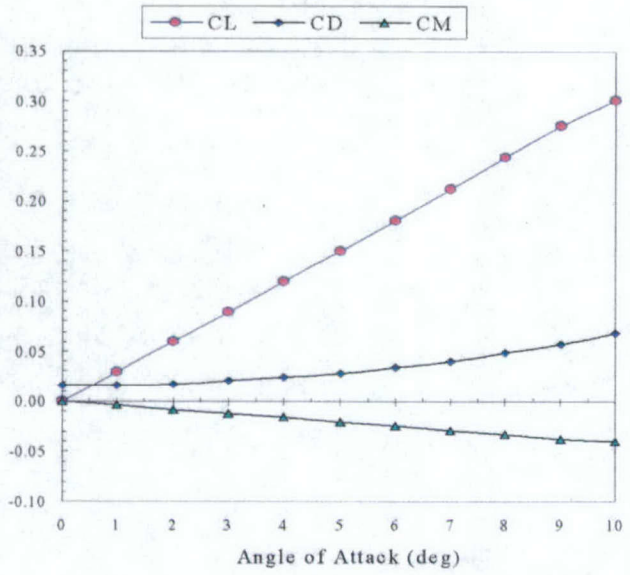


Fig. 10 Aerodynamic Coefficients at Mach 2

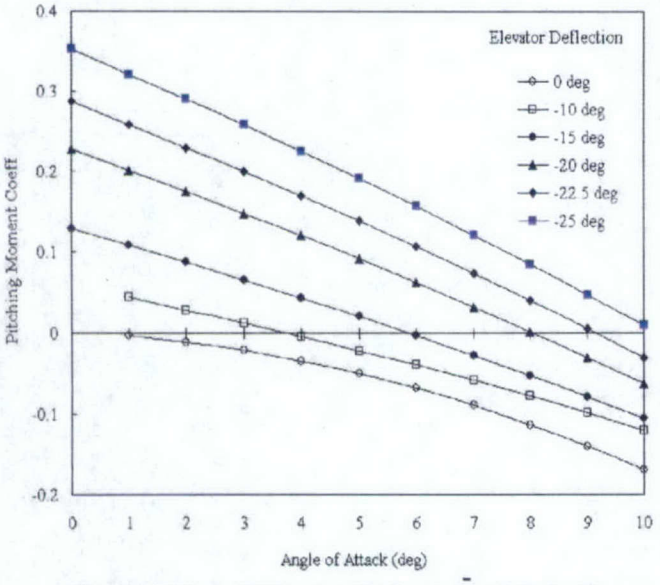


Fig. 11 Effect of Elevator Deflection at Mach 10

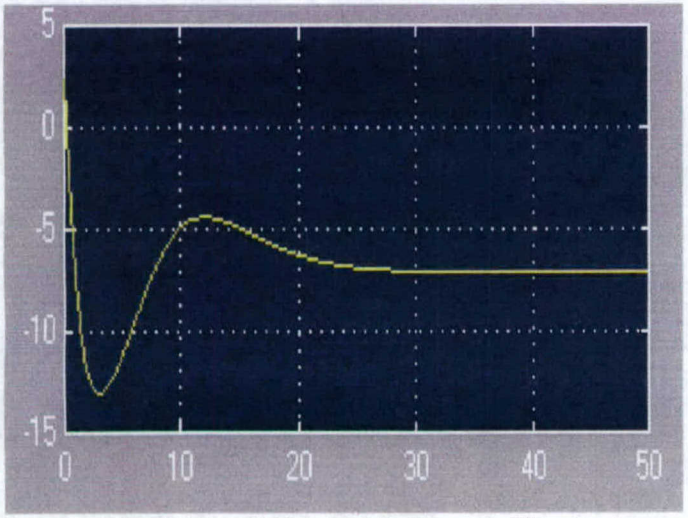


Fig. 12 Elevator Deflection (deg) versus Time (sec)

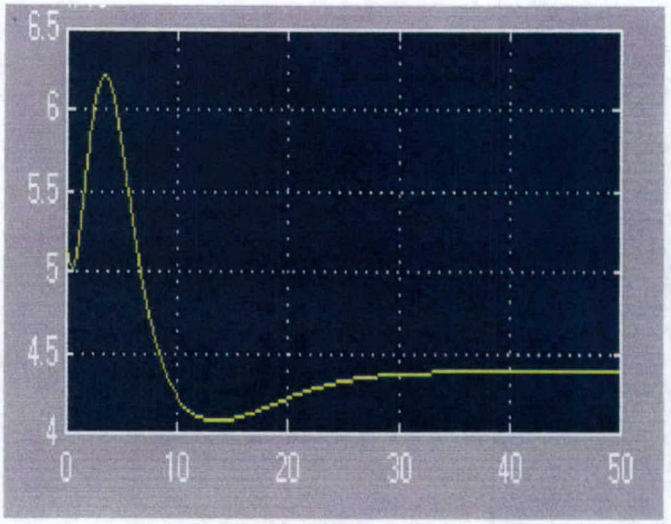


Fig. 13 Thrust (klbf) versus Time (sec)

## REFERENCES


1. Roskam, J., "Airplane Design, Part I-VIII," Roskam Aviation and Engineering Corporation, 1989.
2. Raymer, D. P., "Aircraft Design: A Conceptual Approach," AIAA Education Series, 1999.
3. Gupta, K. K., "STARS-An Integrated, Multidisciplinary, Finite Element, Structural, Fluid, Aeroelastic, and Aeroservoelastic Analysis Computer Program," NASA TM 4795, May 1997.
4. Gupta, K. K. and Meek, J. L., "Finite Element Multidisciplinary Analysis," AIAA Education Series, 2000.
5. Ho, K., "Development and Application of An Interface Between a Solid Modeler and a Multi-Disciplinary Finite Element Analysis Code," CSULA M.S. Thesis, 1999.
6. Bertin J. J. and Smith M. L., "Aerodynamics for Engineers," 3rd Ed., Prentice-Hall, 1998.
7. Wood, W. A., "Hypersonic Pitching-Moment Shift for Stardust Reentry Capsule Forebody," NASA TM 97-206266, Oct. 1997.
8. Tournes C. and Shtessel Y. B., "Aircraft Control Using Sliding Mode Control," AIAA Paper 96-3692, 1996.
9. DeCarlo, R. A., Zak, S. H. and Matthews, G. P., "Variable Structure Control of Nonlinear Multivariable Systems," Proceedings of the IEEE, Vol. 76, No. 3, 1988.
10. Spain, C. V., Soistmann, D. L., Parker, E. C. and Gibbons, M. D., "An Overview of Selected NASP Aeroelastic Studies at the NASA Langley Research Center," AIAA Paper 90-5218, 1990.


## CONTACT


Dr. Chivey Wu, Professor of Mechanical Engineering
California State University, Los Angeles, CA90032.
E-mail: *cwu@calstatela.edu*
Web: *www.calstatela.edu/faculty/cwu/cwu.htm*

Appendix II


1. Y. Huo, P. Ioannou and M. Mirmirani, 'Fault-Tolerant Control and Reconfiguration for High Performance Aircraft: Review', USC CATT Technical Report, Nov 1, 2001,
2. H. Xu and M. Mirmirani, "Robust Adaptive Sliding Mode control Design for a Class of MIMO Nonlinear Systems," Proceedings of the AIAA Guidance, Navigation and Control Conference, Montreal, Canada, August 2002
3. H. Xu, P. Ioannou and M. Mirmirani, 'Adaptive Control For A Class Of Large Scale Nonlinear Systems', accepted in *International Journal of Control,* to appear in 2005
4. H. Xu, M. Mirmirani, and P. A. Ioannou, "Adaptive sliding mode control design for a hypersonic flight vehicle", *AIAA Journal of Guidance, Control, and Dynamics*, Vol. 27, No. 5, September–October 2004 (presented in Appendix D)
5. Y. Huo, M. Mirmirani, P. Ioannou, and R. Colgren, "Adaptive Linear Quadratic Design with Application to F-16 Fighter Aircraft," AIAA Guidance, Navigation, and Control Conference and Exhibit, Providence, Rhode Island, August 2004

# Fault-Tolerant Control and Reconfiguration for High Performance Aircraft: Review

Ying Huo[*] Petros A. Ioannou[#] and Majdedin Mirmirani[£]

[*#] Dept. of Electrical Engineering-Systems

University of Southern California

Los Angeles, CA 90089

[£] Dept. of Mechanical Engineering

California State University, Los Angeles

Los Angeles, CA 90032

[*] email: yhuo@usc.edu, ( tel ) : 1-213-740-6257

[#] email : ioannou@usc.edu, ( tel ) : 1-213-740-4452, ( fax ) : 1-213-740-4418

[£] email : mmirmir@calstatela.edu, ( tel ) : 1-323-343-4492, ( fax ) : 1-323-343-5004

Nov 1, 2001

---

This work has been supported by the Air Force Office of Scientific Research Grant # F4920-01-0489.

**Abstract**

Fault-tolerant control of high performance aircraft is an important area that needs to be developed in order to meet strict performance, safety requirements, and mission satisfaction, especially when operating under adverse flying conditions. The purpose of this paper is to review and present in a compact form a wide range of techniques and approaches developed over the years in the area of fault detection, isolation and control reconfiguration that are applicable to aircraft.

# 1. Introduction

The aim of a fault-tolerant control scheme is to maintain system stability and retain acceptable performance under system failures. Research into fault-tolerant control and applications has attracted more and more attention and references can be found in, for example, Looze et al. (1985), Joshi (1987), Dittmat (1988), Wu (1992), Rauch (1995), Makila et al. (1995), Elaine et al. (1998), Blanke et al. (1997), Stoustrup and Niemann (2001). With the development of modern air vehicles fault tolerant flight control system (FTFCS) has become a critical in the operation of high-performance airplanes, space vehicles, and structures, where safety and mission satisfaction are among the main concerns. With a FTFCS system the flying aircraft can maintain good performance even with impairments to actuators, sensors or control surfaces, and thus increase survivability, and probability of mission success.

With the FTFCS flight is possible even in the presence of failures, however, it may be necessary to modify the control surfaces and reconfigure the control law. Fault-tolerant control methods can be classified into two categories: Those based on fault detection and isolation and those that are independent of fault diagnosis. The first uses on-line fault detection and isolation to monitor the system and when fault occurs the control laws are redesigned to ensure that the faulty system maintains satisfactory performance, i.e., active fault-tolerant controller design. The second is based on designing fixed controllers without consideration of whether the fault has occurred or not. If the effects of certain faults and modeling errors are alike, a fixed robust controller can be carefully designed to achieve fault-tolerance to these faults, which is the so-called passive approach to fault-tolerant control (Eterno et al. 1985, Horowitz et al. 1985, Williams et al. 1990, Jaxobson and Nett 1991,Veillette et al. 1992, Marrison and stengel 1998). Clearly, fixed controllers don't work well for those 'additive' faults that have additive effects on the input/output signals. If the additive faults are physically inseparable from the signal flow in nominal case it is sometimes impossible to use one fixed controller to deal with all possible faulty conditions. Another drawback of the passive fault-tolerant controller is that in the faulty situation

all the damaged signals will be used in the closed-loop system so that stability and performance cannot be guaranteed (Patton 1997). In this paper our emphasis will be on the first category where an overview of methods of fault diagnosis and controller reconfiguration for aircraft is presented.

Fault detection and isolation (FDI) is a critical part of a FTFCS and it is expected to provide warnings and diagnostic information as soon as the failure develops, so that the controllers are reconfigured and further deterioration is prevented. According to generally accepted terminology, the task of the FDI consists of (Gertler 1988, Patton 1991):

- Fault detection, i.e., the indication that something is going wrong in the system.
- Fault isolation, i.e., the settlement of the exact location of the failure.
- Failure identification, i.e., the determination of the size of the failure.

According to the depth of the information used of the physical process, the approaches to the problem of failure detection and isolation fall into two major categories:

- Methods that make use of the quantitative plant model, or, model-based FDI;
- Methods that do not depend on the quantitative model of the plant, or, model-free FDI.

This paper is organized as follows: Section 2 is devoted to methods used in model-based FDI. Section 3 discusses the robustness problems in model-based FDI. The model-free FDI approaches are discussed in section 4. Control reconfiguration is discussed in section 5.

## 2. Model-based Fault Detection and Isolation

A wide class of FDI methods makes explicit use of a mathematical model of the plant, and is referred to as model-based FDI. This approach is motivated by the conviction that deeper knowledge of the system results in more reliable diagnostic decisions. In the last 20 years different approaches for fault detection using system mathematical models have been developed in the following categories: observer-based method, parity space approach, eigenstructure assignment, frequency domain design, parameter identification and nonlinear techniques ( see, e.g. Willskey 1976, Isermann 1984, Gertler 1988, Frank 1990 ). The dynamics of an aircraft are

well studied leading to accurate mathematical models and diagnosis techniques as presented in Deckert, *et al.* (1977), Chandler (1989), Ioannou *et al.* (1989), and Polycarpou (1994).

The main idea behind the model-based FDI is 'analytical redundancy,' the comparison of measurement data with prior known mathematical model of the physical process (Chow and Willsky 1984, Patton 1991). Analytical redundancy is preferable to 'hardware redundancy' in that analytical redundancy offers a simpler, flexible structure, with less equipment and cost (Gertler, 1993).

In this section the concept of model-based FDI is elaborated further by discussing the mathematical models of systems in faulty and fault-free states. Section 2.2 presents a general description of the steps required in model-based FDI, and the remaining two sections give an outline of different methods used in model-based FDI as they apply to aircraft dynamics.

## 2.1 Mathematical Model of a System with faults

Most model-based FDI methods are based on linear dynamic models. In the case of a non-linear system, these methods rely on model linearization around an operating point. Although aircraft dynamics are inherently nonlinear, aerodynamic nonlinearities generally are smooth enough in a trimmed flying condition to warrant linear design techniques (Stengel 1993).

For modeling purposes, an aircraft system with faults can be separated into three subsystems: actuators, aircraft dynamics and sensors as illustrated in figure 1.

[ Insert figure 1 here. ]

In figure 1, $u(t)$ is the known input vector, $y(t)$ is the vector of measured output signals corrupted by sensor faults; $u_R(t)$ , $y_R(t)$ is the actual input and output signals of the aircraft dynamics respectively, and $u_R(t)$ is corrupted by actuator faults. The system dynamics shown in figure 1 can be described by a state-space model as:

$$\begin{cases} \dot{x}(t) = Ax(t) + Bu_R(t) + f_c(t) \\ y_R(t) = Cx(t) + Du_R(t) \end{cases} \tag{1}$$

where $x(t)$ is the state vector, $A,B,C,D$ are matrices of appropriate dimensions, and $f_c(t)$ represents the effect of possible component faults. Substituting in (1)

$$u_R(t) = u(t) + f_a(t), \quad f_a(t) - \text{actuator fault}$$

$$y(t) = y_R(t) + f_s(t), \quad f_s(t) - \text{sensor fault}$$

the model of the dynamic system becomes

$$\begin{cases} \dot{x}(t) = Ax(t) + Bu(t) + Bf_a(t) + f_c(t) \\ y(t) = Cx(t) + Du(t) + Df_a(t) + f_s(t) \end{cases} \tag{2}$$

which can be represented in the general compact form

$$\begin{cases} \dot{x}(t) = Ax(t) + Bu(t) + R_1 f(t) \\ y(t) = Cx(t) + Du(t) + R_2 f(t) \end{cases} \tag{3}$$

where $f(t) = [f_a(t) \quad f_c(t) \quad f_s(t)]^T$ is a $q \times 1$ fault vector, with each element corresponding to a specific fault.

An input-output transfer matrix representation for the system with possible faults is then described as:

$$y(s) = G_p(s)u(s) + G_f(s)f(s) \tag{4}$$

where

$$\begin{cases} G_p(s) = C(sI - A)^{-1}B + D \\ G_f(s) = C(sI - A)^{-1}R_1 + R_2 \end{cases}$$

From a practical point of view, it is reasonable to make no further assumptions about the fault modes but consider them as unknown functions of time. The corresponding distribution matrices $R_1$ and $R_2$ of faults are usually assumed to be known (Frank 1994, Chen and Patton 1999).

## 2.2 Residual Generation and Evaluation

A traditional method of detecting faults is to use limit checking, i.e., to compare process variables with preset limits. Then exceeding of a limit indicates a fault situation. Although simple, this method has a serious drawback in that the process variables may be varying with

different operating states, thus the check limit is dependent on the operating state of the process. As a different indication of occurrence of faults, residual signals are quantities that represent the inconsistency between the actual system variables and those generated from the mathematical model. They are independent of the system operating state and respond only to faults, which makes it a direct development of the limit checking method (Chen and Patton 1999).

In model-based FDI, faults are detected by setting a threshold (fixed or variable) on the residual signal where the exceeding of the threshold indicates a fault occurrence. A number of residuals can be designed, each having special sensitivity to individual faults. Figure 2 illustrates the conceptual structure of a model-based fault diagnosis system comprising two stages of residual generation and decision-making (Chow and Willsky 1984, Isermann 1997).

[ Insert figure 2 here. ]

The residual signal, $r(t)$, carries information on the time and location of the faults. It should be near zero in fault-free case and deviate from zero when a fault occurs. The decision process evaluates the residuals and monitors if and where a fault has occurred.

A typical structure of a residual generator is shown in figure 3, which involves processing of the input and output data of the system (Basseville 1988, Gertler 1988).

[ Insert figure 3 here. ]

The simplest approach to residual generation is the use of system duplication. That is, system $F_1$ is designed to be the aircraft system model and $F_2$ is set to be identity, thus the signal $z$ is the simulated output of the system and the residual $r$ is the difference between the calculated output $z$ and the real output signal $y$. The disadvantage of this method is that the stability of the model $F_1$, referred to as the simulator, cannot be guaranteed when the system being monitored is unstable. A direct extension of the simulator-based residual generation is to replace the simulator by an output estimator, as shown in figure 4 (Patton 1991).

[ Insert figure 4 here. ]

(Beard 1971, Frank 1990) or a Kalman filter in the stochastic case (Willsky 1976, Basseville 1988). The flexibility in selecting the observer gains has been studied by (Frank and Ding 1997).

In practice, it is desired to estimate a linear function of the state, i.e. $Lx(t)$, using a generalized Luenberger observer with the following structure

$$\begin{cases} \dot{z}(t) = Fz(t) + Ky(t) + Ju(t) \\ w(t) = Gz(t) + Ry(t) + Su(t) \end{cases} \tag{7}$$

where $z(t)$ is the state vector of the observer, which is an estimate of a linear function of the state $x(t)$, say, $Tx(t)$, and $F, K, J, R, G$ and $S$ are matrices derived according to the following conditions

$$\begin{cases} F \text{ has stable eigenvalues} \\ TA\text{-}FT = KC \\ J = TB - KD \\ RC + GT = L \\ S + RD = 0 \end{cases}$$

It is worth noting that in the case of a full order observer $T = I$. If the above conditions are satisfied and there are no faults, we can establish that

$$\lim_{t \to \infty} [z(t) - Tx(t)] = 0,$$

and $w(t)$ converges to $Lx(t)$ exponentially fast. If the matrix $L$ is taken to be $L = C$, then the residual vector is defined as

$$r(t) = Q[y(t) - \hat{y}(t)] = L_1 z(t) + L_2 y(t) + L_3 u(t) \tag{8}$$

where $\hat{y}(t) = w(t) + Du(t)$ is the estimate of the output vector, and

$$\begin{cases} L_1 = -QG \\ L_2 = Q - QR \\ L_3 = -Q(S + D) \end{cases}$$

From Eq. (7) and (8) we obtain the following expression for the residual vector

$$r(s) = [L_1(sI - F)^{-1}K + L_2]y(s) + [L_1(sI - F)^{-1}J + L_3]u(s) \tag{9}$$

This structure is expressed mathematically as:

$$r(s) = \begin{bmatrix} H_u(s) & H_y(s) \end{bmatrix} \begin{bmatrix} u(s) \\ y(s) \end{bmatrix} = H_u(s)u(s) + H_y(s)y(s) \tag{5}$$

where $H_u(s)$ and $H_y(s)$ are transfer matrices with stable poles to be designed. In order to guarantee that the residual is zero for the fault-free case the following condition must hold

$$H_u(s) + H_y(s)G_p(s) = 0 \tag{6}$$

Eq. (5) is a generalized representation of all residual generators. The design of the residual generator involves the selection of the transfer matrices $H_u(s)$ and $H_y(s)$. Usually, residuals are generated using analytical approaches, such as observers, parameter estimation or parity equations based on analytical redundancy (Clark, 1989, Ding et al. 1992, Patton et al, 1994, Wang et al. 1996, Chen et al. 1996, Stoustrup et al. 1999). It is important to note that the function of the residual generator is not to estimate the state of the plant but rather to respond promptly to the occurrence of a fault (Patton and Lopez-Toribio 1999).

For residual evaluation the residual generator must posses the following properties of fault detectability and isolability (Frank 1994, Gobbo and Mapolitano 2000).

Fault detectability—A fault $f_i(t)$ is said to be detectable if $g_{fi}(s) \neq 0, \forall s$ where $g_{fi}(s)$ is the $i$ th element of the transfer matrix $G_f(s) = \begin{bmatrix} g_{f1}(s) & \cdots & g_{fq}(s) \end{bmatrix}^T$ defined in Eq.(4).

The detectability condition $g_{fi}(0) \neq 0$ is evident because otherwise the fault effect on the residual will disappear although the fault still exists in the system.

Fault isolability— A fault is isolable if it is distinguishable from other faults using one residual set (or a residual vector) and such residual set is said to have the isolability property.

In the following subsections we present several residual generation approaches.

### 2.2.1 Observer-based Residual Generation

The basic idea of the observer or filter-based approach is to estimate the states or the outputs of the system from the measurements using either a Luenberger observer in the deterministic case

Let us define $e(t) = z(t) - Tx(t)$ to be the observer error, which in the absence of faults converges to zero exponentially fast. The dependence of the residual vector on the fault is obtained using Eq.(3) and (9) that

$$\begin{cases} \dot{e}(t) = Fe(t) - TR_1 f(t) + KR_2 f(t) \\ r(t) = L_1 e(t) + L_2 R_2 f(t) \end{cases} \tag{10}$$

It follows from Eq. (10) that at steady state the residual signal will depend only on the faults. The observer-based residual generator always exists because any input-output transfer function matrix with no zero-pole cancellations has an observable realization (Chen and Patton 1999).

### 2.2.2 Parity Space Approach

The parity equation method was first proposed by (Chow and Willsky 1984) using the redundancy relations of the dynamic system. The main premise of this method is to provide a proper check of the parity (consistency) of the measurements for the monitored system. Consider the discrete-time system

$$\begin{cases} x(k+1) = Ax(k) + Bu(k) + R_1 f(k) \\ y(k) = Cx(k) + Du(k) + R_2 f(k) \end{cases} \tag{11}$$

which can be reorganized into a set of matrix equations for a series of $s$ output measurements:

$$\underbrace{\begin{bmatrix} y(k-s) \\ y(k-s+1) \\ \vdots \\ y(k) \end{bmatrix}}_{Y(k)} - H \underbrace{\begin{bmatrix} u(k-s) \\ u(k-s+1) \\ \vdots \\ u(k) \end{bmatrix}}_{U(k)} = Wx(k-s) + M \underbrace{\begin{bmatrix} f(k-s) \\ f(k-s+1) \\ \vdots \\ f(k) \end{bmatrix}}_{F(k)} \tag{12}$$

where

$$H = \begin{bmatrix} D & 0 & \cdots & 0 \\ CB & D & \cdots & 0 \\ \vdots & \vdots & \ddots & \vdots \\ CA^{s-1}B & CA^{s-2}B & \cdots & D \end{bmatrix}, \quad M = \begin{bmatrix} R_2 & 0 & \cdots & 0 \\ CR_1 & R_2 & \cdots & 0 \\ \vdots & \vdots & \ddots & \vdots \\ CA^{s-1}R_1 & CA^{s-2}R_1 & \cdots & R_2 \end{bmatrix}, \quad W = \begin{bmatrix} C \\ CA \\ \vdots \\ CA^s \end{bmatrix}$$

A residual signal can be defined as:

$$\begin{aligned} r(k) &= V[Y(k) - HU(k)] \\ &= VWx(k-s) + VMF(k) \end{aligned} \tag{13}$$

where $V$ is the matrix chosen to satisfy the conditions

$$VW = 0,\ VM \neq 0 \tag{14}$$

The condition $VW = 0$ implies that $r(k) = 0$ when there is no fault, and the condition $VM \neq 0$ implies that $r(k)$ is observable from $F(k)$.

Once the matrix $V$ is derived, the residual signal can be generated using Eq. (13). For an appropriately chosen $s$, the solution of Eq. (14) always exists. This implies that a parity relation-based residual generator for fault detection always exists (Chen and Patton 1999).

### 2.2.3 Parameter estimation method

Model-based FDI can also be achieved by the use of parameter identification techniques if the basic structure of the model is known (Isermann 1984, 1997). This approach is based on the assumption that faults are reflected in the aircraft system parameters such as mass, inertia, etc. In this method parameters of the mathematical model are estimated on-line using parameter estimation methods and are compared with those obtained initially under the fault-free case. Any inconsistency indicates a fault. Consider the aircraft system model

$$y(t) = f(\theta, u(t)) \tag{15}$$

where $\theta$ is the parameter vector of the aircraft model. By on-line parameter identification, one can obtain the estimation of parameters, $\theta_0$, in the fault-free case. Denote by $\hat{\theta}_{k-1}$ the estimation of the parameters at time step $k-1$, and assume the coefficient estimation at time step $k$ is $\hat{\theta}_k$, the residual can then be defined as

$$\begin{aligned} r(k) &= \hat{\theta}_k - \theta_0 \quad or \\ r(k) &= y(k) - f(\hat{\theta}_{k-1}, u(k)) \end{aligned} \tag{16}$$

Song et al. (2002) compared time-domain based and frequency-domain based online parameter identification methods for application within a fault tolerant flight control systems. The simulation conducted on NASA IFCS F-15 aircraft demonstrated the usefulness of these two schemes. The parameter estimation method is valid not only for linear models, but nonlinear ones

too. Its drawback is that it cannot be easily used to achieve fault isolation since the identified parameters cannot always be converted back to the aircraft physical parameters (Isermann 1984). Furthermore issues associated with parameterization of the parameters to be estimated in a linear in the parameters model (Ioannou and Sun, 1996) as well as the persistence excitation property of the regressor vector need to be resolved before using this method for fault detection. Lack of persistence of excitation for example will lead to parameter estimates that are different from the true ones even in the absence of faults.

After a nonzero residual signal is derived, it is evaluated to distinguish a particular fault from others, i.e., to isolate different faults. In model-based FDI one can establish the structured residual set which is sensitive to specific faults and insensitive to others (Gertler 1993, Frank 1994, Chen and Patton 1999). The other way is to design a directional residual vector that lies in a fixed direction or a plane corresponding to a particular fault in the residual space. We will discuss these cases in the following subsections.

### 2.2.4 Residual Evaluation: Dedicated Observer Scheme (DOS)

The dedicated observer scheme (DOS) in fault isolation uses a bank of residual signals. Each residual is sensitive to a specific fault while insensitive to the rest of possible faults (figure 5) (Wunnenberg 1990). The task of isolating faults is achieved by comparing each residual signal with an initially set threshold and a resulting Boolean decision table. The fault isolation logic can be expressed as

$$\begin{cases} r_i(t) > T_i & \Rightarrow \quad f_i(t) \neq 0; \\ r_i(t) \leq T_i & \Rightarrow \quad f_i(t) = 0; \end{cases} \quad i = 1,2,\cdots,q \tag{17}$$

where $r_i(t)$ is the residual signal output of the $i-$th observer; $T_i$ is the threshold, and $f_i(t)$ is the fault to which the residual $r_i(t)$ is most sensitive. The DOS scheme is simple and all faults can be detected simultaneously. However it is not robust with respect to unknown inputs such as disturbance, uncertainty and noise (Wuennengerg 1990, Frank 1990).

[ Insert figure 5 here. ]

### 2.2.5 Generalized Observer Scheme (GOS)

The generalized observer scheme in fault isolation also uses a set of structured residual signals, but the difference with DOS lies in the fact that all residuals of the residual set are generated to be sensitive to all but one fault, i.e.

$$r_i(t) = R(f_1(t),\cdots,f_{i-1}(t),f_{i+1}(t),\cdots,f_q(t))$$

where $R(.)$ denotes a functional relation. The fault isolation logic is as follows:

$$\left.\begin{array}{c} r_i(t) \le T_i \\ r_j(t) > T_j, \forall j \in \{1,\cdots,i-1,i+1,\cdots,q\} \end{array}\right\} \Rightarrow f_i(t) \neq 0 \qquad (18)$$

Here the $i$-th fault affects all but the $i$-th residual, so that the residual signals isolate only a single fault at a time. For an example shown in figure 6, the residual signal $r_2$ is determined by all three possible faults except $f_2$, and the fault $f_2$ is diagnosed when both $r_1$ and $r_3$ exceeds the thresholds but $r_2$ remains below the threshold $T_2$. The GOS scheme is superior to DOS scheme in that the additional design freedom can be utilized to deal with the robustness to unknown inputs (Frank 1994). The logic of GOS is shown in figure 6 for the case of 3 possible faults.

[ Insert figure 6 here. ]

### 2.2.6 Directional Residual Set Evaluation

A third way to accomplish fault isolation is to use the directional residual vector ( Chen and Patton 1999, Chen and Speyer 2001). Here, the signature directions, $\mathbf{I}(f_i)$, of each possible fault $f_i$ are needed. The signature of fault is a vector referring to a single direction or an invariant subspace in the residual space that does not overlap each other and thus uniquely represents the specific fault. Figure 7 illustrates an example of fault isolation scheme using directional residual vector. In this example there are three signature directions corresponding to three possible faults represented by dashed lines in figure 7. The fault isolation is achieved by comparing the derived residual vector $r$ and the signatures of different faults. The fault whose signature direction is

closest to the residual signal will be the most likely one occurred. Figure 7 shows the residual vector $r$ and its projection to the signature directions. The detection and isolation of the fault is determined by the projected value of $r$ that was the highest magnitude. In the example of figure 7 the fault is $f_2$.

[ Insert figure 7 here. ]

## 3. Robustness Problems in Model-based FDI

Model-based FDI techniques have the advantage of taking full use of the prior quantitative information of the dynamics and the success of on-line FDI. The price to pay is that they are potentially sensitive to modeling errors and require an accurate model of the aircraft. In practice modeling errors such as disturbances, noise, and parameter uncertainties are inevitable, giving rise to the question of robustness in fault detection and isolation. Robustness is defined as the ability to isolate faults in the presence of modeling errors (Gertler 1988, Frank and Ding 1997, Basseville and Parisini 2000). Robustness in an FDI is important since disturbances and uncertainties could interfere with fault isolation and lead to false alarms.

A number of methods have been proposed to address the FDI robustness problem in applications to aircraft and flight control (Patton and Kangethe 1988, Stengel 1991). In the following subsections several methods of robust residual generation and evaluation are discussed.

### 3.1 Robust Residual Generation Problem

Robust residual generation is to design a residual signal that is highly sensitive to faults while decoupled from disturbance and inaccuracies of the model. Taking model errors into consideration the aircraft dynamics described in (3) becomes

$$\begin{cases} \dot{x}(t) = Ax(t) + Bu(t) + E_1 d(t) + R_1 f(t) \\ y(t) = Cx(t) + Du(t) + E_2 d(t) + R_2 f(t) \end{cases} \tag{19}$$

Here $d(t)$ is a function of unknown inputs including disturbances, noise and uncertainty of the model, and $E_1, E_2$ are assumed to be known matrices of proper dimensions. Methods of

determining the matrices $E_1, E_2$ have been exploited during the last decade, together with disturbance de-coupling methods such as eigenstructure assignment (Patton and Chen 1991), frequency domain design (Frank and Ding 1994), and orthogonal parity approach (Gertler and Kunwer 1995).

The output of the system (19) with faults and modeling errors in the frequency domain is:

$$y(s) = (G_p(s) + \Delta G_p(s))u(s) + G_f(s)f(s) + G_d(s)d(s) \tag{20}$$

where

$$\begin{cases} G_p(s) = C(sI - A)^{-1}B + D \\ G_f(s) = C(sI - A)^{-1}R_1 + R_2 \\ G_d(s) = C(sI - A)^{-1}E_1 + E_2 \end{cases}$$

and $\Delta G_p(s)$ describes the modeling uncertainty in matrices $A, B, C,$ and $D$.

Replacing $y(s)$ in (5) with the above output, and assuming the condition

$$H_u(s) + H_y(s)G_u(s) = 0$$

shown in Eq.(6) is satisfied, the residual signal becomes

$$r(s) = H_y(s)\Delta G_p(s)u(s) + H_y(s)G_d(s)d(s) + H_y(s)G_f(s)f(s) \tag{21}$$

To accomplish the task of fault detection and isolation in the presence of unknown inputs and other possible faults in the residual signal, the effect of a specific fault has to be decoupled from the effects of the other faults and unknown inputs. The decoupling of unknown inputs can be achieved if

$$H_y(s)G_d(s) = 0 \tag{22}$$

If the above condition does not hold, perfect decoupling from the unknown inputs is not achievable. An alternative approach is to solve the optimal or the approximate decoupling problem by minimizing the following performance index (Ding and Frank 1991):

$$J = \frac{\left\| H_y(jw)G_d(jw) \right\|}{\left\| H_y(jw)G_f(jw) \right\|} \tag{23}$$

over a specific frequency range. The extreme case $J = 0$ means that the effect of unknown inputs on the residual signal is completely decoupled, as in Eq. (22).

### 3.2 Robust Residual Generation Designs

Many methods have been developed to enhance the robustness of residual generation (Watanabe et al. 1982, Viswanadham et al. 1988, Ding et al. 1992, Hou et al. 1994, Duan et al, 1997, Frank and Ding 1997). Methods such as $H_\infty$ optimization and nonlinear designs have also been exploited to generate robust residual signals (Lou et al. 1986, Gertler et al. 1995, Zhang et al. 2002).

#### 3.2.1 Unknown Input Observer Scheme

An unknown-input observer estimates the state without coupling among faults and unknown inputs (Watanabe and Himmelblau 1982, Wunnenberg 1990). Since the control signal $u(t)$ is always known, the system model described in (19) can be simplified as

$$\begin{cases} \dot{x}(t) = Ax(t) + Bu(t) + E_1 d(t) + R_1 f(t) \\ \overline{y}(t) = Cx(t) + E_2 d(t) + R_2 f(t) \end{cases} \tag{24}$$

where $\overline{y}(t) = y(t) - Du(t)$.

The unknown input observer is given by

$$\begin{cases} \dot{z}(t) = Fz(t) + K\overline{y}(t) + Ju(t) \\ r(t) = L_1 z(t) + L_2 \overline{y} \end{cases} \tag{25}$$

The estimation error defined as $e(t) = z(t) - Tx(t)$ and the residual signal are governed by the equations

$$\begin{cases} \dot{e}(t) = Fe(t) + Ju(t) + KCx(t) + KE_2 d(t) + KR_2 f(t) - TAx(t) - TBu(t) - TE_1 d(t) - TR_1 f(t) \\ r(t) = L_1(e(t) + Tx(t)) + L_2 Cx(t) + L_2 E_2 d(t) + L_2 R_2 f(t) \end{cases} \tag{26}$$

Suppose the system is initially in a fault-free state, i.e. $f_i(t_0) = 0$, $i = 1, \cdots, q$

The conditions to make the fault detectable, say,

$$\begin{cases} f_i(t) = 0, i = 1,2,\cdots,q \Rightarrow r(t \to \infty) = 0 \\ \text{any } f_i(t) \neq 0, i = 1,2,\cdots,q \Rightarrow r(t) \neq 0 \end{cases} \quad t \geq t_0 \tag{27}$$

are satisfied if the following equations hold

$$\begin{cases} F \text{ has stable eigenvalues} \\ TA\text{-}FT = KC \\ TE_1 = 0 \\ KE_2 = 0 \\ L_2E_2 = 0 \\ J = TB \\ L_1T + L_2C = 0 \end{cases} \tag{28}$$

Given the above conditions, the estimation error and the residual signals obeying (26) become

$$\begin{cases} \dot{e}(t) = Fe(t) + KR_2f(t) - TR_1f(t) \\ r(t) = L_1e(t) + L_2R_2f(t) \end{cases} \tag{29}$$

This equation reveals that the residual is independent of disturbances and will only depend on the fault information as the estimation error asymptotically converges to zero.

Hou and Muller (1994) presented a method for designing Unknown Input Observers (UIOs) using an algebraic approach. In this method, the reduced order and full order UIOs are the same if the conditions of disturbance decoupling, Eq. (28), are satisfied. Chen, Patton and Zhang (1996) also presented the method that use the freedom of full order UIOs to make the residual vector 'directional' as introduced in Section 2.2.6.

### 3.2.2 Eigenstructure Assignment for Robust FDI

In the design of UIOs the state estimation error is independent of the disturbance, and the residual is defined as the weighted linear transformation of the state estimation error. Therefore, the residual is independent of the disturbance. An alternative way to accomplish robust residual generation is to de-couple the residual from the disturbance directly, while the state estimation error may be dependent on the unknown inputs. Eigenstructure assignment approach is such a method presented in (Patton, et al 1986) and applied to robust FDI of flight control in (Shen et al 1998).

The main idea of the eigenstructure assignment approach is to assign the left or right eigenvectors of the observer to be orthogonal to the disturbance distribution directions. Using a linear transformation of the output $y(t)$, the state equation in Eq.(19) becomes

$$\begin{cases} \dot{x}(t) = Ax(t) + Bu(t) + E_1 d(t) + R_1 f(t) \\ T_y y(t) = T_y Cx(t) + T_y Du(t) + T_y E_2 d(t) + T_y R_2 f(t) \end{cases}$$

where the matrix $T_y$ is selected such that the disturbance term $T_y E_2$ is null. The system's state-space expression becomes

$$\begin{cases} \dot{x}(t) = Ax(t) + Bu(t) + E_1 d(t) + R_1 f(t) \\ y_T(t) = C_T x(t) + D_T u(t) + R_{2T} f(t) \end{cases} \tag{30}$$

where $y_T(t) = T_y y(t)$, $C_T = T_y C$, $D_T = T_y D$, and $R_{2T} = T_y R_2$. The full order observer for residual generation is given by

$$\begin{cases} \dot{\hat{x}}(t) = (A - KC_T)\hat{x}(t) + (B - KD_T)u(t) + Ky_T(t) \\ \hat{y}(t) = C_T \hat{x}(t) + D_T u(t) \\ r(t) = Q[y_T(t) - \hat{y}(t)] \end{cases} \tag{31}$$

Defining the state estimation error as $e(t) = x(t) - \hat{x}(t)$, the residual vector is generated as

$$\begin{cases} \dot{e}(t) = (A - KC_T)e(t) + E_1 d(t) + R_1 f(t) - KR_{2T} f(t) \\ r(t) = QC_T e(t) + QR_{2T} f(t) \end{cases} \tag{32}$$

To make the residual independent of the disturbances, the following condition must hold

$$G_{rd}(s) = \frac{r(t)}{d(t)} = QC_T (sI - A + KC_T)^{-1} E_1 d(s) = 0 \tag{33}$$

The sufficient conditions for satisfying the disturbance de-coupling requirement are

$$\begin{cases} QC_T E_1 = 0 \\ \text{All rows of } QC_T \text{ are left eigenvectors of } (A\text{-}KC_T) \text{ correponding to any eigenvalues} \end{cases} \tag{34}$$

Methods to assign left observer eigenvectors include, for instance, the parametric approach presented in (Choi et al. 1995, Duan et al. 1997). It is also feasible to achieve disturbance decoupling by assigning right eigenvectors of the observer where the columns of $E_1$ are assigned as right eigenvectors of $(A - KC_T)$ corresponding to the eigenvalues (Patton and Kangethe 1988,

Choi 1998). The limitation of the eigenstructure assignment is that the number of independent disturbances to be decoupled has to be smaller than the number of independent available measurements.

### 3.2.3 Robust FDI using Optimal Parity Relations

Consider the discrete model of an aircraft dynamics with disturbances and faults

$$\begin{cases} x(k+1) = Ax(k) + Bu(k) + E_1 d(k) + R_1 f(k) \\ y(k) = Cx(k) + Du(k) + E_2 d(k) + R_2 f(k) \end{cases} \tag{35}$$

Similar to Eq. (12), the output equations with unknown inputs $d(.)$ and $f(.)$ become

$$\underbrace{\begin{bmatrix} y(k-s) \\ y(k-s+1) \\ \vdots \\ y(k) \end{bmatrix}}_{Y(k)} = H_0 x(k-s) + H_1 \underbrace{\begin{bmatrix} u(k-s) \\ u(k-s+1) \\ \vdots \\ u(k) \end{bmatrix}}_{U(k)} + H_2 \underbrace{\begin{bmatrix} d(k-s) \\ d(k-s+1) \\ \vdots \\ d(k) \end{bmatrix}}_{D(k)} + H_3 \underbrace{\begin{bmatrix} f(k-s) \\ f(k-s+1) \\ \vdots \\ f(k) \end{bmatrix}}_{F(k)} \tag{36}$$

where

$$H_0 = \begin{bmatrix} C \\ CA \\ \vdots \\ CA^s \end{bmatrix}$$

$$H_1 = \begin{bmatrix} D & 0 & \cdots & 0 \\ CB & D & \cdots & 0 \\ \vdots & \vdots & \ddots & \vdots \\ CA^{s-1}B & CA^{s-2}B & \cdots & D \end{bmatrix}$$

$$H_2 = \begin{bmatrix} E_2 & 0 & \cdots & 0 \\ CE_1 & E_2 & \cdots & 0 \\ \vdots & \vdots & \ddots & \vdots \\ CA^{s-1}E_1 & CA^{s-2}E_1 & \cdots & E_2 \end{bmatrix}$$

$$H_3 = \begin{bmatrix} R_2 & 0 & \cdots & 0 \\ CR_1 & R_2 & \cdots & 0 \\ \vdots & \vdots & \ddots & \vdots \\ CA^{s-1}R_1 & CA^{s-2}R_1 & \cdots & R_2 \end{bmatrix}$$

The residual signal is generated using the measurements $u(.)$ and $y(.)$ as

$$r(k) = V[Y(k) - H_1 U(k)] \tag{37}$$

As in the case of Eq.(14), the conditions for fault detectability are

$$VH_0 = 0, \; VH_3 \neq 0 \tag{38}$$

To satisfy perfect disturbance decoupling another condition must also be satisfied:

$$VH_2 = 0 \tag{39}$$

These conditions are rather restrictive and in some cases they may not have a solution. In such case only approximate unknown input decoupling rather than perfect disturbance decoupling could be achieved. In the approximate decoupling the performance index

$$J = \frac{\left\| \partial r / \partial d \right\|}{\left\| \partial r / \partial f \right\|} \tag{40}$$

is minimized in order to strike a compromise between the effect of faults and unknown inputs. Such work can be found in (Lou et al. 1986, Wuennenberg 1990, Frank 1990, Gertler and Kunwer 1995) and a review of parity space approaches to fault diagnosis for aerospace systems is given in (Patton and Chen 1994).

### 3.2.4 Frequency Domain Design and $H_\infty$ Optimization

Frequency domain designs for fault detection are based on the fact that unknown inputs and faults have different frequency characteristics (Viswanadham and Minto 1988, Kinnaert and Peng 1995). For the system and output equation described in (19) and (20), the residual generator via factorization was given by (Ding and Frank 1991)

$$r(s) = Q(s)(\tilde{M}(s)y(s) - \tilde{N}(s)u(s)) \tag{41}$$

Here $G_p(s) = \tilde{M}^{-1}(s)\tilde{N}(s)$ is the left co-prime factorization of the transfer matrix $G_p(s)$ and $\tilde{M}(s)$, $\tilde{N}(s)$ are transfer matrices defined by:

$$\begin{aligned} \tilde{M}(s) &= -C(sI - A + KC)^{-1}K + I \\ \tilde{N}(s) &= C(sI - A + KC)^{-1}(B - KD) + D \end{aligned} \tag{42}$$

K is the feedback matrix chosen to make $(A-KC)$ stable, $I$ is the identity matrix and the matrix $Q(s)$ is a stable proper transfer matrix of weighting functions which can be static or dynamic. Substituting the model in Eq. (19) into (41) the residual signal is obtained as follows:

$$r(s) = Q(s)(N_f(s)f(s) + N_d(s)d(s)) \tag{43}$$

with

$$\begin{cases} N_f(s) = C(sI - A + KC)^{-1}(R_1 - KR_2) + R_2 \\ N_d(s) = C(sI - A + KC)^{-1}(E_1 - KE_2) + E_2 \end{cases} \tag{44}$$

Perfect disturbances decoupling requires (Frank and Ding 1994)

$$\begin{cases} Q(s)N_f(s) = diag(t_1(s), \cdots, t_q(s)) \in RH_\infty \\ Q(s)N_d(s) = 0 \end{cases} \tag{45}$$

where $RH_\infty$ denotes the set of all stable and proper transfer matrices.

In the term of the transfer matrices $G_f(s)$ and $G_d(s)$ the perfect decoupling condition is given by

$$\begin{cases} rank\{[G_f(s) \quad G_d(s)]\} = rank\{G_f(s)\} + rank\{G_d(s)\} \\ rank\{G_f(s)\} = g \quad (the\ number\ of\ independent\ faults) \end{cases} \tag{46}$$

When such conditions do not hold, perfect disturbance decoupling is not achievable. In this case, the best approach is to obtain an optimal approximation by minimizing the following performance index

$$J = \min_{Q(s)} \frac{\|Q(s)N_d(d)\|}{\|Q(s)N_f(s)\|} \tag{47}$$

This optimization problem and the $H_\infty$ approach were studied by Ding and Frank (1991). Other methods using singular value decomposition techniques were proposed by Lou et al. (1986), Mangoubi et.al. (1992), *etc*. Niemann and Stoustrup (1996) introduced modeling error blocks into the $H_\infty$ observer design and similar work for nonlinear systems can be found at (Stoustrup and Niemann 1998). Niemann and Stoustrup (1997) also investigated the feasibility of

designing the robust controller and robust FDI units simultaneously. In their work the fault estimation problem is solved without generating the residual signal, and the estimated fault is used for both the FDI unit and the controller.

### 3.2.5 Nonlinear Residual Generation

The methods discussed in previous sections apply to linear models of the aircraft dynamics, which rarely represent the real case accurately. One way to deal with nonlinearity is to obtain the linear approximation at an operating point and utilize robust techniques to make the residual signals insensitive to model errors, as described above. The problem of using a linearized model is that it works only within a small range near the operating point. If the system operates in a wide dynamic range, the linearized model may fail to describe the dynamics and the linear techniques are not applicable. The preferred way to address nonlinearity is to deal with it directly and develop nonlinear fault detection and isolation techniques. Some of the existing methods include exploiting nonlinear and adaptive observer designs to address the nonlinear fault detection and isolation (Ding and Frank 1992). To find a 'universal' model for nonlinear systems neural networks have been introduced (Narendra and Parthasarthy 1990, Alessandri et al 2000). Similarly, to overcome the problem of precision and accuracy of the models used in FDI, fuzzy logic is integrated in model-based FDI (Takagi and Sugeno 1985, Dexter and Benouarets 1997). Polycarpou (1994) presented a general learning methodology for fault diagnosis and accommodation. The main idea is to monitor the system dynamics using adaptive nonlinear modeling techniques that detect changes in the dynamics and create a rough model of these changes for fault accommodation. The robustness to modeling uncertainties was addressed in Vemuri et al (1996), and a detectability analysis was proposed by Polycarpou and Trunov (2000). Similar work can be found in Demetriou et al. (1998), Polycarpou and Vemuri (1998), and Trunov and Polycarpou (2000).

## 3.3 Methods of Robust Residual Evaluation

As discussed earlier, residual evaluation is to compare the decision function of the residual signal versus threshold set initially in the fault free case. In addition to a number of robust residual generation methods, some approaches that increase the robustness in residual evaluation have been proposed (Emani-Naeini et al 1988, Clark, 1989, Frank, 1995, Zhang et al 2002). These approaches make use of thresholds that are modified with residuals or controls of the system in contrast to the use of fixed thresholds applicable only to one specific operating point.

### 3.3.1 Adaptive Threshold Method

In nonlinear systems residual and decision function may vary with changing control input and system parameter uncertainties causing false alarms when these changes are large enough to exceed the fixed value of the threshold. In order to increase robustness in such cases, an adaptive threshold was proposed (Clark 1989, Frank 1995, Zhang et al. 2002) which depends on the control activity and the noise. In the presence of parameter uncertainties, the threshold is varing with the changing system dynamics even if no fault occurs. Figure 8 gives a graphic illustration of the adaptive threshold for direct residual evaluation.

[ Insert figure 8 here. ]

### 3.3.2 Robust Threshold Selector

In a similar way, to increase robustness in residual evaluation, one can use the robust threshold selector presented by Emani-Naeini et al. (1988) shown in the block diagram in Figure 9.

[ Insert figure 9 here. ]

Consider the residual signal described by Eq.(21), and assume that unknown inputs are decoupled. The residual signal in the fault free case is

$$r(s) = H_y(s)\Delta G_p(s)u(s) \tag{48}$$

Assume the model error is bounded by

$$\left\|\Delta G_p(jw)\right\| \le \delta \tag{49}$$

thus

$$\begin{aligned} \|r(jw)\| &= \|H_h(jw)\Delta G_p(jw)u(jw)\| \\ &\le \|H_h(jw)u(jw)\|\|\Delta G_p(jw)\| \\ &\le \delta\|H_h(jw)u(jw)\| \end{aligned} \tag{50}$$

Then an adaptive threshold $T(t)$ for Eq.(17) and (18) can be selected as

$$T(s) = \delta H_y(s)u(s) \tag{51}$$

Clearly, the control activity and the system operating states will influence the threshold selector and hence improve the fault detection and isolation.

# 4. Model-free FDI Techniques

The methods described so far were all based on quantitative models of the system dynamics. These methods are not applicable when an adequate quantitative model of the system is not available. As a complement, there is a branch of fault detection and isolation that deals with cases when either no model or only a qualitative model of the dynamics is available (Narendra et al 1990, Rauch et al 1993, Raza et al 1994, Kiupel et al 1995, Benkhedda et al 1996, Fenu et al 1999, Precidi and Parisini 2001, *etc.*). In this section we will introduce some of these methods that are applicable to aircraft dynamic and control.

## 4.1 Fault Diagnosis Using Qualitative Models

It is often difficult to develop an accurate mathematical model of the system dynamics, whereas cruder description of the system is easier to achieve. Fault diagnosis of dynamic systems can be accomplished based on the declarative knowledge called 'qualitative models'. Qualitative models require only declarative (heuristic) information of the variables - the tendencies and the magnitudes of the signals - so that robustness to uncertainty is achieved (Chen and Patton 1999). Qualitative-based FDI methods can be used when no analytical model is available, the on-line information is not given in quantitative measurements, or the parameters and system structure are not precisely known.

Qualitative model-based FDI does not use quantitative residual generation to generate the symptoms of faults but turns to qualitative knowledge usage. The qualitative knowledge includes fault-tree, i.e. the connection of symptoms and faults, the process history, fault statistics, and so on ( Huo et al 1998, 1999). Through human observation and inspection heuristic characteristic values in the form of noise, colour, smell, etc. are generated. The heuristic information can also be expressed in linguistic terms like 'little', 'medium' or 'full'. Based on the available heuristic knowledge diagnostic-reasoning (forward and backward reasoning) strategies can be adopted (Isermann 1994) and on-line expert systems can be applied (Frank 1990). An alternative way is to use qualitative observers based on Markov chain models which, like quantitative observers used in model-based FDI, generate and evaluate residuals for stochastic systems (Zhuang et al 1998). Chessa and Santi (2001) presented a graph-based diagnosis with multiple faults in which the error propagation between system components is modeled as a direct graph. Pecht et al. (2001) suggested an on-board hardware-software diagnostic means referred to as built-in test when failure occurrences were uniquely associated with the operating environment and the usage of this method into Boeing 767 and 777 proved its usefulness.

### 4.2 Diagnosis Using Classification Method

The task of fault diagnosis is to identify the most probable fault causing the apparent symptom in system operation. Denote by $S = [S_1 \quad S_2 \quad \cdots \quad S_n]^T$ the features of the system in operation and $S_0 = [S_{1,0} \quad S_{2,0} \quad \cdots \quad S_{n,0}]^T$ the reference vector determined for the normal behaviour in fault free case, $\Delta S^T = S^T - S_0^T$ is the symptom vector that indicates the occurrence of one or more fault(s). The binary vector

$$F = [F_1 \quad F_2 \quad \cdots \quad F_q]^T$$

expresses the fault $f_i$ as either 'happened' with $F_i = 1$ or 'not happened' with $F_i = 0$. If no further information is available for the relations between features and faults, classification or pattern

recognition methods can be used (Isermann 1997). The block diagram of classification methods is shown in figure 10.

[ Insert figure 10 here. ]

In figure 10, the relationship between $S$ and $F$ is learned or trained experimentally and stored, forming the explicit database. By comparison of the observed $S$ with the normal reference $S_0$, the fault indication vector $F$ can be concluded.

Bayesian classification is a main kind of probability-based statistical classification method that works on the premise that classified faulty and fault-free data exist. The nearest neighbor scheme is a geometrical classification similar to Bayesian classifier while it makes no statistical assumptions (Molnar 1997). A more generalized classification method is to use neural-networks because of their ability to approximate nonlinear relations and determine flexible decision regions in continuous or discrete form (Molnar 1997, Hoffman et al 2001). Fuzzy classification is also possible, which is at the edge of the probability theory and expert systems (Isermann 1997).

### 4.3 Application of Computational Artificial Intelligence in FDI

Artificial intelligence (AI) has been exploited for FDI for a period of time (Frank and Kiupel 1997). Integrating the symbolic and quantitative knowledge with a neuro-fuzzy system is a new trend in this area (Benkhedda and Patton 1996, AI-Jarrah and AI-Rousan 2001, Frey and Kuntze 2001). A neuro-fuzzy system combines the learning ability of neural networks with the explicit knowledge representation of fuzzy logic, and thus can model and design nonlinear systems efficiently. Patton and Lopez-Toribio (1999) integrated B-Spline neural network and fuzzy logic to deal with the qualitative information to diagnose faults. The general parameter adaptation of fuzzy neural network is presented by Akhmetov et al. (2001).

Another trend in FDI using AI is to use fuzzy residual evaluation (Kiupel et al. 1995). In their work the objective is to release only weighted alarms instead of the "yes-no" decisions. The final

decision is made by both a decision maker with fuzzy logic and the human operator. The method contains no defuzzification but it has to be understandable for the operating persons.

# 5. Controller Reconfiguration

Using a fault detection and isolation scheme, the system is under monitoring during the operation for any possible fault. To make the aircraft dynamic tolerant to failures and complete the flight and the mission uninterrupted, control reconfiguration, which modifies the controller in either structure or parameters needs to be adopted. (Monaco et al.1997, Joseph and Wise 1998, Blanke et al. 1997, Blanke et al. 2001).

## 5.1 Control Reconfigurability Analysis

The function of a reconfigurable controller is to retain aircraft nominal stability and performance characteristics when a failure occurs. This requires that the on-design controllability and observability be preserved (Stengel 1991). At the same time the reconfiguration should, at least, provide sufficient stability long enough for the FDI process to take place and new controllers switch (Chandler 1989). To implement a reconfiguration strategy the following control surfaces and mechanisms are needed (Napolitano et al 1989)

- control surfaces like speed brakes, wing flaps, rudder below fuselage, etc,
- thrust control mechanisms.

and the quantities to be available for reconfiguration purposes include

- actuator position for each actuator,
- aircraft body angular and linear velocities in three body axes,
- aircraft attitude and angle of attack.

## 5.2 Reconfiguration Law Design

The block diagram in figure 11 illustrates the fault detection, isolation and controller reconfiguration for control surfaces using multiple aircraft models (Rauch 1995).

[ Insert figure 11 here. ]

Here, the decision function monitors the sensors and compares the measured system response with the estimated response from the system models built in the fault-free condition. Once a potential fault is detected fault isolation fulfills the task of isolating the position of the fault, and controller reconfiguration modifies the control law based on the stored control schemes designed for each anticipated fault. However, there is a trade-off between speed of reconfiguration and computer storage requirements since the structures and parameters for all failed states that can be generated off-line and stored for future use require an enormous memory (Stengel 1991).

### 5.2.1 Pseudo-inverse Methods

The reconfigured control can use a pseudo-inverse approach (Raza et al. 1985, Caglayan et al. 1988, Yang and Blanke 2000) to implement a feedback control law similar to that of the primary controls used in the fault-free nominal operation. In other words, the new feedback control is calculated to achieve equal product of the new control matrix ( $K_{new}$ ) and the new control ( $u_{new}$ ) with that of the previous ones, $K$ and $u$, i.e.

$$K_{new}u_{new} = Ku \tag{52}$$

If a fault occurs, the control influence matrix $K_{new}$ is derived from $K$ by eliminating the column corresponding to the failed control input. If the redundancy in the actuators is available the new control signal $u_{new}$ can be calculated using the pseudo-inverse as follows

$$u_{new} = ({K_{new}}^T K_{new})^+ K_{new}^T Ku \tag{53}$$

Rattan (1985), and Ioannou et al (1989) presented the evaluation of control mixer concept for reconfiguration of flight control system. The reconfiguration algorithm computes a new control mixer gain matrix that distributes the forces and moments of the failed control surface to the remaining healthy surfaces. In Rattan's work the failed control surface gets 'locked' to the centre position requiring zero input to the failed surface. In the work of Ioannou et al the surface is

allowed to be jammed at any position although this non-zero stuck needs accommodation by a compensating input signal. Assume the unimpaired, healthy aircraft is modeled as

$$\dot{x}_0 = A_0 x_0 + B_0 \delta \tag{54}$$

The subscript '0 implies the system is working in the normal fault-free case, $x_{n\times 1}$ denotes the state vector of the aircraft and $\delta_{s\times 1}$ the aircraft control surface deflection vector which is governed by the control vector $u$ as

$$\delta = K_0 u \tag{55}$$

Assuming the fault detection and isolation unit diagnosed that the $j$ th control surface failed, i.e. the surface got stuck at $\delta_j = \overline{\delta}_j$, the system dynamic becomes

$$\dot{x} = A_0 x + B_0{}^j [K_{new} u + d] + b_{0j} \overline{\delta}_j \tag{56}$$

where $B_0^j = B_0 - \begin{bmatrix} 0_{1,1} & \cdots & 0_{1,s} \\ & \vdots & \\ 0_{j-1,1} & \cdots & 0_{j-1,s} \\ 1_{j,1} & \cdots & 1_{j,s} \\ 0_{j+1,1} & \cdots & 0_{j+1,s} \\ & \vdots & \\ 0_{n,1} & \cdots & 0_{n,s} \end{bmatrix} B_0$, and $b_{0j}$ is the $j$ th column of $B_0$.

$K_{new}$ and $d$ are control mixer and compensating signal to be designed such that $x$ is as close to $x_0$ as possible, i.e.

$$B_0 K_0 u = B_0{}^j [K_{new} u + d] + b_{0j} \overline{\delta}_j$$

$$\text{or} \qquad B_0 K_0 = B_0^j K_{new}, \quad B_0^j d + b_{0j} \overline{\delta}_j = 0 \tag{57}$$

The solution to (57) is given by

$$\begin{cases} K_{new} = (B_0^j)^+ B_0 K_0 \\ d = -(B_0^j)^+ b_{0j} \overline{\delta}_j \end{cases} \tag{58}$$

where $(B_0^j)^+$ denotes the pseudoinverse of matrix $B_0^j$.

Ostroff (1985) presented a similar method in which $K_{new}$ is determined such that the closed-loop state transition matrix for the system approaches the transition matrix of the normal plant without any fault. Gao et al. (1991) showed that the eigenvalues of the 'faulty' system will be bounded close enough to those of the 'healthy' system if $K_{new}$ minimizes the Frobenius norm of the difference between the 'A' matrices of the 'faulty' and 'healthy' closed-loop systems.

Different fault modes and corresponding $K_{new}$ can be analyzed and stored in the flight-control computer system. Once a fault is diagnosed the appropriate feedback gain matrix is utilized. However for some faults where the feedback gain matrix cannot guarantee system stability an additional constraint should be applied to the calculation of $K_{new}$ (Gao et al. 1991).

### 5.2.2 Model Following Methods

To achieve controller reconfiguration a variable structure model following control which forces the aircraft dynamics to follow the nominal dynamics or a desired model was proposed (Zinober et al 1988, Mudge and Patton 1988). Huang et al. (1990) presented the idea of model following control where the eigenstructure of the nominal system is sustained by minimizing the quadratic function of the difference of actual and modeled state rates. Then in the work of Morse et al. (1990) a multivariable model following adaptive controller (Sobel et al 1982) was used which adjusted the controller gain in real time to follow the desired trajectories. They considered the case when the control surface is stuck and gave a discussion of stability properties.

A similar control allocation method with quadratic programming is proposed at the NASA report (Burken el al. 1999). When the number of independent control surfaces is greater than the rank of required response vector, the control commands can be distributed to 'cancel' the injured jammed surface. Consider the linear dynamics of the aircraft

$$\dot{x} = Ax + Bu \tag{59}$$

In the case of a jammed control surface positioning at $w$ the state equation of the system will be

$$\dot{x} = Ax + B_r u_r + b_j w \tag{60}$$

$B_r$ is the matrix $B$ eliminating the column, $b_j$, which corresponds to the jammed control surface and $u_r \in R^m$ represents the remaining control surfaces. Let

$$z = C_z x \quad \in R^p \tag{61}$$

be the desired output vector to define the control allocation, then

$$\dot{z} = C_z Ax + C_z B_r u_r + C_z b_j w \tag{62}$$

At current state $x(t)$, suppose the output of the nominal controller is $u^* \in R^{m+1}$ in fault free case, then the desired change rate of the output vector is

$$\dot{z}^* = C_z Ax + C_z Bu^* \tag{63}$$

The task of the control allocation is to find $u_r$ such that $z$ is as close to $z^*$ as possible, that is, $\dot{z} \approx \dot{z}^*$. This problem can be organized as the following quadratic programming problem,

$$\begin{aligned} \min_{u_r} j = \frac{1}{2} \times [(1-\varepsilon)(C_z B_r u_r + C_z b_j w - C_z Bu^*)^T Q_1 \\ \times (C_z B_r u_r + C_z b_j w - C_z Bu^*) + \varepsilon {u_r}^T Q_2 u_r] \end{aligned} \tag{64}$$

for $0 < \varepsilon < 1$ and subject to the constraint

$$u_{r\_\min} \le u_r \le u_{r\_\max}$$

$Q_1$ and $Q_2$ are positive definite matrices, and $u_{r\_\min}$ and $u_{r\_\max}$ are the lower and upper bounds of $u_r$.

### 5.2.3 Control Law Reschedule

A more general approach is to develop rescheduled control laws for the case of changing aerodynamic coefficients and flight status with different Mach number and altitude (Shamma et al 1992, Rugh 1991, Lawrence et al. 1995). In the work of Moerder et al (1989) the reconfiguration control law was presented for AFTI F16 aircraft at Mach 0.8 and 5000 ft altitude. Based on an FDI scheme monitoring the system they developed optimal gain scheduling using state estimation. The stabilization is achieved by a proportional-integral-filter (PIF) output feedback regulator given by

$$\begin{cases} u(k+1) = u(k) + \Delta T[\eta(k) - \eta(k-1)] \\ \eta(k) = -Gy(k) \end{cases} \tag{65}$$

where $u(.)$ is the control command vector, $y(.)$ is the plant output vector, and $\Delta T$ is the controller sampling interval. The PIF feedback gain matrix is scheduled as

$$G(\theta) = G_0 + \sum_{j=1}^{n} \theta_j G_j \tag{66}$$

Here $\theta = [\theta_1 \cdots \theta_j \cdots \theta_n]^T$ is the vector representing the surface effectiveness loss of $n$ control surfaces. $\theta_j = 0$ implies full effectiveness while $\theta_j = 1$ indicates faulty or missing effectiveness of the $j$ th control surface. The gain matrix $G_j$ is obtained using LQG output feedback stabilization design.

Similarly, Boskovic et al. (1998a, b) used the multiple parallel identification models together with corresponding controllers to achieve flight performance. Control law reschedule is an open-loop action, that is, there is no feedback to compensate for incorrect reschedules. False alarms may destroy the stability and/or deteriorate performance of the overall system. To improve its robustness, Zheng et al (1997) took into account the modeling errors and inaccuracies of faults and used LMI theory to synthesize the feedback gain as a function of 'fault effect vectors' obtained by the FDI mechanism. They used simulations to demonstrate the effectiveness of the approach for the longitudinal flight control of unmanned aircraft with nonlinear dynamics.

### 5.2.4 Adaptive Control Techniques

Ahmed-Zaid, Ioannou et al (1991) proposed a fault accommodation method based on adaptive control theory (Ioannou and Sun, 1996). In the presence of failures the control law was reconfigured using on-line estimates of the faulty aircraft dynamics. A reduced-order linearized AFTI/F-16 model using Hankel norm model reduction algorithm at the frequency range of interest was used to develop the adaptive fault accommodation scheme that was tested on the full-

order nonlinear dynamics. The method requires no explicit information of the types of faults and hence it simplifies the design and is robust with respect to false alarms.

Other researchers working on fault diagnosis and accommodation with adaptive techniques include Wang and Daley (1996), Wang et al. (1997) and Tao et al. (2001). The latter group described an adaptive-state feedback control scheme of updating the controller parameters to achieve the 'healthy' plant model state matching when some of the actuators are stuck at some fixed or varying values. Chen et al. (2002) derived the necessary and sufficient matching conditions for adaptive state tracking control for a linear time invariant model. Tao et al. (2002) also presented an adaptive actuator failure compensation controller using output feedback. They used the Boeing 747 airplane model to demonstrate stability and asymptotic output tracking despite the uncertainties of the plant. A multivariable adaptive control technique for fault-tolerant control was considered by Bodson and Groszkiewicz (1997) where three adaptive algorithms based on multivariable model reference control ideas were compared in the presence of actuator or control surface failures. Calise et al. (1998) investigated the usage of neural network based direct adaptive control approach to reconfigurable flight control. Similar work can be found in Rysdyk and Calise (1998) where the fault tolerance capabilities of XV-15 tiltrotor was demonstrated with a nonlinear adaptive controller architecture.

Like the FDI, there are also qualitative-model-based and knowledge-based methods for flight dynamics identification and control (Arkin and Vachtsevanos 1990, Ahmed-Zaid et al. 1993, Chandler et al. 1993, Snorrason et al. 1993, Rauch 1994, Youssef et al. 1995, Zhang et al. 2001a, 2001b). Koutsoukos et al. (2000) discussed the supervisory control of hybrid systems, and the control and fault detection were addressed at Mingnone et al. (1999), Parisini et al (1998) and Lunze et al. (2001). Polycarpou(1994) presented a systematic procedure for constructing nonlinear estimation using neural networks and a stable learning scheme for accommodating failures. Recently Zhou and Frank (2001) proposed a PID state feedback control for nonlinear stochastic systems in closed loops combined with fault detection and accommodation.

## 6. Conclusion

In this paper a wide class of fault-tolerant control techniques applicable to aircraft dynamics with emphasis on approaches combining fault diagnosis and controller reconfiguration are reviewed. The main principles and most relevant techniques of model-based and model-free fault diagnosis are discussed. Robustness issues due to the presence of modeling errors and disturbances are discussed together with several robust techniques for detection, isolation and reconfiguration. While most of the results on detection, isolation and reconfiguration are based on linear time invariant models of the aircraft dynamics, recent approaches to extend these results to non-linear models are reviewed and discussed. These approaches include the use of adaptive control, neural networks, fuzzy logic and knowledge-based methods from artificial intelligence (AI).

REFERENCE


AHMED-ZAID, F., IOANNOU, P., GOUSMAN, K., and ROONEY, R., 1991, Accommodation of failures in the F-16 aircraft using adaptive control. *IEEE Control Systems Magazine*, **11**, 73-78.

AHMED-ZAID, F., IOANNOU, P., POLYCARPOU, M.M., and YOUSSEF, H.M., 1993, Identification and control of aircraft dynamics using radial basis function networks. *2nd IEEE Conference on Control Applications*, 567-572.

AI-JARRAH, O. M. and AI-ROUSAN, M., 2001, Fault detection and accommodation in dynamic systems using adaptive neurofuzzy systems. *IEE Proceedings – Control Theory Application,* **148**, 283-290.

AKHMETOV, D.F., DOTE, Y., and OVASKA, S.J., 2001, Fuzzy neural network with general parameter adaptation for modeling of nonlinear time-series. *IEEE Transactions on Neural Networks*, **12**, 148-153.

ALESSANDRI, A., BAGLIETTO, M. and PARISINI, T., 1998, Robust model-based fault diagnosis using neural nonlinear estimators. *Proceedings of the 37th IEEE Conference on Decision and Control*, 72-77

ARKIN, R.C., and VACHTSEVANOS, G., 1990, Qualitative fault propagation in complex systems. *Proceedings of the 29th Conference on Decision and Control, Honolulu, Hawaii*, 1509-1510.

BASSEVILLE, M., 1988, Detecting changes in signals and systems — a survey. *Automatica*, **24**, 309-326.

BASSEVILLE, M. and PARISINI, T., 2000, Editorial for the special issue: Fault Detection and Isolation. *International Journal of Adaptive Control and Signal Processing*, **14**, 681-682.

BEARD, R.V., 1971, Failure accommodation in linear systems through self-reorganization. Ph.D. dissertation, Department of Aeronautics and Astronautics, MIT, Cambridge, Massachusetts.

BENKHEDDA, H. and PATTON, R.J., 1996, Fault diagnosis using quantitative and qualitative knowledge integration. *UKACC International Conference on Control,* **2**, 849-854.

BLANKE, M., IZADI-ZAMANABADI, R., B_GH, S.A., and LUNAU, C.P., 1997, Fault-tolerant control systems- a holistic view, *Control Engineering Practice*, **5**(5), 693-702.

BLANKE, M. STAROSWIECKI M. and WU, N.E., 2001, Concepts and methods in fault-tolerant control. *Proceedings of the American Control Conference*, 2606-2620.

BODSON, M., 1993, Identification with modeling uncertainty and reconfigurable control, *Proceedings of IEEE Conference of Decision and Control*, 2242-2247.

BODSON, M., and GROSZKIEWICZ, J., 1997, Multivariable adaptive algorithms for reconfigurable flight control. *IEEE Transactions on Control Systems Technology*, **5**, 217-229.

BOSKOVIC, J. D. and MEHRA, R. K., 1998a, A multiple model-based reconfigurable flight control system design. *Proceedings of the 37th IEEE Conference on Decision and Control*, Tampa, USA, 4503-4508.

BOSKOVIC, J. D., YU, S. H., and MEHRA, R. K., 1998b, Stable adaptive fault-tolerant control of overactuated aircraft using multiple models, switching and tuning. *Proc. AIAA GNC*, **1**, 739-749.

BURKEN, J.J., LU, P., and WU, ZHENGLU, 1999, Reconfigurable flight control designs with application to the X-33 vehicle. NASA/TM-1999-206582.

CAGLAYAN, A.K., RAHNAMAI, K. and ALLEN, S.M., 1988, detection, identification and estimation of surface damage/actuator failure for high performance aircraft, *Proceedings of American Control Conference.*

CALISE, A.J., LEE, S., and SHARMA, M, 1998, Direct adaptive reconfigurable control of a tailless fighter aircraft, *AIAA-98-4108*

CHANDLER, P.R., 1989, Issues in flight control design for robustness to failures and damage. *Proceedings of IEEE International Conference on Control and Application (ICCON '89), 540-545.*

CHANDLER, P., MEARS, M. and PACHTER, M., 1993, On-line optimizing networks for reconfigurable control. *Proceedings of the 32nd Conference on Decision and Control, 2272-2277.*

CHEN, J. and PATTON, R. J., 1999, *Robust model-based fault diagnosis for dynamic systems* (Kluwer Academic Publishers)

CHEN, J., PATTON, R. J. and ZHANG, H.Y., 1996, Design of unknown input observers and robust fault-detection filters. *International Journal of Control*, **63**, 85-105.

CHEN, R. H., and SPEYER, J. L., 2001, Fault reconstruction from sensor and actuator failures, *Proceedings of 40th IEEE Conference of Decision and Control*, 2277-2282.

CHEN, S., TAO, G. and JOSHI, S. M., 2002, On matching conditions for adaptive state tracking control of systems with actuator failures. *IEEE Transactions on Automatic Control,* **47**, 473-478.

CHESSA, S., and SANTI, P., 2001, Operative diagnosis of graph-based systems with multiple faults. *IEEE Transactions on Systems, Management and Cybernetics-Part A: Systems and Humans*, **31**, 112-119.

CHOI, J.W., LEE, J.G., KIM, Y., and KANG, T., 1995, Design of an effective controller via disturbance accommodating left eigenstucture assignment. *Journal of Guidance, Control & Dynamics*,**18**, 347-354.

CHOI, J.W., 1998, A simultaneous assignment methodology of right/left eigenstructures. *IEEE Transactions of Aerospace & Electronic Systems*, **34**, 625-634.

CHOW, E.Y., and WILLSKY, A., 1984, Analytical redundancy and the design of robust failure detection systems. *IEEE Transactions on Automatic Control*, **29**, 603-614.

CLARK, R.N., 1989, State estimation schemes for instrument fault detection. *Fault Diagnosis in Dynamic Systems: Theory and Application*, edited by Patton R.J., Frank P.M. and Clark R.N. (Englewood Cliffs, NJ: Prentice Hall)

DECKERT, J. C., DESAI, M. N., DEYST, J.J., and WILLSKY, A.S., 1977, F-8 DFBW sensor failure identification using analytic redundancy. *IEEE Transactions on Automatic Control*, **22**, 795-803.

DEXTER, A.L. and BENOUARETS, M., 1997, Model-based fault diagnosis using fuzzy matching. *IEEE Transactions on Systems, Management and Cybernetics-Part A: Systems and Humans*, **27**, 673-682.

DEMETRIOU, M A. and POLYCARPOU, M. M., 1998, Incipient fault diagnosis of dynamical systems using online approximators. *IEEE Transactions on Automatic Control,* **43**, 1612-1617.

DING, X. and FRANK, P.M., 1991, Frequency domain approach and threshold selector for robust model-based fault detection and isolation. *IFAC/IMACS Symposium on Fault Detection, Supervision and Safety for Technical Processes (SAFEPROCESS'91),* Baden-Baden, Germany, 307-312.

DING, X. and FRANK, P.M., 1992, Fault diagnosis using adaptive observers. *Proceedings of Singapore International Conference on Intelligent Control and Instrumentation,* **1**, 103-108.

DITTMAT, C.J., 1988, A hyperstable model-following flight control system used for reconfiguration following aircraft impairment. *Proceedings of Automatic Control Conference,* 2219-2224.

DUAN, G.R., PATTON, R.J., CHEN, J. and CHEN, Z., 1997, A parametric approach for robust fault detection in linear systems with unknown disturbances. *Proceedings of the IFAC Symposium on Fault Detection, Supervision and Safety for Technical Processes (SASFEPROCESS'97)*, Pergamon, Univ. of Hull, UK, 307-312.

ELAINE, A. W., BURKEN, J.J., HANSON, E.C. and WOHLETZ, M. J., 1998, Deterministic reconfigurable control design for the X-33 Vehicle. AIAA-98-4413.

EMANI-NAEINI, A., AKHTER, M.M. and ROCK, S.M., 1988, Effect of model uncertainty on failure detection- the threshold selector. *IEEE Transactions on Automatic Control*, **33**, 1106-1115.

ETERNO, J.S., LOOZE, D.P., WEISS, J.L. and WILLSKY, A.S., 1985, Design issues for fault-tolerant restructurable aircraft control, *Proceedings of the 24$^{th}$ Conference on Decision and Control,* 900-905.

FENU, G., GORINEVSKY, D. and PARISINI, T., 1999, Nonparametric kernel smoothing and FIR filtering for model-free symptom generation. *Proceedings of the 38$^{th}$ Conference on Decision and Control*, 4996-5001.

FRANK, P.M, 1990, Fault diagnosis in dynamic systems using analytical and knowledge-based redundancy - a survey and some new results. *Automatica*, **26**, 459-474.

FRANK, P.M., 1994, Enhancement of robustness in observer-based fault detection. *International Journal of Control*, **59**, 955-981.

FRANK, P.M., 1995, Residual evaluation for fault diagnosis based on adaptive fuzzy thresholds. *IEE Colloquium on Qualitative and Quantitative Modeling Methods for Fault Diagnosis*, 4/1-4/11.

FRANK, P.M. and DING, X., 1994, Frequency domain approach to optimally robust residual generation and evaluation for model-based fault diagnosis. *Automatica*, **30**, 789-804.

FRANK, P.M. and DING, X., 1997, Survey of robust residaul generation and evaluation methods in observer-based fault detection systems. *Journal of Process Control*, **7**, 403-424.

FRANK, P.M., and KIUPEL, N., 1997, FDI with computer-assisted human intelligence. *Proceedings of American Control Conference*, Albuquerque, New Mexico, 913-917.

FREY, C.W. and KUNTZE, H. B., 2001, A neuro-fuzzy supervisory control system for industrial batch processes. *IEEE Transactions on Fuzzy Systems*, **9**, 570-577.

GAO, Z. and ANTSAKLIS, P.J., 1991, Stability of the pseudo-inverse method for reconfigurable control systems. *International Journal of Control*, **53**, 717-729.

GERTLER, JANOS J., 1988, Survey of model-based failure detection and isolation in complex plants. *IEEE Control Systems Magazine*, **8**(6), 3-11.

GERTLER, JANOS, J., 1993, Analytical redundancy methods in failure detection and isolation in complex plants. *Control Theory and Advanced Technology*, **9**, 259-285.

GERTLER, J. and KUNWER, M.K., 1995, Optimal residual decoupling for robust fault diagnosis. *International Journal of Control*, **61**, 395-421.

GOBBO, D.DEL and MAPOLITANO, M.R., 2000, Issues in fault detectability for dynamic systems. *Proceedings of the American Control Conference,* Chicago, Illinois, 3203-3207.

HOFFMAN, A.J., VAN DER MERWE, N.T., STANDER, C. and HEYNS, S.P., 2001, A comparative evaluation of neural classification techniques for identifying multiple fault conditions. *International Workshop on Intelligent Data Acquisition and Advanced Computing Systems: Technology and applications*, Foros, Ukraine, 16-20.

HOROWITZ. I., ARNOLD, P.D. and HOUPIS, C.H., 1985, YF-16-CCV flight control system reconfiguration design using quantitative feedback theory. *Proceedings of the IEEE 1985 National Aerospace and Electronics Conference,* 578-585.

HOU, M. and MULLER, P.C., 1994, Disturbance decoupled observer design: a unified viewpoint. *IEEE Transactions on Automatic Control,* **39**, 1338-1341.

HUANG, C.Y. and STENGEL, R.F., 1990, Restructurable control using proportional-integral implicit model-following. *Journal of Guidance, Control and Dynamics*, **13**, 303-309.

HUO, YING, HOU, CHAOZHEN, and LIU, SHUANGXI, 1998, Application of fuzzy set theory in fault tree analysis. *Chinese Journal of Mechanical Engineering (English Edition)*, **11**, 326-332.

HUO, YING, HOU, CHAOZHEN, and LIU, SHUANGXI, 1999, Fault diagnosis based on fuzzy relation matrix and recognition. *Proceedings of the 14th IFAC World Congress*, Vol. P, 163-167.

IOANNOU, P., GOUSMAN, K. and ROONEY, R., 1989, Surface failure detection and evaluation of control law for reconfiguration of flight control system. *Proceedings of AIAA Guidance & Navigation Control Conference*, Boston, MA, 733-740.

IOANNOU, P. and SUN, J., 1996, *Robust Adaptive Control* ( NJ: Prentice Hall )

ISERMANN, R., 1984, Process fault detection based on modeling and estimation methods: a survey. *Automatica*, **20**, 387-404.

ISERMANN, R., 1994, Integration of fault detection and diagnosis methods. *Reprints of IFAC Symposium on Fault Detection, Supervision and Safety for Technical Processes (SAFEPROCESS'94)*, Espoo, Finland, 575-590.

ISERMANN, R., 1997, Supervision, fault-detection and fault-diagnosis methods - an introduction. *Control Engineering Practice*, **5**, 639-652.

JAXOBSON, C. A. and NETT, C.N., 1991, An integrated approach to controls and diagnostics using the four parameter control. *IEEE Control Systems Magazine*, **11**, 22-29.

JOSEPH, S. BRINKER and WISE, A. KEVIN, 1998, Reconfigurable flight controls for a tailless advanced fighter aircraft. AIAA-98-4107.

JOSHI, S.M., 1987, Design of failure accommodating multiloop LQG-type controller. *IEEE Transactions on Automatic Control*, **32**, 740-741.

KINNAERT, M. and PENG, Y., 1995, Residual generator for sensor and actuator fault detection and isolation: a frequency domain approach. *International Journal of Control*, **61**, 1423-1435.

KIUPEL, N., KOPPEN-SELIGER, B., KELLINGHAUS, H.S., and FRANK, P.M., 1995, Fuzzy residual evaluation concept. *IEEE International Conference on Intelligent Systems for the 21st Century*, 13-18.

KOUTSOUKOS, X.D., ANTSAKLIS P.J., STIVER J.A., and LEMMON M.D., 2000, Supervisory control of hybrid systems. *Proceeding of the IEEE*, **88**, 1026-1049.

LANE, S.H. and STENGEL, R.F., 1988, Flight control design using non-linear inverse dynamics. *Automatica*, **24**, 471-483.

LAWRENCE, D, and RUGH, W., 1995, Gain scheduling dynamic linear controllers for non-linear plant, *Automatica*, **31**, 381.

LOU, X., WILLSKY, A.S. and VERGHESE, G.C, 1986, Optimally robust redundancy relations for failure detection in uncertain systems. *Automatica*, **22**, 333-344.

LOOZE, D.P., WEISS, J.L., ETERNO, J.S. and BARRETT, N.M., 1985, An automatic redesign approach for restructurable control systems. *IEEE Control System Magazine*, 16-22.

LUNZE, J., NIXDORF, B. and RICHTER, H., 2001, Process supervision by means of a hybrid model. Journal of Process Control, **11**, 89-101.

MAKILA P.M., J.R. PARTINGTON and T.K. GUSTAFSSON, 1995, Worst-case control-relevant identification. *Automatica*, *31*, 1799-1819.

MANGOUBI, R., APPLEBY, B.D, and FARRELL, J.R., 1992, Robust estimation in fault detection. *Proceedings of the 31st Conference on Decision & Control*, Tucson, AZ, 2317-2322.

MARRISON, C.I. and STENGEL, R.F., 1998, Design of robust control systems for a hypersonic aircraft. *Journal of Guidance, Control, and Dynamics*, **21**, 58-63.

MARTINS, J.F., DENTE, J.A., PIRES, A.J. and MENDES, VILELA R., 2001, Language identification of controlled systems: modeling, control, and anomaly detection. *IEEE Transactions on Systems, Managements, and Cybernetics-Part:C Applications and Reviews*, **31**, 234-242.

MEYER, G. and HUNT, L, 1984, Application of non-linear transformations to automatic flight control. *Automatica*, **20**, 103-107.

MIGNONE D., A. BEMPORAD and M. MORARI, 1999, A framework for control, fault detection, state estimation and verification of hybrid systems. *Proceedings of the American Control Conference, San Diego*, 134-138.

MOERDER, D.D., HALYO, N., BROUSSARD, J.R. and CAGLAYAN, A.K., 1989, Application of precomputed control laws in a reconfigurable aircraft flight control system. *Journal of Guidance*, **12**, 325-333.

MOLNAR, J. A., 1997, Summary and applicability of analog fault detection/isolation techniques. *IEEE Autotestcon Proceedings*, 383-389.

MONACO, J., WARD, D., BARRON, R., and BIRD, R., 1997, Implementation and flight test assessment of an adaptive reconfigurable flight control system. AIAA-97-3738.

MORSE, W.D. and OSSMAN, K.A., 1990, Model-following reconfigurable flight control system for the AFTI/F-16. *Journal of Guidance, Control and Dynamics,* **13**, 969-976.

MUDGE, S.K. and PATTON, R.J., 1988, Variable structure control laws for aircraft maneuvers. *Reprints of International Conference on Control (Control'88)*, 153-158.

NARENDRA, K.S. and PARTHASARTHY, K., 1990, Identification and control of dynamical systems using neural networks. *IEEE Transactions on Neural Networks*, **1**, 4-27.

NAPOLITANO, M.R., SWAIM, R.L., and GOODNER, C.E., 1989, An aircraft flight control reconfiguration algorithm. *Proceedings of the IEEE 1989 National Aerospace and Electronics Conference NAECON'89*, **1**, 325-332.

NIEMANN, H.H. and STOUSTRUP, J., 1996, Filter design for failure detection and isolation in the presence of modeling errors and disturbances. *Proceedings of the 35th IEEE Conference on Decision and Control*, 1155-1160.

NIEMANN, H.H. and STOUSTRUP, J., 1997, Integration of control and fault detection: nominal and robust design. *Proceedings of the IFAC symposium on fault detection supervision and safety for technical process,* 331-336.

NIEMANN, H.H. and STOUSTRUP, J., 2000, Design of fault detectors using $H_\infty$ optimization. *Proceedings of the 39th IEEE Conference on Decision and Control*, 4327-4328.

OCHI, Y., and KANAI, K., 1991, Design of restructurable flight control systems using feedback linearisation. *Journal of Guidance, Control and Dynamics*, **14**, 903-911.

OSTROFF, A., 1985, Techniques for accommodating control effector failures on mildly statically unstable airplane. *Proceedings of the American Control Conference*, 906-9013.

PARISINI, T. and SACONE, S., 1998, Fault diagnosis and controller reconfiguration: an hybrid approach. *Proceedings of the 1998 IEEE ISIC/CIRA/ISAS Joint Conference, Gaithersburg, MD*, 163-168.

PARK, J.H., and RIZZONI, G., 1994, A new interpretation of the fault-detection filter. 1: closed-form algorithm. *International Journal of Control*, **60**, 767-787.

PARK, J.H., HALEVI, Y. and RIZZONI, G., 1994, A new interpretation of the fault-detection filter. 2: the optimal detection filter. *International Journal of Control*, **60**, 1339-1351.

PATTON, R.J., 1991, Fault detection and diagnosis in aerospace systems using analytical redundancy. *Computing & Control Engineering Journal*, **2**(3), 127-136.

PATTON, R.J., 1997, Fault tolerant control systems: the 1997 situation. *IFAC symposium on fault detection supervision and safety for technical process*, **3**, 1033-1054.

PATTON, R. J. and CHEN, J., 1991, Robust fault detection using eigenstructure assignment: A tutorial consideration and some new results. *Proceedings of the 30th IEEE Conference on Decision and Control*, 2242-2247.

PATTON, R. J. and CHEN, J., 1994, Review of parity space approaches to fault diagnosis for aerospace systems. *Journal of Guidance, Control and Dynamics*, **17**, 278-285.

PATTON, R.J., and KANGETHE, S.M., 1988, Robust fault diagnosis using the model-based approach. *IEE Colloquium on Condition Monitoring and Failure Diagnosis-Part 1*, 2/1-2/13.

PATTON, R.J. and LOPEZ-TORIBIO, C. J., 1999, Artificial intelligence approaches to fault diagnosis. *IEE Colloquium on Condition Monitoring: Machinery, External Structures and Health (Ref. No. 1999/034)*, 5/1 –5/18.

PATTON, R.J., WILLCOX, S.W. and WINTER, S.J., 1986, A parameter insensitive technique for aircraft sensor fault analysis. *Journal of Guidance, Control & Dynamics*, **10**, 359-367.

PECHT, M., DUBE, M., NATISHAN, M, WILLIAMS, R., BANNER, J. and KNOWLES, I., 2001, Evaluation of built-in test. *IEEE Transactions on Aerospace and Electronic Systems*, **37**, 266-271.

POLYCARPOU, M.M., 1994, An on-line approximation approach to fault monitoring, diagnosis and accommodation. *SAE Technical Paper 941217.*

POLYCARPOU, M.M. and TRUNOV, A., 2000, Learning approach to nonlinear fault diagnosis: detectability analysis. *IEEE Transactions on Automatic Control*, **45**, 806-812.

POLYCARPOU, M.M. and VEMURI, A., 1998, Learning approach to fault tolerant control: an overview. *Proceedings of the 1998 IEEE International Symposium on Intelligent Control (ISIC/CIRA/ISAS'98)*, 157-162.

PREVIDI, F, and PARISINI, T., 2001, Model-free fault detection: a spectral estimation approach based on coherency functions. *International Journal of Control*, **74**, 1107-1117.

RATTAN, K.S., 1985, Evaluation of control mixer concept for reconfiguration of flight control system. *Proceedings of IEEE National Aerospace and Electronics Conference*, 560-569.

RAUCH, H.E., 1994, Intelligent fault diagnosis and control reconfiguration. *IEEE Control Systems Magazine,* **14**(3), 6-12.

RAUCH, H.E., 1995, Autonomous control reconfiguration. *IEEE Control Systems Magazine*, **15**(6), 37-48.

RAUCH, H.E., KLINE-SCHODER, R.J., ADAMS, J.C. and YOURSSEF, H.M., 1993, Fault detection, isolation, and reconfiguration for aircraft using neural networks. *Proceedings of AIAA Conference on Guidance, Navigation, and Control.*

RAZA, H., IOANNOU, P. and YOUSSEF, H.M., 1994, Surface failure detection for an F/A-18 aircraft using neural networks and fuzzy logic. *IEEE International Conference on Intelligence*, **5**, 3363-3368.

RAZA, S.J. and SILVERTHORN, J.T., 1985, Use of the pseudo-inverse for the design of a reconfigurable flight control systems. *Proceedings of IEEE National Aerospace and Electronics Conference*, 349-356.

RUGH, W.J., 1991, Analytical framework for gain scheduling. *IEEE Control System Magazine*, **11**, 79-84.

RYSDYK, R.T., and CALISE, A.J., 1998, Fault tolerant flight control via adaptive neural network augmentation, *AIAA-98-4483.*

SHEN., L.C., CHANG, S.K. and HSU, P.L., 1998, Robust fault detection and isolation with unstructured uncertainty using eigenstructure assignment. *Journal of Guidance, Control & Dynamics*, **21**, 50-57.

SCHRICK, D., 1994, A comparison of IFD schemes - a decision aid for designers. *Proceedings of the 3rd IEEE Conference on Control Applications*, **2**, 889-894.

SHAMMA, J. and ATHANS, M., 1992, Gain scheduling: Potential hazards and possible remedies. *IEEE Control System Magazine*, **10**, 101-107.

SMITH, G.A. and MEYER, G., 1987, Aircraft automatic flight control system with model inversion. *Journal of Guidance, Control and Dynamics*, **10**, 269-275.

SNORRASON M. CAGLAYAN, A.K. andBULLER B.T., 1993, Using self-organized and supervised learning neural networks in parallel for automatic target recognition. *Proceedings of the IEEE-SP workshop on Neural Networks for Processing*, 537-548.

SOBEL, K.M., KAUFMAN, H. and BALAS, M., 1982, Implicit adaptive control for a class of MIMO systems. *IEEE Transactions on Aerospace and Electronics System*, **AES-18**, 576-589.

SONG, YONGKYU, CAMPA GIAMPIERO, NAPOLITANO MARCELLO, SEANOR BRAD, and PERHINSCHI , M.G., 2002, Online parameter estimation techniques comparison within a fault tolerant flight control system. *Journal of Guidance, Control, and Dynamics*, **25**, 528-537.

STENGEL, R.F., 1991, Intelligent failure-tolerant control. *IEEE Control Systems Magazine*, **11**(4), 14-23.

STENGEL, R.F., 1993, Toward intelligent flight control. *IEEE Transactions on Systems, Management & Cybernetics*, **23**, 1699-1717.

STOUSTRUP, J. and NIEMANN, H.H., 1998, Fault estimation for nonlinear systems – a standard problem approach. *Proceedings of the 37th IEEE Conference on Decision and Control,* 96-101.

STOUSTRUP, J. and NIEMANN, H.H., 1999, Fault detection and isolation in systems with parametric faults (Invited paper). *Proceedings of the IFAC World Congress*, Volume P, 139-144.

STOUSTRUP, J. and NIEMANN, H.H., 2001, Fault tolerant feedback control. *Proceedings of the European Control Conference, Porto, Portugal,* 1970-1974.

TAKAGI, T. and SUGENO, M., 1985, Fuzzy identification of systems and its applications to modeling and control. *IEEE Transactions on Systems, Management & Cybernetics,* **15**, 116-132.

TAO, G., JOSHI, S. M. and MA, X. L., 2001, Adaptive state feedback and tracking control of systems with actuator failures. *IEEE Transactions on Automatic Control,* **46**, 78-95.

TAO, G., CHEN, S. and JOSHI, S.M., 2002, An adaptive actuator failure compensation controller using output feedback. *IEEE Transactions on Automatic Control,* **47**, 506-511.

TRUNOV, A. and POLYCARPOU,M.M., 2000, Automated fault diagnosis in nonlinear multivariable systems using a learning methodology. *IEEE Transactions on Neural Networks*, **11**, 91-101.

VEILLETTE, R.J., MEDANIC, J.V., and PERKINS, W.R., 1992, Design of reliable control systems. *IEEE Transactions on Automatic Control,* **37**, 290-304.

VEMURI, A.T., POLYCARPOU, M.M., 1996, On-line approximation based methods for robust fault detection. *Proceedings of the 13th IFAC World Congress,* 319-324.

VISWANADHAM, N. and MINTO, K.D, 1988, Robust observer design with application to fault detection. *Proceedings of the American Control Conference*, Atlanta, GA, 1393-1399.

WANG H. and DALEY S., 1996, Actuator fault diagnosis: an adaptive observer-based technique. *IEEE Transactions on Automatic Control,* **41**, 1073-1078.

WANG H., HUANG, Z. J. and DALEY S., 1997, On the use of adaptive updating rules for actuator and sensor fault diagnosis. *Automatica,* **33**, 217-225.

WATANABE, K. and HIMMELBLAU, D.M., 1982, Instrument fault detection in systems with uncertainties. *International Journal of Systems Science*, **13**(2), 137-158.

WHITE, J.E., and SPEYER, J.L., 1987, Detection filter design: spectral theory and algorithm. *IEEE Transactions on Automatic Control,* **32**, 593-603.

WILLIAMS, S., HYDE, R.A., 1990, A comparison of characteristic locus and $H_\infty$ design methods for VSTOL flight control system design. *Proceedings of the American Control Conference,* 2508-2513.

WILLSKEY, A.S., 1976, A survey of design methods for failure detection in dynamic systems. *Automatica*, **12**, 601-611.

WU, N.E., 1992, Failure sensitizing reconfigurable control design. *Proceedings of the 31st IEEE Conference on Control & Decision,* Tucson, *AZ*, 44-49.

WUENNENGERG, J., 1990, Observer-based fault detection in dynamic systems. PhD thesis, Univ. of Duisburg, Germany

YANG, Z. and BLANKE, M., 2000, The robust control mixer module method for control reconfiguration. *Proceedings of the American Control Conference, Chicago, Illinois*, 3407-3411.

YANG, Z. and STOUSTRUP, J., 2000, Design of robust reconfigurable control for parametric and additive faults. *Proceedings of the 39th IEEE Conference on Decision and Control*, 4132-4137.

YOUSSEF, H.M., GOUSMAN, K.G., and COMBS, S.R., 1995, Fuzzy logic approach to automatic recovery system. *Proceedings of the IEEE National Aerospace and Electronics Conference, NAECON'95*, **1**,464-471.

ZHANG, X., POLYCARPOU, M.M. and PARISINI, T., 2001a, Robust fault isolation of a class of nonlinear input-output systems. *International Journal of Control*, **74**, 1295-1310.

ZHANG, X., POLYCARPOU, M.M. and PARISINI, T., 2001b, Integrated design of fault diagnosis and accommodation schemes for a class of nonlinear systems. *Proceeding of the 40$^{th}$ IEEE Conference on Decision and Control Orlando, USA.* 1448-1453.

ZHANG, X., POLYCARPOU, M.M. and PARISINI, T., 2002, A robust detection and isolation scheme for abrupt and incipient faults in nonlinear systems. *IEEE Transactions on Automatic Control,* **47**, 576-593.

ZHENG, C., PATTON, R.J., and CHEN, J., 1997, Robust fault-tolerant systems synthesis via LMI. *Proceedings of IFAC SAFEPROCESS'97*, 347-352.

ZHOU, D. H. and FRANK, P.M, 2001, Fault diagnostics and fault tolerant control. *IEEE Transactions on Aerospace and Electronic Systems*, **34**, 420-427.

ZHUANG, Z., SCHREIER, G., and FRANK, P.M., 1998, A qualitative-observer approach to generating and evaluating residuals. *Proceedings of 37th IEEE Conference on Decision & Control*, Tampa, FL, 102-107.

ZINOBER, A.S.I., YEW, M.K. and PATTON, R.J., 1988, Variable structure model-following control of flight dynamics. *Reprints of International Conference on Control (Control'88)*, 707-712.

## List of Figures

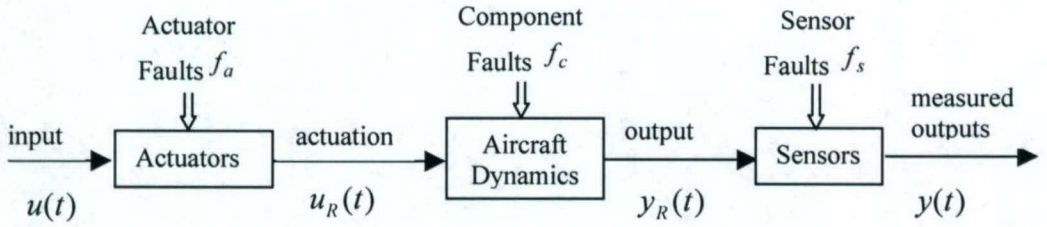


Figure 1. Aircraft system with possible faults

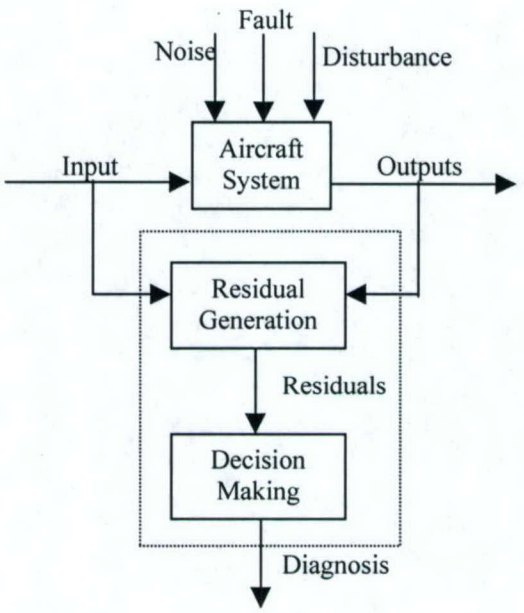


Figure 2. Conceptual Structure of Model-based Fault Diagnosis

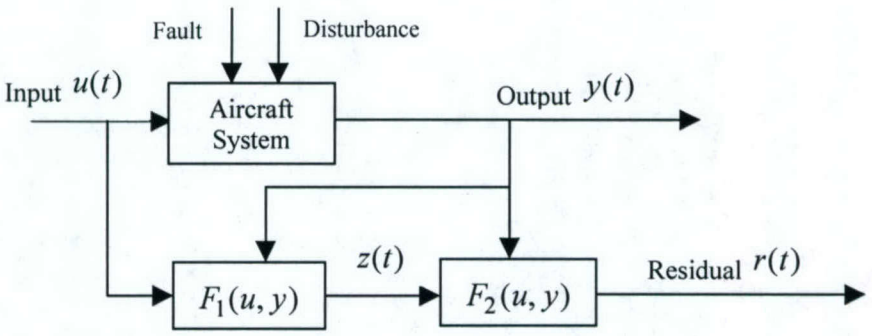


Figure 3 Redundancy signal structure of a residual generator

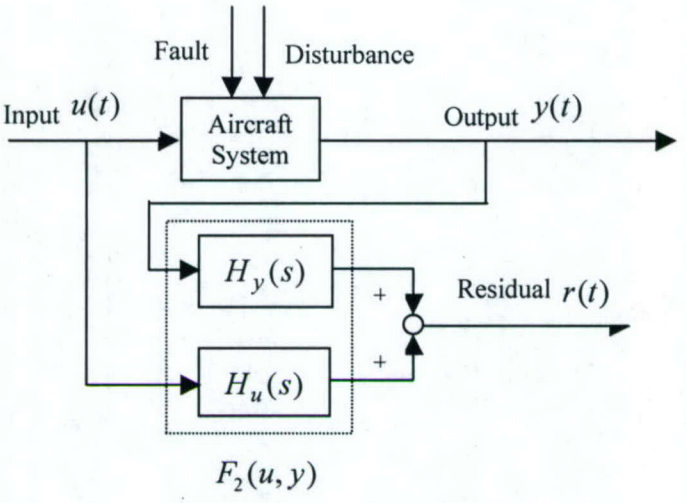


Figure. 4 The General Structure of a residual generator

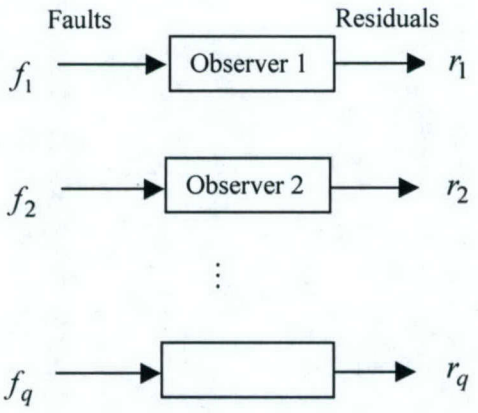


Figure 5 Structured Residual Set (Dedicated Scheme)

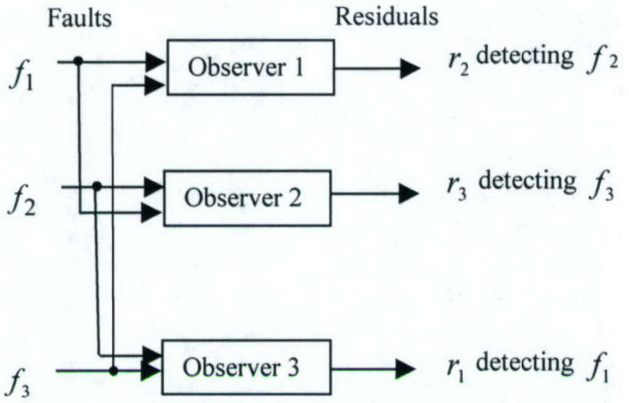


Figure 6 Structured Residual Set (Generalized Observer Scheme)

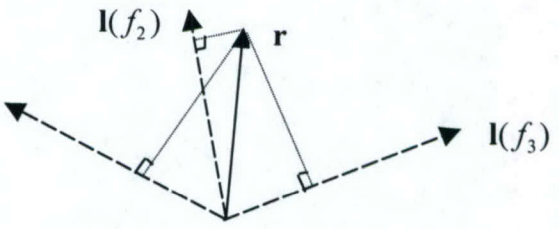


Figure 7 Fault Isolation with Directional Residual Set

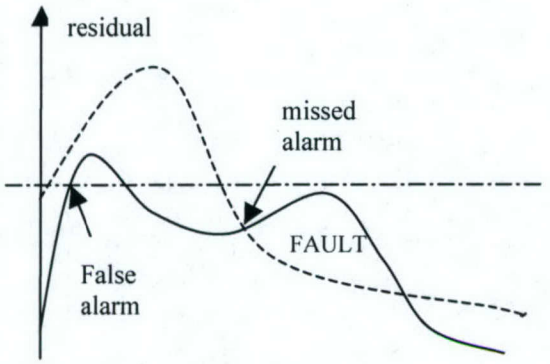


Figure 8 Application of an Adaptive Threshold in Robust FDI

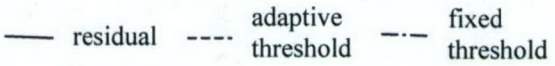

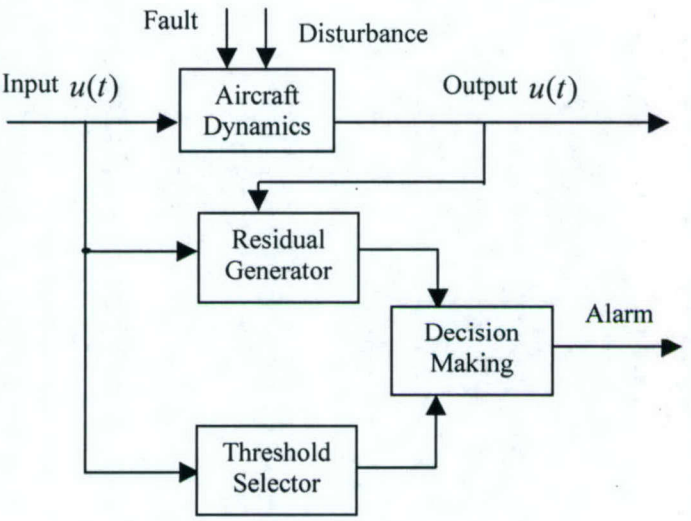


Figure 9 Robust FDI With the Use of Threshold Selector

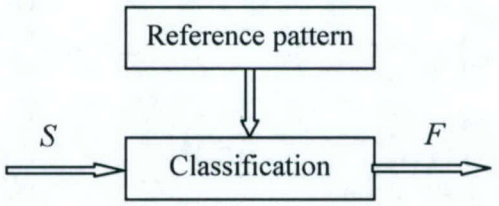


Figure 10 Fault Diagnosis Using Classification Methods

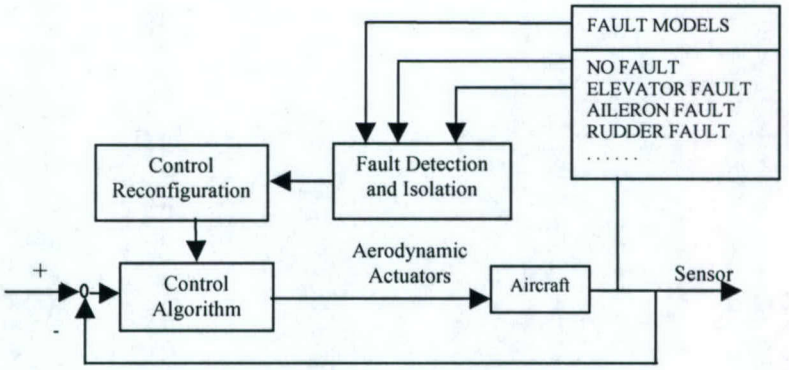


Figure 11 Fault Detection, Isolation and Reconfiguration for Aircraft Control Surfaces

Proceedings of the 41st IEEE
Conference on Decision and Control
Las Vegas, Nevada USA, December 2002



# ROBUST ADAPTIVE CONTROL FOR A CLASS OF MIMO NONLINEAR SYSTEMS*

Haojian Xu and Petros A. Ioannou

Department of Electrical Engineering - Systems
University of Southern California, Los Angeles, CA 90089

**Abstract**

The design of stabilizing controllers for nonlinear plants with unknown nonlinearities is a challenging problem. The inability to identify the nonlinearities on-line or off-line accurately motivates the design of stabilizing controllers based on approximations or on approximate estimates of the plant nonlinearities. The price paid in such case, could be lack of theoretical guarantees for global stability, and/or nonzero tracking or regulation error at steady state. In this paper a nonlinear robust adaptive control algorithm is designed and analyzed for a class of multi-input multi-output nonlinear systems with unknown nonlinearities. The controller guarantees closed loop semi-global stability and convergence of the tracking error to a small residual set. The size of the residual set for the tracking error depends solely on design parameters, which can be chosen to meet desired upper bounds for the tracking error. Consequently the proposed methodology provides a design procedure to meet apriori specified performance guarantees for the steady state tracking error.

## 1. INTRODUCTION

The traditional way of designing feedback control systems is based on the use of Linear Time Invariant (LTI) models for the plant. Off-line frequency domain techniques could be used to fit such an LTI model to experimental data and identify its parameters. In the case, where the parameters of the LTI model change with time, gain scheduling, on-line parameter identification, adaptive control, robust control techniques etc. are developed over the years to address such situations [1]. The reliance on LTI models for control design purposes often puts limitations on the performance improvement that could be achieved for the plant under consideration. For example if the plant consists of strong nonlinearities, its approximation by an LTI model, may considerably reduce the region of attraction in the presence of disturbances and other modeling uncertainties. During the recent years, considerable research efforts have been made to deal with the design of stabilizing controllers for classes of nonlinear plants. These efforts are described in detail in a recent survey paper [2], where a very elegant and informative historical perspective of the evolution of nonlinear control design is presented and discussed. Most of the recent efforts (e.g., surveyed in [2], and [3]-[4]) on nonlinear control design assumed that the plant nonlinearities are known. The case where the plant nonlinearities are products of unknown constant parameters with known nonlinearities gave rise to a number of adaptive control techniques [1], [5]-[10]. Adaptive nonlinear control techniques based on universal function approximators have been found to be particularly useful for controlling more general unknown nonlinearities [11]-[17]. However there are no systematic analytical methods of ensuring the stability, robustness, and performance of the closed loop system. In [18] we designed and analyzed a robust adaptive control scheme for a class of SISO nonlinear linearizable systems with unknown nonlinearities. We developed upper bounds for the tracking error that can be computed apriori. In fact given any desired nonzero upper bound for the tracking error at steady state, a number of design parameters can be chosen apriori to meet such bound.

In this paper we develop a robust adaptive control scheme for a wider class of MIMO nonlinear linearizable systems with unknown nonlinearities. The only assumptions made are that the unknown nonlinear functions are smooth, and a sufficient condition for controllability is satisfied. The proposed scheme guarantees semi-global stability and convergence of the tracking error to a residual set whose size depends on design parameters that can be chosen apriori. For any given desired upper bound for the tracking error at steady state, our approach provides a procedure for choosing the design parameters to meet the tracking error bound.

This paper is organized as follows: In section 2 the problem statement and preliminaries are presented. In section 3 we present the proposed adaptive control scheme is discussed. In section 4, the theoretical results are applied to the control of a two-link robot. Finally, section 5 includes the conclusions. Throughout this paper, $|\cdot|$ indicates the absolute value, and $\|\cdot\|$ indicates the Euclidean vector norm.

## 2. PROBLEM STATEMENT AND PRELIMINARIES

Consider the following multi-input multi-output nonlinear system:

$$\begin{aligned} x_1^{(r_1)} &= f_1(x) + b_{11}(x)u_1 + \cdots + b_{1m}(x)u_m \\ &\vdots \\ x_m^{(r_m)} &= f_m(x) + b_{m1}(x)u_1 + \cdots + b_{mm}(x)u_m \\ y_1 &= x_1, \cdots, y_m = x_m \end{aligned} \tag{1}$$

where, $x := \left[x_1, \cdots, x_1^{(r_1-1)}, \cdots, x_m, \cdots, x_m^{(r_m-1)}\right]^T \in \Re^r$, $r = r_1 + \cdots + r_m$, is the overall state vector, $x_i^{(n)} := d^n x_i / dt^n$, $u_i \in \Re$, $i = 1,2,\cdots,m$, are the inputs and $y_i \in \Re$, $i = 1,2,\cdots,m$, are the outputs of the system. The nonlinear functions $f_1, \cdots, f_m$ and $b_{ij}, i,j = 1,\cdots,m$ are assumed to be smooth functions. The problem is to design the control input $u = [u_1, \cdots, u_m]^T \in \Re^m$ such that the outputs of the system $y_1, \cdots, y_m$ track the desired trajectories $y_{d_1}(t), \cdots, y_{d_m}(t)$ respectively.

The system (1) can also be written in the compact form

$$[x_1^{(r_1)} \quad x_2^{(r_2)} \quad \cdots \quad x_m^{(r_m)}]^T = f(x) + B(x)u \tag{2}$$

where,

$$f(x) = \left[f_1(x) \quad \cdots \quad f_m(x)\right]^T \in \Re^m,$$

$$B(x) = \begin{bmatrix} b_{11}(x) & \cdots & b_{1m}(x) \\ \vdots & \ddots & \vdots \\ b_{m1}(x) & \cdots & b_{mm}(x) \end{bmatrix} \in \Re^{m \times m}$$

We make the following assumptions:

* This work was supported in part by Air Force under grant F4920-01-0489 and in part by a collaborative linkage grant from the NATO Cooperative Science and Technology Sub-Programme.

***Assumption* 1**: The matrix $\frac{1}{2}\left(B(x)+B^T(x)\right)$ is known to be either uniformly positive definite or uniformly negative definite for all $x \in \Omega_1$ where $\Omega_1 \subset \Re^r$ is a compact set, i.e.,

$$\underline{\sigma}\{\tfrac{1}{2}(B(x)+B^T(x))\} \geq \underline{b} > 0, \quad \forall\ x \in \Omega_1 \tag{3}$$

where $\underline{\sigma}(\cdot)$ represents the smallest singular value of the matrix inside the bracket and $\underline{b}$ is its lower bound.

Assumption 1 guarantees that the nonlinear system (1) is uniformly strongly controllable.

***Assumption* 2**: The desired trajectories $y_{d_i}(t)$, $i$=1,2,...,$m$ are known bounded functions of time with bounded known derivatives and $y_d := \left[y_{d_1}, \cdots, y_{d_1}^{(r_1-1)}, \cdots, y_{d_m}, \cdots, y_{d_m}^{(r_m-1)}\right]^T$, $y_d \in \Omega_2 \subset \Re^r$, where $\Omega_2$ is a known compact set.

***Assumption* 3**: The state vector $x$ is available for measurement.

***Assumption* 4**: The functions $f_i(x)$ and $b_{ij}(x)$, $i,j = 1,2,\cdots,m$ are smooth functions but otherwise completely unknown.

Let us first consider the case where $f_i$ and $b_{ij}$, $i,j = 1,2,\cdots,m$, are completely known and examine whether we can meet the control objective. This is a reasonable step to take since if we cannot meet the control objective in the case of known nonlinearities, it is unlikely that we will do so in the case of unknown nonlinearities.

We define the following error metric, $S_i$, that describes the desired dynamics of the error system:

$$\begin{aligned} S_1(t) &= (d/dt + \lambda_1)^{r_1-1} e_1(t), \qquad e_1(t) = y_1 - y_{d_1} \\ &\vdots \\ S_m(t) &= (d/dt + \lambda_m)^{r_m-1} e_m(t), \quad e_m(t) = y_m - y_{d_m} \end{aligned} \tag{4}$$

where $\lambda_1, \cdots, \lambda_m$ are positive constants to be selected. It follows from (4) that for $S_i(t) = 0$, $i = 1,2,\cdots,m$, we have a set of linear differential equations whose solutions imply that $e_i(t)$ converges to zero with time constant $(r_i - 1)/\lambda_i$. In addition all the derivatives of $e_i(t)$ up to $r_i - 1$ also converge to zero [3]-[4].

It follows from (4) that

$$\begin{bmatrix} \dot{S}_1 \\ \vdots \\ \dot{S}_m \end{bmatrix} = \begin{bmatrix} f_1(x) \\ \vdots \\ f_m(x) \end{bmatrix} + \begin{bmatrix} v_1(t) \\ \vdots \\ v_m(t) \end{bmatrix} + \begin{bmatrix} b_{11}(x) & \cdots & b_{1m}(x) \\ \vdots & \ddots & \vdots \\ b_{m1}(x) & \cdots & b_{mm}(x) \end{bmatrix} \begin{bmatrix} u_1 \\ \vdots \\ u_m \end{bmatrix} \tag{5}$$

where,

$$\begin{aligned} v_1(t) &= -y_{d_1}^{(r_1)}(t) + \alpha_{1,r_1-1} e_1^{(r_1-1)}(t) + \cdots + \alpha_{1,1} \dot{e}_1(t) \\ &\vdots \\ v_m(t) &= -y_{d_m}^{(r_m)}(t) + \alpha_{m,r_m-1} e_m^{(r_m-1)}(t) + \cdots + \alpha_{m,1} \dot{e}_m(t) \end{aligned} \tag{6}$$

and $\alpha_{i,r_i-1}, \cdots, \alpha_{i,1}$, $i$=1,2,...,$m$ are coefficients of the binomial expansion of the corresponding error metric in (4).

Equation (5) can be written in the compact form:

$$\dot{S} = f(x) + v(t) + B(x)u \tag{7}$$

where, $S = \begin{bmatrix} S_1 & \cdots & S_m \end{bmatrix}^T \in \Re^m$, $v(t) = \begin{bmatrix} v_1(t) & \cdots & v_m(t) \end{bmatrix}^T \in \Re^m$.

Let us consider the Lyapunov-like function $V(t) = \frac{1}{2} S^T S$. Then

$$\dot{V} = S^T \dot{S} = S^T f(x) + S^T v(t) + S^T B(x) u \tag{8}$$

If we now choose the control law $u$ so that

$$\dot{V} = S^T \dot{S} < 0 \tag{9}$$

then it can be show that $\lim_{t\to\infty} \|S\| \to 0$.

***Lemma* 1**: Let us define $X := [x, y_d]^T$. For any square matrix $B(x)$ satisfying *Assumption* 1, there exists a smooth scalar function $\mu(X)$ such that for any vector $S(X)$, $S^T(X)B(x)S(X) = \mu(X)\|S(X)\|^2$, where $|\mu(X)| > \underline{b}$.

***Proof***: the proof process is omitted due to the limited space.

let us now consider the control law:

$$u = \frac{S}{S^T B(x) S}\left[-k_S \|S\|^2 - S^T f(x) - S^T v(t)\right] \tag{10}$$

where $k_S > 0$ is a design constant. Using lemma 1 we can rewrite (10) as

$$u = \frac{S_e}{\mu(X)}\left[-k_S \|S\| - S_e^T f(x) - S_e^T v(t)\right] \tag{11}$$

where $S_e = S/\|S\|$ is the unit vector. The control law (11) guarantees that

$$\dot{V} = S^T \dot{S} = -k_S \|S\|^2 \leq 0 \tag{12}$$

which in turn implies that $\lim_{t\to\infty} S_i(t) = 0$ and therefore $e_i$ and all its derivatives up to $r_i - 1$ converge to zero asymptotically.

In the case where $f(x)$ and $B(x)$ are unknown nonlinear functions, the control law (11) can no longer be used. In the following section we will modify the control law (11) to guarantee stability and meet the control objective when $f(x)$ and $B(x)$ are unknown.

## 3. ROBUST ADAPTIVE CONTROL SCHEME

Let us consider the system (1) and control problem solved in section 2 for the case of known nonlinearities. In this section we assume that the nonlinear functions in (1) are unknown functions and design a control law to meet the control objective. We assume that the nonlinear functions $f(x)$ and $\mu(X)$ can be approximated by the general one layer neural network [13]-[16],[19] as

$$f_i(x) \approx f_i^a(x) = \sum_{j=1}^{l_i} \theta_{ij} \zeta_{ij}(x), \quad i = 1,2,\cdots,m \tag{13a}$$

$$\mu(X) \approx \mu^a(X) = \sum_{j=1}^{l_0} \theta_{0j} \zeta_{0j}(X) \tag{13b}$$

where $\zeta_{0j}(X)$, $\zeta_{ij}(x)$, $i = 1,2,\cdots,m$ are some known basis functions and $\theta_{ij}$ are constant parameters and $j$=1,2,...,$l_i$. The neural network approximation errors $d_{f_i}(x), d_\mu(X)$ are given by

$$d_{f_i}(x) := f_i(x) - f_i^a(x), \quad d_\mu(X) := \mu(X) - \mu^a(X) \tag{14}$$

Let $\Theta_0 = [\theta_{01}, \theta_{02} \cdots, \theta_{0l_0}]^T$, $\Theta_i = [\theta_{i1}, \theta_{i2} \cdots, \theta_{il_i}]^T$ where $i$=1,2,...,$m$. By "optimal" approximation we mean the weights $\Theta_0 \in \Re^{l_0}, \Theta_i \in \Re^{l_i}$ are chosen to minimize $d_{f_i}(x), d_\mu(X)$ for all $x \in \Omega_1 \subset \Re^r$ and $X \in \Omega_1 \times \Omega_2 \subset \Re^{2r}$ respectively, i.e.,

$$\Theta_0 := \arg\min_{\Theta_0 \in \Re^{l_0}} \{ \sup_{X \in \Omega_1 \times \Omega_2} |\mu(X) - \mu^a(X)| \} \tag{15a}$$

$$\Theta_i := \arg\min_{\Theta_i \in \Re^{l_i}} \{\sup_{x \in \Omega_1} |f_i(x) - f_i^a(x)|\}, \quad i = 1,2,\ldots,m \tag{15b}$$

*Assumption* 5: There exists a set of constant parameters $\theta_{ij}$, $i=0,1,\ldots,m$, referred to as optimal output weights such that the approximation error $d_{f_i}(x)$ is upper bounded by a known constant $\psi_f > 0$ over a compact set $x \in \Omega_1 \subset \Re^r$ and the approximation error $d_\mu(X)$ is upper bounded by a known constant $\psi_\mu > 0$ over the compact set $X \in \Omega_1 \times \Omega_2 \subset \Re^{2r}$, i.e.,

$$\sup_{x\in\Omega_1}|d_{f_i}(x)| \le \psi_f, \quad i=1,\ldots,m, \quad \forall x \in \Omega_1 \tag{16a}$$

$$\sup_{X\in\Omega_1\times\Omega_2}|d_\mu(X)| \le \psi_\mu, \quad \forall X \in \Omega_1 \times \Omega_2 \tag{16b}$$

It is also assumed that the basis functions, number of nodes $l_i$, $i=0,1,\ldots,m$ are specified by the designer, and the only unknowns are the output weights. As shown in [15], [19] and the references therein, different basis functions can be used to satisfy assumption 5. If we denote the estimate of the unknown functions, $f_i^a(x)$ and $\mu^a(X)$, by $\hat{f}_i^a(x,t)$ and $\hat{\mu}^a(X,t)$ respectively, we can write

$$\hat{f}_i^a(x,t) = \sum_{j=1}^{l_i}\hat{\theta}_{ij}(t)\zeta_{ij}(x), \quad i=1,\ldots,m \tag{17a}$$

$$\hat{\mu}^a(X,t) = \sum_{j=1}^{l_0}\hat{\theta}_{0j}(t)\zeta_{0j}(X) \tag{17b}$$

where $\hat{\theta}_{ij}(t)$ $i=0,1,\ldots,m$ are the estimates of $\theta_{ij}$ respectively.

The difference between the estimated and actual parameter values results in the estimation errors

$$\tilde{f}_i^a(x,t) = \sum_{j=1}^{l_i}\tilde{\theta}_{ij}(t)\zeta_{ij}(x) \tag{18a}$$

$$\tilde{\mu}^a(X,t) = \sum_{j=1}^{l_0}\tilde{\theta}_{0j}(t)\zeta_{0j}(X) \tag{18b}$$

where, $\tilde{\theta}_{ij}(t) = \hat{\theta}_{ij}(t) - \theta_{ij}$, $i=0,1,\ldots,m$ are the parameter errors. Given the estimates $\hat{f}_i^a(x,t)$ and $\hat{\mu}^a(X,t)$ we can use the Certainty Equivalence (CE) principle [1] to come up with an initial guess for the control law, i.e.,

$$u = \frac{S_e}{\hat{\mu}^a(X,t)}\left[-k_s\|S\| - S_e^T\hat{f}^a(x,t) - S_e^T v(t)\right] \tag{19}$$

where $\hat{f}^a(x,t) = [\hat{f}_1^a(x,t) \;\cdots\; \hat{f}_m^a(x,t)]^T$ and $k_s > 0$ is a constant chosen by the designer, and design an adaptive law for generating the parameter estimates $\hat{\theta}_{ij}(t)$ and therefore $\hat{f}_i^a(x,t)$ and $\hat{\mu}^a(X,t)$ so that the overall system is stable and the tracking error goes to zero with time. However, the CE control law (19) cannot be used to stabilize the closed loop system for a couple of reasons. First $\hat{f}_i^a(x,t)$, $\hat{\mu}^a(X,t)$ are estimates of the approximate nonlinear functions $f_i^a$, $\mu^a$, and may deviate from the actual functions $f_i$, $\mu$. Second, it is well known in adaptive control that the estimate $\hat{\mu}^a(X,t)$ cannot be guaranteed to be away from zero for any given time $t$. This implies that $u$ cannot be guaranteed to be bounded uniformly with time. Therefore instead of (19) we propose

$$u = \frac{\hat{\mu}^a S_1}{(\hat{\mu}^a)^2 + \delta_\mu}\left[-k_s\|S\| - S_1^T\hat{f}^a - S_1^T v - \sigma_v\|v\| - \sigma_f\|\hat{f}^a\|\right] \tag{20}$$

$$S_1 = \begin{cases} S/\|S\|, & \text{if } \|S\| > \Phi \\ S/\Phi, & \text{if } \|S\| \le \Phi \end{cases} \tag{21}$$

In (20) and (21) $\delta_\mu > 0$, $\sigma_v > 0$, $\sigma_f > 0$, $\Phi > 0$ are small design constants, $k_s > 0$ is a constant chosen by the designer. The small linear boundary layer $\Phi$ is used to smooth out the control discontinuity and avoid possible singularities in calculating $S_1$. By design, the control law in (20) cannot become singular since $(\hat{\mu}^a(X,t))^2 + \delta_\mu \ge \delta_\mu > 0$, $\forall X,t$. Therefore, the proposed controller overcomes the difficulty encountered in many adaptive control laws where the identified model becomes uncontrollable at some points of time. It is also interesting to note that $u \to 0$ with the same speed as $\hat{\mu}^a(X,t) \to 0$. Thus, when the estimate $\hat{\mu}^a(X,t)$ approaches zero, the control input remains bounded and also reduces to zero. In other words in such case it is pointless to control what appears to the controller as uncontrollable plant. This design is critical since the potential loss of controllability has been the main drawback of many nonlinear adaptive laws that are based on feedback linearization.

The control law (20) rewritten in the compact form

$$u = S_1 u_0 \tag{22}$$

$$u_0 = \frac{\hat{\mu}^a}{(\hat{\mu}^a)^2 + \delta_\mu}\left[-k_s\|S\| - S_1^T\hat{f}^a - S_1^T v - \sigma_v\|v\| - \sigma_f\|\hat{f}^a\|\right] \tag{23}$$

provides some insight into the action of the controller. The control vector $u$ is expressed as a normalized directional vector $S_1$ scaled by the control effort $u_0$. $S_1$ represents the direction of the error metric $S$. The control vector $u$ can be viewed as apportioning the total control effort $u_0$ in different directions. The components, corresponding to large values in $S_1$, have relatively larger control energy than those components with smaller values. Intuitively, this suggests that the bigger control energy is directed to those $S_1(t)$ with higher values.

The adaptive laws for generating the estimates $\hat{\theta}_{ij}(t)$ are as follows:

$$\dot{\hat{\theta}}_{ij}(t) = k_{f_i}S_i\frac{S_\Phi}{S_\Phi + \Phi}\zeta_{ij}(x), \quad i=1,\cdots,m \tag{24a}$$

$$\dot{\hat{\theta}}_{0j}(t) = k_\mu S_\Phi u_0\zeta_{0j}(X) + \rho(t)k_\mu\sigma_\mu S_\Phi\,\mathrm{sgn}(\mu)(|u_0| + |u'|)\zeta_{0j}(X) \tag{24b}$$

where

$$u' = \frac{1}{(\hat{\mu}^a)^2 + \delta_\mu}\left[-k_s\|S\| - S_1^T\hat{f}^a - S_1^T v - \sigma_v\|v\| - \sigma_f\|\hat{f}^a\|\right] \tag{25}$$

$$S_\Phi = \|S\| - \Phi\,\mathrm{sat}(\|S\|/\Phi) \tag{26}$$

sat(·) is a saturation function ($\mathrm{sat}(\|S\|/\Phi) = 1$, if $\|S\| > \Phi$ and $\mathrm{sat}(\|S\|/\Phi) = \|S\|/\Phi$, if $\|S\| \le \Phi$). sgn(·) is the sign function (sgn(x)=1, if $x \ge 0$ and sgn(x)=−1, otherwise). Then sgn(μ)=1 if $\frac{1}{2}(B(x) + B^T(x))$ is positive definite and sgn(μ)=−1 if $\frac{1}{2}(B(x) + B^T(x))$ is negative definite. ρ(t) is a switching function defined as:

$$\rho(t)=\begin{cases}1, & \text{if } |\hat{\mu}^a| \le \underline{b}-\psi_\mu-\Delta \\ (\underline{b}-\psi_\mu-|\hat{\mu}^a|)/\Delta, & \text{if } (\underline{b}-\psi_\mu-\Delta)<|\hat{\mu}^a|<(\underline{b}-\psi_\mu) \\ 0, & \text{if } |\hat{\mu}^a| \ge \underline{b}-\psi_\mu\end{cases} \quad (27)$$

where $k_{f_i}>0$, $i=1,\cdots,m$ and $k_\mu>0$ are adaptive gains chosen by the designer, $\sigma_\mu>0$ is a small design parameter, $u_0$ is defined in (23), and $\Delta>0$ is a design parameter used to avoid discontinuity in $\rho(t)$. A continuous switching function $\rho(t)$, instead of a discontinuous one, is used to guarantee that the resulting differential equation representing the closed loop system satisfies the conditions for existence and uniqueness of solutions [20].

***Lemma 2***: The function $S_\Phi$ defined in (26) has the following properties:

$$\dot{S}_\Phi=0 \text{, if } \|S\|\le\Phi \text{ and } \dot{S}_\Phi=S_1^T\dot{S} \text{, if } \|S\|>\Phi \quad (28)$$

***Proof***: If $\|S\|\le\Phi$, $S_\Phi=0$, then $\dot{S}_\Phi=0$. If $\|S\|>\Phi$, $S_\Phi=\|S\|-\Phi$, then $\dot{S}_\Phi=d(\|S\|)/dt=S^T\dot{S}/\|S\|=S_1^T\dot{S}$. ■

The properties of the overall control law (20), (24a-b) are described by the following theorem.

***Theorem***: Consider the system (1), the control law (20) and the adaptive laws (24a-b). Assume that assumptions 1-4 hold. Let $\psi_f,\psi_\mu$ are some positive constants such that (16a) is satisfied on a compact set $\Omega_1\subset\Re^r$ and (16b) is satisfied on the compact set $\Omega_1\times\Omega_2\subset\Re^{2r}$ for some $\Theta:=[\Theta_0,\Theta_1,\cdots\Theta_m]^T$. If the lower bound $\underline{b}$ of $\mu(X)$ satisfies the condition $\underline{b}>\sqrt{\delta_\mu}+3\psi_\mu+\Delta$ for arbitrary small positive constants $\delta_\mu,\Delta$, then there exist positive constants $\delta_1<1$, $\delta_2<1$, $\delta_3<1$ such that if $k_s>\sqrt{m}\psi_f/\{(1-\delta_1)\Phi\}$, $\sigma_v\ge\delta_1/(1-\delta_1)$, $\sigma_f\ge\delta_1/(1-\delta_1)$, and $\sigma_\mu\ge\max(\delta_2,\delta_3)$, for all $x(0)\in\Omega_x\subset\Omega_1$, $\bar{\Theta}(0)\in\Omega_\Theta\subset\Re^l$, where $l=l_0+l_1+\cdots+l_m$, all signals in the closed-loop system (1) are bounded and the tracking errors $e_i(t)$ converge to the residual set $\Omega_{e_i}=\{e_i\,|\,|e_i(t)|\le\lambda_i^{\gamma_i+1}\Phi\}$, $i=1,\ldots,m$, as $t\to\infty$ that can be made small by selecting small $\Phi$.

***Proof***: Let us consider the following Lyapunov-like function:

$$V(t)=\frac{1}{2}S_\Phi^2+\left\{\frac{1}{2k_{f_1}}\sum_{j=1}^{l_1}(\tilde{\theta}_{1j})^2+\cdots+\frac{1}{2k_{f_m}}\sum_{j=1}^{l_m}(\tilde{\theta}_{mj})^2\right\}+\frac{1}{2k_\mu}\sum_{j=1}^{l_0}(\tilde{\theta}_{0j})^2 \quad (29)$$

Using the adaptive laws (24a-b), we can establish that

$$\dot{V}(t)=0, \text{ if } \|S\|\le\Phi \quad (30)$$

if $\|S\|>\Phi$,

$$\dot{V}(t)=S_\Phi\dot{S}_\Phi+\left\{\frac{1}{k_{f_1}}\sum_{j=1}^{l_1}\tilde{\theta}_{1j}\dot{\tilde{\theta}}_{1j}+\cdots+\frac{1}{k_{f_m}}\sum_{j=1}^{l_m}\tilde{\theta}_{mj}\dot{\tilde{\theta}}_{mj}\right\}+\frac{1}{k_\mu}\sum_{j=1}^{l_0}\tilde{\theta}_{0j}\dot{\tilde{\theta}}_{0j} \quad (31)$$

In the following proof, we only consider the region $\|S\|>\Phi$. Rewrite $u_0$ in (23) as:

$$u_0=\frac{\hat{\mu}^a(X,t)}{(\hat{\mu}^a(X,t))^2+\delta_\mu}\bar{u} \quad (32)$$

$$\bar{u}=-k_s\|S\|-S_1^T\hat{f}^a(x,t)-S_1^Tv(t)-\sigma_v\|v(t)\|-\sigma_f\|\hat{f}^a(x,t)\| \quad (33)$$

In view of (32),(33) and using Lemma 2,

$$\begin{aligned}\dot{S}_\Phi&=S_1^T\dot{S}=S_1^Tf(x)+S_1^Tv(t)+\mu(X)u_0\\&=S_1^Tf(x)+S_1^Tv(t)+\frac{(\hat{\mu}^a)^2}{(\hat{\mu}^a)^2+\delta_\mu}\bar{u}+(\mu-\hat{\mu}^a)u_0\\&=S_1^Tf(x)+S_1^Tv(t)+\bar{u}-\frac{\delta_\mu}{(\hat{\mu}^a)^2+\delta_\mu}\bar{u}+(\mu-\hat{\mu}^a)u_0\\&=-k_s\|S\|-\sigma_v\|v\|-\sigma_f\|\hat{f}^a\|+S_1^T\{f-\hat{f}^a\}+(\mu-\hat{\mu}^a)u_0-\delta_\mu u'\end{aligned} \quad (34)$$

Using the identities,

$$f(x)-\hat{f}^a(x,t)=(f-f^a)-(\hat{f}^a-f^a)=d_f(x)-\tilde{f}^a(x,t) \quad (35a)$$

$$\mu(X)-\hat{\mu}^a(X,t)=(\mu-\mu^a)-(\hat{\mu}^a-\mu^a)=d_\mu(X)-\tilde{\mu}^a(X,t) \quad (35b)$$

It follows that

$$\begin{aligned}\dot{S}_\Phi=&-k_s\|S\|-\sigma_v\|v\|-\sigma_f\|\hat{f}^a\|-S_1^T\tilde{f}^a-\tilde{\mu}^au_0\\&+S_1^Td_f+(d_\mu u_0-\delta_\mu u')\end{aligned} \quad (36)$$

The term $\{d_\mu(X)u_0-\delta_\mu u'\}$ in (36) is a modeling error term representing the effect of the design parameter $\delta_\mu$ and the approximation error $d_\mu(X)$. The modeling error term will become dominant when the estimate $\hat{\mu}^a(X,t)\to 0$. Define:

$$\delta_1:=\psi_\mu/(\underline{b}-\psi_\mu-\Delta)+\delta_\mu/\{(\underline{b}-\psi_\mu-\Delta)^2+\delta_\mu\} \quad (37a)$$

$$\delta_2:=2\delta_\mu/(\underline{b}-\psi_\mu) \quad (37b)$$

$$\delta_3:=\psi_\mu/(\underline{b}-\psi_\mu) \quad (37c)$$

Follow the similar process in [18], the absolute value of the last term in $\dot{S}_\Phi$ can be expressed as:

$$|d_\mu(X)u_0-\delta_\mu u'|\le\delta_1|\bar{u}|+\rho\delta_2|\tilde{\mu}^a\|u'|+\rho\delta_3|\tilde{\mu}^a\|u_0| \quad (38)$$

Since $\|S\|=S_\Phi+\Phi$, one has

$$|\bar{u}|\le k_sS_\Phi+k_s\Phi+(1+\sigma_v)\|v\|+(1+\sigma_f)\|\hat{f}^a\|$$

Then (38) can be rewritten as

$$\begin{aligned}&|d_\mu(X)u_0-\delta_\mu u'|\le\delta_1k_sS_\Phi+\delta_1k_s\Phi+\delta_1(1+\sigma_v)\|v\|\\&+\delta_1(1+\sigma_f)\|\hat{f}^a\|+\rho\delta_2|\tilde{\mu}^a(X,t)\|u'|+\rho\delta_3|\tilde{\mu}^a(X,t)\|u_0|\end{aligned} \quad (39)$$

Using (36), the first term in $\dot{V}$ is,

$$\begin{aligned}S_\Phi\dot{S}_\Phi=&-k_s\|S\|S_\Phi-\sigma_v\|v\|S_\Phi-\sigma_f\|\hat{f}^a\|S_\Phi-S_1^T\tilde{f}^aS_\Phi\\&-\tilde{\mu}^au_0S_\Phi+S_1^Td_fS_\Phi+(d_\mu u_0-\delta_\mu u')S_\Phi\end{aligned} \quad (40)$$

By substituting $\|S\|=S_\Phi+\Phi$ and (39) into (40), we obtain:

$$\begin{aligned}S_\Phi\dot{S}_\Phi\le&-(1-\delta_1)k_sS_\Phi^2-\{(1-\delta_1)k_s\Phi-\sqrt{m}\psi_f\}S_\Phi\\&-\{\sigma_v-\delta_1(1+\sigma_v)\}\|v\|S_\Phi-\{\sigma_f-\delta_1(1+\sigma_f)\}\|\hat{f}^a\|S_\Phi\\&-S_1^T\tilde{f}^aS_\Phi-\tilde{\mu}^au_0S_\Phi+\rho\delta_2|\tilde{\mu}^a\|u'|+\rho\delta_3|\tilde{\mu}^a\|u_0|\end{aligned} \quad (41)$$

Let us now consider the second term of $\dot{V}$ in (31). Using the adaptive law (24a) we have

$$\frac{1}{k_{f_1}}\sum_{j=1}^{l_{f_1}}\tilde{\theta}_{1j}\dot{\theta}_{1j}+\cdots+\frac{1}{k_{f_m}}\sum_{j=1}^{l_{f_m}}\tilde{\theta}_{mj}\dot{\theta}_{mj} \tag{42}$$
$$=S_1\tilde{f}_1^a S_\Phi/(S_\Phi+\Phi)+\cdots+S_m\tilde{f}_m^a S_\Phi/(S_\Phi+\Phi)=S_1^T\tilde{f}^a(x,t)S_\Phi$$

Finally, in view of the adaptive law (24b), the last term of $\dot{V}$ in (31) can be written as:

$$\frac{1}{k_\mu}\sum_{j=1}^{l_\theta}\tilde{\theta}_{0j}\dot{\theta}_{0j}=\frac{1}{k_\mu}\sum_{j=1}^{l_\theta}\tilde{\theta}_{0j}\{k_\mu S_\Phi u_0\zeta_{0j}+\rho k_\mu\sigma_\mu S_\Phi\,\mathrm{sgn}(\mu)(|u_0|+|u'|)\zeta_{0j}\}$$
$$=\tilde{\mu}^a S_\Phi u_0-\rho\sigma_\mu|\tilde{\mu}^a||u_0|S_\Phi-\rho\sigma_\mu|\tilde{\mu}^a||u'|S_\Phi \tag{43}$$

Now, $\tilde{\mu}^a=\hat{\mu}^a-\mu^a=(\hat{\mu}^a+d_\mu)-\mu$. This together with the fact that $\rho\neq 0$ only for $|\hat{\mu}^a|<\underline{b}-\psi_\mu$ and $|\hat{\mu}^a+d_\mu|\le|\hat{\mu}^a|+|d_\mu|\le\underline{b}$ implies that for $\rho\neq 0$, the sign of $\rho\tilde{\mu}^a$ is always the opposite sign of $\mu(X)$, $\forall\ t\ge 0$.

Combining (41), (42), and (43), $\dot{V}$ can be expressed as:

$$\dot{V}\le-(1-\delta_1)k_s S_\Phi^2-\{(1-\delta_1)k_s\Phi-\sqrt{m}\psi_f\}S_\Phi$$
$$-\{(1-\delta_1)\sigma_v-\delta_1\}\|v\|S_\Phi-\{(1-\delta_1)\sigma_f-\delta_1\}\|\tilde{f}^a\|S_\Phi \tag{44}$$
$$-\rho(\sigma_\mu-\delta_2)|\tilde{\mu}^a||u'|S_\Phi-\rho(\sigma_\mu-\delta_3)|\tilde{\mu}^a||u_0|S_\Phi$$

Assume that $\underline{b}>\sqrt{\delta_\mu}+3\psi_\mu+\Delta$, we have

$$\delta_1=\psi_\mu/(\underline{b}-\psi_\mu-\Delta)+\delta_\mu/\{(\underline{b}-\psi_\mu-\Delta)^2+\delta_\mu\}<1 \tag{45}$$

Given (45) Let us now choose the design constants $k_s$, $\Phi$, $\sigma_v$, $\sigma_f$, $\sigma_\mu$ so that the following inequalities are satisfied.

$$\delta_1<1 \tag{46a}$$
$$k_s\Phi\ge\sqrt{m}\psi_f/(1-\delta_1) \tag{46b}$$
$$\sigma_v,\sigma_f\ge\delta_1/(1-\delta_1) \tag{46c}$$
$$\sigma_\mu\ge\max\{\delta_2,\delta_3\} \tag{46d}$$

Given that the above inequalities are satisfied, it follows that

$$\dot{V}=0,\ \text{if}\ \|S\|\le\Phi \tag{47a}$$
$$\dot{V}\le-(1-\delta_1)k_s S_\Phi^2<0,\ \text{if}\ \|S\|>\Phi \tag{47b}$$

The results (47a-b) are arrived under assumptions 1 and 5. Since assumptions 1 and 5 only hold on a compact set, i.e., $x\in\Omega_1$, all states need to remain in this compact set for all $t\ge 0$. Consider the set

$$M=\{x,\tilde{\Theta}|\ V(t)\le V_0\} \tag{48}$$

where $V_0>V(0)$ and $V_0>\Phi$ is chosen as the largest constant for which $M=\Omega_x\times\Omega_\Theta$, where $\Omega_x\subset\Omega_1$, $\Omega_\Theta\subset\Re^l$. Then for $x(0)\in\Omega_x$ and $\tilde{\Theta}(0)\in\Omega_\Theta$, it follows from (29) and (47a-b) that $V(t)$ is bounded from above by $V_0$ for all $t\ge 0$, which implies that $x\in\Omega_x\subset\Omega_1$, $\forall t\ge 0$. Hence assumptions 1 and 5 will never be violated. This condition together with $\dot{V}\le 0$ implies that $V(t)$ and therefore $S_\Phi,\tilde{\theta}_{ij}(t)$ are bounded for all $t\ge 0$, i.e, $S_\Phi,\tilde{\theta}_{ij}(t)\in L_\infty$. This in turn implies that $x$, $u$ are bounded and $V(t)$ has a limit, i.e. $\lim_{t\to\infty}V(t)=V_\infty$. Using the fact that $S_\Phi=0$ for $\|S\|\le\Phi$ and (47b), we have $\lim_{t\to\infty}\int_0^\infty S_\Phi^2 dt=(V(0)-V_\infty)/(1-\delta_1)k_s<\infty$ which implies that $S_\Phi\in L_2$. From $S_\Phi,\tilde{\theta}_{ij}(t)\in L_\infty$, it follows that all signals are bounded which implies that $\dot{S}_\Phi\in L_\infty$. From $\dot{S}_\Phi\in L_\infty$ and $S_\Phi\in L_2$ we have $S_\Phi\to 0$ as $t\to\infty$ which implies that $\|S\|$ converges to the residual set $\Omega_S=\{S|\ \|S\|\le\Phi\}$ [1]. Inside the residual set we also have $|S_i|\le\Phi$ which in turn implies that $|e_i(t)|\le\lambda_i^{-n+1}\Phi$, $i=1,\cdots,m$ [3], [9]. ■

## 4. SIMULATION RESULTS

We demonstrate the performance of the proposed adaptive control system using a dynamical model of a planar, two-link, articulated robotic manipulator [4], [12]. The dynamics of this robotic system are nonlinear with strong coupling between the two degrees of freedom. The equations of motion in terms of the generalized coordinates $q_1$ and $q_2$, representing the angular positions of joints 1 and 2 and applied torques $\tau_1$ and $\tau_2$ at these joints is given by:

$$\begin{bmatrix}\ddot{q}_1\\ \ddot{q}_2\end{bmatrix}=-\begin{bmatrix}H_{11} & H_{12}\\ H_{21} & H_{22}\end{bmatrix}^{-1}\begin{bmatrix}-h\dot{q}_2 & -h(\dot{q}_1+\dot{q}_2)\\ h\dot{q}_1 & 0\end{bmatrix}\begin{bmatrix}\dot{q}_1\\ \dot{q}_2\end{bmatrix}+\begin{bmatrix}H_{11} & H_{12}\\ H_{21} & H_{22}\end{bmatrix}^{-1}\begin{bmatrix}\tau_1\\ \tau_2\end{bmatrix}$$

where,

$$H_{11}=a_1+2a_3\cos(q_2)+2a_4\sin(q_2),$$
$$H_{12}=H_{21}=a_2+a_3\cos(q_2)+a_4\sin(q_2),$$
$$H_{22}=a_2,\ h=a_3\sin(q_2)-a_4\cos(q_2)$$

The robot initially is at rest at the position $q_1=0, q_2=0$. It is desired to determine control inputs $\tau_1(t)$ and $\tau_2(t)$ such that $q_1$ and $q_2$ follow a desired trajectory defined by:

$$q_{d_1}(t)=30^\circ\cos(2\pi t)\ ;\ q_{d_2}(t)=45^\circ\cos(2\pi t)$$

with the tracking performance defined by:

$$|e_1|=|q_1-q_{d_1}|\le 1.0^\circ\ ;\ |e_2|=|q_2-q_{d_2}|\le 1.0^\circ$$

The inertia matrix $H(q)$ is positive definite. The above equation is in the general nonlinear form of (1) with $B(x)=H^{-1}$. Because the workspace is a closed set, it is easy to show that both $H$ and $H^{-1}$ are uniformly positive definite for all positions $q$ in the robot's workspace. In this simulation, the lower bound of the minimum singular value of $H^{-1}$ is $\underline{b}$=0.152. Assuming a completely unknown nonlinear plant, one layer radial basis neural network was used to approximate the unknown functions $f$ and $\mu$. The upper bounds for the approximation errors are estimated using offline training as $|f_i-f_i^a|\le 1.0$, $i$=1,2 and $|\mu-\mu^a|\le 0.01$, i.e., $\psi_f=1.0$ and $\psi_\mu=0.01$. The value of $\delta_\mu$ is chosen to be 0.002. Using (37a-c), we calculate $\delta_1=0.12<1$, $\delta_2=0.141$, $\delta_3=0.141$. Based on (46c-d), we choose $\sigma_f=0.15$, $\sigma_v=0.15$ and $\sigma_\mu=0.15$. Selecting $k_s=20$ and $\Phi=0.3$, such that (46b) is satisfied. Taking $\lambda_1=20$, $\lambda_2=20$, the performance requirements for tracking errors are satisfied, i.e., $|e_1|\le\Phi/\lambda_1=0.9^\circ<1^\circ$ and $|e_2|\le\Phi/\lambda_2=0.9^\circ<1^\circ$. In

this simulation, the system is assumed initially at rest and the initial conditions for the parameter estimates are taken to be zero, reflecting the fact that the system is completely unknown. The simulation results in Fig. 1,2 demonstrate the theory and calculated steady state error bounds. We note that as shown Fig. 3 the switching function $\rho(t)$ reaches a steady state in a short period of time after which no more switching takes place.

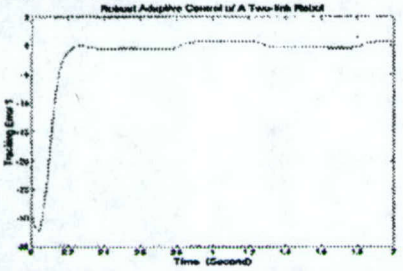

Fig. 1. Tracking error response of link 1 during the first 2 seconds The dotted lines indicate the required error bound of ±1 degree

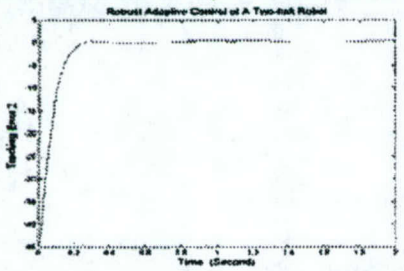

Fig. 2. Tracking error response of link 2 during the first 2 seconds The dotted lines indicate the required error bound of ±1 degree

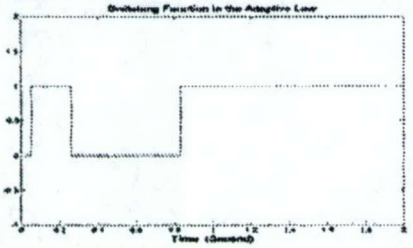

Fig. 3. The action of the switch function ρ during the first 2 seconds

## 5. CONCLUSIONS

In this paper, we consider the control problem of a class of nonlinear MIMO with unknown nonlinearities. The nonlinearities are assumed to be smooth functions and as such can be approximated and estimated on-line using a single layer neural network. A nonlinear robust adaptive control algorithm is designed and analyzed. The controller guarantees closed loop semi-global stability and convergence of the tracking error to a small residual set. The size of the residual set for the tracking error depends solely on design parameters, which can be chosen to meet desired upper bounds for the tracking error. Consequently the proposed methodology provides a design procedure to meet apriori specified performance guarantees for the steady state tracking error.

## REFERENCES


[1] P. A. Ioannou and J. Sun, *Robust Adaptive Control*, Upper Saddle River, NJ: Prentice Hall, 1996.

[2] P. Kokotovic and M. Arcak, "Constructive nonlinear control: a historical perspective", *Automatica*, vol. 37, pp. 637-662, 2001.

[3] B. Fernandez R. and J. K. Hedrick, "Control of multivariable non-linear systems by the sliding model", *Int. J. Control*, vol. 46, no. 3, pp. 1019-1040, 1987.

[4] J.-J. E. Slotine and W. Li, *Applied Nonlinear Control*, Englewood Cliffs, NJ: Prentice Hall, 1991.

[5] I. Kanellakopoulos, P. Kokotovic, and A. Morse, "Systematic design of adaptive controllers for feedback linearizable systems", *IEEE Trans. Automatic. Contr.*, vol. 36, pp. 1241-1253, 1991.

[6] E. B. Kosmatopoulos and P. A. Ioannou, "A switch adaptive controller for feedback linearizable systems", *IEEE Trans. Automat. Contr.*, vol. 44, no.4, pp. 742-750, April 1999.

[7] M. Krstic, I. Kanellakopoulos, and P. Kokotovic, *Nonlinear and Adaptive Control Design*, New York: Wiley Interscience, 1995.

[8] S. S. Sastry and A. Isidori, "Adaptive control of linearizable systems", *IEEE Trans. Automat. Contr.*, vol. 34, no. 11, pp. 1123-1131, Nov. 1989.

[9] J.-J. E. Slotine, and J. A. Coetsee, "Adaptive sliding controller synthesis for non-linear systems", *Int. J. Control*, vol. 43, no. 6, 1631-1651, 1986.

[10] D. G. Taylor, P. V. Kokotovic, R. Marino and I. Kanellakopoulos, "Adaptive regulation of nonlinear systems with unmodeled dynamics", *IEEE Trans. Automat. Contr.*, vol. 34, no. 4, pp. 405-412, April 1989.

[11] F.-C. Chen and H. K. Khalil, "Adaptive control of nonlinear systems using neural networks", *Int. J. Control*, vol. 55, no. 6, pp. 1299-1317, 1992.

[12] C.-C. Liu and F.-C. Chen, "Adaptive control of nonlinear continuous-time systems using neural networks – general relative degree and MIMO cases", *Int. J. Control*, vol. 58, no. 2, pp. 317-335, 1993.

[13] M. M. Polycarpou, "Stable adaptive neural control scheme for nonlinear systems", *IEEE Trans. Automat. Contr.*, vol. 41, no. 3, pp. 447-451, Mar. 1996.

[14] M. M. Polycarpou and P. A. Ioannou, "Modeling, identification and stable adaptive control of continuous-time nonlinear dynamical systems using neural networks", in *Proc. 1992 Amer. Contr. Conf.*, June 1992, pp. 36-40.

[15] R. Sanner and J.-J. E. Slotine, "Gaussian networks for direct adaptive control", *IEEE Trans. Neural Networks*, vol. 3, no. 6, pp. 837-863, Nov. 1992.

[16] S. Seshagiri and H. Khalil, "Output feedback control of nonlinear systems using RBF neural networks", *IEEE Trans. Automat. Contr.*, vol. 11, no. 1, pp. 69-79, Jan. 2000.

[17] F. L. Lewis, K. Liu, and A. Yesildirek, "Neural net robot controller with guaranteed tracking performance", *IEEE Trans. Neural Networks*, vol. 6, no. 3, pp. 703-715, May 1995.

[18] H. Xu and P. A. Ioannou, "Robust Adaptive Control of Linearizable Nonlinear Single Input Systems", in *Proc 2002 XV IFAC world congress*, Barcelona, Spain, July 2002.

[19] J. Park and I. W. Sandberg, "Approximation and radial-basis-function networks", *Neural Computation*, vol. 5, pp. 305-316, 1993.

[20] M. M. Polycarpou and P. A. Ioannou, "On the existence and uniqueness of solutions in adaptive control systems", *IEEE Trans. Automat. Contr.*, vol. 38, no. 3, pp. 474-479, Mar. 1993.

# ADAPTIVE CONTROL FOR A CLASS OF LARGE SCALE NONLINEAR SYSTEMS *

Haojian Xu and Petros A. Ioannou

Department of Electrical Engineering
University of Southern California
Los Angeles, CA 90089
Phone: (213)740-4452
FAX: (213)821-1109
Email: ioannou@usc.edu

Maj Dean Mirmirani

Department of Mechanical Engineering
California State University Los Angeles
Los Angeles, CA 90032

**Abstract**

The design of stabilizing controllers for multi-input multi-output (MIMO) nonlinear plants with unknown nonlinearities is a challenging problem. The inability to identify the nonlinearities on-line or off-line accurately motivates the design of stabilizing controllers based on approximations or on approximate estimates of the plant nonlinearities. However, the design of a centralized controller for large scale nonlinear systems is often complex due to the high dimensionality and difficulty to implement in real time. In this paper a decentralized-like nonlinear adaptive control algorithm is designed and analyzed for a class of large scale nonlinear systems with unknown nonlinearities. The controller guarantees closed loop semi-global stability and convergence of the tracking error to a small residual set whose size can be specified *a priori* provided the neglected in the control design nonlinear interconnections are small relative to the modeled nonlinear parts. A procedure for choosing the various design parameters to guarantee that the tracking error bound will converge to within the specified *a priori* bound is presented. Even though the proposed controller is not purely decentralized it does reduce computations and makes the control design easier than a corresponding centralized approach.

* This work was supported in part by NASA under Grant NCC4-158, in part by Air Force Office of Scientific Research under grant F49620-01-1-0489, and in part by NSF under grant ECS-9877193.

# 1. INTRODUCTION

In recent years, considerable research efforts have been devoted to deal with the design of stabilizing controllers for classes of nonlinear plants. These efforts are described in detail in a recent survey paper (Kokotovic and Arcak 2001). Most of the recent efforts on nonlinear control design assumed that the plant nonlinearities are known (e.g., see Fernandez and Hedrick, 1987, Godbole and Sastry 1995, Kokotovic and Arcak 2001, and references therein). The case where the plant nonlinearities are in the form of the products of unknown constant parameters with known nonlinearities gave rise to a number of adaptive control techniques (Slotine and Coetsee 1986, Taylor *et al.* 1989, Sastry and Isidori 1989, Kanellakopoulos *et al.* 1991, Seto *et al.* 1994, Slotine and Li 1991, Krstic *et al.* 1995, Ioannou and Sun 1996, Khalil 1996a, b, Kosmatopoulos and Ioannou 1999). An adaptive control scheme for a class of single input single output (SISO) systems based on a min-max optimization approach is proposed in (Kojic and Annaswamy 2002) by assuming that the nonlinear functions are convex/concave (as opposed to linear assumed in almost every adaptive system) with respect to the unknown parameters.

Neural approximation together with adaptive control techniques has been found to be particularly useful for controlling highly uncertain or completely unknown nonlinear systems (Sanner and Slotine 1992, Polycarpou and Ioannou 1992, Chen and Khalil 1992, Liu and Chen 1993, Chen and Liu 1994, Johansen 1994, Yesildirek and Lewis 1995, Polycarpou 1996, Spooner and Passino 1996, Ordonez and Passino 1999, Seshagiri and Khalil 2000, Rovithakis 2001). In this case, neural networks are used as approximation models of the unknown nonlinearities. The control design is then based on the neural network model rather than the actual system. Most of these studies however are focused on the SISO systems (Sanner and Slotine 1992, Polycarpou and Ioannou 1992, Chen and Khalil 1992, Chen and Liu 1994, Yesildirek and Lewis 1995, Polycarpou 1996, Spooner and Passino 1996, Seshagiri and Khalil 2000, Rovithakis 2001).

Control of MIMO nonlinear systems, in particular large-scale nonlinear systems, with unknown nonlinearities introduces additional complexities. The high dimensionality and inability to identify the nonlinearities on-line or offline accurately motivates the design of simple adaptive decentralized control schemes. In this case the high-dimensional nonlinear system is decomposed into interconnected subsystems of smaller dimension and a local controller is designed for each subsystem by assuming zero interconnections between subsystems. A decentralized adaptive control systems alleviates the computational burden required by a centralized adaptive control and is easier to implement on-line. Most of the existing work on decentralized adaptive control focuses on linear systems (Ioannou 1986, Datta and Ioannou 1991, Siljak 1991). Some efforts have been made to deal with the decentralized adaptive control of nonlinear systems using back-stepping techniques (Jain and Khorrami 1997, Jiang 2000, Liu and Li 2002). For a class of MIMO systems with unknown

is established that $\hat{\Theta}_{ij}(t)$ remains inside an invariant set where $\underline{\sigma}(\hat{\boldsymbol{B}}^a) > 0$. However, since $\Theta_{ij}$ is unknown and does not have any physical meaning, the assumption that $\hat{\Theta}_{ij}(0)$ is close to the desired value is difficult if at all possible to guarantee. In (Ordonez and Passino 1999), an indirect adaptive control algorithm based on fuzzy-neural systems is proposed provided that convex sets $\Omega_{ij}$ can be constructed such that $\underline{\sigma}(\hat{\boldsymbol{B}}^a) \geq \sigma_{\min}$ and $\overline{\sigma}(\hat{\boldsymbol{B}}^a) \geq \sigma_{\max}$ for all $\hat{\Theta}_{ij}(t) \in \Omega_{ij}$, $i,j=1,2,\ ,m$, where $\overline{\sigma}(\hat{\boldsymbol{B}}^a)$ denotes the maximum and $\underline{\sigma}(\hat{\boldsymbol{B}}^a)$ the minimum singular value of $\hat{\boldsymbol{B}}^a$ respectively and $\sigma_{\min}, \sigma_{\max}$ are two positive constants. The estimated weights of the fuzzy/neural systems are then guaranteed to remain inside $\Omega_{ij}$ by using projection. However, such sets $\Omega_{ij}$ are difficult to construct in general even if the weights were known let alone knowing them *a priori* where such weights are completely unknown. Moreover, even when sets $\Omega_{ij}$ are constructed to be convex in the parameter space, there is no guarantee that the unknown $\Theta_{ij}$ that corresponds to the "optimal" approximation falls inside these sets. If $\Theta_{ij} \notin \Omega_{ij}$ the possibility of instability or degraded performance cannot be excluded. A discontinuous decentralized-like controller was proposed to handle the classes of MIMO systems consider in (Ordonez and Passino 1999) with some restrictive assumptions. In this study, it was shown that if $\boldsymbol{B}(\boldsymbol{x})$ is strictly diagonally dominant with known lower and upper bounds for the main diagonal entries, and if the first derivatives of the main diagonal entries in $\boldsymbol{B}(\boldsymbol{x})$ are upper bounded by known functions and the upper bounds of all off-diagonal elements $b_{ij}(\boldsymbol{x})$, $i,j=1,\ ,m$, $i \neq j$, are known, the MIMO system can be decomposed into a set of SISO subsystems. The desired controller is assumed to be of the form of a fuzzy system plus a discontinuous robust term. A direct fuzzy adaptive controller is designed for each SISO subsystem provided that the fuzzy part of the desired control input is upper bounded by a known continuous function.

Another important issue in adaptive nonlinear control with unknown nonlinearities is that of tracking error performance. By performance in this context we mean the size of the region of attraction for signal boundedness and the size of the tracking or regulation error at steady state. Performance issues such as transient behavior are difficult to establish analytically even in the case of known nonlinearities and is not addressed in most of nonlinear control literature at least analytically. In most papers on adaptive nonlinear control with unknown nonlinearities, signal boundedness is established first for some region of attraction within which the assumed neural approximations are valid. Signal boundedness then implies that the approximation or modeling error is also bounded. The upper bound for the tracking or regulation error is shown to be of the order of the bound on the modeling or approximation error (Polycarpou and Ioannou 1992, Johansen 1994, Seshagiri and Khalil 2000, Rovithakis 2001). In some cases the approximation error is assumed to be upper bounded by some known

nonlinearities (Seshagiri and Khalil 2000) leading to an upper bound for the tracking error at steady state that is a function of some design parameters. In (Chen and Khalil 1992, Liu and Chen 1993, Chen and Liu 1994) the tracking error is shown to converge inside a small residual set that depends on the bounds of the unknown signals and design parameters. In (Yesildirek and Lewis 1995), the tracking error may be made smaller by increasing the control gain. In all these cases, it is not clear, from the analysis how changes in the design parameters to improve tracking performance will affect the region of attraction for signal boundedness. Furthermore, the upper bound for the tracking error cannot be easily computed and therefore the controller gain cannot be designed *a priori* to achieve a desired tracking error bound at steady state.

In this paper we develop a decentralized-like adaptive controller for a class of large scale nonlinear systems with unknown nonlinearities. By designing the control law based on the local isolated subsystems, the computational burden is reduced and the calculation of the matrix inverse $\hat{\boldsymbol{B}}^{-1}(\boldsymbol{x},t)$ is avoided. The proposed decentralized-like adaptive controller is continuous and guarantees closed loop system semi-global stability even in the case where the estimated plant loses controllability. The adaptive law uses a new σ-modification function and a new deadzone technique in order to guarantee closed loop stability and robustness with respect to modeling errors and neglected interconnections among the subsystems. The tracking error of each subsystem at steady state converges inside a small residual set whose size can be guaranteed by selecting certain design parameters appropriately. Furthermore, for any given desired upper bound of the tracking error at steady state, we provide the corresponding design procedure for choosing these design parameters to guarantee the tracking error bound. However, the proposed decentralized adaptive control scheme involves exchange of information between subsystems and is referred to as a decentralized-like adaptive controller.

This paper is organized as follows. In section 2 the problem statement is presented. In section 3 a decentralized-like control scheme for the case of known nonlinearities is constructed. In section 4 the proposed decentralized-like adaptive control scheme for unknown nonlinear systems is discussed. In section 5, the properties of the proposed controller are illustrated using an example. Finally, section 6 includes the conclusions.

Throughout this paper, $|\cdot|$ indicates the absolute value, and $\|\cdot\|$ indicates the Euclidean vector norm.

## 2. PROBLEM STATEMENT

Consider the following class of large scale nonlinear systems described as an interconnected set of $m$ subsystems,

$$\begin{aligned} x_i^{(n_i)} &= f_i(\boldsymbol{x}) + \sum_{j=1}^{m} b_{ij}(\boldsymbol{x}) u_j \\ y_i &= x_i \,, \; i=1,2, \quad ,m \end{aligned} \tag{1}$$

where for the $i$th subsystem: $x_i^{(n_i)} := d^{n_i} x_i / dt^{n_i}$, $\boldsymbol{x} \in \Re^n$ is the state vector, $u_i \in \Re$ is the control input, $y_i \in \Re$ is the output. $\boldsymbol{x} := [x_1, \cdots, x_1^{(n_1-1)}, \cdots, x_m, \cdots, x_m^{(n_m-1)}]^T \in \Re^n$, $n = n_1 + \cdots + n_m$, is the composite state vector. The nonlinear functions $f_i(\boldsymbol{x}) \in \Re$ and $b_{ij}(\boldsymbol{x}) \in \Re$ are assumed to be continuous unknown functions. $b_{ij}(\boldsymbol{x}) \in \Re$, $i \neq j$, contains the nonlinear interaction among the other subsystems.

In this representation the composite system can be described as

$$\boldsymbol{x}^{(n)} = \boldsymbol{f}(\boldsymbol{x}) + \boldsymbol{B}(\boldsymbol{x})\boldsymbol{u} \tag{2}$$

where $\boldsymbol{u} = [u_1, \cdots, u_m]^T \in \Re^m$ is the composite control vector and

$$\boldsymbol{x}^{(n)} = [x_1^{(n_1)} \quad x_2^{(n_2)} \quad \cdots \quad x_m^{(n_m)}]^T \in \Re^m \tag{3}$$

$$\boldsymbol{f}(\boldsymbol{x}) = [f_1(\boldsymbol{x}) \quad \cdots \quad f_m(\boldsymbol{x})]^T \in \Re^m \tag{4}$$

$$\boldsymbol{B}(\boldsymbol{x}) = \begin{bmatrix} b_{11}(\boldsymbol{x}) & \cdots & b_{1m}(\boldsymbol{x}) \\ \vdots & \ddots & \vdots \\ b_{m1}(\boldsymbol{x}) & \cdots & b_{mm}(\boldsymbol{x}) \end{bmatrix} \in \Re^{m \times m} \tag{5}$$

The problem is to design control inputs such that the outputs of each subsystems $y_i(t)$ track the desired trajectories $y_{d_i}(t)$ respectively.

We make the following assumptions:

**Assumption 1:** $b_{ii}(\boldsymbol{x})$ is bounded from below by a known function $g_i(\boldsymbol{x})$ with $|g_i(\boldsymbol{x})| \geq g_i^* > 0$, $\forall\, \boldsymbol{x} \in \Re^n$, where $g_i^*$ is a known constant, and the sign of $b_{ii}(\boldsymbol{x})$ is known.

**Assumption 2:** Let $\boldsymbol{G}(\boldsymbol{x}) := \text{diag}\{g_1(\boldsymbol{x}), \cdots, g_m(\boldsymbol{x})\}$, $\boldsymbol{B}_0(\boldsymbol{x}) := \text{diag}\{b_{11}(\boldsymbol{x}), \cdots, b_{mm}(\boldsymbol{x})\}$, $\Delta\boldsymbol{B}(\boldsymbol{x}) := \boldsymbol{B}(\boldsymbol{x}) - \boldsymbol{B}_0(\boldsymbol{x})$. The interconnection matrix $\Delta\boldsymbol{B}(\boldsymbol{x})$ satisfies the condition

$$\max_{i=1,\cdots,m} \{\|\Delta\boldsymbol{B}(:,i)\| / g_i(\boldsymbol{x})\} \leq \delta_0 < 1 \tag{6}$$

where $\Delta\boldsymbol{B}(:,i)$ indicates the $i$th column of the matrix $\Delta\boldsymbol{B}(\boldsymbol{x})$, and $\delta_0$ is a known constant representing the strength of the interconnection. Equation (6) also implies that $\max_{i=1,\cdots,m} \{\|\Delta\boldsymbol{B}(:,i)\| / |b_{ii}(\boldsymbol{x})|\} \leq \delta_0 < 1$ which in turn implies that $\bar{\sigma}\{\Delta\boldsymbol{B}(\boldsymbol{x})\boldsymbol{B}_0^{-1}(\boldsymbol{x})\} \leq \sqrt{m}\delta_0$, where $\bar{\sigma}(\cdot)$ represents the maximum singular value of the matrix inside the bracket.

Assumption 2 guarantees that the main diagonal entries of $\boldsymbol{B}(\boldsymbol{x})$ are dominant over the off-diagonal elements.

**Assumption 3**: The desired trajectories $y_{d_i}(t)$, $i$=1,2, ,$m$, are known bounded functions of time with bounded known derivatives.

**Assumption 4**: The state $\boldsymbol{x}$ of the system is available for measurement.

**Assumption 5**: The functions $f_i(\boldsymbol{x})$ and $b_{ii}(\boldsymbol{x})$, $i$=1,2, ,$m$, are continuous but otherwise completely unknown.

Assumption 1 guarantees that each subsystem is controllable by its local input. If b(x)=0 for some $\boldsymbol{x}$, then the controllability of the subsystem cannot be guaranteed. However the requirement of the knowledge for the lower bound for the function g(x) may be restrictive. Assumption 2 requires that the main diagonal entries of $\boldsymbol{B}(\boldsymbol{x})$ to be dominant over the off-diagonal elements. This requirement is essential for decentralization and is stronger than the assumption of invertible $\boldsymbol{B}(\boldsymbol{x})$. Assumption 3 is used to guarantee that bounded control inputs exist to achieve the tracking objective. Assumption 4 requires the knowledge of the state. Since the nonlinearities in system (1) are functions of all states, assumption 4 is used to show the existence of a controller to meet the control objective in the case of known nonlinearities. In the case of unknown nonlinearities the knowledge of the state $\boldsymbol{x}$ is used as an input to the neural network model. Relaxation of assumption 4 remains a topic for future research. Assumption 5 is used to guarantee the existence of a neural network that approximates the unknown nonlinearities reasonably well.

## 3. DECENTRALIZED-LIKE CONTROL FOR THE CASE OF KNOWN NONLINEARITIES

In this section we consider the design of decentralized controllers for the case where $f_i(\boldsymbol{x})$ and $b_{ii}(\boldsymbol{x})$, $i$=1,2, ,$m$, are completely known and examine whether the control objective can be met. This is a reasonable step to take since if we cannot meet the control objective in the case of known nonlinearities, it is unlikely that we will do so in the case of unknown nonlinearities.

We define the scalar function $S_i(t)$ as the metric for describing the tracking error dynamics of the $i$th subsystem:

$$\begin{aligned} S_i(t) &= (d/dt + \lambda_i)^{n_i - 1} e_i(t) \\ e_i(t) &= y_i(t) - y_{d_i}(t) \end{aligned} \tag{7}$$

where $\lambda_i > 0$, $i$=1,2, ,$m$, are constants to be selected. It follows from (7) that for $S_i(t) = 0$, $i$=1,2, ,$m$, we have a set of linear differential equations whose solutions imply that $e_i(t)$ converges to zero with time constant $(n_i - 1)/\lambda_i$. In addition, the derivatives of $e_i(t)$ up to $n_i - 1$ also converge to zero (Slotine and Li 1991).

Differentiating $S_i(t)$ with respect to time results in:

$$\begin{aligned} \dot{S}_i &= e_i^{(n_i)} + \alpha_{i,n_i-1} e_i^{(n_i-1)} + \cdots + \alpha_{i,1} \dot{e}_i \\ &= f_i(\boldsymbol{x}) + \sum_{j=1}^{m} b_{ij}(\boldsymbol{x}) u_j - y_{d_i}^{(n_i)} + (\alpha_{i,n_i-1} e_i^{(n_i-1)} + \cdots + \alpha_{i,1} \dot{e}_i) \end{aligned} \tag{8}$$

where, $\alpha_{i,n-1}, \cdots, \alpha_{i,1}$, $i$=1,2, ,$m$, represent the coefficients in the binomial expansion of (7). Let

$$v_i(t) = -y_{d_i}^{(n_i)} + \alpha_{i,n_i-1} e_i^{(n_i-1)} + \cdots + \alpha_{i,1} \dot{e}_i \tag{9}$$

Then, $\dot{S}_i(t)$ can be written in the compact form:

$$\dot{S}_i = f_i(\boldsymbol{x}) + v_i(t) + \sum_{j=1}^{m} b_{ij}(\boldsymbol{x}) u_j \tag{10}$$

When the interconnection matrix $\Delta \boldsymbol{B}$=**0**, the error metric in $i$th isolated subsystem is of the form

$$\dot{S}_i = f_i(\boldsymbol{x}) + v_i(t) + b_{ii}(\boldsymbol{x}) u_i \tag{11}$$

If $f_i$ and $b_{ii}$ were completely known functions, then the control law

$$u_i = \frac{1}{b_{ii}(\boldsymbol{x})} \left[ - f_i(\boldsymbol{x}) - v_i(t) - k_i S_i(t) \right] \tag{12}$$

where $k_i > 0$ is a design parameter, could be used to meet the control objective provided of course that the controllability condition $b_{ii}(\boldsymbol{x}) \neq 0$ for all $\boldsymbol{x}$ is satisfied.

Using (12) we obtain $\dot{S}_i = -k_i S_i$, which implies that $S_i(t)$ and therefore $e_i(t)$ converge to zero exponentially fast.

Now let $\boldsymbol{S}(t) := [S_1(t), \cdots, S_m(t)]^T$, $\boldsymbol{v}(t) := [v_1(t), \cdots, v_m(t)]^T$. In this representation the composite error system can be described as

$$\dot{\boldsymbol{S}} = \boldsymbol{f}(\boldsymbol{x}) + \boldsymbol{v}(t) + \boldsymbol{B}(\boldsymbol{x}) \boldsymbol{u} \tag{13}$$

When the interconnection matrix $\Delta \boldsymbol{B} \neq$**0**, in order to take care of the interconnection, we modify the control law (12) as

$$u_i = \frac{1}{b_{ii}(\boldsymbol{x})} \left\{ - f_i(\boldsymbol{x}) - v_i(t) - k_i S_i(t) - \sigma_{f_i} \left\| \boldsymbol{f}(\boldsymbol{x}) + \boldsymbol{v}(t) \right\| S_i(t) \right\} \tag{14}$$

with $\sigma_{f_i} > 0$ as an additional design parameter. To synthesize this control law for the $i$th subsystem, however, we use some information of the other subsystems, i.e., the term $\sigma_{f_i}\|f(x)+v(t)\|S_i(t)$, which indicates that (14) is not a pure decentralized control scheme. However, the control law (14) decentralizes the input channels.

**Lemma 1**: The function $S_\Phi$ defined as

$$S_\Phi := \|S\| - \Phi \,\mathrm{sat}(\|S\|/\Phi) \tag{15}$$

$$\mathrm{sat}(\|S\|/\Phi) = \begin{cases} 1, & \text{if } \|S\| > \Phi \\ \|S\|/\Phi, & \text{if } \|S\| \le \Phi \end{cases} \tag{16}$$

has the following properties:

$$S_\Phi = 0,\ \dot{S}_\Phi = 0, \text{ if } \|S\| \le \Phi \tag{17}$$

$$S_\Phi > 0,\ \dot{S}_\Phi = S^T\dot{S}/(S_\Phi + \Phi), \text{ if } \|S\| > \Phi \tag{18}$$

*Proof*: From (15) and (16), we have $S_\Phi = 0$ when $\|S\| \le \Phi$ which also implies that $\dot{S}_\Phi = 0$ for $\|S\| \le \Phi$. If $\|S\| > \Phi$, $S_\Phi = \|S\| - \Phi > 0$, then $\dot{S}_\Phi = d(\|S\|)/dt = S^T\dot{S}/\|S\| = S^T\dot{S}/(S_\Phi + \Phi)$. ■

The following theorem establishes the stability and performance properties of the closed loop system with (14) as the control law.

**Theorem 1**: Consider the system (1) and the control law (14). Assume that assumptions 1-4 hold. If $\delta_0 < 1/\sqrt{m}$, then for any given positive constant $\Phi$, there exist constants, $c_1 > 0$, $c_2 > \dfrac{2m\delta_0^2}{(1-m\delta_0^2)\Phi}$, such that if design constants $k_i, \sigma_{f_i}$, $i$=1,2, ,$m$, satisfy

$$\frac{c_1}{\sqrt{m}\delta_0}\left(1-\sqrt{1-m\delta_0^2}\right) < k_i < \frac{c_1}{\sqrt{m}\delta_0}\left(1+\sqrt{1-m\delta_0^2}\right),$$

$$\frac{c_2}{\sqrt{m}\delta_0}\left(1-\sqrt{1-m\delta_0^2-2m\delta_0^2/(c_2\Phi)}\right) \le \sigma_{f_i} \le \frac{c_2}{\sqrt{m}\delta_0}\left(1+\sqrt{1-m\delta_0^2-2m\delta_0^2/(c_2\Phi)}\right),$$

all signals in the closed-loop system are bounded and the tracking errors $e_i(t)$ converge to the residual sets $R_{e_i} = \{e_i \mid |e_i(t)| \le \lambda_i^{-n_i+1}\Phi\}$, $i$=1,2, ,$m$, as $t \to \infty$ exponentially fast. The sizes of the residual sets depend only on the design constants $\lambda_i$ ,$\Phi$ and can be established *a priori*.

*Proof*: Consider the positive definite function

$$V(t) = \frac{1}{2} S_\Phi^2(t) \tag{19}$$

Using Lemma 1, the time derivative of $V(t)$ is given by

$$\dot{V}(t) = 0, \text{ if } \|\boldsymbol{S}\| \le \Phi \tag{20a}$$

$$\dot{V}(t) = \frac{S_\Phi}{S_\Phi + \Phi} \boldsymbol{S}^T \dot{\boldsymbol{S}}, \text{ if } \|\boldsymbol{S}\| > \Phi \tag{20b}$$

Therefore only the region $\|\boldsymbol{S}\| > \Phi$ is considered in the subsequent proof. The composite control law can be written as

$$\boldsymbol{u} = \boldsymbol{B}_0^{-1}(\boldsymbol{x})\{-\boldsymbol{f}(\boldsymbol{x}) - \boldsymbol{v}(t) - \boldsymbol{K}\boldsymbol{S}(t) - \|\boldsymbol{f}(\boldsymbol{x}) + \boldsymbol{v}(t)\|\boldsymbol{\sigma}\boldsymbol{S}(t)\} \tag{21}$$

where $\boldsymbol{K}$=diag( $k_1, \cdots, k_m$ ),$\boldsymbol{\sigma}$=diag( $\sigma_{f_1}, \cdots, \sigma_{f_m}$ ). Substituting (21) in (13), $\boldsymbol{S}^T\dot{\boldsymbol{S}}$ can be obtained as

$$\begin{aligned} \boldsymbol{S}^T\dot{\boldsymbol{S}} &= \boldsymbol{S}^T\boldsymbol{f}(\boldsymbol{x}) + \boldsymbol{S}^T\boldsymbol{v}(t) + \boldsymbol{S}^T\boldsymbol{B}_0(\boldsymbol{x})\boldsymbol{u} + \boldsymbol{S}^T\Delta\boldsymbol{B}(\boldsymbol{x})\boldsymbol{u} \\ &= -\sum_{i=1}^{m} k_i S_i^2(t) - \|\boldsymbol{f}(\boldsymbol{x}) + \boldsymbol{v}(t)\|\sum_{i=1}^{m} \sigma_{f_i} S_i^2(t) + \boldsymbol{S}^T\Delta\boldsymbol{B}(\boldsymbol{x})\boldsymbol{B}_0^{-1}(\boldsymbol{x})\overline{\boldsymbol{u}} \end{aligned} \tag{22}$$

where

$$\overline{\boldsymbol{u}} = -\boldsymbol{f}(\boldsymbol{x}) - \boldsymbol{v}(t) - \boldsymbol{K}\boldsymbol{S}(t) - \|\boldsymbol{f}(\boldsymbol{x}) + \boldsymbol{v}(t)\|\boldsymbol{\sigma}\boldsymbol{S}(t) \tag{23}$$

The last term in (22), $\boldsymbol{S}^T\Delta\boldsymbol{B}(\boldsymbol{x})\boldsymbol{u}$, is the modeling error due to the interconnections of the subsystems. Noting that

$$\begin{aligned} \left|\boldsymbol{S}^T\Delta\boldsymbol{B}(\boldsymbol{x})\boldsymbol{B}_0^{-1}(\boldsymbol{x})\overline{\boldsymbol{u}}\right| &\le \|\boldsymbol{S}\|\overline{\sigma}\{\Delta\boldsymbol{B}(\boldsymbol{x})\boldsymbol{B}_0^{-1}(\boldsymbol{x})\}\|\overline{\boldsymbol{u}}\| \\ &\le \sqrt{m}\delta_0\|\boldsymbol{f}(\boldsymbol{x}) + \boldsymbol{v}(t)\|\|\boldsymbol{S}\| + \sqrt{m}\delta_0\|\boldsymbol{S}\|\|\boldsymbol{K}\boldsymbol{S}\| + \sqrt{m}\delta_0\|\boldsymbol{f}(\boldsymbol{x}) + \boldsymbol{v}(t)\|\|\boldsymbol{S}\|\|\boldsymbol{\sigma}\boldsymbol{S}\| \end{aligned} \tag{24}$$

and using inequalities

$$\|\boldsymbol{S}\|\|\boldsymbol{K}\boldsymbol{S}\| \le \frac{c_1}{2}\|\boldsymbol{S}\|^2 + \frac{1}{2c_1}\|\boldsymbol{K}\boldsymbol{S}\|^2 = \sum_{i=1}^{m}(\frac{c_1}{2} + \frac{1}{2c_1}k_i^2)S_i^2 \tag{25}$$

$$\|\boldsymbol{S}\|\|\boldsymbol{\sigma}\boldsymbol{S}\| \le \frac{c_2}{2}\|\boldsymbol{S}\|^2 + \frac{1}{2c_2}\|\boldsymbol{\sigma}\boldsymbol{S}\|^2 = \sum_{i=1}^{m}(\frac{c_2}{2} + \frac{1}{2c_2}\sigma_{f_i}^2)S_i^2 \tag{26}$$

where $c_1$ , $c_2$ , are positive constants, we obtain

$$\left|\boldsymbol{S}^T \Delta \boldsymbol{B}(\boldsymbol{x})\boldsymbol{B}_0^{-1}(\boldsymbol{x})\overline{\boldsymbol{u}}\right| \le \sqrt{m}\delta_0 \left\|\boldsymbol{f}(\boldsymbol{x}) + \boldsymbol{v}(t)\right\| \left\|\boldsymbol{S}\right\| + \sum_{i=1}^{m} \sqrt{m}\delta_0 (\frac{c_1}{2} + \frac{1}{2c_1} k_i^2) S_i^2(t)$$
$$+ \left\|\boldsymbol{f}(\boldsymbol{x}) + \boldsymbol{v}(t)\right\| \sum_{i=1}^{m} \sqrt{m}\delta_0 (\frac{c_2}{2} + \frac{1}{2c_2} \sigma_{f_i}^2) S_i^2(t) \tag{27}$$

Let $k_{\min} = \min_{i=1,\cdots,m} (k_i)$, $\sigma_{\min} = \min_{i=1,\cdots,m} (\sigma_{f_i})$. Applying (27) to (22) results in

$$\begin{aligned}
\boldsymbol{S}^T \dot{\boldsymbol{S}} &= -\sum_{i=1}^{m} (k_i - \frac{\sqrt{m}\delta_0 c_1}{2} - \frac{\sqrt{m}\delta_0}{2c_1} k_i^2) S_i^2(t) \\
&\quad - \left\|\boldsymbol{f}(\boldsymbol{x}) + \boldsymbol{v}(t)\right\| \sum_{i=1}^{m} (\sigma_{f_i} - \frac{\sqrt{m}\delta_0 c_2}{2} - \frac{\sqrt{m}\delta_0}{2c_2} \sigma_{f_i}^2) S_i^2(t) + \sqrt{m}\delta_0 \left\|\boldsymbol{f}(\boldsymbol{x}) + \boldsymbol{v}(t)\right\| \left\|\boldsymbol{S}\right\| \\
&\le - \min_{i=1,\cdots,m} \{k_i - \frac{\sqrt{m}\delta_0 c_1}{2} - \frac{\sqrt{m}\delta_0}{2c_1} k_i^2\} \left\|\boldsymbol{S}\right\|^2 \\
&\quad - \min_{i=1,\cdots,m} \{\sigma_{f_i} - \frac{\sqrt{m}\delta_0 c_2}{2} - \frac{\sqrt{m}\delta_0}{2c_2} \sigma_{f_i}^2\} \left\|\boldsymbol{f}(\boldsymbol{x}) + \boldsymbol{v}(t)\right\| \left\|\boldsymbol{S}\right\|^2 + \sqrt{m}\delta_0 \left\|\boldsymbol{f}(\boldsymbol{x}) + \boldsymbol{v}(t)\right\| \left\|\boldsymbol{S}\right\|
\end{aligned} \tag{28}$$

Applying (28) and $\left\|\boldsymbol{S}\right\| = S_\Phi + \Phi$ to $\dot{V}(t)$, we have

$$\begin{aligned}
\dot{V} &\le - \min_{i=1,\cdots,m} \{k_i - \frac{\sqrt{m}\delta_0 c_1}{2} - \frac{\sqrt{m}\delta_0}{2c_1} k_i^2\} \left\|\boldsymbol{S}\right\| S_\Phi \\
&\quad - \min_{i=1,\cdots,m} \{\sigma_{f_i} - \frac{\sqrt{m}\delta_0 c_2}{2} - \frac{\sqrt{m}\delta_0}{2c_2} \sigma_{f_i}^2\} \left\|\boldsymbol{f}(\boldsymbol{x}) + \boldsymbol{v}(t)\right\| \left\|\boldsymbol{S}\right\| S_\Phi + \sqrt{m}\delta_0 \left\|\boldsymbol{f}(\boldsymbol{x}) + \boldsymbol{v}(t)\right\| S_\Phi \\
&= - \min_{i=1,\cdots,m} \{k_i - \frac{\sqrt{m}\delta_0 c_1}{2} - \frac{\sqrt{m}\delta_0}{2c_1} k_i^2\} S_\Phi^2 - \min_{i=1,\cdots,m} \{k_i - \frac{\sqrt{m}\delta_0 c_1}{2} - \frac{\sqrt{m}\delta_0}{2c_1} k_i^2\} \Phi S_\Phi \\
&\quad - \min_{i=1,\cdots,m} \{\sigma_{f_i} - \frac{\sqrt{m}\delta_0 c_2}{2} - \frac{\sqrt{m}\delta_0}{2c_2} \sigma_{f_i}^2\} \left\|\boldsymbol{f}(\boldsymbol{x}) + \boldsymbol{v}(t)\right\| S_\Phi^2 \\
&\quad - \left( [\min_{i=1,\cdots,m} \{\sigma_{f_i} - \frac{\sqrt{m}\delta_0 c_2}{2} - \frac{\sqrt{m}\delta_0}{2c_2} \sigma_{f_i}^2\}] \Phi - \sqrt{m}\delta_0 \right) \left\|\boldsymbol{f}(\boldsymbol{x}) + \boldsymbol{v}(t)\right\| S_\Phi
\end{aligned} \tag{29}$$

By choosing the design parameters, $k_i$, $\sigma_{f_i}$, such that

$$\min_{i=1,\cdots,m} \{k_i - \frac{\sqrt{m}\delta_0 c_1}{2} - \frac{\sqrt{m}\delta_0}{2c_1} k_i^2\} > 0 \tag{30}$$

$$\min_{i=1,\cdots,m} \{\sigma_{f_i} - \frac{\sqrt{m}\delta_0 c_2}{2} - \frac{\sqrt{m}\delta_0}{2c_2} \sigma_{f_i}^2\} \ge \frac{\sqrt{m}\delta_0}{\Phi} \tag{31}$$

It follows that

$$\dot{V}(t) \le -2 \min_{i=1,\cdots,m} \{k_i - \frac{\sqrt{m}\delta_0 c_1}{2} - \frac{\sqrt{m}\delta_0}{2c_1} k_i^2\} V(t) \tag{32}$$

Inequalities (30)-(31) can be satisfied if

$$k_i - \frac{\sqrt{m}\delta_0 c_1}{2} - \frac{\sqrt{m}\delta_0}{2c_1} k_i^2 > 0 \,,\ i=1,2,\quad ,m \tag{33}$$

$$\sigma_{f_i} - \frac{\sqrt{m}\delta_0 c_2}{2} - \frac{\sqrt{m}\delta_0}{2c_2}\sigma_{f_i}^2 \geq \frac{\sqrt{m}\delta_0}{\Phi} \,,\ i=1,2,\quad ,m \tag{34}$$

which in turn imply that $k_i$ , $\sigma_{f_i}$ , have to be selected such that

$$\frac{c_1}{\sqrt{m}\delta_0}\left(1-\sqrt{1-m\delta_0^2}\right) < k_i < \frac{c_1}{\sqrt{m}\delta_0}\left(1+\sqrt{1-m\delta_0^2}\right),\ i=1,2,\quad ,m \tag{35}$$

$$\frac{c_2}{\sqrt{m}\delta_0}\left(1-\sqrt{1-m\delta_0^2-\frac{2m\delta_0^2}{c_2\Phi}}\right) \leq \sigma_{f_i} \leq \frac{c_2}{\sqrt{m}\delta_0}\left(1+\sqrt{1-m\delta_0^2-\frac{2m\delta_0^2}{c_2\Phi}}\right),\ i=1,2,\quad ,m \tag{36}$$

(35)-(36) hold only if $m\delta_0^2 < 1$ and $m\delta_0^2 + 2m\delta_0^2/(c_2\Phi) < 1$. By assuming

$$\delta_0 < 1/\sqrt{m} \tag{37}$$

and then choosing the constant $c_2$ to satisfy

$$c_2 > \frac{2m\delta_0^2}{(1-m\delta_0^2)\Phi} \tag{38}$$

ensure that (35)-(36) hold. Given (35)-(36), inequality (32) will follow which implies that $V(t)$ converges to zero exponentially fast. It follows that $S_\Phi$ converges to zero exponentially fast and that which implies that $\|\boldsymbol{S}\|$ converges to the residual set $R_S = \{\boldsymbol{S} \,|\, \|\boldsymbol{S}\| \leq \Phi\}$ exponentially fast (Ioannou and Sun 1996). The boundedness of all signals in the closed loop follows from the boundedness of $V(t)$. Inside the residual set we have $|S_i(t)| \leq \Phi$, which implies that $R_{e_i} = \{e_i \,|\, |e_i(t)| \leq \lambda_i^{-n_i+1}\Phi\}$ , $i=1,2,\quad ,m$ (Slotine and Li 1991, Slotine and Coetsee 1986). ■

The control law (14) can no longer be used in the case where $\boldsymbol{f}(\boldsymbol{x})$ and $\boldsymbol{B}(\boldsymbol{x})$ are unknown. We assume that $f_i(\boldsymbol{x})$ and $b_{ii}(\boldsymbol{x})$ can be approximated by the general one layer neural network (Funahashi 1989, Sanner and Slotine 1992, Polycarpou and Ioannou 1992, Park and Sandberg 1993, Kosmatopoulos *et al.* 1995, Polycarpou 1996, Seshagiri and Khalil 2000, Rovithakis 2001) on compact sets $\boldsymbol{x} \in \Omega_x \subset \Re^n$ as

$$f_i(\boldsymbol{x}) \approx f_i^a(\boldsymbol{x}) = \Theta_{f_i}^{*\,T}\zeta_{f_i}(\boldsymbol{x}) \,,\ i=1,2,\quad ,m \tag{39a}$$

$$b_{ii}(\boldsymbol{x}) \approx b_{ii}^a(\boldsymbol{x}) = \Theta_{b_{ii}}^{*\,T}\zeta_{b_{ii}}(\boldsymbol{x}) \,,\ i=1,2,\quad ,m \tag{39b}$$

where $\Theta_{f_i}^* \in \Re^{l_i}$, $\Theta_{b_{ii}}^* \in \Re^{m_i}$, are unknown constant parameters, and $\zeta_{f_i} : \Re^{n_i} \mapsto \Re^{l_i}$, $\zeta_{b_{ii}} : \Re^{n_i} \mapsto \Re^{m_i}$ are selected basis functions. The neural network approximation errors $d_{f_i}(\boldsymbol{x})$, $d_{b_i}(\boldsymbol{x})$ are given by

$$d_{f_i}(\boldsymbol{x}) := f_i(\boldsymbol{x}) - f_i^a(\boldsymbol{x}) \tag{40a}$$

$$d_{b_i}(\boldsymbol{x}) := b_{ii}(\boldsymbol{x}) - b_{ii}^a(\boldsymbol{x}) \tag{40b}$$

By "optimal" approximation it is meant that the weights $\Theta_{f_i}^*$, $\Theta_{b_{ii}}^*$, are chosen to minimize $d_{f_i}(\boldsymbol{x}), d_{b_i}(\boldsymbol{x})$ for all $\boldsymbol{x} \in \Omega_x \subset \Re^n$:

$$\Theta_{f_i}^* := \arg \min_{\Theta_{f_i} \in \Re^{l_i}} \{ \sup_{\boldsymbol{x} \in \Omega_x} \left| f_i(\boldsymbol{x}) - \Theta_{f_i}^T \zeta_{f_i}(\boldsymbol{x}) \right| \}, \quad i=1,2, \quad ,m \tag{41a}$$

$$\Theta_{b_{ii}}^* := \arg \min_{\Theta_{b_{ii}} \in \Re^{m_i}} \{ \sup_{\boldsymbol{x} \in \Omega_x} \left| b_{ii}(\boldsymbol{x}) - \Theta_{b_{ii}}^T \zeta_{b_{ii}}(\boldsymbol{x}) \right| \}, \quad i=1,2, \quad ,m \tag{41b}$$

**Assumption 6**: There exists a set of constant parameters $\Theta_{f_i}^*$, $\Theta_{b_{ii}}^*$, $i=1,2, \quad ,m$, referred to as optimal output weights such that the approximation error $d_{f_i}(\boldsymbol{x})$ is upper bounded by a known constant $\psi_{f_i} > 0$ and $d_{b_i}(\boldsymbol{x}) / g_i(\boldsymbol{x})$ is upper bounded by a known constant, $\psi_{b_i}$, where $0 < \psi_{b_i} < 1$, over the compact set $\boldsymbol{x} \in \Omega_x$:

$$\sup_{\boldsymbol{x} \in \Omega_x} \left| d_{f_i}(\boldsymbol{x}) \right| \le \psi_{f_i}, \quad i=1, \quad ,m \tag{42a}$$

$$\sup_{\boldsymbol{x} \in \Omega_x} \{ \left| d_{b_i}(\boldsymbol{x}) \right| / g_i(\boldsymbol{x}) \} \le \psi_{b_i} < 1, \ \forall \boldsymbol{x} \in \Omega_x \tag{42b}$$

It is noted that (42a) and (42b) do not require the approximation errors to be arbitrary small.

Let the estimates of the unknown functions $f_i^a(\boldsymbol{x})$, $b_{ii}^a(\boldsymbol{x})$ at time $t$ be formed as

$$\hat{f}_i^a(\boldsymbol{x},t) = \hat{\Theta}_{f_i}^T(t) \zeta_{f_i}(\boldsymbol{x}), \quad i=1,2, \quad ,m \tag{43a}$$

$$\hat{b}_{ii}^a(\boldsymbol{x},t) = \hat{\Theta}_{b_{ii}}^T(t) \zeta_{b_{ii}}(\boldsymbol{x}), \quad i=1,2, \quad ,m \tag{43b}$$

where $\hat{\Theta}_{f_i}(t)$, $\hat{\Theta}_{b_{ii}}(t)$, are the estimates of $\Theta_{f_i}^*$, $\Theta_{b_{ii}}^*$, at time $t$ respectively.

The difference between the estimated and actual parameter values results in the estimation errors

$$\tilde{f}_i^a(\boldsymbol{x},t) = \tilde{\Theta}_{f_i}^T(t) \zeta_{f_i}(\boldsymbol{x}) \tag{44a}$$

$$\tilde{b}_{ii}^{a}(\boldsymbol{x},t) = \tilde{\Theta}_{b_{ii}}^{T}(t)\zeta_{b_{ii}}(\boldsymbol{x}) \tag{44b}$$

where,

$$\tilde{\Theta}_{f_i}(t) = \hat{\Theta}_{f_i}(t) - \Theta_{f_i}^{*}\ ;\ \tilde{\Theta}_{b_{ii}}(t) = \hat{\Theta}_{b_{ii}}(t) - \Theta_{b_{ii}}^{*} \tag{45}$$

are the parameter errors. For short, we define $\tilde{\Theta}(t) := [(\tilde{\Theta}_1^f,\cdots,\tilde{\Theta}_m^f),(\tilde{\Theta}_1^b,\cdots,\tilde{\Theta}_m^b)]^T$.

Given the estimates $\hat{f}_i^a(\boldsymbol{x},t)$ and $\hat{b}_{ii}^a(\boldsymbol{x},t)$ we can use the Certainty Equivalence (CE) principle (Ioannou and Sun 1996) to come up with an initial guess for the adaptive control law. In this case replacing $f_i(\boldsymbol{x}), b_{ii}(\boldsymbol{x})$, with $\hat{f}_i^a(\boldsymbol{x},t), \hat{b}_{ii}^a(\boldsymbol{x},t)$, in the control law (14) will be a straightforward approach,

$$u_i = \frac{1}{\hat{b}_{ii}^a(\boldsymbol{x},t)}\left[-\hat{f}_i^a(\boldsymbol{x},t) - v_i(t) - k_i S_i(t) - \sigma_{f_i}\left\|\hat{\boldsymbol{f}}^a(\boldsymbol{x},t) + v(t)\right\| S_i(t)\right] \tag{46}$$

where $\hat{\boldsymbol{f}}^a(\boldsymbol{x},t) := [\hat{f}_1^a(\boldsymbol{x},t) \ \cdots \ \hat{f}_m^a(\boldsymbol{x},t)]^T$. Then design an adaptive law for generating the parameter estimates $\hat{\Theta}_{f_i}(t), \hat{\Theta}_{b_{ii}}(t)$, and hence $\hat{f}_i^a(\boldsymbol{x},t), \hat{b}_{ii}^a(\boldsymbol{x},t)$, so that the overall system is stable and the tracking error of each subsystem goes to a small residual set with time. However, it is well known in adaptive control that the estimate $\hat{b}_{ii}^a(\boldsymbol{x},t)$ cannot be guaranteed to be away from zero for any given time *t*, which in turn implies that $u_i$ cannot be guaranteed to be bounded uniformly with time. Therefore the CE control law (46) is ineffective for closed loop system stability for the case when the estimate plant loses its controllability, i.e., $\hat{b}_{ii}^a(\boldsymbol{x},t) \approx 0$ at some time *t*. In the following section we will modify the control law (46) to bypass this problem and guarantee stability when $\boldsymbol{f}(\boldsymbol{x})$ and $\boldsymbol{B}(\boldsymbol{x})$ are unknown.

## 4. ADAPTIVE DECENTRALIZED-LIKE CONTROL SCHEME

Let us consider system (1) and the control problem solved in Section 3 for the case of known nonlinearities. In this section we assume that the nonlinear functions in (1) are unknown and design a control law to meet the control objective. In order to take care the case where the estimated plant becomes uncontrollable at some points of time. We modify the CE control law (46) as:

$$u_i = \frac{\hat{b}_{ii}^a(\boldsymbol{x},t)}{(\hat{b}_{ii}^a(\boldsymbol{x},t))^2 + \delta_{b_i}}\left[-\hat{f}_i^a(\boldsymbol{x},t) - v_i(t) - k_i S_i(t) - \sigma_{f_i}\left\|\hat{\boldsymbol{f}}^a(\boldsymbol{x},t) + v(t)\right\| S_i(t)\right] \tag{47}$$

where $\delta_{b_i} > 0$ is a small design constant. By design, control law (47) cannot become singular since $(\hat{b}_{ii}^a(\boldsymbol{x},t))^2 + \delta_{b_i} \geq \delta_{b_i} > 0$, $\forall\ \boldsymbol{x},t$. It is also worthy note that $u_i \to 0$ as fast as $\hat{b}_{ii}^a(\boldsymbol{x},t) \to 0$. Thus, when the estimate

$\hat{b}_{ii}^a(\boldsymbol{x},t)$ approaches zero, the control input remains bounded and reduces to zero. In other words, in such a case it is pointless to control what appears to the controller as an uncontrollable plant. The design merits attention since the potential loss of controllability has been the main drawback of many nonlinear adaptive laws that are based on feedback linearization.

The adaptive laws for generating the estimates $\hat{\Theta}_{f_i}(t)$, $\hat{\Theta}_{b_{ii}}(t)$, in $\hat{f}_i^a(\boldsymbol{x},t)$, $\hat{b}_{ii}^a(\boldsymbol{x},t)$, $i$=1,2 ,$m$, are as follows:

$$\dot{\hat{\Theta}}_{f_i}(t) = \Gamma_{f_i} \frac{S_\Phi}{S_\Phi + \Phi} S_i \zeta_{f_i}(\boldsymbol{x}) \tag{48a}$$

$$\dot{\hat{\Theta}}_{b_{ii}}(t) = \Gamma_{b_{ii}} \frac{S_\Phi}{S_\Phi + \Phi} S_i u_i \zeta_{b_{ii}}(\boldsymbol{x}) + \rho_i(t) \Gamma_{b_{ii}} \sigma_{b_{ii}} \operatorname{sign}(b_{ii}(\boldsymbol{x})) \left( \frac{S_\Phi}{S_\Phi + \Phi} |S_i \| u_i| + \frac{S_\Phi}{S_\Phi + \Phi} |S_i \| u_i'| + S_\Phi |u_i| \right) \zeta_{b_{ii}}(\boldsymbol{x}) \tag{48b}$$

where,

$$u_i' = \frac{1}{(\hat{b}_{ii}^a(\boldsymbol{x},t))^2 + \delta_{b_i}} \left[ -\hat{f}_i^a(\boldsymbol{x},t) - v_i(t) - k_i S_i(t) - \sigma_{f_i} \left\| \hat{\boldsymbol{f}}^a(\boldsymbol{x},t) + \boldsymbol{v}(t) \right\| S_i(t) \right] \tag{49}$$

and where $\Gamma_{f_i} > 0$, $\Gamma_{b_i} > 0$, $i$=1,2, ,$m$, are positive definite adaptive gain matrixes, $\sigma_{b_i} > 0$ is a design parameter, and sign(·) is the sign function (sign($x$)=1, if $x \geq 0$ and sign($x$)=−1, otherwise). $\rho_i(t)$ is a switching function defined as:

$$\rho_i(t) = \begin{cases} 1, & \text{if } \left| \hat{b}_{ii}^a(\boldsymbol{x},t) \right| / g_i(\boldsymbol{x}) \leq 1 - \psi_{b_i} \\ \{1 - \psi_{b_i} - \left| \hat{b}_{ii}^a(\boldsymbol{x},t) \right| / g_i(\boldsymbol{x})\} / \Delta_i, & \text{if } 1 - \psi_{b_i} - \Delta_i \leq \left| \hat{b}_{ii}^a(\boldsymbol{x},t) \right| / g_i(\boldsymbol{x}) \leq 1 - \psi_{b_i} \\ 0, & \text{if } \left| \hat{b}_{ii}^a(\boldsymbol{x},t) \right| / g_i(\boldsymbol{x}) \geq 1 - \psi_{b_i} - \Delta_i \end{cases} \tag{50}$$

where $0 < \Delta_i < 1$ is a small quotient used to avoid discontinuity in $\rho_i(t)$. A continuous switching function $\rho_i(t)$ instead of a discontinuous one is used to guarantee that the resulting differential equation representing the closed loop system satisfies the conditions for existence and uniqueness of solutions (Polycarpou and Ioannou 1993).

**Lemma 2**: The following equality holds for all $t \geq 0$

$$\rho_i(t) \tilde{b}_{ii}^a(\boldsymbol{x},t) \operatorname{sign}(b_{ii}(\boldsymbol{x})) = -\rho_i(t) \left| \tilde{b}_{ii}^a(\boldsymbol{x},t) \right|, \quad i=1,2, \quad ,m \tag{51}$$

*Proof*: If $\rho_i(t) = 0$, (51) is trivially satisfied. If $\rho_i(t) \neq 0$, we have $\left| \hat{b}_{ii}^a(\boldsymbol{x},t) \right| \leq (1 - \psi_{b_i}) g_i(\boldsymbol{x})$. This gives

$$\left| \hat{b}_{ii}^a(\boldsymbol{x},t) + d_{b_i}(\boldsymbol{x}) \right| \leq \left| \hat{b}_{ii}^a(\boldsymbol{x},t) \right| + \left| d_{b_i}(\boldsymbol{x}) \right| \leq g_i(\boldsymbol{x}) \tag{52}$$

Now noting that

$$\begin{aligned}\tilde{b}_{ii}^{a}(\boldsymbol{x},t) &= \hat{b}_{ii}^{a}(\boldsymbol{x},t) - b_{ii}^{a}(\boldsymbol{x}) = \{\hat{b}_{ii}^{a}(\boldsymbol{x},t) + d_{b_i}(\boldsymbol{x})\} - b_{ii}(\boldsymbol{x}) \\ &\le g_i(\boldsymbol{x}) - b_{ii}(\boldsymbol{x})\end{aligned} \tag{53}$$

this together with the fact $|b_{ii}(\boldsymbol{x})| \ge g_i(\boldsymbol{x})$ implies that for $\rho_i(t) \ne 0$, the sign of $\rho_i(t)\tilde{b}_{ii}^{a}(\boldsymbol{x},t)$ is always the opposite sign of $b_{ii}(\boldsymbol{x})$, $\forall\ t \ge 0$, and (51) follows directly. ■

**Lemma 3**: Define:

$$\delta_{i1} := \frac{\psi_{b_i}}{1-\psi_{b_i}-\Delta_i} + \frac{\delta_{b_i}}{[(1-\psi_{b_i}-\Delta_i)g_i^*]^2 + \delta_{b_i}},\ i=1,2,\quad ,m \tag{54a}$$

$$\delta_{i2} := \frac{\psi_{b_i}}{1-\psi_{b_i}},\ i=1,2,\quad ,m \tag{54b}$$

$$\delta_{i3} := \frac{2\delta_{b_i}}{(1-\psi_{b_i})g_i^*},\ i=1,2,\quad ,m \tag{54c}$$

$$\delta_{i4} := \frac{\delta_0}{1-\psi_{b_i}-\Delta_i},\ i=1,2,\quad ,m \tag{54d}$$

$$\delta_{i5} := \frac{\delta_0}{1-\psi_{b_i}},\ i=1,2,\quad ,m \tag{54e}$$

Then the following inequalities hold true:

$$\begin{aligned}\left|d_{b_i}(\boldsymbol{x})u_i - \delta_{b_i}u_i'\right| &\le \delta_{i1}k_i|S_i| + \delta_{i1}\left|\hat{f}_i^{a}(\boldsymbol{x},t) + v_i(t)\right| + \delta_{i1}\sigma_{f_i}\left\|\hat{\boldsymbol{f}}^{a}(\boldsymbol{x},t) + \boldsymbol{v}(t)\right\||S_i| \\ &+ \rho_i(t)\delta_{i2}\left|\tilde{b}_{ii}^{a}(\boldsymbol{x},t)\right||u_i| + \rho_i(t)\delta_{i3}\left|\tilde{b}_{ii}^{a}(\boldsymbol{x},t)\right||u_i'|\end{aligned} \tag{55}$$

$$\begin{aligned}\left|\boldsymbol{S}^T\Delta\boldsymbol{B}(\boldsymbol{x})\boldsymbol{u}\right| &\le \sum_{i=1}^{m}\delta_4\left(\frac{c_1}{2} + \frac{1}{2c_1}k_i^2\right)S_i^2(t) + \left\|\hat{\boldsymbol{f}}^{a}(\boldsymbol{x},t) + \boldsymbol{v}(t)\right\|\sum_{i=1}^{m}\delta_4\left(\frac{c_2}{2} + \frac{1}{2c_2}\sigma_{f_i}^2\right)S_i^2(t) \\ &+ \delta_4\left\|\hat{\boldsymbol{f}}^{a}(\boldsymbol{x},t) + \boldsymbol{v}(t)\right\|\|\boldsymbol{S}\| + \|\boldsymbol{S}\|\sum_{i=1}^{m}\rho_i(t)\delta_{i5}\left|\tilde{b}_{ii}^{a}(\boldsymbol{x},t)\right||u_i|\end{aligned} \tag{56}$$

where $\delta_4 = \sqrt{\delta_{14}^2 + \cdots + \delta_{m4}^2}$.

*Proof*: The proof is presented in the Appendix.

The properties of the overall control law (47),(48a-b) are summarized by the following theorem.

**Theorem 2**: Consider the system (1), the control law (47) and the adaptive laws (48a-b). Assume that assumptions 1-6 hold. If $2\max_{i=1,\cdots,m}(\psi_{b_i}) + \sqrt{m}\delta_0 + \max_{i=1,\cdots,m}(\Delta_i) < 1$ is satisfied for an arbitrary small positive constant $\Delta_i$, there exist positive

constants $\delta_{i1}, \delta_{i2}, \delta_{i3}, \delta_{i4}, \delta_{i5}$, sets $\overline{\Omega}_x \subset \Omega_x$ and $\overline{\Omega}_\Theta \subset \Re^L$, where $L = \sum_{i=1}^{m}(l_i + m_i)$, and design constants $\Phi$, $\delta_{b_i}$, $k_i$, $\sigma_{f_i}$, $\sigma_{b_i}$, $i$=1,2, ,$m$, that satisfy

$$\delta_{b_i} < (1 - 2\psi_{b_i} - \delta_0 - \Delta_i)[(1 - \psi_{b_i} - \Delta_i)g_i^*]^2 / (\psi_{b_i} + \delta_0)$$

$$\frac{(1-\delta_{i1})c_1}{\delta_4}\left(1 - \sqrt{1 - \frac{\delta_4^2}{(1-\delta_{i1})^2} - \frac{2\delta_4\psi_f}{c_1(1-\delta_{i1})^2\Phi}}\right) \le k_i \le \frac{(1-\delta_{i1})c_1}{\delta_4}\left(1 + \sqrt{1 - \frac{\delta_4^2}{(1-\delta_{i1})^2} - \frac{2\delta_4\psi_f}{c_1(1-\delta_{i1})^2\Phi}}\right)$$

$$\frac{(1-\delta_{i1})c_2}{\delta_4}\left(1 - \sqrt{1 - \frac{\delta_4^2}{(1-\delta_{i1})^2} - \frac{2\delta_4^2}{c_2(1-\delta_{i1})^2\Phi}}\right) \le \sigma_{f_i} \le \frac{(1-\delta_{i1})c_2}{\delta_4}\left(1 + \sqrt{1 - \frac{\delta_4^2}{(1-\delta_{i1})^2} - \frac{2\delta_4^2}{c_2(1-\delta_{i1})^2\Phi}}\right)$$

$$\sigma_{b_i} \ge \max(\delta_{i2}, \delta_{i3}, \delta_{i5})$$

with $c_1 > \dfrac{2\delta_4\psi_f}{\{[1 - \max_{i=1,\cdots,m}(\delta_{i1})]^2 - \delta_4^2\}\Phi}$, $c_2 > \dfrac{2\delta_4^2}{\{[1 - \max_{i=1,\cdots,m}(\delta_{i1})]^2 - \delta_4^2\}\Phi}$, $\psi_f = \sqrt{\psi_{f_1}^2 + \cdots + \psi_{f_m}^2}$, such that for all $x(0) \in \overline{\Omega}_x$ and all $\widetilde{\Theta}(0) \in \overline{\Omega}_\Theta$, all signals in the closed-loop system are bounded and the tracking errors $e_i(t)$ converge to the residual sets $R_{e_i} = \{e_i \mid |e_i(t)| \le \lambda_i^{-n_i+1}\Phi\}$, $i$=1,2, ,$m$, as $t \to \infty$. The sizes of these residue sets depend only on the design constants $\lambda_i$ ,$\Phi$, and can be specified *a priori*.

*Proof*: Let us consider the following Lyapunov-like function:

$$V(t) = \frac{1}{2}\left\{S_\Phi^2 + \sum_{i=1}^{m}\widetilde{\Theta}_{f_i}^T\Gamma_{f_i}^{-1}\widetilde{\Theta}_{f_i} + \sum_{i=1}^{m}\widetilde{\Theta}_{b_{ii}}^T\Gamma_{b_{ii}}^{-1}\widetilde{\Theta}_{b_{ii}}\right\} \tag{57}$$

Applying Lemma 1 and the adaptive laws (48a)-(48b), we can establish that

$$\dot{V}(t) = 0, \text{ if } \|\boldsymbol{S}\| \le \Phi \tag{58}$$

$$\dot{V}(t) = \frac{S_\Phi}{S_\Phi + \Phi}\boldsymbol{S}^T\dot{\boldsymbol{S}} + \sum_{i=1}^{m}\widetilde{\Theta}_{f_i}^T\Gamma_{f_i}^{-1}\dot{\widetilde{\Theta}}_{f_i} + \sum_{i=1}^{m}\widetilde{\Theta}_{b_{ii}}^T\Gamma_{b_{ii}}^{-1}\dot{\widetilde{\Theta}}_{b_{ii}}, \text{ if } \|\boldsymbol{S}\| > \Phi \tag{59}$$

In the following proof, we only consider the region $\|\boldsymbol{S}\| > \Phi$.

Rewrite $u_i$ in (47) as:

$$u_i = \frac{\hat{b}_{ii}^a(\boldsymbol{x},t)}{(\hat{b}_{ii}^a(\boldsymbol{x},t))^2 + \delta_{b_i}}\overline{u}_i \tag{60}$$

$$\overline{u}_i = -\hat{f}_i^a(\boldsymbol{x},t) - v_i(t) - k_i S_i(t) - \sigma_{f_i}\left\|\hat{\boldsymbol{f}}^a(\boldsymbol{x},t) + \boldsymbol{v}(t)\right\| S_i(t) \tag{61}$$

Using (60)-(61), the tracking error dynamics of each subsystem can be expressed as

$$\begin{aligned}
\dot{S}_i &= f_i(\boldsymbol{x}) + v_i(t) + b_{ii}(\boldsymbol{x})u_i + \sum_{j=1;j\neq i}^{m} b_{ij}(\boldsymbol{x})u_j \\
&= f_i(\boldsymbol{x}) + v_i(t) + \frac{(\hat{b}_{ii}^a(\boldsymbol{x},t))^2}{(\hat{b}_{ii}^a(\boldsymbol{x},t))^2 + \delta_{b_i}}\overline{u}_i + \{b_{ii}(\boldsymbol{x}) - \hat{b}_{ii}^a(\boldsymbol{x},t)\}u_i + \sum_{j=1;j\neq i}^{m} b_{ij}(\boldsymbol{x})u_j \\
&= f_i(\boldsymbol{x}) + v_i(t) + \overline{u}_i - \frac{\delta_{b_i}}{(\hat{b}_{ii}^a(\boldsymbol{x},t))^2 + \delta_{b_i}}\overline{u}_i + \{b_{ii}(\boldsymbol{x}) - \hat{b}_{ii}^a(\boldsymbol{x},t)\}u_i + \sum_{j=1;j\neq i}^{m} b_{ij}(\boldsymbol{x})u_j \\
&= -k_i S_i(t) - \sigma_{f_i}\left\|\hat{\boldsymbol{f}}^a(\boldsymbol{x},t) + \boldsymbol{v}(t)\right\| S_i(t) + \{f_i(\boldsymbol{x}) - \hat{f}_i^a(\boldsymbol{x},t)\} + \{b_{ii}(\boldsymbol{x}) - \hat{b}_{ii}^a(\boldsymbol{x},t)\}u_i - \delta_{b_i}u_i' + \sum_{j=1;j\neq i}^{m} b_{ij}(\boldsymbol{x})u_j
\end{aligned} \tag{62}$$

Utilizing the identities

$$f_i(\boldsymbol{x}) - \hat{f}_i^a(\boldsymbol{x},t) = (f_i(\boldsymbol{x}) - f_i^a(\boldsymbol{x})) - (\hat{f}_i^a(\boldsymbol{x},t) - f_i^a(\boldsymbol{x})) = d_{f_i}(\boldsymbol{x}) - \tilde{f}_i^a(\boldsymbol{x},t) \tag{63a}$$

$$b_{ii}(\boldsymbol{x}) - \hat{b}_{ii}^a(\boldsymbol{x},t) = [b_{ii}(\boldsymbol{x}) - b_{ii}^a(\boldsymbol{x})] - [\hat{b}_{ii}^a(\boldsymbol{x},t) - b_{ii}^a(\boldsymbol{x})] = d_{b_i}(\boldsymbol{x}) - \tilde{b}_{ii}^a(\boldsymbol{x},t) \tag{63b}$$

it follows that

$$\dot{S}_i = -k_i S_i - \sigma_{f_i}\left\|\hat{\boldsymbol{f}}^a(\boldsymbol{x},t) + \boldsymbol{v}(t)\right\| S_i - \tilde{f}_i^a(\boldsymbol{x},t) - \tilde{b}_{ii}^a(\boldsymbol{x},t)u_i + d_{f_i}(\boldsymbol{x}) + \{d_{b_i}(\boldsymbol{x})u_i - \delta_{b_i}u_i'\} + \sum_{j=1,j\neq i}^{m} b_{ij}(\boldsymbol{x})u_j \tag{64}$$

In (64), the term $\sum_{j=1,j\neq i}^{m} b_{ij}(\boldsymbol{x})u_j$ is the modeling error term due to the interactions between the *i*-th subsystem with all other subsystems; $\{d_{b_i}(\boldsymbol{x})u_i - \delta_{b_i}u_i'\}$ is a modeling error representing the effect of the design parameter $\delta_{b_i}$ and the approximation error $d_{b_i}(\boldsymbol{x})$. This is the price paid for avoiding the singularity in control law (47) by introducing the design parameter $\delta_{b_i}$ which appears as a disturbance in the closed loop system.

Using (64), the composite tracking error dynamics may be described as

$$\begin{aligned}
\boldsymbol{S}^T\dot{\boldsymbol{S}} = &-\sum_{i=1}^{m} k_i S_i^2 - \left\|\hat{\boldsymbol{f}}^a(\boldsymbol{x},t) + \boldsymbol{v}(t)\right\|\sum_{i=1}^{m}\sigma_{f_i}S_i^2 - \sum_{i=1}^{m} S_i\tilde{f}_i^a(\boldsymbol{x},t) - \sum_{i=1}^{m} S_i\tilde{b}_{ii}^a(\boldsymbol{x},t)u_i \\
&+ \boldsymbol{S}^T\boldsymbol{d}_f(\boldsymbol{x}) + \sum_{j=1}^{m} S_i\{d_{b_i}(\boldsymbol{x})u_i - \delta_{b_i}u_i'\} + \boldsymbol{S}^T\Delta\boldsymbol{B}(\boldsymbol{x})\boldsymbol{u}
\end{aligned} \tag{65}$$

where $\boldsymbol{d}_f(\boldsymbol{x}) := [d_{f_1}(\boldsymbol{x}),\cdots,d_{f_m}(\boldsymbol{x})]^T$.

Applying Lemma 3, the modeling error term, $\{d_{b_i}(\boldsymbol{x})u_i - \delta_{b_i}u_i'\}$, and the interconnection term, $\boldsymbol{S}^T\Delta\boldsymbol{B}(\boldsymbol{x})\boldsymbol{u}$, in (65) can be expressed as

$$\left|d_{b_i}(\boldsymbol{x})u_i - \delta_{b_i}u_i'\right| \le \delta_{i1}k_i\left|S_i\right| + \delta_{i1}\left|\hat{f}_i^a(\boldsymbol{x},t) + v_i(t)\right| + \delta_{i1}\sigma_{f_i}\left\|\hat{\boldsymbol{f}}^a(\boldsymbol{x},t) + v(t)\right\|S_i\| + \rho_i(t)\delta_{i2}\left|\tilde{b}_{ii}^a(\boldsymbol{x},t)\right\|u_i\| + \rho_i(t)\delta_{i3}\left|\tilde{b}_{ii}^a(\boldsymbol{x},t)\right\|u_i'\| \tag{66}$$

$$\left|\boldsymbol{S}^T\Delta\boldsymbol{B}(\boldsymbol{x})\boldsymbol{u}\right| \le \sum_{i=1}^{m}\delta_4\left(\frac{c_1}{2} + \frac{1}{2c_1}k_i^2\right)S_i^2(t) + \left\|\hat{\boldsymbol{f}}^a(\boldsymbol{x},t) + v(t)\right\|\sum_{i=1}^{m}\delta_4\left(\frac{c_2}{2} + \frac{1}{2c_2}\sigma_{f_i}^2\right)S_i^2(t) + \delta_4\left\|\hat{\boldsymbol{f}}^a(\boldsymbol{x},t) + v(t)\right\|\|\boldsymbol{S}\| + \|\boldsymbol{S}\|\sum_{i=1}^{m}\rho_i(t)\delta_{i5}\left|\tilde{b}_{ii}^a(\boldsymbol{x},t)\right\|u_i\| \tag{67}$$

Substituting (66)-(67) in (65) gives

$$\begin{aligned}\boldsymbol{S}^T\dot{\boldsymbol{S}} \le & -\sum_{i=1}^{m}\{(1-\delta_{i1})k_i - \frac{\delta_4 c_1}{2} - \frac{\delta_4}{2c_1}k_i^2\}S_i^2 - \left\|\hat{\boldsymbol{f}}^a(\boldsymbol{x},t) + v(t)\right\|\sum_{i=1}^{m}\{(1-\delta_{i1})\sigma_{f_i} - \frac{\delta_4 c_2}{2} - \frac{\delta_4}{2c_2}\sigma_{f_i}^2\}S_i^2 \\ & + \boldsymbol{S}^T\boldsymbol{d}_f(\boldsymbol{x}) + \delta_4\left\|\hat{\boldsymbol{f}}^a(\boldsymbol{x},t) + v(t)\right\|\|\boldsymbol{S}\| - \sum_{i=1}^{m}S_i\tilde{f}_i^a(\boldsymbol{x},t) - \sum_{i=1}^{m}S_i\tilde{b}_{ii}^a(\boldsymbol{x},t)u_i \\ & + \sum_{j=1}^{m}\rho_i(t)\delta_{i2}\left|\tilde{b}_{ii}^a(\boldsymbol{x},t)\right\|u_i'\|S_i\| + \sum_{j=1}^{m}\rho_i(t)\delta_{i3}\left|\tilde{b}_{ii}^a(\boldsymbol{x},t)\right\|u_i\|S_i\| + \|\boldsymbol{S}\|\sum_{i=1}^{m}\rho_i(t)\delta_{i5}\left|\tilde{b}^a(\boldsymbol{x},t)\right\|u_i\|\end{aligned} \tag{68}$$

The above equation can be developed further as

$$\begin{aligned}\boldsymbol{S}^T\dot{\boldsymbol{S}} \le & -\min_{i=1,\cdots,m}\{(1-\delta_{i1})k_i - \frac{\delta_4 c_1}{2} - \frac{\delta_4}{2c_1}k_i^2\}\|\boldsymbol{S}\|^2 - \min_{i=1,\cdots,m}\{(1-\delta_{i1})\sigma_{f_i} - \frac{\delta_4 c_2}{2} - \frac{\delta_4}{2c_2}\sigma_{f_i}^2\}\left\|\hat{\boldsymbol{f}}^a(\boldsymbol{x},t) + v(t)\right\|\|\boldsymbol{S}\|^2 \\ & + \psi_f\|\boldsymbol{S}\| + \delta_4\left\|\hat{\boldsymbol{f}}^a(\boldsymbol{x},t) + v(t)\right\|\|\boldsymbol{S}\| - \sum_{i=1}^{m}S_i\tilde{f}_i^a(\boldsymbol{x},t) - \sum_{i=1}^{m}S_i\tilde{b}_{ii}^a(\boldsymbol{x},t)u_i \\ & + \sum_{j=1}^{m}\rho_i(t)\delta_{i2}\left|\tilde{b}_{ii}^a(\boldsymbol{x},t)\right\|u_i'\|S_i\| + \sum_{j=1}^{m}\rho_i(t)\delta_{i3}\left|\tilde{b}_{ii}^a(\boldsymbol{x},t)\right\|u_i\|S_i\| + \|\boldsymbol{S}\|\sum_{i=1}^{m}\rho_i(t)\delta_{i5}\left|\tilde{b}_{ii}^a(\boldsymbol{x},t)\right\|u_i\|\end{aligned} \tag{69}$$

where we use $\left|\boldsymbol{S}^T\boldsymbol{d}_f(\boldsymbol{x})\right| \le \psi_f\|\boldsymbol{S}\|$, $\psi_f = \sqrt{\psi_{f_1}^2 + \cdots + \psi_{f_m}^2}$ .

Noting that $\|\boldsymbol{S}\| = S_\Phi + \Phi$ and rearranging the terms, the first term in $\dot{V}(t)$ can be described as

$$\begin{aligned}\frac{S_\Phi}{S_\Phi + \Phi}\boldsymbol{S}^T\dot{\boldsymbol{S}} \le & -\min_{i=1,\cdots,m}\{(1-\delta_{i1})k_i - \frac{\delta_4 c_1}{2} - \frac{\delta_4}{2c_1}k_i^2\}S_\Phi^2 - \left(\min_{i=1,\cdots,m}\{(1-\delta_{i1})k_i - \frac{\delta_4 c_1}{2} - \frac{\delta_4}{2c_1}k_i^2\}\Phi - \psi_f\right)S_\Phi \\ & - \min_{i=1,\cdots,m}\{(1-\delta_{i1})\sigma_{f_i} - \frac{\delta_4 c_2}{2} - \frac{\delta_4}{2c_2}\sigma_{f_i}^2\}\left\|\hat{\boldsymbol{f}}^a(\boldsymbol{x},t) + v(t)\right\|S_\Phi^2 \\ & - \left(\min_{i=1,\cdots,m}\{(1-\delta_{i1})\sigma_{f_i} - \frac{\delta_4 c_2}{2} - \frac{\delta_4}{2c_2}\sigma_{f_i}^2\}\Phi - \delta_4\right)\left\|\hat{\boldsymbol{f}}^a(\boldsymbol{x},t) + v(t)\right\|S_\Phi \\ & - \frac{S_\Phi}{S_\Phi + \Phi}\sum_{i=1}^{m}S_i\tilde{f}_i^a(\boldsymbol{x},t) - \frac{S_\Phi}{S_\Phi + \Phi}\sum_{i=1}^{m}\tilde{b}_{ii}^a(\boldsymbol{x},t)u_iS_i + \frac{S_\Phi}{S_\Phi + \Phi}\sum_{i=1}^{m}\rho_i(t)\delta_{i2}\left|\tilde{b}_{ii}^a(\boldsymbol{x},t)\right\|u_i'\|S_i\| \\ & + \frac{S_\Phi}{S_\Phi + \Phi}\sum_{i=1}^{m}\rho_i(t)\delta_{i3}\left|\tilde{b}_{ii}^a(\boldsymbol{x},t)\right\|u_i\|S_i\| + S_\Phi\sum_{i=1}^{m}\rho_i(t)\delta_{i5}\left|\tilde{b}_{ii}^a(\boldsymbol{x},t)\right\|u_i\|\end{aligned} \tag{70}$$

Let us now consider the second term of $\dot{V}(t)$ in (59). Using the adaptive law (48a) yields

$$\sum_{i=1}^{m}\tilde{\Theta}_{f_i}^T\Gamma_{f_i}^{-1}\dot{\tilde{\Theta}}_{f_i} = \tilde{f}_1^a(\boldsymbol{x},t)\frac{S_\Phi}{S_\Phi + \Phi}S_1 + \cdots + \tilde{f}_m^a(\boldsymbol{x},t)\frac{S_\Phi}{S_\Phi + \Phi}S_m \tag{71}$$

Applying Lemma 2 and adaptive law (48b), the last term of $\dot{V}(t)$ in (59) can be written as:

$$\begin{aligned}\sum_{i=1}^{m}\tilde{\Theta}_{b_{ii}}^{T}\Gamma_{b_{ii}}^{-1}\dot{\hat{\Theta}}_{b_{ii}} &= \frac{S_\Phi}{S_\Phi+\Phi}\sum_{i=1}^{m}\tilde{b}_{ii}^{a}(\boldsymbol{x},t)u_i S_i - \frac{S_\Phi}{S_\Phi+\Phi}\sum_{i=1}^{m}\rho_i(t)\sigma_{b_i}\left|\tilde{b}_{ii}^{a}(\boldsymbol{x},t)\right|\|u_i\|S_i| \\ &- \frac{S_\Phi}{S_\Phi+\Phi}\sum_{i=1}^{m}\rho_i(t)\sigma_{b_i}\left|\tilde{b}_{ii}^{a}(\boldsymbol{x},t)\right|\|u_i'\|S_i| - S_\Phi\sum_{i=1}^{m}\rho_i(t)\sigma_{b_i}\left|\tilde{b}_{ii}^{a}(\boldsymbol{x},t)\right|\|u_i|\end{aligned} \tag{72}$$

Combining (70)-(72), $\dot{V}(t)$ is finally given by

$$\begin{aligned}\dot{V}(t) \le & -\min_{i=1,\cdots,m}\{(1-\delta_{i1})k_i - \frac{\delta_4 c_1}{2} - \frac{\delta_4}{2c_1}k_i^2\}S_\Phi^2 - \left(\min_{i=1,\cdots,m}\{(1-\delta_{i1})k_i - \frac{\delta_4 c_1}{2} - \frac{\delta_4}{2c_1}k_i^2\}\Phi - \psi_f\right)S_\Phi \\ & -\min_{i=1,\cdots,m}\{(1-\delta_{i1})\sigma_{f_i} - \frac{\delta_4 c_2}{2} - \frac{\delta_4}{2c_2}\sigma_{f_i}^2\}\|\hat{\boldsymbol{f}}^a(\boldsymbol{x},t)+\boldsymbol{v}(t)\|S_\Phi^2 \\ & -\left(\min_{i=1,\cdots,m}\{(1-\delta_{i1})\sigma_{f_i} - \frac{\delta_4 c_2}{2} - \frac{\delta_4}{2c_2}\sigma_{f_i}^2\}\Phi - \delta_4\right)\|\hat{\boldsymbol{f}}^a(\boldsymbol{x},t)+\boldsymbol{v}(t)\|S_\Phi \\ & -\frac{S_\Phi}{S_\Phi+\Phi}\sum_{i=1}^{m}\rho_i(t)(\sigma_{b_i}-\delta_{i2})\delta_{i2}\left|\tilde{b}_{ii}^{a}(\boldsymbol{x},t)\right|\|u_i'\|S_i| - \frac{S_\Phi}{S_\Phi+\Phi}\sum_{i=1}^{m}\rho_i(t)(\sigma_{b_i}-\delta_{i3})\left|\tilde{b}_{ii}^{a}(\boldsymbol{x},t)\right|\|u_i\|S_i| \\ & -S_\Phi\sum_{i=1}^{m}\rho_i(t)(\sigma_{b_i}-\delta_{i5})\left|\tilde{b}_{ii}^{a}(\boldsymbol{x},t)\right|\|u_i|\end{aligned} \tag{73}$$

If now we choose the design constants $\Phi, k_i, \sigma_{f_i}, \sigma_{b_i}$, such that

$$\min_{i=1,\cdots,m}\{(1-\delta_{i1})k_i - \frac{\delta_4 c_1}{2} - \frac{\delta_4}{2c_1}k_i^2\} \ge \frac{\psi_f}{\Phi} \tag{74}$$

$$\min_{i=1,\cdots,m}\{(1-\delta_{i1})\sigma_{f_i} - \frac{\delta_4 c_2}{2} - \frac{\delta_4}{2c_2}\sigma_{f_i}^2\} \ge \frac{\delta_4}{\Phi} \tag{75}$$

$$\sigma_{b_i} \ge \delta_{i2};\ \sigma_{b_i} \ge \delta_{i3};\ \sigma_{b_i} \ge \delta_{i5} \tag{76}$$

It results in

$$\dot{V} \le -\frac{\psi_f}{\Phi}S_\Phi^2 \le 0 \tag{77}$$

Conditions (74)-(76) imply that the design parameters, $\Phi, k_i, \sigma_{f_i}, \sigma_{b_i}$, $i$=1,2, ,$m$, have to satisfy the following inequalities:

$$\frac{(1-\delta_{i1})c_1}{\delta_4}\left(1-\sqrt{1-\frac{\delta_4^2}{(1-\delta_{i1})^2}-\frac{2\delta_4\psi_f}{c_1(1-\delta_{i1})^2\Phi}}\right) \le k_i \le \frac{(1-\delta_{i1})c_1}{\delta_4}\left(1+\sqrt{1-\frac{\delta_4^2}{(1-\delta_{i1})^2}-\frac{2\delta_4\psi_f}{c_1(1-\delta_{i1})^2\Phi}}\right) \tag{78}$$

$$\frac{(1-\delta_{i1})c_2}{\delta_4}\left(1-\sqrt{1-\frac{\delta_4^2}{(1-\delta_{i1})^2}-\frac{2\delta_4^2}{c_1(1-\delta_{i1})^2\Phi}}\right) \le \sigma_{f_i} \le \frac{(1-\delta_{i1})c_2}{\delta_4}\left(1+\sqrt{1-\frac{\delta_4^2}{(1-\delta_{i1})^2}-\frac{2\delta_4^2}{c_2(1-\delta_{i1})^2\Phi}}\right) \tag{79}$$

$$\sigma_{b_i} \geq \max\{\delta_{i2}, \delta_{i3}, \delta_{i5}\} \tag{80}$$

We now need to establish that such design constants exist to satisfy inequalities (78)-(80). In (78)-(79), we require

$$\frac{\delta_4^2}{(1-\delta_{i1})^2} + \frac{2\delta_4\psi_f}{c_1(1-\delta_{i1})^2\Phi} < 1 \tag{81}$$

$$\frac{\delta_4^2}{(1-\delta_{i1})^2} + \frac{2\delta_4^2}{c_2(1-\delta_{i1})^2\Phi} < 1 \tag{82}$$

Assuming

$$2\max_{i=1,\cdots,m}(\psi_{b_i}) + \sqrt{m}\delta_0 + \max_{i=1,\cdots,m}(\Delta_i) < 1 \tag{83}$$

and choosing

$$\delta_{b_i} < (1 - 2\psi_{b_i} - \delta_0 - \Delta_i)[(1 - \psi_{b_i} - \Delta_i)g_i^*]^2/(\psi_{b_i} + \delta_0) \tag{84}$$

ensures that $\delta_{i1} + \delta_4 < 1$, $i$=1,2, ,$m$, which imply $\delta_4^2/(1-\delta_{i1}^2) < 1$. Then by choosing

$$c_1 > \frac{2\psi_f\delta_4}{\{[1 - \max_{i=1,\cdots,m}(\delta_{i1})]^2 - \delta_4^2\}\Phi} \tag{85}$$

$$c_2 > \frac{2\delta_4^2}{\{[1 - \max_{i=1,\cdots,m}(\delta_{i1})]^2 - \delta_4^2\}\Phi} \tag{86}$$

conditions (81)-(82) can be satisfied. Given (81)-(82) $\Phi, k_i, \sigma_{f_i}, \sigma_{b_i}$, $i$=1,2, ,$m$, can be selected to satisfy equations (78)-(80), which in turn imply

$$\dot{V}(t) = 0, \text{ if } \|\boldsymbol{S}\| \leq \Phi \tag{87a}$$

$$\dot{V} \leq -\frac{\psi_f}{\Phi}S_\Phi^2 < 0, \text{ if } \|\boldsymbol{S}\| > \Phi \tag{87b}$$

The results (87a)-(87b) hold under the assumption $\boldsymbol{x} \in \Omega_x$, therefore we need to establish that all states do indeed remain inside the compact set $\Omega_x$ for all $t \geq 0$.

Let $y_d = [y_{d_1}, \cdots, y_{d_1}^{(n_1-1)}, \cdots, y_{d_m}, \cdots, y_{d_m}^{(n_m-1)}] \in \Omega_d$, where $\Omega_d \subset \Re^n$ is a known compact set. Suppose $\widetilde{\Theta}(t) \in \Omega_\Theta \subset \Re^L$, and $\boldsymbol{e}(t) \in \Omega_e$, where set $\Omega_e$ is defined as

$$\Omega_e := \{\boldsymbol{e}(t) = \boldsymbol{x}(t) - \boldsymbol{y}_d(t) \,|\, \boldsymbol{x}(t) \in \Omega_x, \boldsymbol{y}_d(t) \in \Omega_d\} \tag{88}$$

Now consider the set

$$M = \{\boldsymbol{e}(t), \widetilde{\Theta}(t) \,|\, V(t) \le V_0\} \tag{89}$$

where $V_0 > \Phi$ is chosen as the largest constant for which $M \subset \Omega_e \times \Omega_\Theta$. Then for all $\boldsymbol{e}(0) \in \overline{\Omega}_e$, $\widetilde{\Theta}(0) \in \overline{\Omega}_\Theta$, such that $\overline{\Omega}_e \times \overline{\Omega}_\Theta \subset M$, it follows from (57) and (87a-b) that $V(t)$ is bounded from above by $V_0$ for all $t \ge 0$, which implies that $\boldsymbol{e}(t) \in \Omega_e$, $\forall\, t \ge 0$. Using the definition of $\Omega_e$ it follows for all $\boldsymbol{x}(0) \in \overline{\Omega}_x \subset \Omega_x$, where $\boldsymbol{x}(0) \in \overline{\Omega}_x \Leftrightarrow \boldsymbol{e}(0) \in \overline{\Omega}_e$, implies $\boldsymbol{x} \in \Omega_x$ for all $t \ge 0$. Therefore $\boldsymbol{x}$ cannot leave $\Omega_x$ at any time $t \ge 0$.

The boundedness of $V(t)$ together with $\dot{V}(t) \le 0$ ensures that $S_\Phi, \widetilde{\Theta}_{f_i}(t), \widetilde{\Theta}_{b_{ii}}(t)$, are bounded for all $t \ge 0$, i.e, $S_\Phi, \widetilde{\Theta}_{f_i}(t), \widetilde{\Theta}_{b_{ii}} \in L_\infty$. This in turn implies that $\boldsymbol{x}$, $\boldsymbol{u}$ are bounded and $V(t)$ has a limit, i.e. $\lim_{t\to\infty} V(t) = V_\infty$. Applying the fact that $S_\Phi = 0$ for $\|\boldsymbol{S}\| \le \Phi$ and (87b), we have $\lim_{t\to\infty} \int_0^t S_\Phi^2(\tau)d\tau = \int_0^\infty S_\Phi^2(t)dt \le \dfrac{V(0) - V_\infty}{\psi_f / \Phi} < \infty$ which gives $S_\Phi \in L_2$. From $S_\Phi, \widetilde{\Theta}(t) \in L_\infty$, it follows that all signals are bounded implying that $\dot{S}_\Phi \in L_\infty$. From $\dot{S}_\Phi \in L_\infty$ and $S_\Phi \in L_2$ we can conclude that $S_\Phi \to 0$ as $t \to \infty$, which implies that $\|\boldsymbol{S}\|$ converges to the residual set $R_S = \{\boldsymbol{S} \,|\, \|\boldsymbol{S}\| \le \Phi\}$ (Ioannou and Sun 1996). Inside the residual set we also have $|S_i| \le \Phi$ which in turn implies that $|e_i(t)| \le \lambda_i^{-n_i+1}\Phi$, $i$=1,2, ,$m$. (Slotine and Li 1991, Slotine and Coetsee 1986). ■

Design Parameter Procedure

Using the procedure described below, the design parameters can be chosen to guarantee that the tracking error is within a desired prespecified bound at steady state provided the lower bound $g_i^*$, which is related to the controllability of each subsystem, $\psi_{b_i}, \psi_{f_i}$, the upper bounds for the approximation errors of each subsystem, and $\delta_0$, the strength of the interconnection among the subsystems, are known *a priori*.

(1) Using $\psi_{b_i}$, the upper bound of the approximation error $d_{b_i}(\boldsymbol{x})$, and $\delta_0$, the strength of the interconnection among the subsystems, check if $2 \max_{i=1,\cdots,m}(\psi_{b_i}) + \sqrt{m}\delta_0 < 1$ is satisfied in each subsystem. If so, choose the design parameter, $\Delta_i$, such that $2 \max_{i=1,\cdots,m}(\psi_{b_i}) + \sqrt{m}\delta_0 + \max_{i=1,\cdots,m}(\Delta_i) < 1$. Then choose the design constant, $\delta_{b_i}$, to satisfy $\delta_{b_i} < (1 - 2\psi_{b_i} - \delta_0 - \Delta_i)[(1 - \psi_{b_i} - \Delta_i)g_i^*]^2 / (\psi_{b_i} + \delta_0)$. It is worth noting that the quotient, $\psi_{b_i} < 1/2$, gives an upper bound for the approximation error $d_{b_i}(\boldsymbol{x})$ that can be tolerated by the each subsystem.

(2) Set the desired upper bound of the tracking error for each subsystem at steady state equal to $\lambda_i^{-n_i+1}\Phi$ and choose $\lambda_i$, $\Phi$, to satisfy the bound.

(3) Using the results of $\delta_{b_i}$, $\Delta_i$, obtained from step (1), calculate $\delta_{i1}, \delta_{i2}, \delta_{i3}, \delta_{i4}, \delta_{i5}$, through (54a-e).

(4) Calculate $\delta_4, \psi_f$. Select the constants, $c_1, c_2$, such that $c_1 > \dfrac{2\delta_4\psi_f}{\{[1 - \max\limits_{i=1,\cdots,m}(\delta_{i1})]^2 - \delta_4^2\}\Phi}$,

$$c_2 > \frac{2\delta_4^2}{\{[1 - \max\limits_{i=1,\cdots,m}(\delta_{i1})]^2 - \delta_4^2\}\Phi}.$$

(5) Choose the controller gains $k_i, \sigma_{f_i}$, for each subsystem such that they are within the range indicated by (78)-(79).

(6) Choose $\sigma_{b_i}$ in the adaptive law (48b) of each subsystem such that $\sigma_{b_i} \geq \max(\delta_{i2}, \delta_{i3}, \delta_{i5})$.

Remark: The σ-modification term $\rho_i \Gamma_{b_{ii}} \sigma_{b_{ii}} \operatorname{sign}(b_{ii}) \left( \frac{S_\Phi}{S_\Phi + \Phi} |S_i \| u_i| + \frac{S_\Phi}{S_\Phi + \Phi} |S_i \| u_i'| + S_\Phi |u_i| \right) \zeta_{b_{ii}}$ has been incorporated in the adaptive law of each subsystem to ensure stability and robustness. In $\dot{V}(t)$ the modeling error term, $\{d_{b_i}(\boldsymbol{x})u_i - \delta_{b_i}u_i'\}$, appears because of the design parameter $\delta_{b_i}$ and the approximation error $d_{b_i}(\boldsymbol{x})$. The modeling error term, $\boldsymbol{S}^T \Delta \boldsymbol{B}(\boldsymbol{x})\boldsymbol{u}$, appears because of the interconnection of the subsystems. These two terms may become dominant in the case where $\hat{b}_{ii}^a(\boldsymbol{x})$ approaches zero. This implies the signals in the closed loop system may become unbounded when $\hat{b}_{ii}^a(\boldsymbol{x}) \to 0$. The σ-modification in the adaptive law of each subsystem is activated to guarantee stability when the estimate $\hat{b}_{ii}^a(\boldsymbol{x})$ becomes smaller than the lower bound of $b_{ii}^a(\boldsymbol{x})$. In fact, it guarantees the convergence of the tracking error even if $\hat{b}_{ii}^a(\boldsymbol{x})$ approaches zero since it appears as a negative term in the derivative of the Lyapunov-like function to cancel the effect of the modeling errors, $\{d_{b_i}(\boldsymbol{x})u_i - \delta_{b_i}u_i'\}$ and $\boldsymbol{S}^T \Delta \boldsymbol{B}(\boldsymbol{x})\boldsymbol{u}$. Therefore, this special σ-modification ensures robustness whereas the classical σ-modification is used to avoid the estimates of the parameters to drift to infinity (Ioannou and Sun 1996).

## 5. EXAMPLES

In this section, we demonstrate the properties of the proposed decentralized-like adaptive controller using an example. Consider the following MIMO nonlinear system:

$\delta_{11} = 0.094$, $\delta_{12} = 0.11$, $\delta_{13} = 0.081$, $\delta_{14} = 0.34$, $\delta_{15} = 0.32$, $\delta_{21} = 0.13$, $\delta_{22} = 0.11$, $\delta_{23} = 0.11$, $\delta_{24} = 0.35$, $\delta_{25} = 0.33$ are obtained. Then constants, $c_1 = 43.4$, $c_2 = 47.8$, are selected to satisfy

$$(c_1 = 43.4) > \frac{2\delta_4\psi_f}{\{[1-\max(\delta_{11},\delta_{21})]^2 - \delta_4^2\}\Phi} = 42.4$$
$$(c_2 = 47.8) > \frac{2\delta_4^2}{\{[1-\max(\delta_{11},\delta_{21})]^2 - \delta_4^2\}\Phi} = 46.8 \tag{97}$$

Substituting $c_1, c_2$ into (78)-(79), the design parameters $k_1, k_2, \sigma_{f_1}, \sigma_{f_2}$, need to satisfy

$$55.7 < k_1 < 108\ ;\ 68.5 < k_2 < 87.8$$
$$61.3 < \sigma_{f_1} < 118.4\ ;\ 75.7 < \sigma_{f_2} < 95.9 \tag{98}$$

Therefore following (98), $k_1 = 60, k_2 = 70, \sigma_{f_1} = 65, \sigma_{f_2} = 80$ are chosen. Finally $\sigma_{b_1} = 0.33$, $\sigma_{b_2} = 0.34$ are taken to satisfy conditions:

$$(\sigma_{b_1} = 0.33) \geq \max(\delta_{12}, \delta_{13}, \delta_{15}) = 0.32$$
$$(\sigma_{b_2} = 0.34) \geq \max(\delta_{22}, \delta_{23}, \delta_{25}) = 0.33 \tag{99}$$

In simulation, all initial conditions are taken as zero. The simulation results demonstrate that the desired upper bounds of the tracking errors in two subsystems are satisfied as shown in Figure 1 and 2. Figure 3 shows the action of the switching functions $\rho_1(t), \rho_2(t)$. The simulation also shows that the closed loop system becomes unstable if $\rho_1(t), \rho_2(t)$ are turned off.

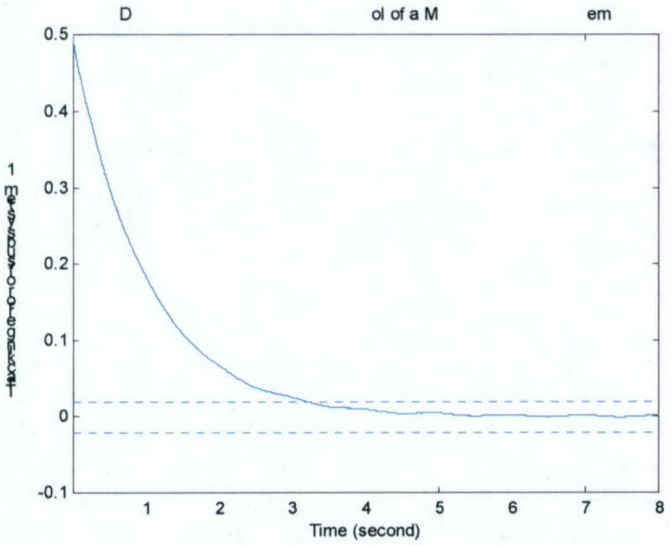


Figure 1: The tracking error of subsystem 1 during the first 8 seconds.

The dotted line indicates the required error bounds ±0.002.

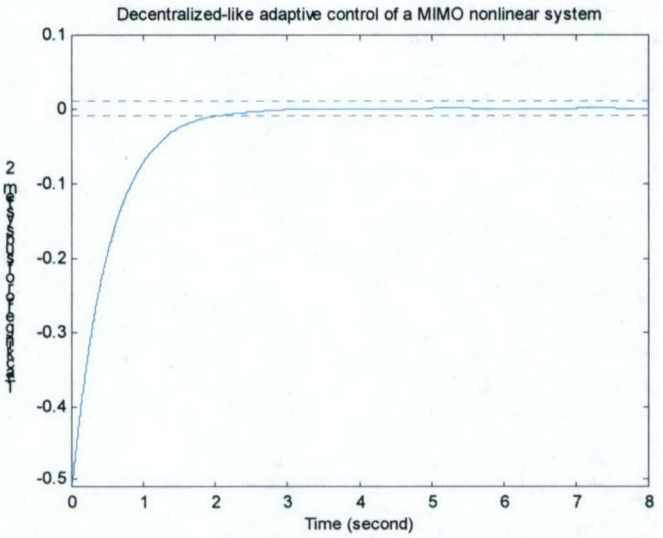


Figure 2: The tracking error of the subsystem 2 during the first 8 seconds. The dotted lines indicate the required error bounds ±0.01.

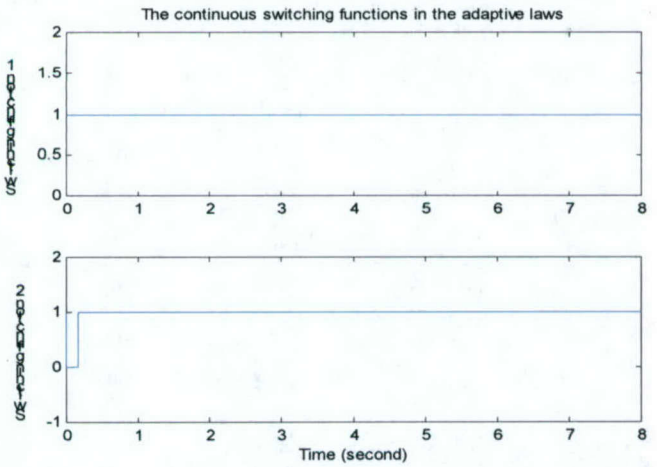


Figure 3: The continuous switching functions $\rho_1(t)$ and $\rho_2(t)$ during the first 8 seconds.

## 6. CONCLUSION

In this paper, we consider the control problem of a class of large scale nonlinear systems with unknown nonlinearities. The nonlinearities are assumed to be continuous functions and as such can be approximated and estimated on-line using a single layer neural network. A decentralized-like adaptive control scheme that bypasses the stabilizability problem for unknown MIMO systems is designed and analyzed. The controller guarantees closed loop semi-global stability and convergence of the tracking error to a small residual set even in the case where the estimated plant loses controllability. The semi-global stability is characterized by a region of attraction for stability whose size depends on the compact set used to approximate

the nonlinear functions of the plant. The size of the residual set for the tracking error at steady state depends solely on design parameters, which can be chosen to meet desired upper bounds for the tracking error. Consequently the proposed methodology provides a design parameter procedure to meet *a priori* specified performance guarantees for the steady state tracking error. Even though the proposed controller is not purely decentralized it does reduce computations and makes the control design easier to implement than a corresponding centralized approach. The problem of designing a purely decentralized controller for this class of nonlinear systems is a topic for future research. In addition relaxing the assumption of knowing the full state of the plant is another topic of research which is also present in the case of centralized control of nonlinear systems.

## REFERENCES


Chen, F.-C., and Khalil, H. K., 1992, Adaptive control of nonlinear systems using neural networks. *Int. J. Control*, **55**, 1299-1317.

Chen, F.-C., and Liu, C.-C., 1994, Adaptively controlling nonlinear continuous-time systems using multilayer neural networks. *IEEE Trans. Automat. Contr.*, **39**, 1306-1310.

Da, F., 2000, Decentralized sliding mode adaptive controller design based on fuzzy neural networks for interconnected uncertain nonlinear systems. *IEEE Trans. Neural Networks*, **11**, 1471-1480.

Datta, A., and Ioannou, P. A., 1991, Decentralized indirect adaptive control of interconnected systems. *Int. J. Adaptive Contr. Signal Processing*, **5**, 259-281.

Fernandez R., B., and Hedrick, J. K., 1987, Control of multivariable non-linear systems by the sliding model. *Int. J. Control*, **46**, 1019-1040.

Funahashi, K., 1989, On the approximate realization of continuous mappings by neural networks. *Neural Networks*, **2**, 183-192.

Godbole, D. N., and Sastry, S. S., 1995, Approximate decoupling and asymptotic tracking for MIMO systems. *IEEE Trans. Automat. Contr.*, **40**, 441-450.

Ioannou, P. A., 1986, Decentralized adaptive control of interconnected systems. *IEEE Trans. Automat. Contr.*, **AC-31**, 291-298.

Ioannou, P. A., and Sun, J., 1996, *Robust Adaptive Control* (Upper Saddle River, NJ: Prentice Hall).

Jain, S., and Khorrami, F., 1997, Decentralized adaptive output feedback design for large-scale nonlinear systems. *IEEE Trans. Automatic Contr.*, **42**, 729-735.

Jiang, Z.-P., 2000, Decentralized and adaptive nonlinear tracking of large-scale systems via output feedback. **45**, 2122-2128.

Johansen, T. A., 1994, Fuzzy model based control: stability, robustness, and performance issues. *IEEE Trans. Fuzzy Systems*, **2**, 221-234.

Kanellakopoulos, I., Kokotovic, P. V., and Morse, A. S., 1991, Systematic design of adaptive controllers for feedback linearizable systems. *IEEE Trans. Automatic. Contr.*, **36**, 1241-1253.

Khalil, H. K., 1996, Adaptive output feedback control of nonlinear systems represented by input-output models. *IEEE Trans. Automat. Contr.*, **41**, 177-188.

Khalil, H. K., 1996, *Nonlinear Systems* (Upper Saddle River, NJ: Prentice Hall).

Kojic, A., and Annaswamy, A. M., 2002, Adaptive control of nonlinearly parameterized systems with a triangular structure. *Automatica*, **38**, 115-123.

Kokotovic, P., and Arcak, M., 2001, Constructive nonlinear control: a historical perspective. *Automatica*, **37**, 637-662.

Kosmatopoulos, E. B., Polycarpou, M., Christodoulou, M., and Ioannou, P. A., 1995, High-order neural network structures for identification of dynamical systems. *IEEE Trans. Neural Networks*, **6**, 422-431.

Kosmatopoulos, E. B., and Ioannou, P. A., 1999, A switch adaptive controller for feedback linearizable systems. *IEEE Trans. Automat. Contr.*, **44**, 742-750.

Krstic, M., Kanellakopoulos, I., and Kokotovic, P., 1995, *Nonlinear and Adaptive Control Design* (New York: Wiley Interscience).

Liu, C.-C., and Chen, F.-C., 1993, Adaptive control of nonlinear continuous-time systems using neural networks – general relative degree and MIMO cases. *Int. J. Control*, **58**, 317-335.

Liu, Y., and Li, X., 2002, Decentralized robust adaptive control of nonlinear systems with unmodeled dynamics. *IEEE Trans. Automat. Contr.*, **47**, 848-856.

Ordonez, R., and Passino, K. M., 1999, Stable multi-input multi-output adaptive fuzzy/neural control. *IEEE Trans. Fuzzy Systems*, **7**, 345-353.

Park, J., and Sandberg, I. W., 1993, Approximation and radial-basis-function networks. *Neural Computation*, **5**, 305-316.

Polycarpou, M. M., 1996, Stable adaptive neural control scheme for nonlinear systems. *IEEE Trans. Automat. Contr.*, **41**, 447-451.

Polycarpou, M. M., and Ioannou, P. A., 1993, On the existence and uniqueness of solutions in adaptive control systems. *IEEE Trans. Automat. Contr.*, **38**, 474-479.

Polycarpou, M. M., and Ioannou, P. A., 1992, Modeling, identification and stable adaptive control of continuous-time nonlinear dynamical systems using neural networks. *Proc. 1992 Amer. Contr. Conf.*, 36-40.

Rovithakis, G. A., 2001, Stable adaptive neuro-control design via Lyapunov function derivative estimation. *Automatica*, **37**, 1213-1221.

Sanner, R., and Slotine, J.-J. E., 1992, Gaussian networks for direct adaptive control. *IEEE Trans. Neural Networks*, **3**, 837-863.

Sastry, S. S., and Isidori, A., 1989, Adaptive control of linearizable systems. *IEEE Trans. Automat. Contr.*, **34**, 1123-1131.

Seshagiri, S., and Khalil, H., 2000, Output feedback control of nonlinear systems using RBF neural networks. *IEEE Trans. Automat. Contr.*, **11**, 69-79.

Seto, D., Annaswamy, A. M., and Baillieul, J., 1994, Adaptive control of nonlinear systems with a triangular structure. *IEEE Trans. Automat. Contr.*, **39**, 1411-1428.

Siljak, D. D., 1991, *Decentralized Control of Complex Systems* (New York: Academic).

Slotine, J.-J. E., and Coetsee, J. A., 1986, Adaptive sliding controller synthesis for non-linear systems. *Int. J. Control*, **43**, 1631-1651.

Slotine, J.-J. E., and Li, W., 1991, *Applied Nonlinear Control* (Englewood Cliffs, NJ: Prentice Hall).

Spooner, J. T., and Passino, K. M., 1999, Decentralized adaptive control of nonlinear systems using radial basis neural networks. *IEEE Trans. Automat. Contr.*, **44**, 2050-2057.

Spooner, J. T., and Passino, K. M., 1996, Stable adaptive control using fuzzy systems and neural networks. *IEEE Trans. Neural Networks*, **4**, 339-359.

Taylor, D. G., Kokotovic, P. V., Marino, R., and Kanellakopoulos, I., 1989, Adaptive regulation of nonlinear systems with unmodeled dynamics. *IEEE Trans. Automat. Contr.*, **34**, 405-412.

Yesildirek, A., and Lewis, F. L., 1995, Feedback linearization using neural networks. *Automatica*, **31**, 1659-1664.

## APPENDIX – Proof of Lemma 3

In this appendix, we prove Lemma 3 used in the proof of Theorem 2. The proof process consists of two parts: proof of the inequality (55) and proof of the inequality (56).

**A. Proof of the inequality (55)**

Let us start with the following equation:

$$d_{b_i}(\boldsymbol{x})u_i - \delta_{b_i}u_i' = \rho_i(t)\{d_{b_i}(\boldsymbol{x})u_i - \delta_{b_i}u_i'\} + (1-\rho_i(t))\{d_{b_i}(\boldsymbol{x})u_i - \delta_{b_i}u_i'\} \tag{A.1}$$

From (60), we have

$$\hat{b}_{ii}^a(\boldsymbol{x},t)u_i = \frac{(\hat{b}_{ii}^a(\boldsymbol{x},t))^2}{(\hat{b}_{ii}^a(\boldsymbol{x},t))^2 + \delta_{b_i}}\overline{u}_i \tag{A.2}$$

Substituting $\hat{b}_{ii}^a(\boldsymbol{x},t) = b_{ii}^a(\boldsymbol{x}) + \tilde{b}_{ii}^a(\boldsymbol{x},t)$ into (A.2) gives that

$$b_{ii}^a(\boldsymbol{x})u_i = \frac{(\hat{b}_{ii}^a(\boldsymbol{x},t))^2}{(\hat{b}_{ii}^a(\boldsymbol{x},t))^2 + \delta_{b_i}}\overline{u}_i - \tilde{b}_{ii}^a(\boldsymbol{x},t)u_i \tag{A.3}$$

Therefore, the control input $u_i$ at each subsystem can be written as:

$$u_i = \left\{\frac{(\hat{b}_{ii}^a(\boldsymbol{x},t))^2}{(\hat{b}_{ii}^a(\boldsymbol{x},t))^2 + \delta_{b_i}}\right\}\frac{1}{b_{ii}^a(\boldsymbol{x})}\overline{u}_i - \frac{1}{b_{ii}^a(\boldsymbol{x})}\tilde{b}_{ii}^a(\boldsymbol{x},t)u_i \tag{A.5}$$

From (A.5) we have,

$$|u_i| \le \frac{1}{|b_{ii}^a(\boldsymbol{x})|}\{|\overline{u}_i| + |\tilde{b}_{ii}^a(\boldsymbol{x},t)||u_i|\} \tag{A.6}$$

Using the fact $|b_{ii}^a(\boldsymbol{x})| = |1 - d_{b_i}(\boldsymbol{x})/b_{ii}(\boldsymbol{x})||b_{ii}(\boldsymbol{x})| \ge (1-\psi_{b_i})|b_{ii}(\boldsymbol{x})|$, it follows that

$$|u_i| \le \frac{1}{|b_{ii}(\boldsymbol{x})|}\left\{\frac{1}{1-\psi_{b_i}-\Delta_i}|\overline{u}_i| + \frac{1}{1-\psi_{b_i}}|\tilde{b}_{ii}^a(\boldsymbol{x},t)||u_i|\right\} \tag{A.7}$$

Applying (61), the scalar function $u_i'$ in (49) can be written as:

$$u_i' = \frac{1}{(\hat{b}_{ii}^a(\boldsymbol{x},t))^2 + \delta_{b_i}} \overline{u}_i \tag{A.8}$$

Then we have

$$\{[b_{ii}^a(\boldsymbol{x}) + \tilde{b}_{ii}^a(\boldsymbol{x},t)]^2 + \delta_{b_i}\} u_i' = \overline{u}_i \tag{A.9}$$

and

$$\{(b_{ii}^a(\boldsymbol{x}))^2 + (\tilde{b}_{ii}^a(\boldsymbol{x},t))^2 + \delta_{b_i}\} u_i' = \overline{u}_i - 2b_{ii}^a(\boldsymbol{x})\tilde{b}_{ii}^a(\boldsymbol{x},t)u_i' \tag{A.10}$$

From (A.10), $u_i'$ can be expressed as

$$u_i' = \frac{1}{(b_{ii}^a(\boldsymbol{x}))^2 + (\tilde{b}_{ii}^a(\boldsymbol{x},t))^2 + \delta_{b_i}} \overline{u}_i - \frac{2b_{ii}^a(\boldsymbol{x})}{(b_{ii}^a(\boldsymbol{x}))^2 + (\tilde{b}_{ii}^a(\boldsymbol{x},t))^2 + \delta_{b_i}} \tilde{b}_{ii}^a(\boldsymbol{x},t)u_i' \tag{A.11}$$

Therefore, we have

$$\begin{aligned} |u_i'| &\le \frac{1}{(b_{ii}^a(\boldsymbol{x}))^2 + \delta_{b_i}} |\overline{u}_i| + \frac{2|b_{ii}^a(\boldsymbol{x})|}{(b_{ii}^a(\boldsymbol{x}))^2 + \delta_{b_i}} |\tilde{b}_{ii}^a(\boldsymbol{x},t)||u_i'| \\ &\le \frac{1}{(b_{ii}^a(\boldsymbol{x}))^2 + \delta_{b_i}} |\overline{u}_i| + \frac{2}{|b_{ii}^a(\boldsymbol{x})|} |\tilde{b}_{ii}^a(\boldsymbol{x},t)||u_i'| \\ &\le \frac{1}{(1-\psi_{b_i})^2 b_{ii}^2(\boldsymbol{x}) + \delta_{b_i}} |\overline{u}_i| + \frac{2}{(1-\psi_{b_i})|b_{ii}(\boldsymbol{x})|} |\tilde{b}_{ii}^a(\boldsymbol{x},t)||u_i'| \end{aligned} \tag{A.12}$$

Using (A.7), (A.12), the first term at the right side of (A.1) can be rewritten as

$$\begin{aligned} |\rho_i(t)\{d_{b_i}(\boldsymbol{x})u_i - \delta_{b_i}u_i'\}| &\le \rho_i(t)\left\{\frac{|d_{b_i}(\boldsymbol{x})/b_{ii}(\boldsymbol{x})|}{1-\psi_{b_i}-\Delta_i} + \frac{\delta_{b_i}}{(1-\psi_{b_i})^2 b_{ii}^2(\boldsymbol{x}) + \delta_{b_i}}\right\}|\overline{u}| \\ &+ \rho_i(t)\frac{|d_{b_i}(\boldsymbol{x})/b_{ii}(\boldsymbol{x})|}{1-\psi_{b_i}} |\tilde{b}_{ii}^a(\boldsymbol{x},t)||u_i| + \rho_i(t)\frac{2\delta_{b_i}}{(1-\psi_{b_i})|b_{ii}(\boldsymbol{x})|} |\tilde{b}_{ii}^a(\boldsymbol{x},t)||u_i'| \end{aligned} \tag{A.13}$$

Since $|d_{b_i}(\boldsymbol{x})/b_{ii}(\boldsymbol{x})| \le \psi_{b_i}$ and $|b_{ii}(\boldsymbol{x})| \ge g_i^*$, we have

$$\begin{aligned} |\rho_i(t)\{d_{b_i}(\boldsymbol{x})u_i - \delta_{b_i}u_i'\}| &\le \rho_i(t)\left\{\frac{\psi_{b_i}}{1-\psi_{b_i}-\Delta_i} + \frac{\delta_{b_i}}{[(1-\psi_{b_i})g_i^*]^2 + \delta_{b_i}}\right\}|\overline{u}| \\ &+ \rho_i(t)\frac{\psi_{b_i}}{1-\psi_{b_i}} |\tilde{b}_{ii}^a(\boldsymbol{x},t)||u_i| + \rho_i(t)\frac{2\delta_{b_i}}{(1-\psi_{b_i})g_i^*} |\tilde{b}_{ii}^a(\boldsymbol{x},t)||u_i'| \end{aligned} \tag{A.14}$$

For $|\hat{b}_{ii}^a(\boldsymbol{x},t)| > 0$, we have

$$|u_i| = \frac{\left|\hat{b}_{ii}^a(x,t)\right|}{(\hat{b}_{ii}^a(x,t))^2 + \delta_{b_i}}|\overline{u}_i| \le \frac{1}{\left|\hat{b}_{ii}^a(x,t)\right|}|\overline{u}_i| \tag{A.15}$$

Using (A.15) together with the fact $(1-\rho_i(t)) \neq 0$ only if $\left|\hat{b}_{ii}^a(x,t)\right| > (1-\psi_{b_i}-\Delta_i)g_i(x)$, the second term at the right side of (A.1) can be described as

$$\begin{aligned}\left|(1-\rho_i(t)\{d_{b_i}(x)u_i - \delta_{b_i}u_i'\}\right| &\le (1-\rho_i(t))\frac{\left|d_{b_i}(x)\right|}{\left|\hat{b}_{ii}^a(x,t)\right|}|\overline{u}_i| + (1-\rho_i(t))\frac{\delta_{b_i}}{(\hat{b}_{ii}^a(x,t))^2 + \delta_{b_i}}|\overline{u}_i| \\ &\le (1-\rho_i(t))\left\{\frac{\left|d_{b_i}(x)\right|/g_i(x)}{1-\psi_{b_i}-\Delta_i} + \frac{\delta_{b_i}}{(1-\psi_{b_i}-\Delta_i)^2 g_i^2(x) + \delta_{b_i}}\right\}|\overline{u}_i|\end{aligned} \tag{A.16}$$

Using $\left|d_{b_i}(x)\right|/g_i(x) \le \psi_{b_i}$ and $g_i(x) \ge g_i^*$,

$$\left|(1-\rho_i(t)\{d_{b_i}(x)u_i - \delta_{b_i}u_i'\}\right| \le (1-\rho_i(t))\left\{\frac{\psi_{b_i}}{1-\psi_{b_i}-\Delta_i} + \frac{\delta_{b_i}}{[(1-\psi_{b_i}-\Delta_i)g_i^*]^2 + \delta_{b_i}}\right\}|\overline{u}_i| \tag{A.17}$$

Combining the results of (A.14) and (A.17), it follows that:

$$\begin{aligned}\left|d_{b_i}(x)u_i - \delta_{b_i}u_i'\right| &\le \left\{\frac{\psi_{b_i}}{1-\psi_{b_i}-\Delta_i} + \frac{\delta_{b_i}}{[(1-\psi_{b_i}-\Delta_i)g_i^*]^2 + \delta_{b_i}}\right\}|\overline{u}_i| \\ &\quad + \rho_i(t)\frac{\psi_{b_i}}{1-\psi_{b_i}}\left|\tilde{b}_{ii}^a(x,t)\right\|u_i| + \rho_i(t)\frac{2\delta_{b_i}}{(1-\psi_{b_i})g_i^*}\left|\tilde{b}_{ii}^a(x,t)\right\|u_i'| \\ &= \delta_{i1}|\overline{u}_i| + \rho_i(t)\delta_{i2}\left|\tilde{b}_{ii}^a(x,t)\right\|u_i| + \rho_i(t)\delta_{i3}\left|\tilde{b}_{ii}^a(x,t)\right\|u_i'|\end{aligned} \tag{A.18}$$

where $\delta_{i1}, \delta_{i2}, \delta_{i3}$, are defined in (54a-c). Using

$$|\overline{u}_i| \le k_i|S_i| + \left|\hat{f}_i^a(x,t) + v_i(t)\right| + \sigma_{f_i}\left\|\hat{\boldsymbol{f}}^a(x,t) + \boldsymbol{v}(t)\right\|S_i| \tag{A.19}$$

Yields

$$\left|d_{b_i}(x)u_i - \delta_{b_i}u_i'\right| \le \delta_{i1}|\overline{u}_i| + \rho_i(t)\delta_{i2}\left|\tilde{b}_{ii}^a(x,t)\right\|u_i| + \rho_i(t)\delta_{i3}\left|\tilde{b}_{ii}^a(x,t)\right\|u_i'| \tag{A.20}$$

**Proof of the inequality (56)**

From (A.6)

$$\rho_i(t)|u_i| \le \rho_i(t)\frac{1}{g_i(x)}\left\{\frac{1}{1-\psi_{b_i}-\Delta_i}|\overline{u}_i| + \frac{1}{1-\psi_{b_i}}\left|\tilde{b}_{ii}^a(x,t)\right\|u_i|\right\} \tag{A.21}$$

Using the fact $(1-\rho_i) \neq 0$ only if $\left|\hat{b}_{ii}^a(x,t)\right| > (1-\psi_{b_i}-\Delta_i)g_i(x)$, we have

$$(1-\rho_i(t))|u_i| \le (1-\rho_i(t))\frac{1}{g_i(\boldsymbol{x})}\left\{\frac{1}{1-\psi_{b_i}-\Delta_i}|\overline{u}_i|\right\} \tag{A.22}$$

Combining (A.21) and (A.22), it follows that

$$|u_i| \le \frac{1}{g_i(\boldsymbol{x})}\left\{\frac{1}{1-\psi_{b_i}-\Delta_i}|\overline{u}_i| + \rho_i(t)\frac{1}{1-\psi_{b_i}}|\tilde{b}_{ii}^a(\boldsymbol{x},t)||u_i|\right\} \tag{A.23}$$

Using (A.23), we have

$$\begin{aligned}
|\boldsymbol{S}^T\Delta\boldsymbol{B}(\boldsymbol{x})\boldsymbol{u}| \le \|\boldsymbol{S}\|\|\Delta\boldsymbol{B}(\boldsymbol{x})\boldsymbol{u}\| &\le \|\boldsymbol{S}\|\sum_{i=1}^m\|\Delta\boldsymbol{B}(:,i)\||u_i| \\
&\le \|\boldsymbol{S}\|\delta_0\sum_{i=1}^m\left\{\frac{1}{1-\psi_{b_i}-\Delta_i}|\overline{u}_i| + \rho_i(t)\frac{1}{1-\psi_{b_i}}|\tilde{b}_{ii}^a(\boldsymbol{x},t)||u_i|\right\} \\
&\le \|\boldsymbol{S}\|\sum_{i=1}^m\delta_{i4}|\overline{u}_i| + \|\boldsymbol{S}\|\sum_{i=1}^m\rho_i(t)\delta_{i5}|\tilde{b}_{ii}^a(\boldsymbol{x},t)||u_i|
\end{aligned} \tag{A.24}$$

where $\delta_{i4}$, $\delta_{i5}$, are defined in (54d-e). Applying (A.19) in (A.24) yields

$$\begin{aligned}
\|\boldsymbol{S}\|\sum_{i=1}^m\delta_{i4}|\overline{u}_i| &\le \|\boldsymbol{S}\|\sum_{i=1}^m\delta_{i4}k_i|S_i| + \|\boldsymbol{S}\|\sum_{i=1}^m\delta_{i4}|\hat{f}_i^a(\boldsymbol{x},t)+v_i(t)| + \|\boldsymbol{S}\|\|\hat{\boldsymbol{f}}^a(\boldsymbol{x},t)+\boldsymbol{v}(t)\|\left(\sum_{i=1}^m\delta_{i4}\sigma_{f_i}|S_i|\right) \\
&\le \delta_4\|\boldsymbol{S}\|\|\boldsymbol{K}\boldsymbol{S}\| + \delta_4\|\hat{\boldsymbol{f}}^a(\boldsymbol{x},t)+\boldsymbol{v}(t)\|\|\boldsymbol{\sigma}_f\boldsymbol{S}\|\|\boldsymbol{S}\| + \delta_4\|\boldsymbol{S}\|\|\hat{\boldsymbol{f}}^a(\boldsymbol{x},t)+\boldsymbol{v}(t)\| \\
&\le \sum_{i=1}^m\delta_4\left(\frac{c_1}{2}+\frac{1}{2c_1}k_i^2\right)S_i^2(t) + \|\hat{\boldsymbol{f}}^a(\boldsymbol{x},t)+\boldsymbol{v}(t)\|\sum_{i=1}^m\delta_4\left(\frac{c_2}{2}+\frac{1}{2c_2}\sigma_{f_i}^2\right)S_i^2(t) + \delta_4\|\hat{\boldsymbol{f}}^a(\boldsymbol{x},t)+\boldsymbol{v}(t)\|\|\boldsymbol{S}\|
\end{aligned} \tag{A.25}$$

where $\delta_4 = \sqrt{\delta_{14}^2+\cdots+\delta_{m4}^2}$, and $c_1$, $c_2$, are some positive constants. By substituting (A.25) into (A.24), (56) follows.

JOURNAL OF GUIDANCE, CONTROL, AND DYNAMICS
Vol. 27, No. 5, September–October 2004

# Adaptive Sliding Mode Control Design for a Hypersonic Flight Vehicle

Haojian Xu
*University of Southern California, Los Angeles, California 90089*
Maj D. Mirmirani
*California State University, Los Angeles, California 90032*
and
Petros A. Ioannou
*University of Southern California, Los Angeles, California 90089*

**A multi-input/multi-output adaptive sliding controller is designed and analyzed for the longitudinal dynamics of a generic hypersonic air vehicle. This vehicle model is nonlinear, multivariable, and unstable and includes uncertain parameters. Simulation studies are conducted for trimmed cruise conditions of 110,000 ft and Mach 15 where the responses of the vehicle to a step change in altitude and airspeed are evaluated. The commands are 100-ft/s step velocity and 2000-ft step altitude. The controller is evaluated for robustness with respect to parameter uncertainties using simulations. Simulation studies demonstrate that the proposed controller is robust with respect to parametric uncertainty and meets the performance requirements with relatively low-amplitude control inputs.**

## Nomenclature

$a$ = combined uncertainty parameter, ft · s$^2$
$b$ = combined uncertainty parameter, ft$^3$/s
$C_D$ = drag coefficient
$C_L$ = lift coefficient
$C_M(q)$ = moment coefficient due to pitch rate
$C_M(\alpha)$ = moment coefficient due to angle of attack
$C_M(\delta_e)$ = moment coefficient due to elevator deflection

**Haojian Xu received his B.S. degree from Nanjing University of Aeronautics and Astronautics, the People's Republic of China, in 1990 and M.S. and Ph.D. degrees in electrical engineering from the University of Southern California, Los Angeles, California, in 1999 and 2002, respectively. From 1990 to 1997, he worked as an engineer at the Beijing Aerospace Automatic Control Institute, China Academy of Launch Vehicle Technology. He is currently working as a postdoctoral research associate in the Department of Electrical Engineering, University of Southern California. He has served as a reviewer for various journals and conferences. His current research interests include robust adaptive control, nonlinear system control with application to high-performance aircraft, control of unknown systems using neural networks, and system identification and control of hard disk drive systems. Member AIAA. He may be contacted at haojian@usc.edu.**

**Maj Dean Mirmirani received his B.S. degree from Tehran Polytechnic in 1969, and M.S. and Ph.D. degrees in mechanical engineering from the University of California, Berkeley, in 1971 and 1976, respectively. Before joining the Department of Mechanical Engineering at California State University, Los Angeles, in 1981, he was an academic visitor for one year at the Department of Electrical Engineering, Imperial College of Science and Technology, London. Currently he is a professor and Chairman of the Mechanical Engineering Department and Director of the Multidisciplinary Flight Dynamics and Control Laboratory at California State University, Los Angeles, which is funded by NASA Dryden Flight Research Center and the Air Force Office of Scientific Research. His research interests are in the areas of multidisciplinary modeling and analysis of flight vehicles, control of hypersonic airbreathing flight vehicles, and aeroservoelasticity. M. D. Mirmirani is the recipient of the 2002–2003 California State University Los Angeles Outstanding Professor Award and a member of AIAA. His e-mail address is mmirmir@exchange.calstatela.edu.**

**Petros A. Ioannou received his B.Sc. degree with first class honors from University College, London, England, in 1978 and the M.S. and Ph.D. degrees from the University of Illinois, Urbana, Illinois, in 1980 and 1982, respectively. In 1982, he joined the Department of Electrical Engineering Systems, University of Southern California, Los Angeles, California. He is currently a professor in the same department and Director of the Center of Advanced Transportation Technologies. His research interests are in the areas of adaptive control, neural networks, nonlinear systems, vehicle dynamics and control, intelligent transportation systems, and marine transportation. He was Visiting Professor at the University of Newcastle, Australia in the fall of 1988, the Technical University of Crete in summer of 1992, and served as Dean of the School of Pure and Applied Science at the University of Cyprus in 1995. In 1984 he was a recipient of the Outstanding IEEE Transactions Paper Award and the recipient of 1985 Presidential Young Investigator Award. He is the author/coauthor of 5 books and more than 150 research papers in the area of controls, neural networks, nonlinear dynamical systems, and intelligent transportation systems. His e-mail address is ioannou@usc.edu.**

Presented as Paper AAS 01-240 at the AAS/AIAA 11th Space Flight Mechanics Meeting, Santa Barbara, February 2001; received 19 February 2002; revision received 15 August 2003; accepted for publication 5 January 2004. 

$C_T$ = thrust coefficient
$\bar{c}$ = mean aerodynamic chord, ft
$D$ = drag, lbf
$h$ = altitude, ft
$I_{yy}$ = moment of inertia, slug · ft$^2$
$k_h, k_q$ = observer sliding gains, 1/s
$k_1, k_2$ = controller sliding gains, 1/s
$k_\alpha$ = observer sliding gain
$k_\gamma$ = observer sliding gain, rad/ft · s
$L$ = lift, lbf
$M$ = Mach number
$M_{yy}$ = pitching moment, lbf · ft
$m$ = mass, slug
$q$ = pitch rate, rad/s
$R_E$ = radius of the Earth, ft
$r$ = radial distance from Earth's center, ft
$S$ = reference area, ft$^2$
$T$ = thrust, lbf
$V$ = velocity, ft/s
$\alpha$ = angle of attack, rad
$\beta$ = throttle setting
$\gamma$ = flight-path angle, rad
$\delta_e$ = elevator deflection, rad
$\eta_1, \eta_2$ = observer damping coefficients, 1/s
$\eta_3$ = observer damping coefficient, rad/ft · s
$\eta_4$ = observer damping coefficient
$\lambda_1, \lambda_2$ = bandwidth of tracking error dynamics, 1/s
$\mu$ = gravitational constant
$\rho$ = density of air, slug/ft$^3$
$\Phi_1, \Phi_2$ = boundary-layer widths, ft/s$^3$

## Introduction

HYPERSONIC air vehicles are sensitive to changes in flight condition as well as physical and aerodynamic parameters due to their design and flight conditions of high altitudes and Mach numbers. For example, at cruise flight at altitude of 110,000 ft and Mach 15, a 1-deg increase in angle of attack produces a load factor of about 0.33 $g$. Furthermore, it is difficult to measure or estimate the atmospheric properties and aerodynamic characteristics at the hypersonic flight altitude. As a result, modeling inaccuracies can result and can have strong adverse effects on the performance of air vehicle's control systems. Therefore, robust control has been the main technique used for hypersonic flight control.[1,2]

The sliding mode control method provides a systematic approach to the problem of maintaining stability and consistent performance in the face of modeling imprecision. The main advantage of sliding mode control is that the system's response remains insensitive to model uncertainties and disturbances.[3,4] The most completely developed area of sliding mode control is for single-input/single-output systems (SISO).[3] In Ref. 4, SISO sliding mode control is extended to a class of nonlinear multi-input/multi-output (MIMO) systems. Although the technique has good robustness properties, pure sliding mode control presents drawbacks that include large control authority requirements and chattering. The performance of pure sliding mode control can be improved by coupling it with an online parameter estimation scheme.[5] Also, a sliding mode controller can be implemented only if full state feedback is available, a requirement not readily achieved in a hypersonic flight. The design of a state observer for the unmeasurable states based on sliding modes has been proposed in Ref. 6, where it is shown that sliding mode observers have inherent robustness properties in the face of parametric uncertainty and measurement noise. An adaptive sliding mode controller combined with an observer was applied to a SISO magnetic suspension system in Ref. 7 and to a linear MIMO robotic system in Ref. 8.

In this paper, design of a MIMO adaptive controller for a hypersonic air vehicle based on the sliding mode control technique is presented. The plant is the longitudinal model of a generic hypersonic air vehicle.[1,2] This model is nonlinear, multivariable, and unstable with seven uncertain inertial and aerodynamic parameters. The open-loop dynamics of the air vehicle exhibits unstable short-period and height modes, as well as a lightly damped phugoid mode. The control design described in the following sections consists of four steps. First, full-state feedback is applied to linearize the dynamics of the air vehicle with respect to air speed $V$ and altitude $h$. Next, a pure sliding mode controller is designed. An adaptive sliding mode controller is then designed to improve performance in the presence of parametric uncertainty. In addition, a sliding mode observer is designed to estimate the angle of attack and the flight-path angle, which are difficult to measure in a hypersonic flight. [Although with global positioning system- (GPS-) aided inertial navigation it is reasonable to assume that the flight-path angle could be calculated from the rate change of altitude and velocity.] However, in this study we consider the worst case where neither the flight-path angle measurement nor its calculated value is available. Finally, the overall controller is synthesized by combining the adaptive controller with the observer. Simulation studies are conducted for trimmed cruise conditions of 110,000 ft and Mach 15 to evaluate the response of the vehicle to a step change of 2000 ft in altitude and 100 ft/s in airspeed. Parameter uncertainties are included in the inertial and aerodynamic coefficients and are allowed to take their maximum possible deviation in the simulation studies. The results demonstrate that at the trimmed flight conditions used for the simulations the combined adaptive sliding controller is robust with respect to parametric uncertainty and provides good performance with limited control authority.

## Hypersonic Air Vehicle Model

A model for the longitudinal dynamics of a generic hypersonic vehicle developed at NASA Langley Research Center is presented in Refs. 1 and 2. The equations of motion include an inverse-square-law gravitational model and the centripetal acceleration for the nonrotating Earth. The longitudinal dynamics of the air vehicle model can be described by a set of differential equations for velocity, flight-path angle, altitude, angle of attack, and pitch rate as

$$\dot{V} = \frac{T\cos\alpha - D}{m} - \frac{\mu \sin\gamma}{r^2} \tag{1}$$

$$\dot{\gamma} = \frac{L + T\sin\alpha}{mV} - \frac{(\mu - V^2 r)\cos\gamma}{Vr^2} \tag{2}$$

$$\dot{h} = V\sin\gamma \tag{3}$$

$$\dot{\alpha} = q - \dot{\gamma} \tag{4}$$

$$\dot{q} = \frac{M_{yy}}{I_{yy}} \tag{5}$$

where

$$L = \tfrac{1}{2}\rho V^2 S C_L \tag{6}$$

$$D = \tfrac{1}{2}\rho V^2 S C_D \tag{7}$$

$$T = \tfrac{1}{2}\rho V^2 S C_T \tag{8}$$

$$M_{yy} = \tfrac{1}{2}\rho V^2 S\bar{c}[C_M(\alpha) + C_M(\delta_e) + C_M(q)] \tag{9}$$

$$r = h + R_E \tag{10}$$

The engine dynamics are modeled by a second-order system:

$$\ddot{\beta} = -2\zeta\omega_n\dot{\beta} - \omega_n^2\beta + \omega_n^2\beta_c \tag{11}$$

For the purpose of this study, the aerodynamic coefficients are simplified around the nominal cruising flight. The nominal flight of the vehicle is at a trimmed cruise condition ($M = 15$, $V =$ 15,060 ft/s, $h = 110{,}000$ ft, $\gamma = 0$ deg, and $q = 0$ deg/s). Parametric uncertainty is modeled as an additive variance $\Delta$ to the nominal

values used for control design. For illustration, only limited number of uncertain parameters is considered,

$$C_L = 0.6203\alpha \tag{12}$$

$$C_D = 0.6450\alpha^2 + 0.0043378\alpha + 0.003772 \tag{13}$$

$$C_T = \begin{cases} 0.02576\beta & \text{if} \quad \beta < 1 \\ 0.0224 + 0.00336\beta & \text{if} \quad \beta > 1 \end{cases} \tag{14}$$

$$C_M(\alpha) = -0.035\alpha^2 + 0.036617(1 + \Delta C_{M\alpha})\alpha + 5.3261 \times 10^{-6} \tag{15}$$

$$C_M(q) = (\bar{c}/2V)q(-6.796\alpha^2 + 0.3015\alpha - 0.2289) \tag{16}$$

$$C_M(\delta_e) = c_e(\delta_e - \alpha) \tag{17}$$

$$m = m_0(1 + \Delta m) \tag{18}$$

$$I_{yy} = I_0(1 + \Delta I) \tag{19}$$

$$S = S_0(1 + \Delta S) \tag{20}$$

$$\bar{c} = \bar{c}_0(1 + \Delta\bar{c}) \tag{21}$$

$$\rho = \rho_0(1 + \Delta\rho) \tag{22}$$

$$c_e = 0.0292(1 + \Delta c_e) \tag{23}$$

where the nominal values are given by $m_0 = 9375$, $I_0 = 7 \times 10^6$, $S_0 = 3603$, $\bar{c}_0 = 80$, and $\rho_0 = 0.24325 \times 10^{-4}$. The maximum values of the additive uncertainties used in the simulation studies are taken as follows:

$$|\Delta m| \le 0.03, \qquad |\Delta I| \le 0.02, \qquad |\Delta S| \le 0.01$$

$$|\Delta\bar{c}| \le 0.01, \qquad |\Delta\rho| \le 0.06$$

$$|\Delta c_e| \le 0.03, \qquad |\Delta C_{M\alpha}| \le 0.1 \tag{24}$$

The control inputs are the throttle setting $\beta_c$ and the elevator deflection $\delta_e$. The outputs are the velocity $V$ and the altitude $h$. The commanded desired values of velocity and altitude are denoted by $V_d(t)$ and $h_d(t)$, respectively.

## Input/Output Linearization

The longitudinal model of the generic hypersonic air vehicle described by Eqs. (1–5) is a special case of a general MIMO nonlinear system of the form

$$\dot{\boldsymbol{x}}(t) = \boldsymbol{f}(\boldsymbol{x}) + \sum_{k=1}^{m} \boldsymbol{g}_k(\boldsymbol{x})u_k \tag{25}$$

$$y_i(t) = h_i(\boldsymbol{x}), \qquad i = 1, \ldots, m \tag{26}$$

where $\boldsymbol{f}$, $\boldsymbol{g}$, and $\boldsymbol{h}$ are sufficiently smooth functions of $\boldsymbol{x} \in \Re^n$. Input/output linearization uses full state feedback to globally linearize the nonlinear dynamics of selected controlled outputs. Following the approach in Ref. 4, each of the output channels $y_i$ is differentiated a sufficient number of times until a control input component appears in the resulting equation. Let $r_i$, the linearizability index, be the minimum order of the derivative of $y_i$ for which the coefficient of at least one $u_k$ is not zero. When the Lie derivative notation is used, this derivative can be expressed as

$$y_i^{(r_i)} = L_f^{r_i}(h_i) + \sum_{k=1}^{m} L_{g_k}\left[L_f^{r_i-1}(h_i)\right]u_k \tag{27}$$

where the Lie derivatives are defined as

$$L_f(h_i) = \frac{\partial h_i}{\partial x_1} f_1 + \cdots + \frac{\partial h_i}{\partial x_n} f_n$$

$$L_f^r(h_i) = L_f\left[L_f^{r-1}(h_i)\right], \qquad L_{g_k}(h_i) = \frac{\partial h_i(\boldsymbol{x})}{\partial \boldsymbol{x}} \boldsymbol{g}_k$$

Given that the nonlinear system is I/O linearizable, for each output $y_i$ there exists a linearizability index $r_i$. Accordingly,

$$r = \sum_{i=1}^{m} r_i$$

is called the relative degree of the nonlinear system. The necessary and sufficient condition for the existence of a transformation linearizing the system completely from the I/O point of view is that the relative degree $r$ be the same as the order of the system, $n$, that is, $r = n$. If $r < n$, however, the nonlinear system can only be partially linearized. In this case, the stability of the nonlinear system given by Eqs. (25) and (26) depends not only on the linearized system, but also on the stability of the internal dynamics (zero dynamics).

When the described technique is applied to the longitudinal model of the hypersonic vehicle, the output dynamics for velocity $V$ and altitude $h$ can be derived by differentiating $V$ three times and $h$ four times as shown later. Therefore, the relative degree of the system, $r = 3 + 4 = 7 = n$, equals to the order of the system. Thus, the nonlinear longitudinal model can be linearized completely, and the closed-loop system has no zero dynamics.[2] The linearized model is developed by repeated differentiation of $V$ and $h$ as follows:

$$\dot{V} = f_1(\boldsymbol{x}), \qquad \ddot{V} = \omega_1\dot{\boldsymbol{x}}/m, \qquad \dddot{V} = (\omega_1\ddot{\boldsymbol{x}} + \dot{\boldsymbol{x}}\Omega_2\dot{\boldsymbol{x}})/m \tag{28}$$

$$\dot{h} = \dot{V}\sin\gamma + V\dot{\gamma}\cos\gamma$$

$$\ddot{h} = \ddot{V}\sin\gamma + 2\dot{V}\dot{\gamma}\cos\gamma - V\dot{\gamma}^2\sin\gamma + V\ddot{\gamma}\cos\gamma$$

$$h^{(4)} = \dddot{V}\sin\gamma + 3\ddot{V}\dot{\gamma}\cos\gamma - 3\dot{V}\dot{\gamma}^2\sin\gamma + 3\dot{V}\ddot{\gamma}\cos\gamma - 3V\dot{\gamma}\ddot{\gamma}\sin\gamma - V\dot{\gamma}^3\cos\gamma + V\dddot{\gamma}\cos\gamma \tag{29}$$

In Eq. (29),

$$\dot{\gamma} = f_2(\boldsymbol{x}), \qquad \ddot{\gamma} = \pi_1\dot{\boldsymbol{x}}, \qquad \dddot{\gamma} = \pi_1\ddot{\boldsymbol{x}} + \dot{\boldsymbol{x}}^T\Pi_2\dot{\boldsymbol{x}} \tag{30}$$

where $\boldsymbol{x}^T = [V\ \gamma\ \alpha\ \beta\ h]$, $f_1$ and $f_2$ are the short-hand expressions of the right-hand side of Eqs. (1) and (2), respectively, and $\omega_1 = \partial f_1(\boldsymbol{x})/\partial\boldsymbol{x}$, $\Omega_2 = \partial\omega_1/\partial\boldsymbol{x}$, $\pi_1 = \partial f_2(\boldsymbol{x})/\partial\boldsymbol{x}$, and $\Pi_2 = \partial\pi_1/\partial\boldsymbol{x}$. The detailed expressions of $\omega_1$, $\Omega_2$, $\pi_1$, and $\Pi_2$ are given in the Appendix.

The right-hand sides of Eqs. (28) and (29) involve second derivatives of $\alpha$ and $\beta$. The expression of the second derivatives for $\alpha$ and $\beta$ can be viewed as consisting of two parts: a part that is control relevant and a part that is not,

$$\ddot{\alpha} = \ddot{\alpha}_0 + \left(\frac{c_e\rho V^2 S\bar{c}}{2I_{yy}}\right)\delta_e \tag{31}$$

$$\ddot{\beta} = \ddot{\beta}_0 + \omega_n^2\beta_c \tag{32}$$

where

$$\ddot{\alpha}_0 = \tfrac{1}{2}\rho V^2 S\bar{c}[C_M(\alpha) + C_M(q) - c_e\alpha]/I_{yy} - \ddot{\gamma} \tag{33}$$

$$\ddot{\beta}_0 = -2\zeta\omega_n\dot{\beta} - \omega_n^2\beta \tag{34}$$

When $\ddot{\boldsymbol{x}}_0^T = [\ddot{V}\ \dddot{\gamma}\ \ddot{\alpha}_0\ \ddot{\beta}_0\ \dddot{h}]$ is defined, the output dynamics of $V$ and $h$ can be written in a form in which control inputs $\beta_c$ and $\delta_e$ appear explicitly,

$$\ddot{V} = f_V + b_{11}\beta_c + b_{12}\delta_e \tag{35}$$

$$h^{(4)} = f_h + b_{21}\beta_c + b_{22}\delta_e \tag{36}$$

where

$$f_V = \frac{\left(\omega_1 \ddot{\boldsymbol{x}}_0 + \dot{\boldsymbol{x}}^T \Omega_2 \dot{\boldsymbol{x}}\right)}{m} \tag{37}$$

$$f_h = 3\ddot{V}\dot{\gamma}\cos\gamma - 3\dot{V}\dot{\gamma}^2\sin\gamma + 3\dot{V}\ddot{\gamma}\cos\gamma - 3V\dot{\gamma}\ddot{\gamma}\sin\gamma - V\dot{\gamma}^3\cos\gamma + \frac{\left(\omega_1 \ddot{\boldsymbol{x}}_0 + \dot{\boldsymbol{x}}^T \Omega_2 \dot{\boldsymbol{x}}\right)\sin\gamma}{m} + V\cos\gamma\left(\pi_1 \ddot{\boldsymbol{x}}_0 + \dot{\boldsymbol{x}}^T \Pi_2 \dot{\boldsymbol{x}}\right) \tag{38}$$

$$b_{11} = \left(\frac{\rho V^2 S c_\beta \omega_n^2}{2m}\right)\cos\alpha \tag{39}$$

$$b_{12} = -\left(\frac{c_e \rho V^2 S \bar{c}}{2m I_{yy}}\right)\left(T\sin\alpha + \frac{\partial D}{\partial \alpha}\right) \tag{40}$$

$$b_{21} = \left(\frac{\rho V^2 S c_\beta \omega_n^2}{2m}\right)\sin(\alpha+\gamma) \tag{41}$$

$$b_{22} = \left(\frac{c_e \rho V^2 S \bar{c}}{2m I_{yy}}\right)\left[T\cos(\alpha+\gamma) + \left(\frac{\partial L}{\partial \alpha}\right)\cos\gamma - \left(\frac{\partial D}{\partial \alpha}\right)\sin\gamma\right] \tag{42}$$

$$c_\beta = \begin{cases} 0.02576, & \beta < 1 \\ 0.00336, & \beta > 1 \end{cases} \tag{43}$$

$$\frac{\partial D}{\partial \alpha} = \frac{1}{2}\rho V^2 S(1.290\alpha + 0.0043378)$$

$$\frac{\partial L}{\partial \alpha} = \frac{1}{2}\rho V^2 S \times 0.6203$$

## Sliding Mode Controller Design

The control design problem is to select a vector $[\beta_c \ \delta_e]^T$ that forces the velocity $V$ and altitude $h$ to track some desired commanded values $V_d(t)$ and $h_d(t)$ in the presence of parametric uncertainty. When the techniques introduced in Ref. 4 are applied, first two decoupled sliding surfaces $s_1$ and $s_2$ are defined by

$$s_1 = \left(\frac{\mathrm{d}}{\mathrm{d}t} + \lambda_1\right)^3 \int_0^t e_1(\tau)\,\mathrm{d}\tau, \qquad e_1(t) = V - V_d \tag{44}$$

$$s_2 = \left(\frac{\mathrm{d}}{\mathrm{d}t} + \lambda_2\right)^4 \int_0^t e_2(\tau)\,\mathrm{d}\tau, \qquad e_2(t) = h - h_d \tag{45}$$

where $\lambda_1$ and $\lambda_2$ are strictly positive constants defining the bandwidth of the error dynamics. The sliding surfaces $s_i = 0$, $i = 1, 2$, represent linear differential equations whose solutions imply

$$\int e_i(t), \qquad i = 1, 2$$

approach to zero exponentially with the time constants $2/\lambda_1$ and $3/\lambda_2$, respectively, where the integrals of the tracking errors are used to cancel the steady-state errors.[3]

Differentiating $s_1$ and $s_2$, we have

$$\dot{s}_1 = -\dddot{V}_d + f_V + 3\lambda_1\ddot{e}_1 + 3\lambda_1^2\dot{e}_1 + \lambda_1^3 e_1 + b_{11}\beta_c + b_{12}\delta_e \tag{46}$$

$$\dot{s}_2 = -h_d^{(4)} + f_h + 4\lambda_2\dddot{e}_2 + 6\lambda_2^2\ddot{e}_2 + 4\lambda_2^3\dot{e}_2 + \lambda_2^4 e_2 + b_{21}\beta_c + b_{22}\delta_e \tag{47}$$

which can be written in a compact vector form as

$$\begin{bmatrix}\dot{s}_1 \\ \dot{s}_2\end{bmatrix} = \begin{bmatrix}v_1(\boldsymbol{x}, t) \\ v_2(\boldsymbol{x}, t)\end{bmatrix} + \begin{bmatrix}b_{11} & b_{12} \\ b_{21} & b_{22}\end{bmatrix}\begin{bmatrix}\beta_c \\ \delta_e\end{bmatrix} \tag{48}$$

where

$$v_1(\boldsymbol{x}, t) = -\dddot{V}_d + f_V + 3\lambda_1\ddot{e}_1 + 3\lambda_1^2\dot{e}_1 + \lambda_1^3 e_1 \tag{49}$$

$$v_2(\boldsymbol{x}, t) = -h_d^{(4)} + f_h + 4\lambda_2\dddot{e}_2 + 6\lambda_2^2\ddot{e}_2 + 4\lambda_2^3\dot{e}_2 + \lambda_2^4 e_2 \tag{50}$$

The sliding control design is then choosing the control inputs such that the following attractive equations are satisfied:

$$\frac{1}{2}\frac{\mathrm{d}s_1^2}{\mathrm{d}t} \le -k_1|s_1| \tag{51}$$

$$\frac{1}{2}\frac{\mathrm{d}s_2^2}{\mathrm{d}t} \le -k_2|s_2| \tag{52}$$

where $k_1$ and $k_2$ are strictly positive constants that determine the desired reaching time to the sliding surfaces. The attractive Eqs. (51) and (52), also called sliding conditions, imply that the distance to the sliding surface decreases along all system trajectories. Furthermore, the sliding condition makes the sliding surfaces an invariant set, that is, once a system trajectory reaches the surface, it will remain on it for the rest of the time. In addition, for any initial condition, the sliding surface will be reached in a finite time.[3]

When Eq. (48) is used, the controller that satisfies the sliding conditions (51) and (52) can be chosen as

$$\begin{bmatrix}\beta_c \\ \delta_e\end{bmatrix} = \boldsymbol{B}^{-1}\begin{bmatrix}-v_1(\boldsymbol{x}, t) - k_1\,\mathrm{sgn}(s_1) \\ -v_2(\boldsymbol{x}, t) - k_2\,\mathrm{sgn}(s_2)\end{bmatrix}, \qquad \boldsymbol{B} = \begin{bmatrix}b_{11} & b_{12} \\ b_{21} & b_{22}\end{bmatrix} \tag{53}$$

where $\boldsymbol{B}$ is assumed to be invertible. It is easy to see that $\boldsymbol{B}$ inverse does indeed exist for the entire flight envelope except on a vertical flight path.[2] The control law (53) can be viewed as consisting of two parts: the term $-\boldsymbol{B}^{-1}[v_1 \ v_2]^T$, called the equivalent control, which guarantees $\dot{s}_i = 0$, $i = 1, 2$, for the nominal model, and the other term $-\boldsymbol{B}^{-1}[k_1\mathrm{sgn}(s_1) \ k_2\mathrm{sgn}(s_2)]$, incorporated to deal with parameter uncertainties. With this design, the sliding surfaces will be reached even in the presence of parameter uncertainties. In fact, in the presence of parameter uncertainty, one has

$$\begin{bmatrix}\dot{s}_1 \\ \dot{s}_2\end{bmatrix} = \begin{bmatrix}\Delta f_V + v_1 \\ \Delta f_h + v_2\end{bmatrix} + (\Delta\boldsymbol{B} + \boldsymbol{B})\boldsymbol{B}^{-1}\begin{bmatrix}-v_1 - k_1\,\mathrm{sgn}(s_1) \\ -v_2 - k_2\,\mathrm{sgn}(s_2)\end{bmatrix} \tag{54}$$

As discussed in Ref. 3, when large enough $k_1$ and $k_2$ are chosen, the sliding conditions (51) and (52) can be satisfied. However, because of the discontinuity across the sliding surfaces, the preceding control law may result in control chattering. As a practical matter, chattering is undesirable because it involves very high control action and may excite high-frequency dynamics neglected in the modeling. The discontinuity in the control law can be dealt with by defining two thin boundary layers of widths $\Phi_1$ and $\Phi_2$ around the sliding surfaces, that is, replacing $\mathrm{sgn}(s_i)$ with continuous saturation functions $\mathrm{sat}(s_i/\Phi_i)$, $i = 1, 2$, where $\mathrm{sat}(x) = x$ if $|x| \le 1$ and $\mathrm{sat}(x) = \mathrm{sgn}(x)$ otherwise. Therefore, our sliding controller is modified as follows:

$$\begin{bmatrix}\beta_c \\ \delta_e\end{bmatrix} = \boldsymbol{B}^{-1}\begin{bmatrix}-v_1(\boldsymbol{x}, t) - k_1\,\mathrm{sat}(s_1/\Phi_1) \\ -v_2(\boldsymbol{x}, t) - k_2\,\mathrm{sat}(s_2/\Phi_2)\end{bmatrix} \tag{55}$$

With this scheme, the control law achieves a tradeoff between tracking precision and robustness. Analysis demonstrated by simulations shows that both the sliding surfaces and the attractive conditions influence how fast the system responds to a step input.[4]

Also, to guarantee closed-loop stability, it is necessary to identify the condition where the maximum effect of the combined parameter uncertainties is encountered. Both analytical and simulation studies conducted revealed that the closed-loop system is far more sensitive to variation in the gain matrix $\Delta\boldsymbol{B}$ than it is to $\Delta f_V$ and $\Delta f_h$. To calculate $\Delta\boldsymbol{B}$ for the worst case, the gain matrix is written as a

product of a fixed basis matrix $Y$ and an uncertainty parameter matrix,

$$\boldsymbol{B} = \begin{bmatrix} (1/a)Y_{11} & (1/b)Y_{12} \\ (1/a)Y_{21} & (1/b)Y_{22} \end{bmatrix} = \begin{bmatrix} Y_{11} & Y_{12} \\ Y_{21} & Y_{22} \end{bmatrix} \begin{bmatrix} (1/a) & 0 \\ 0 & (1/b) \end{bmatrix} \tag{56}$$

where

$$a = \frac{2 \times 10^{-4} m}{\rho S c_\beta \omega_n^2} \tag{57}$$

$$b = \frac{4 \times 10^{-14} I_{yy} m}{\rho^2 S^2 c_e \bar{c}} \tag{58}$$

$$Y_{11} = V^2 \cos\alpha \times 10^{-4} \tag{59}$$

$$Y_{21} = V^2 \sin(\alpha + \gamma) \times 10^{-4} \tag{60}$$

$$Y_{12} = -V^4 \left( C_T \sin\alpha + \frac{\partial C_D}{\partial \alpha} \right) \times 10^{-14} \tag{61}$$

$$Y_{22} = V^4 \left\{ C_T \cos(\alpha + \gamma) + \left( \frac{\partial C_L}{\partial \alpha} \right) \cos\gamma - \left( \frac{\partial C_D}{\partial \alpha} \right) \sin\gamma \right\} \times 10^{-14} \tag{62}$$

Constants $a$ and $b$ embody the combinations of all uncertainty parameters in $\boldsymbol{B}$. The worst case occurs when $\Delta m$ and $\Delta I$ take their maximum negative values, while $\Delta\rho$, $\Delta S$, $\Delta c_e$, and $\Delta\bar{c}$ take their maximum positive values. In this study, the nominal values of $a$ and $b$ are 1.1926 ft · s$^2$ and 0.1463 ft$^3$/s, and the true values of $a$ and $b$ are 1.0805 ft · s$^2$ and 0.1166 ft$^3$/s, respectively. Therefore, the parameter $a$ contains 10.4% uncertainty and the parameter $b$ contains 25.4% uncertainty. In a hypersonic vehicle, these uncertainties are significant. The uncertainties in $f_V$ and $f_h$ are nonlinear combinations of the uncertainty in parameters. When a Taylor series expansion of these terms around their nominal values is used and the high-order error terms are neglected, the terms $\Delta f_V$ and $\Delta f_h$ can be estimated from their nominal values.

The simulation results are shown in Figs. 1–4. Figures 1 and 2 show the response of the nominal model, that is, no parameter uncertainty. In the simulation studies for the nominal model, $k_1$ and $k_2$ are both taken as 2, and $\Phi_1$ and $\Phi_2$ are both chosen as 0.1. Figure 1 shows the vehicle response to a 100-ft/s step-velocity command at the trimmed condition. It is observed that the velocity converges to the desired value in a short time, whereas the altitude remains almost unchanged. Figure 2 shows the vehicle response to a 2000-ft step-altitude command. Similarly, the altitude converges to its desired value with a short response time. In both cases, the controller

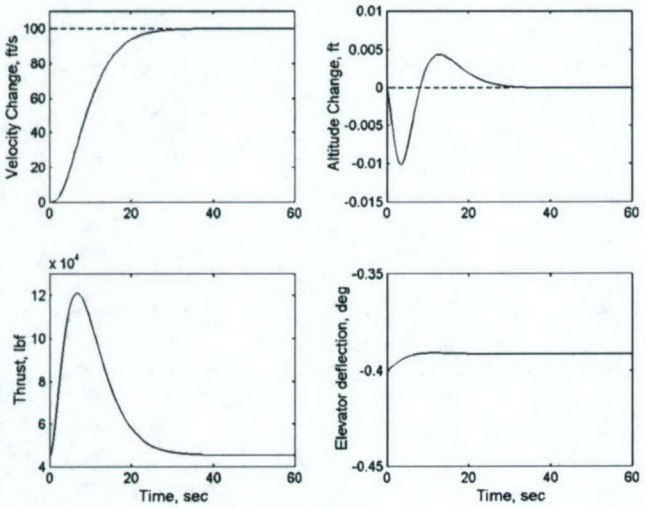


**Fig. 1 Response to a 100-ft/s step-velocity command for the nominal model.**

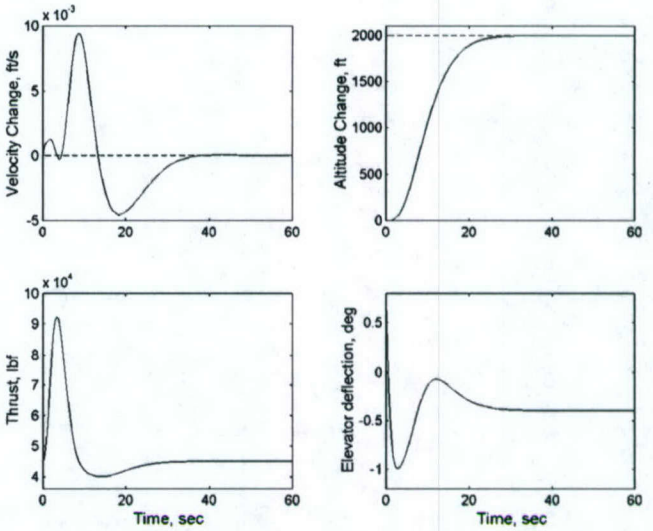


**Fig. 2 Response to a 2000-ft step-altitude command for the nominal model.**

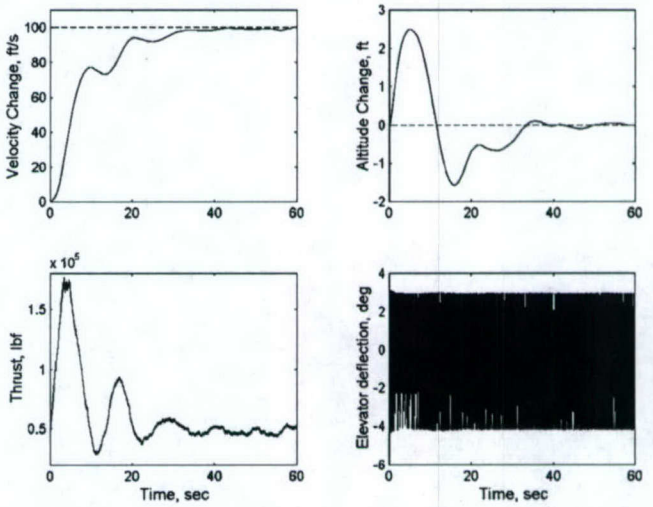


**Fig. 3 Response to a 100-ft/s step-velocity command with parameter uncertainties.**

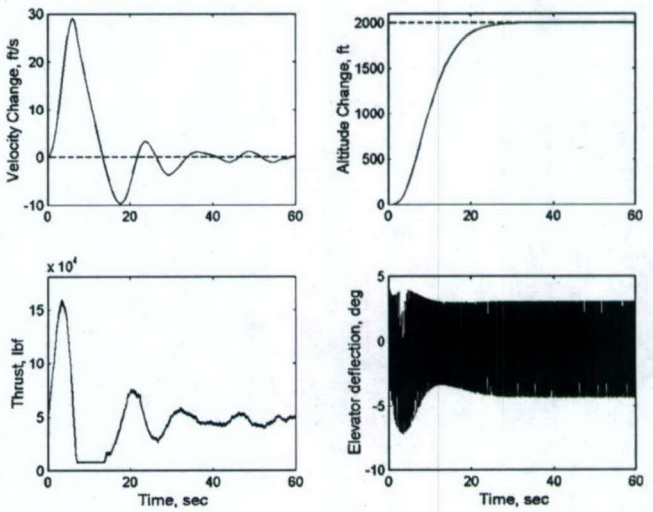


**Fig. 4 Response to a 2000-ft step-altitude command with parameter uncertainties.**

achieves quick convergence, no overshoot and no steady-state error, for the nominal model. Figures 3 and 4 show the simulation results for the same maneuvers albeit in the presence of parameter uncertainty for the worst case discussed earlier. In this case, $k_1$ and $k_2$ are taken as 1400 and 100, and $\Phi_1$ and $\Phi_2$ are chosen as 0.8 and 0.6, respectively. The results show that robustness and stability have indeed been achieved. The price paid to achieve robustness in this case is in the form of large gains $k_1$ and $k_2$ and control chattering. However, the control gains cannot be chosen arbitrary large due to practical considerations such as reaching control surface deflection limits. Furthermore, control chattering is undesirable in practice because it involve high control activity and may excite high-frequency unmodeled dynamics. In simulation, the widths of the boundary layers have expanded to reduce chattering. To eliminate chattering, the widths of the boundary layers have to be further expanded, which will result in large steady-state errors. Therefore, in the presence of large parameter uncertainty, pure sliding mode controller requires a tradeoff between steady-state error and control chattering. This drawback of the sliding mode controller is addressed in the next section, where an online parameter estimator is combined with the sliding mode controller to improve performance when parameter uncertainty is present.

## Adaptive Sliding Mode Controller Design

As demonstrated in the preceding section, the sliding mode controller achieves good tracking in the presence of parametric uncertainty at the expense of high gains and control chattering. The performance of the sliding mode controller is dependent on the size of the parametric uncertainties involved. An undesirable characteristic of this controller is the quick erosion of performance to gain robustness. This shortcoming of the pure sliding controller has motivated combining the earlier given control law with online parameter adaptation. In this section, we develop an adaptive sliding mode controller that combines an online parameter estimator with the sliding mode controller of the preceding section. The adaptive laws for updating parameters are generated using the Lyapunov synthesis approach (see Ref. 9). As mentioned before, the dynamics of the system is more sensitive to the uncertainty parameters in the gain matrix $\boldsymbol{B}$. The gain matrix $\boldsymbol{B}$ itself is the product of a fixed basis matrix $\boldsymbol{Y}$ and a diagonal matrix with two parameters $a$ and $b$ involving uncertainties. The constant $a$ embodies the combination of a number of uncertain parameters including $S$, $\rho$, $I_{yy}$, and $m$, and the constant $b$ embodies the combination of uncertain parameters $\bar{c}$, $S$, $c_e$, $\rho$, $I_{yy}$, and $m$. For a hypersonic vehicle, these parameters are fixed and strictly positive but difficult to measure exactly at any given time. To deal with the parametric uncertainty, we combine the sliding mode controller with an online parameter estimator forming an adaptive sliding mode controller,

$$\begin{bmatrix} \beta_c \\ \delta_e \end{bmatrix} = \begin{bmatrix} \hat{a} & 0 \\ 0 & \hat{b} \end{bmatrix} \begin{bmatrix} Y_{11} & Y_{12} \\ Y_{21} & Y_{22} \end{bmatrix}^{-1} \bar{\boldsymbol{u}} \tag{63}$$

$$\bar{\boldsymbol{u}} = \begin{bmatrix} -v_1(\boldsymbol{x}, t) - k_1 \operatorname{sat}(s_1/\Phi_1) \\ -v_2(\boldsymbol{x}, t) - k_2 \operatorname{sat}(s_2/\Phi_2) \end{bmatrix} \tag{64}$$

where $\hat{a}$ and $\hat{b}$ are the online estimates of the uncertain parameters $a$ and $b$.

The adaptive laws can be derived using the Lyapunov synthesis approach. Consider the Lyapunov-like function,

$$V = \tfrac{1}{2} \boldsymbol{s}_\Delta^T \boldsymbol{s}_\Delta + (1/2ak_a)\tilde{a}^2 + (1/2bk_b)\tilde{b}^2 \tag{65}$$

where

$$\tilde{a} = \hat{a} - a, \qquad \tilde{b} = \hat{b} - b, \qquad \boldsymbol{s}_\Delta^T = [s_{1\Delta} \quad s_{2\Delta}]$$

$$s_{1\Delta} = s_1 - \Phi_1 \operatorname{sat}(s_1/\Phi_1), \qquad s_{2\Delta} = s_2 - \Phi_2 \operatorname{sat}(s_2/\Phi_2)$$

where $\Phi_1$ and $\Phi_2$ are two small positive constants. In this construction, $\boldsymbol{s}_\Delta$ can be thought of a measure of the algebraic distances of the current states to the boundary layers. The adaptation ceases as the states reach the boundary layers to avoid parameter estimate drifting.[5] Following the treatment in Ref. 9, we have

$$\dot{V} = \boldsymbol{s}_\Delta^T \begin{bmatrix} -\Delta f_V - k_1 \operatorname{sat}\left(\dfrac{s_1}{\Phi_1}\right) \\ -\Delta f_h - k_2 \operatorname{sat}\left(\dfrac{s_2}{\Phi_2}\right) \end{bmatrix} + \boldsymbol{s}_\Delta^T \begin{bmatrix} Y_{11} & Y_{12} \\ Y_{21} & Y_{22} \end{bmatrix} \begin{bmatrix} \dfrac{\tilde{a}}{a} & 0 \\ 0 & \dfrac{\tilde{b}}{b} \end{bmatrix}$$

$$\times \begin{bmatrix} Y_{11} & Y_{12} \\ Y_{21} & Y_{22} \end{bmatrix}^{-1} \bar{\boldsymbol{u}} + \frac{1}{ak_a}\tilde{a}\dot{\hat{a}} + \frac{1}{bk_b}\tilde{b}\dot{\hat{b}} \tag{66}$$

Equation (66) can be further expanded as

$$\dot{V} = -(k_1 - |\Delta f_V|)|s_{1\Delta}| - (k_2 - |\Delta f_h|)|s_{2\Delta}| + \frac{\tilde{a}}{a}\frac{1}{\Delta}\boldsymbol{s}_\Delta^T$$

$$\times \begin{bmatrix} Y_{11}Y_{22} & -Y_{11}Y_{12} \\ Y_{21}Y_{22} & -Y_{21}Y_{12} \end{bmatrix} \bar{\boldsymbol{u}} + \frac{\tilde{b}}{b}\frac{1}{\Delta}\boldsymbol{s}_\Delta^T \begin{bmatrix} -Y_{12}Y_{21} & Y_{11}Y_{12} \\ -Y_{22}Y_{21} & Y_{11}Y_{22} \end{bmatrix} \bar{\boldsymbol{u}}$$

$$+ \frac{1}{ak_a}\tilde{a}\dot{\hat{a}} + \frac{1}{bk_b}\tilde{b}\dot{\hat{b}}$$

Then, the adaptive laws for estimating uncertain parameters can be derived as

$$\dot{\hat{a}} = -\frac{k_a}{\Delta}\boldsymbol{s}_\Delta^T \begin{bmatrix} Y_{11}Y_{22} & -Y_{11}Y_{12} \\ Y_{21}Y_{22} & -Y_{21}Y_{12} \end{bmatrix} \bar{\boldsymbol{u}} \tag{67}$$

$$\dot{\hat{b}} = -\frac{k_b}{\Delta}\boldsymbol{s}_\Delta^T \begin{bmatrix} -Y_{12}Y_{21} & Y_{11}Y_{12} \\ -Y_{22}Y_{21} & Y_{11}Y_{22} \end{bmatrix} \bar{\boldsymbol{u}} \tag{68}$$

where $\Delta = Y_{11}Y_{22} - Y_{12}Y_{21}$ is the determinant of the matrix $\boldsymbol{Y}$. The sliding gains are chosen as $k_1 \geq |\Delta f_V|_{\max} + l_1$ and $k_2 > |\Delta f_h|_{\max} + l_2$ (where $l_1$ and $l_2$ are two positive constants) such that $\dot{V} \leq -l_1|s_{1\Delta}| - l_2|s_{2\Delta}|$, which guarantees all trajectories converge to the boundary layers.

The sliding gains of $k_1$ and $k_2$ in this case are taken as 150 and 10, respectively, which are much reduced compared with those in the pure sliding mode control. The simulation results using the adaptive sliding mode controller are shown in Figs. 5–8. When these results are compared with the results obtained using the pure sliding mode controller shown in Figs. 3 and 4, a notable improvement in performance is observed. It is seen that the level of the control effort in the adaptive case is significantly smaller. Figures 6 and 8 show that the parameters converge to their true values. In Fig. 6, the true values are $a = 1.0805$ ft $\cdot$ s$^2$ and $b = 0.1166$ ft$^3$/s. Initial nominal values in the estimation were $\hat{a}(0) = 1.1926$ ft $\cdot$ s$^2$ and $\hat{b}(0) = 0.1463$ ft$^3$/s. In Fig. 8, true values are $a = 1.0805$ ft $\cdot$ s$^2$ and $b = 0.1166$ ft$^3$/s.

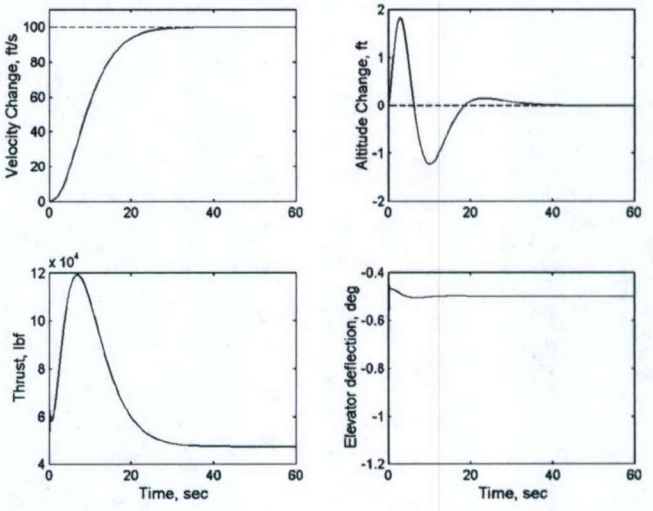


**Fig. 5 Adaptive sliding mode controller: response to a 100-ft/s step-velocity command.**

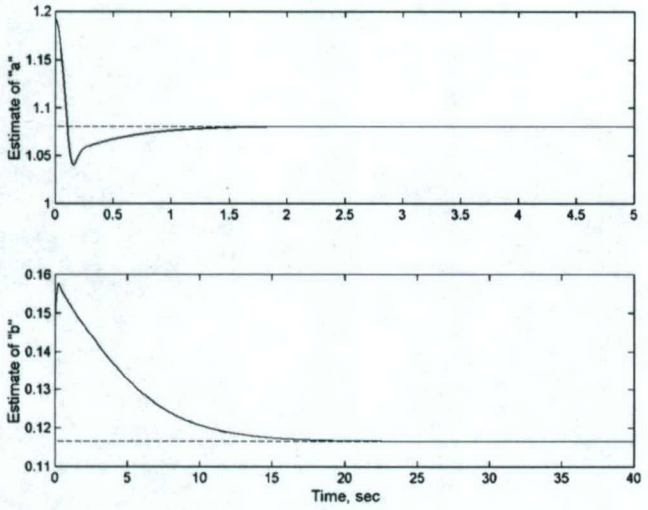


**Fig. 6 Parameter estimation in response to a 100-ft/s step-velocity command.**

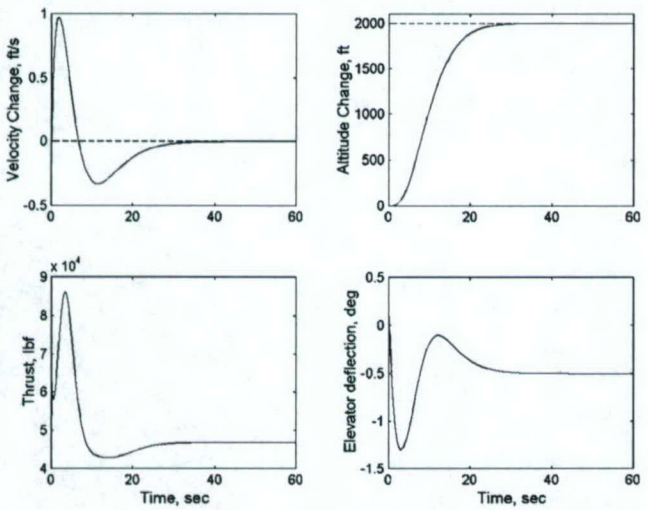


**Fig. 7 Adaptive sliding mode controller: response to a 2000-ft step command.**

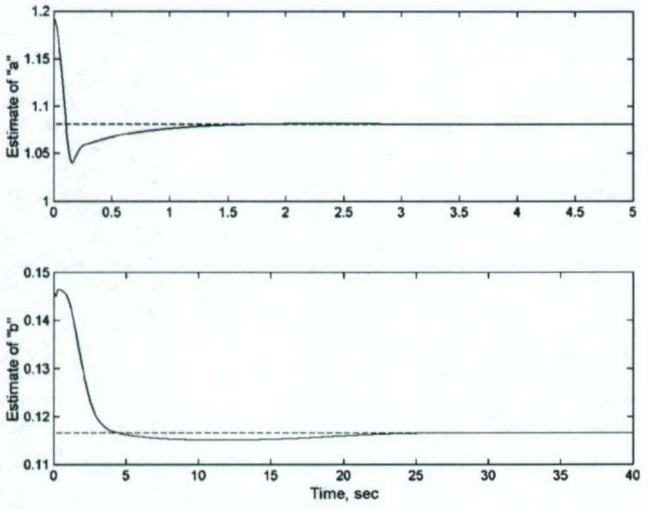


**Fig. 8 Parameter estimation in response to a 2000-ft step-altitude command.**

Initial nominal values in estimation were $\hat{a}(0) = 1.1926$ ft $\cdot$ s$^2$ and $\hat{b}(0) = 0.1463$ ft$^3$/s.

## Sliding Mode Observer Design

The sliding mode and the adaptive sliding mode controllers developed in the preceding sections assume that full states are available for measurement. In practice, however, only the states that correspond to velocity $V$, altitude $h$, and pitch rate $q$ are expected to be measured. The state variables corresponding to the angle of attack $\alpha$ and flight-path angle $\gamma$ may be difficult to measure in an actual hypersonic flight because they are generally very small. Accurate measurements are costly and difficult if at all possible to obtain practically. In this section, a sliding mode observer is designed that can provide the estimates of the angle of attack and flight-path angle based on the measurements of velocity, altitude, and pitch rate. When the techniques developed in Ref. 6 are applied, a sliding mode observer is designed whose structure is given by

$$\dot{\hat{h}} = V \sin\hat{\gamma} - \eta_1\tilde{h} - k_h \mathrm{sgn}(\tilde{h}) \tag{69}$$

$$\dot{\hat{q}} = \frac{\hat{M}_{yy}}{I_0} - \eta_2\tilde{q} - k_q \mathrm{sgn}(\tilde{q}) \tag{70}$$

$$\dot{\hat{\gamma}} = \frac{\hat{L} + T\sin\hat{\alpha}}{mV} - \frac{(\mu - V^2 r)\cos\hat{\gamma}}{Vr^2} - \eta_3\tilde{h} - k_\gamma \mathrm{sgn}(\tilde{h}) \tag{71}$$

$$\dot{\hat{\alpha}} = \hat{q} - \dot{\hat{\gamma}} - \eta_4\tilde{q} - k_\alpha \mathrm{sgn}(\tilde{q}) \tag{72}$$

where

$$\hat{L} = \tfrac{1}{2}\rho_0 V^2 S_0 \times 0.6203\hat{\alpha}$$

$$\hat{M}_{yy} = \tfrac{1}{2}\rho_0 V^2 S_0 \bar{c}_0 \big[(-0.035\hat{\alpha}^2 + 0.036617\hat{\alpha} + 5.3261 \times 10^{-6}) + (\bar{c}_0/2V)q(-6.796\hat{\alpha}^2 + 0.3015\hat{\alpha} - 0.2289) + 0.0292(\delta_e - \hat{\alpha})\big]$$

$$\tilde{h} = \hat{h} - h, \qquad \tilde{q} = \hat{q} - q$$

and where $\eta_1$, $\eta_2$, $\eta_3$, and $\eta_4$ are positive constants selected as 2.0, 1.8, 0.0001, and 0.001, respectively, and $k_h$, $k_q$, $k_\gamma$, and $k_\alpha$ are the sliding gains chosen by the designer.

The sliding surfaces of the observer are defined by $s_0 = 0$, where $s_0 = [\tilde{h}\ \tilde{q}]^T$. The average error dynamics during sliding where $s_0 = 0$ and $\dot{s}_0 = 0$ are

$$\tilde{h} = 0 \tag{73}$$

$$\tilde{q} = 0 \tag{74}$$

$$V(\sin\hat{\gamma} - \sin\gamma) - k_h \mathrm{sgn}(\tilde{h}) = 0 \tag{75}$$

$$\left(\frac{1}{2I_0}\right)\rho_0 V^2 S_0 \bar{c}_0 \left\{-0.035(\hat{\alpha}^2 - \alpha^2) + \left[0.00742 - 0.3015\left(\frac{\bar{c}_0}{2V}\right)q\right]\tilde{\alpha} - 6.796\left(\frac{\bar{c}_0}{2V}\right)q(\hat{\alpha}^2 - \alpha^2)\right\} - k_q \mathrm{sgn}(\tilde{q}) = 0 \tag{76}$$

$$\dot{\tilde{\gamma}} = \frac{0.3102\rho_0 V^2 S_0\tilde{\alpha} + T(\sin\hat{\alpha} - \sin\alpha)}{mV} - \frac{(\mu - V^2 r)(\cos\hat{\gamma} - \cos\gamma)}{Vr^2} - k_\gamma \mathrm{sgn}(\tilde{h}) \tag{77}$$

$$\dot{\tilde{\alpha}} = -\dot{\tilde{\gamma}} - k_\alpha \mathrm{sgn}(\tilde{q}) \tag{78}$$

where

$$\tilde{\alpha} = \hat{\alpha} - \alpha, \qquad \tilde{\gamma} = \hat{\gamma} - \gamma$$

The preceding error dynamics are nonlinear and difficult to analyze. Further simplification can be made, however, by noting that, in a hypersonic flight, the velocity $V$ is high and the angle of attack $\alpha$ and flight-path angle $\gamma$ are typically very small, which justifies the following approximations:

$$\sin\alpha \approx \alpha, \qquad \sin\hat{\alpha} \approx \alpha, \qquad \cos\gamma, \qquad \cos\hat{\gamma} \approx 1$$

$$\hat{\alpha}^2, \alpha^2 \approx 0, \qquad (\bar{c}_0/2V)q \approx 0$$

An approximation for the local error dynamics can be derived from the nonlinear error dynamics of Eqs. (73–78) as

$$\dot{\tilde{h}} = 0 \tag{79}$$

$$\dot{\tilde{q}} = 0 \tag{80}$$

$$\dot{\tilde{\gamma}} \approx -V\left(\frac{k_\gamma}{k_h}\right)\tilde{\gamma} + \left\{\frac{(0.3102\rho_0 V^2 S_0 + T)}{mV}\right\}\tilde{\alpha} \tag{81}$$

$$\dot{\tilde{\alpha}} \approx \left\{-0.00371\left(\frac{k_\alpha}{k_q}\right)\left(\frac{\rho_0 V^2 S_0 \bar{c}_0}{I_0}\right) - \frac{(0.3102\rho_0 V^2 S_0 + T)}{mV}\right\}\tilde{\alpha} + V\left(\frac{k_\gamma}{k_h}\right)\tilde{\gamma} \tag{82}$$

When the trimmed conditions are substituted, the last two error equations can be further simplified as

$$\dot{\tilde{\gamma}} \approx -15060(k_\gamma/k_h)\tilde{\gamma} + 0.0440\tilde{\alpha} \tag{83}$$

$$\dot{\tilde{\alpha}} \approx -\{0.8425(k_\alpha/k_q) + 0.044\}\tilde{\alpha} + 15060(k_\gamma/k_h)\tilde{\gamma} \tag{84}$$

The convergence of $\tilde{\gamma}$ and $\tilde{\alpha}$ depend on the ratios of $k_\gamma/k_h$ and of $k_\alpha/k_q$, respectively. As a rule of thumb, the error dynamics of the observer on sliding surfaces $s_0 = 0$ should be much faster than the tracking error dynamics, that is,

$$\min\{15060(k_\gamma/k_h), 0.8425(k_\alpha/k_q)\} \gg \max\{\lambda_1, \lambda_2\}$$

In this study, $\lambda_1 = 0.3$, $\lambda_2 = 0.38$, $k_\gamma/k_h$ is chosen as 0.001, and $k_\alpha/k_q$ is chosen as 15, thus, placing the poles of the reduced-order error dynamics of Eqs. (83) and (84) at $-15.06$ and $-12.64$. The simulation results in Figs. 9 and 10 show the convergence behavior of the off-line observer, that is, it is not being used for the sliding controller. Figure 9 shows that the errors converge to zero fast when no measurement noise is assumed. In Fig. 10, the errors converge close to zero when a measurement noise with zero mean and standard deviation 80 ft and 0.15 deg/s, respectively, is present. The results demonstrate that the sliding observer has good performance and exhibits robustness with respect to measurement noise.

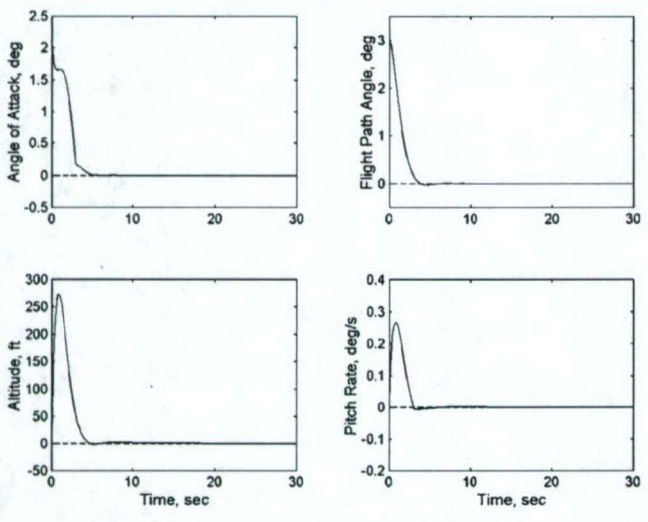


**Fig. 9 Off-line sliding observer without measurement noise, initial state errors $\tilde{\gamma}(0) = 3.0$ deg/s and $\tilde{\alpha}(0) = 2.0$ deg.**

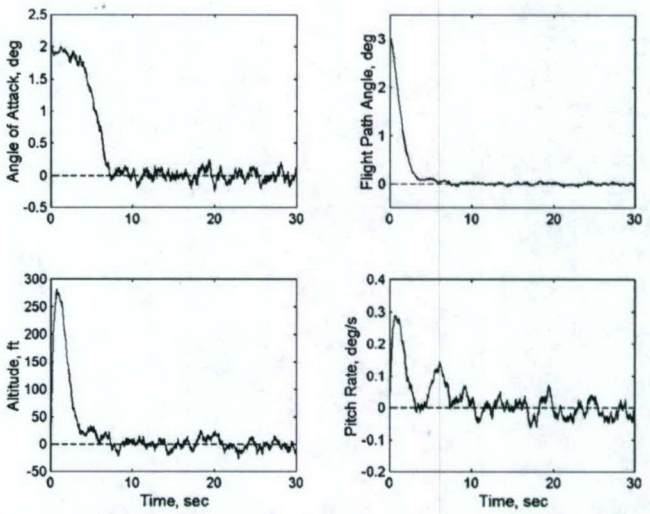


**Fig. 10 Off-line sliding observer with Gaussian measurement noise, initial state errors $\tilde{\gamma}(0) = 3.0$ deg/s and $\tilde{\alpha}(0) = 2.0$ deg.**

## Adaptive Sliding Controller–Observer Synthesis

In the preceding sections we discussed the behavior of the adaptive sliding mode controller and of the sliding mode observer separately. In this section we combine the adaptive sliding mode controller with the observer to synthesize an adaptive sliding mode controller that does not require full state measurement as follows:

$$\hat{\bar{u}} = \begin{bmatrix} -v_1(\hat{\alpha}, \hat{\gamma}, t) - k_1 \,\mathrm{sat}\left(\dfrac{s_1}{\Phi_1}\right) \\ -v_2(\hat{\alpha}, \hat{\gamma}, t) - k_2 \,\mathrm{sat}\left(\dfrac{s_2}{\Phi_2}\right) \end{bmatrix} \tag{85}$$

$$\begin{bmatrix} \beta_c \\ \delta_e \end{bmatrix} = \begin{bmatrix} \hat{a} & 0 \\ 0 & \hat{b} \end{bmatrix} \begin{bmatrix} Y_{11} & Y_{12} \\ Y_{21} & Y_{22} \end{bmatrix}^{-1} \hat{\bar{u}} \tag{86}$$

$$\dot{\hat{a}} = -\frac{k_a}{\Delta} s_\Delta^T \begin{bmatrix} Y_{11}Y_{22} & -Y_{11}Y_{12} \\ Y_{21}Y_{22} & -Y_{21}Y_{12} \end{bmatrix} \hat{\bar{u}} \tag{87}$$

$$\dot{\hat{b}} = -\frac{k_b}{\Delta} s_\Delta^T \begin{bmatrix} -Y_{12}Y_{21} & Y_{11}Y_{12} \\ -Y_{22}Y_{21} & Y_{11}Y_{22} \end{bmatrix} \hat{\bar{u}} \tag{88}$$

$$\dot{\tilde{h}} = V\sin\hat{\gamma} - \eta_1\tilde{h} - k_h \mathrm{sgn}(\tilde{h}) \tag{89}$$

$$\dot{\tilde{q}} = \frac{\hat{M}_{yy}}{I_0} - \eta_2\tilde{q} - k_q \mathrm{sgn}(\tilde{q}) \tag{90}$$

$$\dot{\hat{\gamma}} = \frac{\hat{L} + T\sin\hat{\alpha}}{mV} - \frac{(\mu - V^2 r)\cos\hat{\gamma}}{Vr^2} - \eta_3\tilde{h} - k_\gamma \mathrm{sgn}(\tilde{h}) \tag{91}$$

$$\dot{\tilde{\alpha}} = \hat{q} - \dot{\hat{\gamma}} - \eta_4\tilde{q} - k_\alpha \mathrm{sgn}(\tilde{q}) \tag{92}$$

where, $v_1(\hat{\alpha}, \hat{\gamma}, t)$ and $v_2(\hat{\alpha}, \hat{\gamma}, t)$ are the same function as $v_1(\boldsymbol{x}, t)$ and $v_2(\boldsymbol{x}, t)$ in which arguments $\alpha$ and $\gamma$ are replaced by $\hat{\alpha}$ and $\hat{\gamma}$.

The preceding controller is simulated for the same maneuvers and conditions discussed in the preceding sections. The values of $k_1$ and $k_2$ are taken as 150 and 10, respectively, which are same as in the adaptive sliding control case. The simulation results are shown in Figs. 11 and 12. It is seen that the adaptive sliding

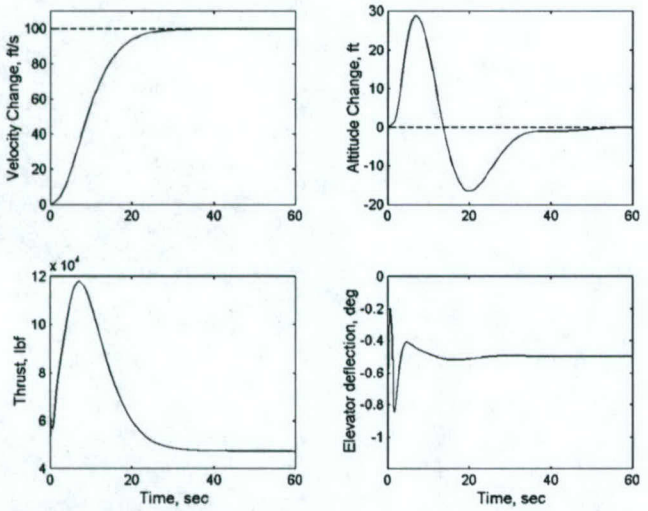


**Fig. 11 Adaptive sliding mode controller–observer: response to a 100-ft/s step-velocity command with parameter uncertainties with initial state errors $\tilde{\gamma}(0) = 0.25$ deg/s and $\tilde{\alpha}(0) = 1.5$ deg.**

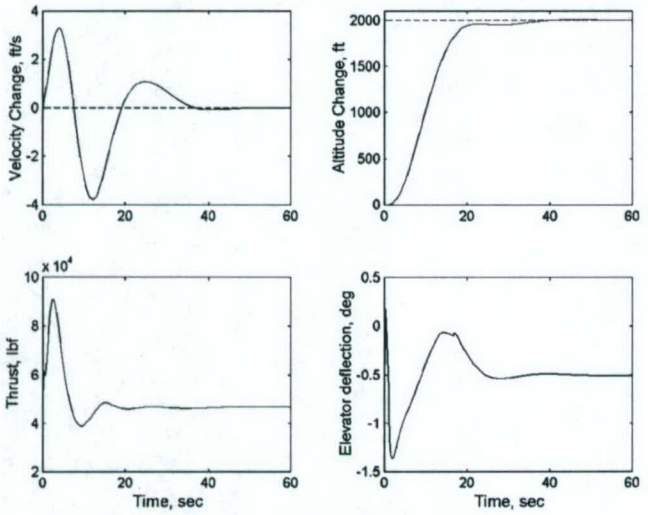


**Fig. 12 Adaptive sliding mode controller–observer: response to a 2000-ft step-altitude command with parameter uncertainties with initial state errors $\tilde{\gamma}(0) = 0.25$ deg/s and $\tilde{\alpha}(0) = 1.5$ deg.**

mode controller–observer does provide good tracking, despite the presence of parametric uncertainty and assumption of incomplete state measurement.

## Conclusions

In this paper, a MIMO adaptive sliding mode controller is designed for the nonlinear longitudinal model of a generic hypersonic vehicle. The controller is developed in several stages. First, a sliding mode controller is developed using full state feedback. Then, the sliding mode controller is made adaptive to deal with parametric uncertainty more efficiently. A nonlinear sliding mode observer is developed to estimate the states that are not available for measurement as in a typical hypersonic flight. The combination of the observer with the adaptive sliding mode controller leads to the final adaptive sliding mode control design that requires only partial state variables to be available for measurement. Simulations conducted demonstrate that the combined adaptive sliding controller–observer has good tracking performance and robustness in the in the presence of parametric uncertainty and the assumption of partial state measurements for the one point in the flight envelop considered in this study.

## Appendix

The detailed expressions of the vectors $\omega_1$ and $\pi_1$ and matrices $\Omega_2$ and $\Pi_2$ are a simplified version of those in Ref. 2:

$$\omega_1^T = \begin{bmatrix} \left(\frac{\partial T}{\partial V}\right)\cos\alpha - \frac{\partial D}{\partial V} \\ \frac{-m\mu\cos\gamma}{r^2} \\ \frac{-T\sin\alpha - \partial D}{\partial\alpha} \\ \left(\frac{\partial T}{\partial\beta}\right)\cos\alpha \\ \frac{2m\mu\sin\gamma}{r^3} \end{bmatrix}$$

$$\pi_1^T = \begin{bmatrix} \frac{\partial L/\partial V + (\partial T/\partial V)\sin\alpha}{mV} - \frac{L + T\sin\alpha}{mV^2} + \frac{\mu\cos\gamma}{V^2r^2} + \frac{\cos\gamma}{r} \\ \frac{\mu\sin\gamma}{Vr^2} - \frac{V\sin\gamma}{r} \\ \frac{\partial L/\partial\alpha + T\cos\alpha}{mV} \\ \frac{(\partial T/\partial\beta)\sin\alpha}{mV} \\ \frac{2\mu\cos\gamma}{Vr^3} - \frac{V\cos\gamma}{r^2} \end{bmatrix}$$

$$\Omega_2 = [\omega_{21} \quad \omega_{22} \quad \omega_{23} \quad \omega_{24} \quad \omega_{25}]$$

where

$$\omega_{21} = \begin{bmatrix} \left(\frac{\partial^2 T}{\partial V^2}\right)\cos\alpha - \frac{\partial^2 D}{\partial V^2} \\ 0 \\ -\left(\frac{\partial T}{\partial V}\right)\sin\alpha - \frac{\partial^2 D}{\partial V\partial\alpha} \\ \left(\frac{\partial^2 T}{\partial V\partial\beta}\right)\cos\alpha \\ 0 \end{bmatrix}$$

$$\omega_{22} = \begin{bmatrix} 0 \\ \frac{m\mu\sin\gamma}{r^2} \\ 0 \\ 0 \\ \frac{2m\mu\cos\gamma}{r^3} \end{bmatrix}$$

$$\omega_{23} = \begin{bmatrix} -\left(\frac{\partial T}{\partial V}\right)\sin\alpha - \left(\frac{\partial^2 D}{\partial V\partial\alpha}\right) \\ 0 \\ -T\cos\alpha - \left(\frac{\partial^2 D}{\partial\alpha^2}\right) \\ -\left(\frac{\partial T}{\partial\beta}\right)\sin\alpha \\ 0 \end{bmatrix}$$

$$\omega_{24} = \begin{bmatrix} \left(\dfrac{\partial^2 T}{\partial V \partial \beta}\right)\cos\alpha \\ 0 \\ -\left(\dfrac{\partial T}{\partial \beta}\right)\sin\alpha \\ 0 \\ 0 \end{bmatrix}, \qquad \omega_{25} = \begin{bmatrix} 0 \\ \dfrac{2m\mu\cos\gamma}{r^3} \\ 0 \\ 0 \\ \dfrac{-6m\mu\sin\gamma}{r^4} \end{bmatrix}$$

$$\Pi_2 = [\pi_{21} \quad \pi_{22} \quad \pi_{23} \quad \pi_{24} \quad \pi_{25}]$$

where

$$\pi_{21} = \begin{bmatrix} \dfrac{\partial^2 L/\partial V^2 + (\partial^2 T/\partial V^2)\sin\alpha}{mV} - \dfrac{2[\partial L/\partial V + (\partial T/\partial V)\sin\alpha]}{mV^2} + \dfrac{2(L + T\sin\alpha)}{mV^3} - \dfrac{2\mu\cos\gamma}{V^3 r^2} \\ -\dfrac{\mu\sin\gamma}{V^2 r^2} - \dfrac{\sin\gamma}{r} \\ \dfrac{(\partial^2 L/\partial\alpha\partial V) + (\partial T/\partial V)\cos\alpha}{mV} - \dfrac{\partial L/\partial\alpha + T\cos\alpha}{mV^2} \\ \dfrac{(\partial^2 T/\partial\beta\partial V)\sin\alpha}{mV} - \dfrac{(\partial T/\partial\beta)\sin\alpha}{mV^2} \\ -\dfrac{2\mu\cos\gamma}{V^2 r^3} - \dfrac{\cos\gamma}{r^2} \end{bmatrix}$$

$$\pi_{22} = \begin{bmatrix} -\dfrac{\mu\sin\gamma}{V^2 r^2} - \dfrac{\sin\gamma}{r} \\ \dfrac{\mu\cos\gamma}{Vr^2} - \dfrac{V\cos\gamma}{r} \\ 0 \\ 0 \\ -\dfrac{2\mu\sin\gamma}{Vr^3} + \dfrac{V\sin\gamma}{r^2} \end{bmatrix}, \qquad \pi_{23} = \begin{bmatrix} \dfrac{(\partial^2 L/\partial V\partial\alpha) + (\partial T/\partial V)\cos\alpha}{mV} - \dfrac{\partial L/\partial\alpha + T\cos\alpha}{mV^2} \\ 0 \\ \dfrac{\partial^2 L/\partial\alpha^2 - T\sin\alpha}{mV} \\ \dfrac{(\partial T/\partial\beta)\cos\alpha}{mV} \\ 0 \end{bmatrix}$$

$$\pi_{24} = \begin{bmatrix} \dfrac{(\partial^2 T/\partial V\partial\beta)\sin\alpha}{mV} - \dfrac{(\partial T/\partial\beta)\sin\alpha}{mV^2} \\ 0 \\ \dfrac{(\partial T/\partial\beta)\cos\alpha}{mV} \\ 0 \\ 0 \end{bmatrix}, \qquad \pi_{25} = \begin{bmatrix} -\dfrac{2\mu\cos\gamma}{V^2 r^3} - \dfrac{\cos\gamma}{r^2} \\ -\dfrac{2\mu\sin\gamma}{Vr^3} + \dfrac{V\sin\gamma}{r^2} \\ 0 \\ 0 \\ -\dfrac{6\mu\cos\gamma}{Vr^4} + \dfrac{2V\cos\gamma}{r^3} \end{bmatrix}$$

## Acknowledgments

This work was supported in part by the Air Force Office of Scientific Research under Grant F49620-01-1-0489 and in part by NASA Dryden Flight Research Center under Grant NAGA-175.

## References

[1]Marrison, C. I., and Stengel, R. F., "Design of Robust Control System for a Hypersonic Aircraft," *Journal of Guidance, Control, and Dynamics*, Vol. 21, No. 1, 1998, pp. 58–62.

[2]Wang, Q., and Stengel, R. F., "Robust Nonlinear Control of a Hypersonic Aircraft," *Journal of Guidance, Control, and Dynamics*, Vol. 23, No. 4, 2000, pp. 577–585.

[3]Slotine, J.-J. E., and Li, W., *Applied Nonlinear Control*, Prentice Hall, Englewood Cliff, NJ, 1991, Chap. 7.

[4]Fernandez, R. B., and Hedrick, J. K., "Control of Multivariable Non-Linear Systems by the Sliding Mode Method," *International Journal of Control*, Vol. 46, No. 3, 1987, pp. 1019–1040.

[5]Slotine, J.-J. E., and Coetsee, J. A., "Adaptive Controller Synthesis for Nonlinear Systems," *International Journal of Control*, Vol. 43, No. 6, 1986, pp. 1631–1651.

[6]Slotine, J.-J. E., Hedrick, J. K., and Misawa, E. A., "On Sliding Observers for Nonlinear Systems," *ASME Journal of Dynamics Systems, Measurement and Control*, Vol. 109, Sept. 1987, pp. 245–252.

[7]Hedrick, J. K., and Yao, W. H., "Adaptive Sliding Control of a Magnetic Suspension System," *Variable Structure Control For Robotics and Aerospace Applications*, edited by K.-K. D. Young, Elsevier Science, New York, 1993, pp. 141–155.

[8]Zak, S. H., Walcott, B. L., and Hui, S., "Variable Structure Control and Observation of Nonlinear/Uncertain Systems," *Variable Structure Control For Robotics and Aerospace Applications*, edited by K.-K. D. Young, Elsevier Science, New York, 1993, pp. 59–88.

[9]Ioannou, P. A., and Sun, J., *Robust Adaptive Control*, Prentice Hall, Upper Saddle River, NJ, 1996.

# Adaptive Linear Quadratic Design with Application to F-16 Fighter Aircraft

Ying Huo[1]
*University of Southern California, Los Angeles, CA 90089*

Majdedin Mirmirani[2]
*California State University, Los Angeles, CA 90032*

Petros Ioannou[3]
*University of Southern California, Los Angeles, CA 90089*

*and*

Richard Colgren[4]
*University of Kansas, 2120 Learned Hall, Lawrence, KS 66045.*

**This paper investigates an adaptive linear quadratic (ALQ) control design with its application to the longitudinal model of the F-16 fighter aircraft. The certainty equivalence principle is used to combine the adaptive law with the control structure of the standard linear quadratic (LQ) problems. The aerodynamics of the F-16 fighter aircraft is linearized at different trimmed conditions, and the traditional gain scheduling LQ design is also implemented. Simulation results demonstrate the effectiveness of ALQ control design over LQ design with gain scheduling, in that it can discern aerodynamics changes and adapt the control laws accordingly. This also helps the system to achieve fault-tolerance to control surface damage. The large computer storage requirement required for a gain scheduled LQ design is also avoided.**

**Nomenclature**

$V$ = true velocity, ft/sec

$u$ = velocity in $x$-axis direction, ft/sec

$w$ = velocity in $z$-axis direction, ft/sec

$\alpha$ = angle of attack, radian ( range $-10°$ to $45°$ )

$\theta$ = Euler (pitch) angle, radian

$q$ = pitch rate, rad/sec

$h$ = altitude, ft

$P_{pow}$ = engine power

$\delta_T$ = throttle setting, ( 0.0 – 1.0 )

$\delta_E$ = elevator setting, degree

$T$ = total instantaneous engine thrust, lb

$m$ - total airplane mass, slugs

---

[1] Ph.D. Student., Dept. of Electrical Engineering, Email: yhuo@usc.edu. Student Member AIAA.
2 Professor, Dept. of Mechanical Engineering, Email: mmirmir@calstatela.edu. Member AIAA.
3 Professor, Dept. of Electrical Engineering, Email: ioannou@usc.edu. Member AIAA.
4 Associate Professor, Dept. of Aerospace Engineering, Email: rcolgren@ku.edu. Associate Fellow AIAA.

$C_{X,t}$ - total x-axis force coefficient, table

$C_{Z,t}$ = total z-axis force coefficient, table

$C_{M,t}$ = total pitching-moment coefficient, table

$C_T$ = the look-up table defining engine dynamics

$\overline{q}$ = dynamic pressure, psf

$b$ = wing span (ft)

$S$ = wing platform area ($ft^2$)

$\overline{c}$ = mean aerodynamic chord (ft)

$g$ = gravitational constant ($ft/sec^2$)

$I_y$ = pitch moment of inertia ($slug\text{-}ft^2$)

## I. Introduction

Flight control law design for high-performance aircraft is a challenging problem, due to the sensitivity to changes in flight condition and the difficulty in measuring and estimating the aerodynamic characteristics of the vehicle. A common control design approach has been to use robust control. Some robust flight control design examples can be found in references [1] through [6]. However, traditional robust control is inadequate for the wide range of flight conditions fighter aircraft encounter. This problem can be addressed by making the controller 'learn' the aircraft's dynamics and then to adjust its parameters or structure. This is an example of 'intelligent' flight control. Multivariable adaptive control is one such 'intelligent' design (references [7] and [8]). Since frequently the flight dynamics are non-minimum phase, multivariable adaptive pole placement control is often chosen (references [9] and [10]). This paper investigates the application of adaptive linear quadratic (ALQ) design, which combines an adaptive law with the standard linear quadratic (LQ) control structure. The proposed robust adaptive law measures and estimates the most recent aircraft aerodynamics according to the current flight condition, then adjusts the controller parameters by solving the corresponding LQ problems. As an illustrative example, the longitudinal subsystem in steady state flight is considered in this paper. The method can readily be extended to the aircraft's lateral-directional dynamics and to other flight conditions. The aerodynamics of the F-16 fighter aircraft are linearized at different operating points, and a traditional gain scheduled LQ design implemented for comparison and validation. Simulation results of the ALQ and gain-scheduled LQ designs are analyzed and compared. It is seen that the ALQ methodology is superior to the gain-scheduled LQ controller in both performance and computer storage requirements.

This paper is organized as follows. Section II presents the aerodynamic model of the F-16 aircraft. The traditional gain-scheduled LQ design is illustrated in Section III. In Section IV the ALQ controller with adaptive laws is developed. Simulation results are presented in Section V. Finally, concluding remarks are presented in Section VI.

## II. Mathematical Model of the F-16 Aircraft

As an example of a mature fighter aircraft, the F-16 was chosen as the aircraft model for conducting the controller design. The full six-degree-of-freedom (6DOF) non-linear aircraft model can be found in references [11] and [12]. The mathematical model uses aerodynamic data from NASA Langley wind tunnel tests based on a 1/16 scale model of the F-16 aircraft. The data applies to speeds up to Mach=0.6, and were used in a NASA piloted simulation reported in reference [12]. In general, the 6DOF dynamics of the aircraft are highly coupled. However, for straight and level flight (zero bank angle), the longitudinal dynamics can be decoupled from the lateral-directional dynamics. In this study we will consider the decoupled model of the longitudinal aircraft dynamics as an illustrative example for our ALQ design.

$$\dot{u} = -qw - g\sin\theta + \frac{1}{m}(\bar{q}SC_{X,t} + T) \tag{1}$$

$$T = C_T(\delta_T, V, h, P_{poe}) \tag{2}$$

$$\dot{w} = qu + g\cos\theta + \frac{\bar{q}S}{m}C_{Z,t} \tag{3}$$

$$\dot{V} = \frac{u\dot{u} + w\dot{w}}{V} \tag{4}$$

$$\dot{\alpha} = \frac{u\dot{w} - w\dot{u}}{V^2} \tag{5}$$

$$\dot{\theta} = q \tag{6}$$

$$\dot{q} = \frac{\bar{q}S\bar{c}}{I_y}C_{M,t} \tag{7}$$

$$\dot{h} = V\cos\alpha\sin\theta - V\sin\alpha\cos\theta \tag{8}$$

$$\dot{P}_{pow} = -P_{pow} \tag{9}$$

In straight and level flight, the non-linear dynamic Eq. (1-9) can be linearized at different points within the flight envelope as defined by the aircraft's velocity and altitude. By trimming the aircraft at the specified velocity and altitude, then numerically linearizing equations of motion at the trim point, the longitudinal dynamics of the aircraft can be described by a family of LTI models as follows:

$$\begin{aligned} \dot{\mathbf{x}} &= \mathbf{A}\mathbf{x} + \mathbf{B}\mathbf{u} \\ \mathbf{y} &= \mathbf{C}\mathbf{x} \end{aligned} \tag{10}$$

where $\mathbf{x} = [V \quad \alpha \quad \theta \quad q \quad h \quad P_{pow}]^T$ is the state vector, $\mathbf{u} = [\delta_T \quad \delta_E]^T$ is the control vector, and $\mathbf{y} = [V \quad h]$ is the output vector. The control objective is to track the command velocity and altitude vector $[V_{com} \quad h_{com}]$. Without loss of generality we make the assumption that the pair $(\mathbf{A}, \mathbf{B})$ is stabilizable, and use Eq. (10) as the basis for the control design.

## III. Gain Scheduling LQ Tracker Design

For the LTI model (10), the LQ design can achieve zero output tracking error defined as:

$$e_v = V_{com} - V\,,\; e_h = h_{com} - h \tag{11}$$

The LTI model of the system can be augmented as:

$$\begin{aligned} \dot{\mathbf{x}}_{aug} &= \mathbf{A}_{aug}\mathbf{x}_{aug} + \mathbf{B}_{aug}\mathbf{u} \\ \mathbf{y} &= \mathbf{C}_{aug}\mathbf{x}_{aug} \end{aligned} \tag{12}$$

where $\mathbf{x}_{aug} = [e_v \quad e_h \quad V \quad \alpha \quad \theta \quad q \quad h \quad P_{pow}]^T$ is the augmented state vector, whereas $\mathbf{u} = [\delta_T \quad \delta_E]^T$ and $\mathbf{y} = [V \quad h]$ remain the same as before. For a step command vector $[V_{com} \quad h_{com}]$, the system matrices $A_{aug}$, $B_{aug}$ and $C_{aug}$ become:

$$\mathbf{A}_{aug} = \begin{bmatrix} -1 & 0 & 0 \\ 0 & -1 & 0 \\ 0 & 0 & \mathbf{A} \end{bmatrix}, \mathbf{B}_{aug} = \begin{bmatrix} 0 & 0 & 0 \\ 0 & 0 & 0 \\ 0 & 0 & \mathbf{B} \end{bmatrix}, \text{and } \mathbf{C}_{aug} = \begin{bmatrix} 0 & 0 & \mathbf{C} \end{bmatrix} \tag{13}$$

Using the augmented system, the tracking problem for model (10) is equivalent to a regulator problem for model (12). Following the LQ control structure, the performance index is defined as:

$$J = \int_0^\infty (\mathbf{x}_{aug}^T \mathbf{Q} \mathbf{x}_{aug}^T + \mathbf{u}^T \mathbf{R} \mathbf{u}) dt \,, \; \mathbf{Q} > \mathbf{0}, \quad \mathbf{R} > \mathbf{0} \tag{14}$$

The solution using full state feedback control is given by:

$$\mathbf{u} = -\mathbf{K}\mathbf{x}_{\mathbf{aug}} \tag{15}$$

where the optimal gain $\mathbf{K}$ is obtained from:

$$\mathbf{K} = \mathbf{R}^{-1} \mathbf{B}_{aug}^T \mathbf{P} \tag{16}$$

and the matrix $\mathbf{P}$ is the positive-definite solution of the algebraic Riccati equation:

$$\mathbf{A}_{\mathbf{aug}}^{\mathbf{T}} \mathbf{P} + \mathbf{P} \mathbf{A}_{\mathbf{aug}} - \mathbf{P} \mathbf{B}_{\mathbf{aug}} \mathbf{R}^{-1} \mathbf{B}_{\mathbf{aug}}^{\mathbf{T}} \mathbf{P} + \mathbf{Q} = 0 \tag{17}$$

Here we assume that the state variables are measurable either directly or indirectly, thus we implement Eq. (15) directly within the system. The closed-loop stability is therefore ensured, and the performance index is minimized. For each specified velocity and altitude, the LTI model can be derived. The above procedure can be repeated to generate the database of optimal gains $\mathbf{K}$ at the different combinations of aircraft velocity and altitude. In the on-line implementation, the optimal gain $\mathbf{K}$ is obtained from this database using gain-scheduling.

In this paper a two-dimensional interpolation is used to calculate the optimal gain $\mathbf{K}$ at any combination of velocity and altitude. The descriptive diagram is shown in Figure 1. Let the triple ( $\mathbf{K}_{ij}$, $V_i$ , $h_j$ ) i,j=1,2 be the representation of the optimal gain $\mathbf{K}_{ij}$ derived from the LTI model of a specified $V_i$ , $h_j$ pair. Then the gain $\mathbf{K}$ at any point inside the rectangle can be decided by the following interpolation algorithm in Eq. (18) through (20) and shown in Fig. 1.

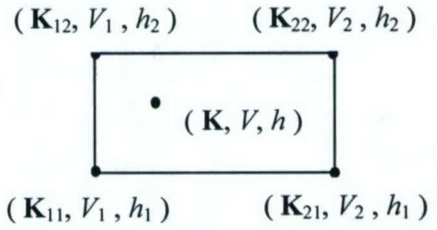


**Figure 1. Interpolation of Optimal Gain $\mathbf{K}$ at any Velocity $V$ and Altitude $h$**

$$\mathbf{K}_1 = \mathbf{K}_{11} + \frac{V - V_1}{V_2 - V_1} \cdot (\mathbf{K}_{21} - \mathbf{K}_{11}) \tag{18}$$

$$\mathbf{K}_2 = \mathbf{K}_{12} + \frac{V - V_1}{V_2 - V_1} \cdot (\mathbf{K}_{22} - \mathbf{K}_{12}) \tag{19}$$

$$\mathbf{K} = \mathbf{K}_1 + \frac{h - h_1}{h_2 - h_1} \cdot (\mathbf{K}_2 - \mathbf{K}_1) \tag{20}$$

## IV. Adaptive LQ Control Design

The key advantage of using an adaptive LQ design is that it combines an adaptive law with the LQ control structure. In this scheme, the adaptive law estimates and updates the system information to update the controller parameters. Using Eq. (10) as the nominal system description, matrices $\mathbf{A}$ and $\mathbf{B}$ are determined and updated for the flight condition. This includes the body axis aerodynamic forces and moments. The aerodynamic data including stability derivatives cannot be accurately determined in some flow regimes (e.g. transonic flight) either by wind tunnel experiments or computational fluid dynamic (CFD) studies. Experiments and measurements in wind-tunnel tests contain modeling errors. The matrices $\mathbf{A}$ and $\mathbf{B}$ derived from linearization introduce further deviations from the exact system. One way to obtain an accurate description of the system is to estimate and update these matrices on-line using in-flight system dynamic response information. A general procedure for designing a robust adaptive law is outlined in the described herewith. From the first scalar equation in model (10), we have:

$$\dot{x}_1 = a_{11}x_1 + a_{12}x_2 + \cdots + a_{16}x_6 + b_{11}\delta_T + b_{12}\delta_E \tag{21}$$

where $a_{ij}, b_{ij}$ are elements of $\mathbf{A}$ and $\mathbf{B}$ matrices at the $i$-th row and $j$-th column.

Reorganizing Eq. (21), and assuming that the measurements of the state variables and their derivatives are available either directly or indirectly, we have:

$$z = \zeta^{*T}\phi \tag{22}$$

where $z = \dot{x}_1$;

$\zeta^* = [a_{11} \quad a_{12} \quad \cdots \quad a_{16} \quad b_{11} \quad b_{12}]^T$ is the true value of the elements in $\mathbf{A}$ and $\mathbf{B}$;

$\phi = [x_1 \quad x_2 \quad \cdots \quad x_6 \quad \delta_T \quad \delta_E]^T$ is the regressor vector.

The robust adaptive law chosen here is the gradient method with $\sigma$-modification described in reference [7]. The estimate $\zeta(t)$ of $\zeta^*$ is given by:

$$\dot{\zeta} = \Gamma\varepsilon\phi - \Gamma\sigma\zeta \tag{23}$$

where

$$\varepsilon = \frac{z - \zeta^T\phi}{1 + \phi^T\phi} \tag{24}$$

$$\sigma = \begin{cases} 0 & \|\zeta\| < M_0 \\ \sigma_0\left(\dfrac{\|\zeta\|}{M_0} - 1\right) & M_0 \le \|\zeta\| < 2M_0 \\ \sigma_0 & \|\zeta\| \ge 2M_0 \end{cases} \tag{25}$$

with $\sigma_0 > 0$, $M_0 \ge 2\|\zeta^*\|$, and $\Gamma = \Gamma^T > 0$.

Applying the same procedure to the other scalar state equations in model (10), estimates for all the elements in $\mathbf{A}$ and $\mathbf{B}$ matrices can be obtained. Denote the estimated matrices by $\hat{\mathbf{A}}$ and $\hat{\mathbf{B}}$, and using the certainty equivalence principle, the LQ design process can proceed in much the same way as in Section 3 using the estimated model:

$$\begin{aligned} \dot{\mathbf{x}} &= \hat{\mathbf{A}}\mathbf{x} + \hat{\mathbf{B}}\mathbf{u} \\ \mathbf{y} &= \mathbf{C}\mathbf{x} \end{aligned} \tag{26}$$

Since the estimated matrices $\hat{\mathbf{A}}$ and $\hat{\mathbf{B}}$ are obtained using the current measurements of the state and control variables, they capture the most recent system changes, hence more accurately represent the system dynamics. Intuitively, one expects the ALQ design to perform better than the gain-scheduled LQ design. This is confirmed by the simulation results given in Section IV. The block diagram of the ALQ design is shown in Fig. 2.

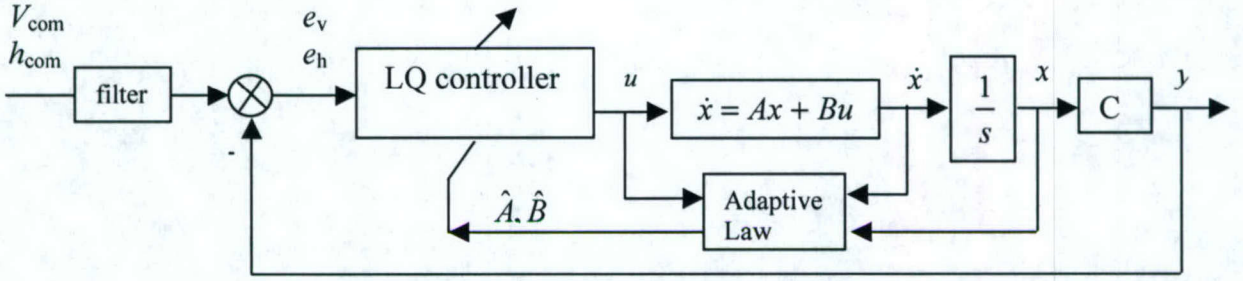


**Figure 2. Block diagram of ALQ control design**

*Remark 1*: The drawback to using the adaptive law to achieve more accurate estimates of the system parameters is the introduction of increased computational complexity within the on-line flight control computer. The computational burden can be somewhat reduced by noting that not all element of $\hat{\mathbf{A}}$ and $\hat{\mathbf{B}}$ need to be estimated. For example, from equation (6), one can directly set:

$$[a_{31} \quad a_{32} \quad \cdots \quad a_{36} \quad b_{31} \quad b_{32}] = [0 \quad 0 \quad 0 \quad 1 \quad 0 \quad 0 \quad 0 \quad 0]$$

*Remark 2*: In many cases, off-line analysis can render useful knowledge about the elements of $\hat{\mathbf{A}}$ and $\hat{\mathbf{B}}$. For example, estimates of their upper and lower bounds can be used in updating the $\hat{\mathbf{A}}$ and $\hat{\mathbf{B}}$ matrices. In this work, the projection in the adaptive law benefited from the utilization of the estimated elements' bounds. For example, let $\overline{\zeta}$ and $\underline{\zeta}$ denote the upper and lower bound of the estimated parameter $\zeta$. The gradient method with projection gives:

$$\dot{\zeta} = \begin{cases} \text{Eq(23)} & \underline{\zeta} < \zeta < \overline{\zeta} \\ 0 & \text{elsewhere} \end{cases} \tag{27}$$

*Remark 3*: The purpose of the parameter identification is to design the control law. One problem we have to solve is that the presented adaptive law cannot guarantee system controllability. In this case, the adaptive law needs to be modified, for example, using the switching excitation. The details can be found in [6].

*Remark 4*: Finally, to reduce the computational burden, one can develop the discretized version of the above adaptive law. The computational effort to directly implement the discrete adaptive LQ design is significantly less than the continuous-time scheme, since the Riccati equation is solved at time intervals rather than continuously.

## V. Simulation for an F-16 aircraft

Both of the control designs in Section 3 and Section 4 were implemented using the longitudinal dynamics of the F-16 fighter aircraft. The mathematical model of the F-16 aircraft uses data from NASA Langley wind tunnel tests based on a 1/16 scale model. The data is valid up to Mach=0.6. Correspondingly the velocity and altitude range examined in the simulations are:

Velocity: 400 to 900 ft/sec, with points spaced 125 ft/sec apart from each other

Altitude: 0 to 40,000 ft, with points spaced 2,500ft apart from each other

*Case I -- Nominal case*

In the nominal case, where the aircraft's mathematical model and its dynamics are identical, both the gain scheduled LQ and ALQ designs generate satisfactory responses to the velocity and altitude tracking commands. The following plot (Fig. 3) shows the transient responses of the outputs and the control commands to a commanded step change in the velocity and altitude.

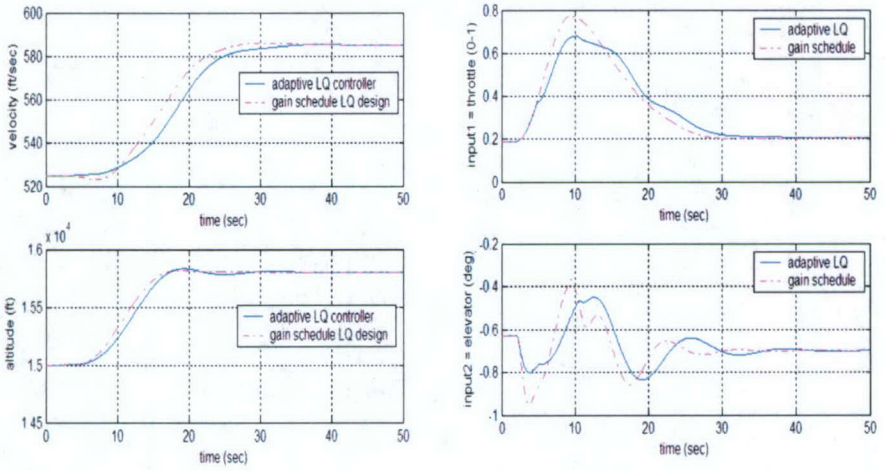


**Figure 3. Simulation for the nominal case**

*Case II -- Pitch moment coefficient uncertainty*

During the wind tunnel tests, the experimental data are used to generate look-up tables for all the aerodynamic coefficients. In these experiments, the accuracy of the measurements vary depending on the quality of the test and on which aerodynamic coefficient is being generated. Typically, the measurement of the pitching moment coefficient $C_m$ is associated with some degree of uncertainty, as much as 70% and 80% on the lower and upper bounds respectively. Let $C_{m,0}$ denote the look-up table value to set the uncertainty bounds on the true value for $C_m$ as:

$$30\% \times C_{m,0} \leq C_m \leq 180\% \times C_{m,0}$$

In this simulation, the lower value of $C_m$ has been assumed, i.e.,

$$C_m = 30\% \times C_{m,0}$$

The simulation results are shown in Fig. 4. It shows a comparison between the adaptive LG and gain schedule LG for the velocity and altitude outputs to a commanded step change in both.

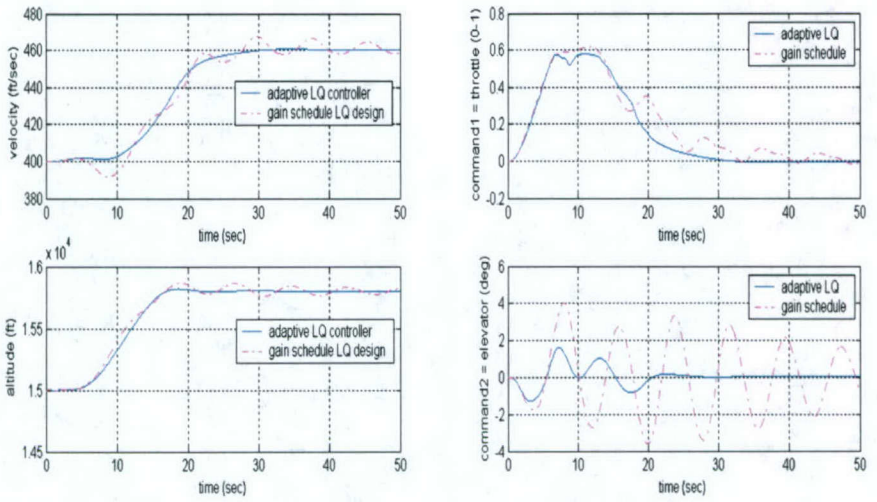


**Figure 4. Simulation for the Pitch Moment Coefficient Uncertainty**

*Case III – Control Actuator Failure*

In this experiment we simulate the control actuator failure that the throttle setting get stuck at some unknown position and the elevator deflection angle is drifting with time. In order to do the failure simulation we add an artificial redundant throttle command and split the elevator panel into two pairs. The control objective is to keep the aircraft at the constant velocity and altitude in the presence of failures. The resultant velocity and altitude responses are shown below in figure 5, and the control commands are shown in figure 6.

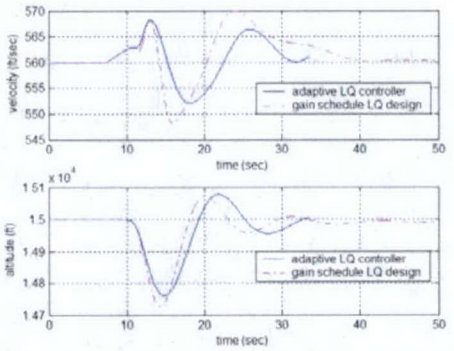


**Figure 5. Velocity and Altitude Responses with Actuator Failures**

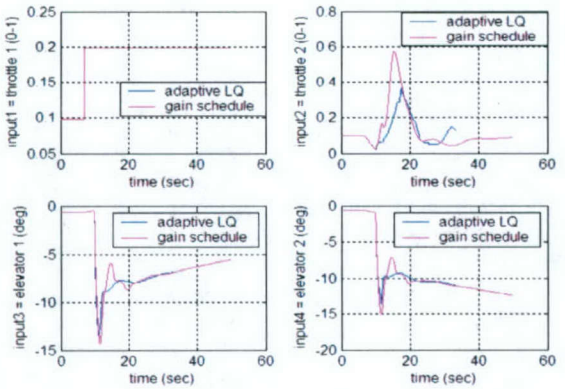


**Figure 6. Control Commands with Actuator Failures**

From these experiments, we see that the ALQ design is superior to the traditional gain-scheduled LQ design in that the ALQ design updates the system's information and uses it to modify the controller parameters on-line. Also, the ALQ control design is more robust to modeling errors and uncertainties. On the other hand, the ALQ design has greater potential to cope with unexpected changes in the system. These uncertainties include battle damage and control surface actuation failures that will affect the systems' aerodynamic behavior and dynamic response.

## VI. Summary and Conclusions

This paper investigates two control methods used in designing the flight control law for the F-16 fighter aircraft. These are the ALQ control design method and the traditional gain-scheduled LQ design method. Both of these methods are outlined in this paper. Simulations of both control law designs are shown and the results compared. The ALQ control design combines a robust adaptive law with the LQ control structure. The robust adaptive law estimates the system's most recent model from measurements of the current flight condition. Then this estimation is used to adjust the controller parameters by solving the LQ problem. The ALQ method can 'learn' the dynamics, addressing a deficiency in the gain-scheduling method, where the models are fixed and there is no 'learning' capability. These simulations, which use the longitudinal dynamics trimmed in steady-state flight, verify this conclusion. It was demonstrated that the ALQ methodology is superior to the gain-scheduled LQ design in fault-tolerance performance, while storage requirements when compared to gain scheduled LQ designs is reduced.

## References


[1]. C. I. Marrison and R. F. Stengel, Design of Robust Control Systems for a Hypersonic Aircraft, Journal of Guidance, Control, and Dynamics, Vol. 21, No. 1, pp58-63, 1998.

[2]. J.-F. Magni, S. Bennani, and J. Terlouw (eds.). Robust flight control: a design challenge, Springer, 1997.

[3]. R. J. Adams, et al., Robust multivariable flight control, Springer-Verlag, 1994.

[4]. R. Hyde, $H_\infty$ aerospace control design: a VSTOL flight application, Springer, 1995.

[5]. R. D. Colgren, D. Enns, et. al. "Structured Singular Value Synthesis Applied to the F-117A," 1996 IFAC World Congress, San Francisco, CA, 1-5 July 1996.

[6]. R. D. Colgren, "Non-linear H∞ Control of a Missile's Roll Axis," 1994 American Control Conference, Baltimore, MD, Vol. 2, pp. 2109-2113, 29 June-1 July 1994.

[7]. J. Sun and P. Ioannou, Robust Adaptive LQ Control Schemes, IEEE Transactions on Automatic Control, Vol.37, No.1, pp100-106, 1992.

[8]. P. Ioannou and J. Sun, Robust Adaptive Control, Prentice-Hall Inc., 1996.

[9]. C.-L. Lin, Neural Net-Based Adaptive Linear Quadratic Control, Proceedings of the 12th IEEE International Symposium on Intelligent Control, Istanbul, Turkey, pp187-192, 1997.

[10]. L. Mo and M. M. Bayoumi, Adaptive Pole Placement Control of MIMO Systems, IEEE Transactions on Automatic Control, Vol.38, No.6, pp967-970, 1993.
[11]. B. L. Stevens, F. L. Lewis, Aircraft Control and Simulation, John Wiley & Sons, Inc. 1992.
[12]. L. T. Nguyen, et al., Simulator study of stall/post-stall characteristics of a fighter airplane with relaxed longitudinal static stability, NASA Tech. Pap. 1538, NASA, Washington, D.C., Dec. 1979.

## Appendix III


1. S. Choi, H. Xu, and M. Mirmirani, "LQG Control of a CFD-Based Aeroelastic Wing Model,", IEEE Conference on Decision and Control, Maui, Hawaii, December 2003
2. S. Choi, "Nonlinear Dynamics and Control for an Aeroservoelastic System Using Neural Networks", California State University, Los Angeles, California, March 2003
3. C. He, S. Choi, M. Mirmirani, and C. Wu, "CFD-based Aeroelasticity Analysis in Transonic Flow Regime," ASME 2004 International Mechanical Engineering Congress and RD&D Expo, Anaheim, California, November 2004

# LQG Control of a CFD-based Aeroelastic Wing Model

Sang Bum Choi†, Haojian Xu‡, and Maj Dean Mirmirani†

† Multidisciplinary Flight Dynamics and Control Lab
California State University
Los Angeles, CA 90032, USA
mmirmir@calstatela.edu

‡ Department of Electrical Engineering
University of Southern California
Los Angeles, CA 90089, USA
haojian@usc.edu

*Abstract* – **This paper presents a Linear Quadratic Gaussian (LQG) algorithm for suppression of flutter in an aeroelastic wing. CFD-based input output data and autoregressive moving average identification method were employed to develop a state space model for aerodynamic forces. A finite element model of the wing was constructed to obtain the flexible modes and a second set of linear state space equations representing the structural dynamics of the wing. The outputs of the coupled aeroelastic model, pitch, plunge, and the movement of the control surface at the trailing edge of the wing were used to design a combined state estimator and a linear quadratic regulator. Simulation results presented validates the effectiveness of the controller to suppress flutter induced by increasing dynamic pressure.**

## I. INTRODUCTION

The interaction between aerodynamic, inertia and structural forces can result in aeroelastic instability such as flutter in the airframe or wing of an aircraft. Flutter can manifest itself in large amplitude limit cycles or unacceptable wing motions and can potentially be catastrophic and result in destruction of the airframe or the wing during the flight. That is why flight flutter testing is a mandatory part of certification process that must be undertaken to demonstrate that the aircraft is flutter free in its entire flight envelop. So far aeroelastic instabilities such as flutter has been treated only passively through proper airframe and wing structural design. However, for the high-performance air vehicles of the future suppression of aeroelastic instabilities must depend on active control as they are designed to be increasingly lightweight and to operate over a wide range of speed and altitude. Interaction between structural dynamics, aerodynamics and flight control system is called aeroservoelasticity. A prerequisite to active control design is to have a good model which captures the salient characteristics of the aeroelastic phenomenon but at the same time is manageable for control design. The progress in computational fluid dynamics (CFD) has lead to construction of accurate aeroelastic models [1-10]. A number of researchers have proposed control strategies for active suppression of flutter for linear and nonlinear structures [9]. Most of these works have been performed on rather simple aeroelastic models for an airfoil, which lack the potential to be extended to more realistic configurations involving complex mode shapes. CFD-based aeroelasticity is an emerging technology that has the potential for the development of accurate aeroelastic models and design of active controllers for complex airframe and wing configurations [1]. In this paper, we present an algorithm for active suppression of flutter in an aeroservoelastic wing model based on the Linear Quadratic Regulator controller with Gaussian measurement noise (LQG). Our aeroelastic model is obtained using CFD-based input-output data for identification of aerodynamic forces and finite element model for the flexible mode shapes of the wing. The approach is applicable to any complex airframe or wing geometry.

## II. THE AEROELASTIC MODEL

The wing model, shown in Fig. 1 was obtained from NASA Dryden Flight Research Center. It is a cantilever wing that utilizes a NACA 0012 airfoil. The wing has a 2.0178m span and a 1.0089 m chord length. The control surface, an aileron, attached to the trailing edge of the wing has a 0.6053m span and a 0.2522m chord. It is centered at 1.22m from the wingspan.

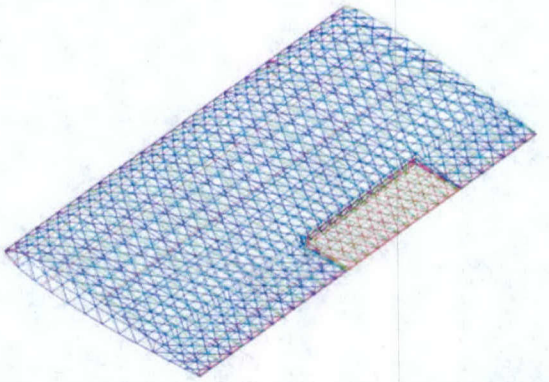

Fig. 1 Structural FEA Model of a Cantilever wing with NACA 0012 airfoil

Unlike most of the previous research in this area, our model is obtained using a set of CFD-based aerodynamic data and a finite element (FE) model of the wing to generate the structural modes for the coupled aeroelastic blocks shown in Fig. 4. The plant consists of two sets of

linear state space models: one modeling the aerodynamic loads, the other representing the elastic deformation of the wing and the motion of the control surface.

The state space model for the structural dynamics is obtained using a FE model of the wing. The FE model was created in I-DEAS. The result of this analysis is a set of undamped equations of motion for, the nodal displacement vector $\xi$:

$$M\ddot{\xi} + K\xi = 0 \tag{1}$$

where $M$ and $K$ are the mass and stiffness matrices, respectively. Equation (1) is solved to yield the natural frequencies, and mode shapes that contain both the elastic modes and the control surface motion. Only two fundamental modes (the first bending and the first tensional) and the first mode related to the motion of the control surface ($\delta_E$) are retained. The first bending mode simulates the plunge ($h$), and the first twisting mode simulates changes in the angle of attack ($\alpha$). These mode shapes and the associated frequencies are shown in Table 1.

TABLE I
NORMAL MODES AND FREQUENCIES

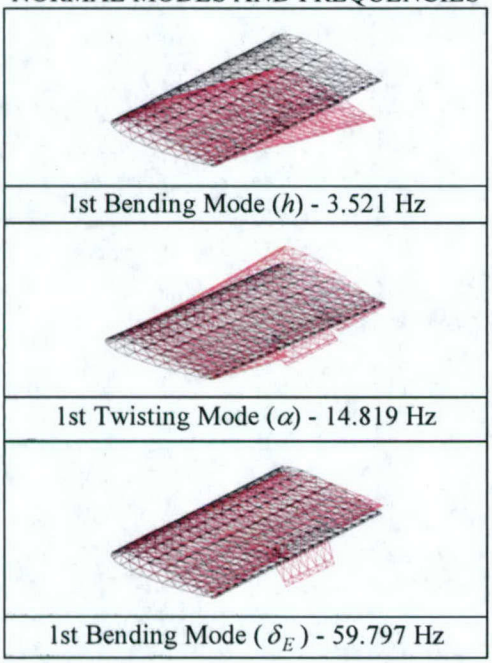

| |
|---|
| 1st Bending Mode ($h$) - 3.521 Hz |
| 1st Twisting Mode ($\alpha$) - 14.819 Hz |
| 1st Bending Mode ($\delta_E$) - 59.797 Hz |

Arbitrary motions of the wing and the control surface can then be formulated by a linear combination of mode shapes multiplied by a generalized displacement. The aerodynamic force applied on a surface around a structural node is obtained by creating a CFD mesh around the wing. The combined structure and CFD-based aerodynamic loads will give rise to the following matrix equation of motion for the aeroelastic wing in terms of the generalized coordinates $q$:

$$\hat{M}\ddot{q} + \hat{K}\dot{q} + \hat{C}q + f_a(t) + f_I(t) = 0 \tag{2}$$

where,

| | |
|---|---|
| $\hat{M} = \Phi^T M \Phi$ | Generalized mass matrix |
| $\hat{K} = \Phi^T K \Phi$ | Generalized stiffness matrix |
| $\hat{C} = \Phi^T C \Phi$ | Generalized damping matrix |
| $q = \Phi^T \xi$ | Vector of generalized displacements |
| $\Phi$ | Modal matrix |
| $f_a = \Phi_a^T pS$ | Aerodynamic load vector, where $p$ is the Euler pressure, $S$ is the appropriate surface area around the node, $\Phi_a$ pertains is the modal vector interpolated for structural nodes. |
| $f_I$ | User input, impulse force vector |

Once mode shapes and the associated frequencies are determined the linear discrete-time state space model for small structural deformations is obtained using the generalized displacements and their corresponding velocities as the states.

The state space equation form can be formulated from (2) as:

$$x_s(k+1) = G_s x_s(k) + H_s[f_a(k) + f_I(k)]$$
$$y_s(k) = C_s x_s(k) + D_s[f_a(k) + f_I(k)]$$

The aerodynamic model is obtained using a discrete autoregressive moving average (ARMA) system identification method applied to a trimmed condition of the wing. The system identification makes the assumption that the aerodynamics behaves linearly about potentially nonlinear steady state flow in each discrete iteration step associated with a given flexible configuration of the wing and the rigid motion of the control surface. As such, the dynamics of the airflow and the associated pressure can be identified as a linear state space model using a set of appropriate input and output data generated by steady and unsteady CFD solutions of the flow [1]. To obtain the state space model for the aerodynamics the corresponding IO representation for the ARMA model at time step $k$ is written as:

$$f_a(k) = \sum_{i=1}^{na}[a_i]f_a(k-i) + \sum_{j=0}^{nb-1}[b_j]q(k-j) \tag{3}$$

Equation (3) relates the current generalized aerodynamic force output to *na* past outputs and *nb* past inputs of the unsteady CFD solver. Matrices *a*'s and *b*'s (scaled by the training density) is determined by fitting the model to a set of CFD-generated "training" IO data using NASA-developed multidisciplinary software *STARS*. Fig. 2 shows the Y-wing CFD model.

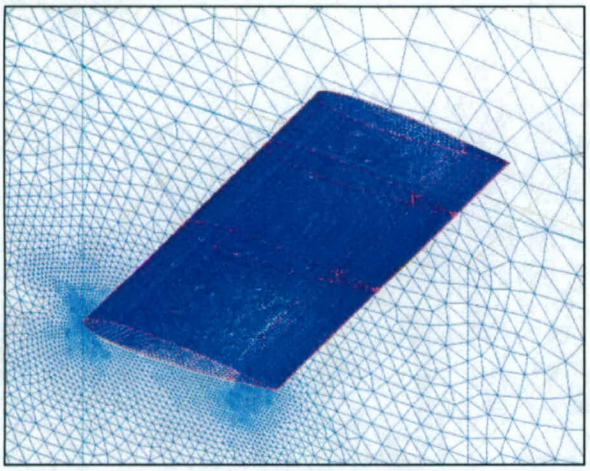

Fig. 2 CFD Model of "Y-Wing"

The state space form of the unsteady CFD aerodynamic system can be obtained as [1]:

$$x_a(k+1) = G_a x_a(k) + H_a q(k)$$
$$\hat{f}_a(k) = C_a x_a(k) + D_a q(k) + f_o$$

where,

$$G_a = \begin{bmatrix} a_1 & \cdots & a_{na-1} & a_{na} & b_1 & \cdots & b_{nb-2} & b_{nb-1} \\ I & & & & & & & \\ & \ddots & & & & & & \\ & & I & & & & & \\ & & & 0 & & & & \\ & & & & I & & & \\ & & & & & \ddots & & \\ & & & & & & & I \end{bmatrix}$$

$$H_a = [b_0 \quad 0 \quad \cdots \quad 0 \quad I \quad 0 \quad \cdots \quad 0]^T$$

$$C_a = [a_1 \quad \cdots \quad a_{na-1} \quad a_{na} \quad b_1 \quad \cdots \quad b_{nb-2} \quad b_{nb-1}]$$

$$D_a = [b_0]$$

The flight conditions assumed in this study are described in Table 2.

TABLE II
FLIGHT CONDITION

| | |
|---|---|
| Mach number | 2.0 |
| Angle of attack | 0° |
| Speed of sound at infinity | 340.29 m/s |

In the coupled aeroelastic interaction, the motion of the whole wing or the control surface will change the aerodynamic flow near the wing which in turn excites the structural modes, a process that can result in limit cycles with growing amplitude.

## III. CONTROLLER DESIGN

The analysis of the open-loop combined structural and aerodynamic state space model for the "Y-Wing" shows that the system can become unstable for certain values of $\rho_{\inf}$. The objective is to design a controller such that the outputs of closed-loop system, pitch and plunge remain near zero subject to the control constraint $|u| \le 15°$ which describes the limits of the control surface movement. In addition, we assume that the measurements of the outputs and the plant itself contain Gaussian white noise. Linear Quadratic Regulator design was chosen because the controller can achieve a trade-off between performance and control effort in the present of measurement noise. The LQG controller consists of an optimal feedback gain and a Kalman state estimator. The two components are designed independently using the so-called "separation principle". The design process includes the following steps:

### *A. Model Reduction*

The open-loop system is a discrete time model with 1 input, 3 outputs and 17 states. The large size of the plant brings undesirable complexity to the controller design. Furthermore, a controller designed for a large order system will be of large order too. Therefore, a model reduction method was used to reduce the size of aerodynamic model from 9 states to only 3 states. The model reduction method used is a frequency approximation with input/output balancing. The balanced gramians reflect the combined controllability and observability of individual states of the balanced model. The balanced gramians of aerodynamic model is:

gs = 1.0e+07*[3.4798 0.1050 0.0006 0.0002 0.0001
0.000 0.0 0.0 0.0]

Six states with small gramians (indicating the weakest coupling with the input and output) were deleted while the remaining 3 states retain the most salient input-output characteristics of the original system. The singular values of the original system and the reduced-order aerodynamic model are shown in Fig. 3. The solid line indicates the original system and the dash line indicates the reduced-order system.

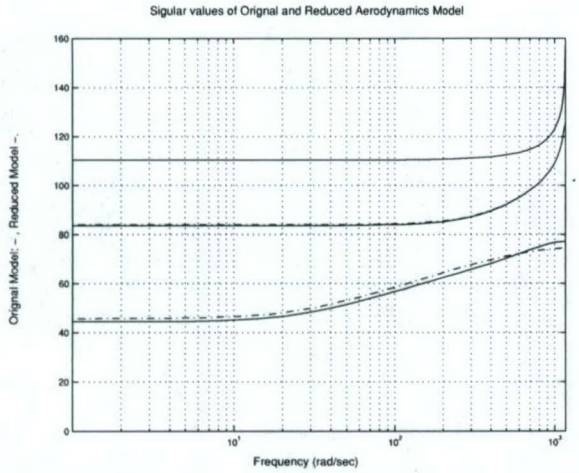


Fig. 3 Singular values of original aerodynamic model and reduced model

The closed loop system including the coupled aerodynamic – structural system and the Kalman filter – LQG gain matrix is shown in Fig. 4. A second order actuator model converting the output of the controller to the control surface movement is also included.

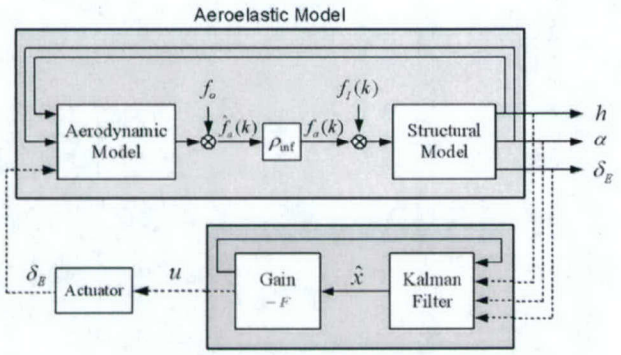


Fig. 4 The block diagram of aeroservoelastic model of "Y-Wing"

The detailed description of each block is as follows:

| Aerodynamic Model | |
|---|---|
| $G_a(9\times9)$, $H_a(9\times3)$, $C_a(3\times9)$, $D_a(3\times3)$ | State Space Matrices |
| $h$, $\alpha$, $\delta_E$ | Inputs |
| $\hat{f}(k)$ $(3\times1)$ | Outputs |
| **Structural Model** | |
| $G_s(6\times6)$, $H_s(6\times3)$, $C_s(3\times6)$, $D_s(3\times3)$ | State Space Matrices |
| $f_a(k)$ $(3\times1)$ | Inputs |
| $h$, $\alpha$, $\delta_E$ | Outputs |
| **Actuator Model** | |
| $G_c(2\times2)$, $H_c(2\times1)$, $C_c(1\times2)$, $D_c(1\times1)$ | State Space Matrices |
| $u$ | Input |
| $\delta_E$ | Output |

| Other Variables | |
|---|---|
| $h$ | Plunge |
| $\alpha$ | Pitch |
| $\delta_E$ | Control Surface Displacement |
| $u$ | Control Command. |
| $\rho_{\inf}$ | Representing Air Density (Scale Factor) |
| $f_a(k)$ $(3\times1)$ | Aerodynamic Force Vector |
| $f_o(k)$ $(3\times1)$ | Static Offset Force Vector |
| $f_I(k)$ $(3\times1)$ | Applied Structural Impulse Force Vector |

The open-loop system has one input $u$ and three outputs, $h$, $\alpha$, and $\delta_E$.

*B. LQG Controller*

The solution of the LQG Design is a combination of Kalman filtering and full-state feedback based on the so-called separation principle. Consider the following discrete time plant.

$$x(k+1) = Ax(k) + Bu(k) + Bw$$
$$y(k) = Cx(k) + Du(k)$$
$$y_v = y + v$$

The goal is to regulate the noisy output $y$ to zero. The plant is driven by control $u$ and the process noise $w$. The regulator uses the noisy measurements $y_v$ to generate the control input. Both $w$ and $v$ are modeled as white noise. In the "Y- wing" case, $x$ is 17x1, $y$ is 3x1, and $u$ is a scalar.

- Optimal State-Feedback Gain with Output Weighting

The first step in design is to seek a state-feedback law $u(k) = -Fx(k)$ that minimizes the cost function defined by:

$$J = \sum_{k=0}^{\infty} [y^T(k)Qy(k) + ru^2(k)]$$

The minimizing gain $F$ is obtained by solving an algebraic Riccati equation. The gain is called the LQ-optimal gain. The weighting matrix $Q$ and the scalar $r$ are user specified to define the trade-off between regulation performance (how fast $y$ goes to zero) and control effort. In the "Y-Wing" case $Q$=diag(10, 10, 10) and $r$=0.1 were chosen.

- Kalman State Estimator

The LQ-optimal state feedback $u(k) = -Fx(k)$ is not implementable if a full state measurement is not available. However, one can obtain a state estimate $\hat{x}$ such that

$u(k) = -F\hat{x}(k \mid k-1)$ remains optimal for the output-feedback problem. The state estimator generated by the Kalman filter is:

$$\hat{x}(k+1 \mid k) = A\hat{x}(k \mid k-1) + Bu(k) + L[y_v(k) - C\hat{x}(k \mid k-1) - Du(k)]$$

$L$ is the Kalman filter gain. The gain is determined by the noise covariance data, i.e., $E(ww^T) = q_n$ and $E(vv^T) = R_n$. In the "Y-Wing" case, $q_n$ was chosen 1 and $R_n$ was chosen as $diag(10,10,10)$. A large noise covariance $R_n$ is set to limit the high frequency gain. The Kalman filter is an optimal estimator minimizing the asymptotic covariance of the estimation error, i.e., $\lim_{t\to\infty} E[(x-\hat{x})(x-\hat{x})^T]$.

### C. Controller Reduction

The designed LQG controller has 9 states, too large for the simple system on hand. High order digital controllers are undesirable for real implementation. The same model reduction algorithm is applied to the controller to reduce the control law complexity with little change in the control system performance. The gramians of balanced controller in this case are:

gf = [0.9618 0.9092 0.2035 0.0245
0.0168 0.0148 0.0071 0.0064
0.0 0.0 0.0]

The last 6 states with relative small gramians were deleted. The reduced-order controller has only 3 states. Fig. 5 compares the singular value of original controller and reduced-order controller in frequency domain. The reduced-order controller has almost the same frequency response in high frequency area as original controller and 1db lower in amplitude in the low frequency region.

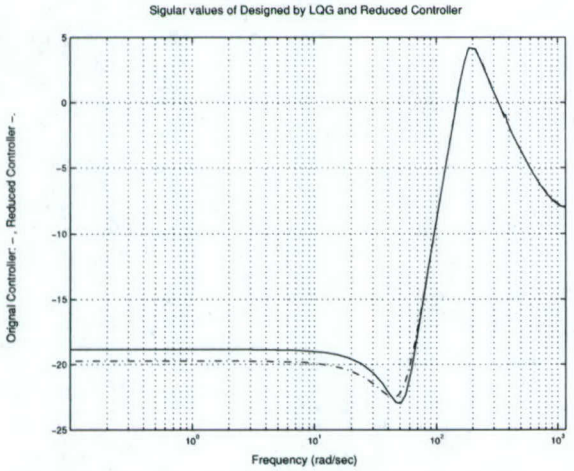


Fig. 5 Singular value of original controller and reduced-order controller

The state space model of the final LQG controller, $F$ is obtained as:

AF = [ 0.51791 0.46507 -0.21597
-0.44923 0.86064 0.08589
-0.21698 -0.07262 0.67765 ]

BF = [ 0.63026 -0.31400 -0.04273
-0.14962 0.13306 0.00581
0.19132 -0.15024 -0.01484 ]

CF = [-0.71467 -0.16320 -0.24139 ]

DF = [ 0 0 0 ]

## IV. SIMULATION RESULTS

In this section, we present the simulation results for the "Y-wing". The simulation results using the designed controller are shown in Figs. 6 and 7. It is seen that the open-loop system is unstable as the amplitude of oscillations grows unbounded. However, when the control is applied the plunge and pitch are stable and converge to zero. In Figs. 6 and 7, the controller starts acting at 0.2 second and at 0.5 second, respectively. In both the control effort satisfies the requirement $|u| \le 15°$.

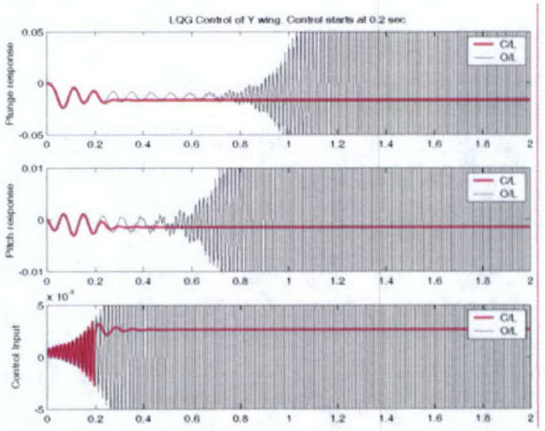


Fig. 6 Plunge and pitch response, control starts at 0.2 second

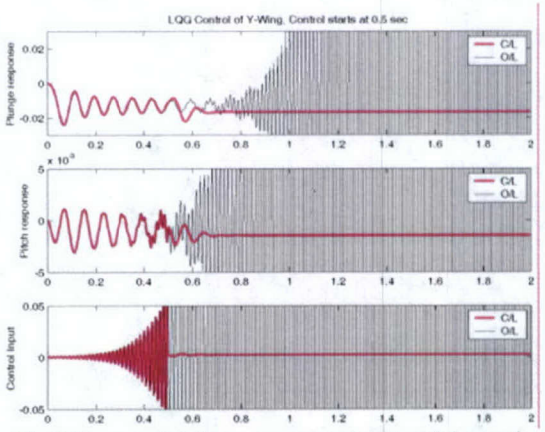


Fig. 7 Plunge and pitch response, control starts at 0.5 second

## V. CONCLUSIONS

The design of an LQG controller is for an aeroservoelastic wing was presented. The model was developed using CFD-based identification of aerodynamic forces and FEA generated elastic modes. The controller was designed in 4 steps: (a) the order of plant was reduced; (b) an optimal full-state feedback gain was designed; (c) a Kalman filter was designed to estimate the states based on the noisy measured outputs; (d) the order of controller was reduced to obtain a simple control law. The simulation results demonstrated that the controller is able to stabilize the wing.

## VI. ACKNOWLEDGMENTS

This project was supported by NASA Dryden Flight Research Center under Grant No. NAG4-175.

## VII. REFERENCES

[1] K. K. Gupta and J. L. Meek, *Finite Element Multidisciplinary Analysis*, AIAA Education Series; 2000.

[2] K. K. Gupta, L. S. Voelker, and C. Bach, "Finite Element CFD-Based Aeroservoelastic Analysis", *40th AIAA Aerospace Sciences Meeting & Exhibit*, Reno, NV, 2002, AIAA Paper 2002-0953.

[3] K. K. Gupta *et. al.*, "CFD-Based Aeroelastic Analysis of X-43 Hypersonic Flight Vehicle", *39th AIAA Aerospace Sciences Meeting & Exhibit*, Reno, NV, 2001, AIAA Paper 2001-0712.

[4] K. K. Gupta, *STARS – An Integrated, Multidisciplinary, Finite-Element, Structural, Fluids, Aeroelastic, and Aeroservoelastic Analysis Computer Program, STARS' User Manual*, 2003.

[5] M. Mirmirani, H. Xu, and S. Choi, "CFD-Based Aeroservoelasticity - Design Document, Technical Report", Department of Engineering, California State University, Los Angeles, 2001.

[6] C. H. Stephens and A. S. Arena, "Application of the Transpiration Method for Aeroservoelastic Prediction using CFD", 39th AIAA/ASME/ASCE/AHS/ASC Structures, Structural Dynamics, and Materials Conference and Exhibit, and AIAA/ASME/AHS Adaptive Structures Forum, Long Beach, CA, 1998, AIAA Paper 98-2071.

[7] T. J. Cowan, A. S. Arena, and K. K. Gupta, "Development of a Discrete-Time Aerodynamic Model for CFD-Based Aeroelastic Analysis", 37th AIAA, Aerospace Sciences Meeting and Exhibit, Reno, NV, 1999, AIAA Paper 99-0765.

[8] H. C. Gilliatt, T. W. Strganac, and A. J. Kurdila, "On the Presence of Internal Resonances in Aeroelastic Systems", 39th AIAA/ASME/ASCE/AHS/ASC Structures, Structural Dynamics, and Materials Conference and Exhibit and AIAA/ASME/AHS Adaptive Structures Forum, Long Beach, CA, 1998, AIAA Paper 98-1954.

[9] R. Bisplinghoff, H. Ashley, and R. Halfman, *Aeroelasticity*, Addison Wesley Publishing Company, Reading, Massachusetts, 1954.

[10] W. Silva, and D. Raveh, "Development of Unsteady Aerodynamic State-Space Models from CFD-Based Pulse Responses", 42nd AIAA/ASME/ASCE/AHS/ASC Structures, Structural Dynamics, and Materials Conference and Exhibit, Seattle, WA, 2001, AIAA Paper 2001-1213.

[11] D. M. Guillot and P. P. Friedmann, "Fundamental Aeroservoelastic Study Combining Unsteady Computational Fluid Mechanics with Adaptive Control", *Journal of Guidance, Control, and Dynamics*, Vol. 23, No. 6, 2000, pp 1117-1126.

# NONLINEAR DYNAMICS AND CONTROL FOR AN AEROSERVOELASTIC SYSTEM USING NEURAL NETWORKS

A Thesis

Presented to

The Faculty of the Department of Mechanical Engineering

California State University, Los Angeles

In Partial Fulfillment

Of the Requirements for the Degree

Master of Science

By

Sang Bum Choi

March 2003

ACKNOWLEDGMENTS

I must have done a lot of good in my past life to be blessed to have so many nice people around me. This work could not have been done without their help.

First, I would like to thank my advisor Dr. Mirmirani. I would like to thank him for his knowledge, for his patience with me during the writing stage of this thesis, and for the moral support he provided me throughout.

I would like to thank Dr. Wu. Without his support during my first year in the United State I might have given up my pursuit of this degree. I thank Dr. Guillaume for agreeing to be on my thesis committee despite his busy schedule.

I also would like to thank Dr. Gupta, Can Bach, and Dr. Lung for providing STARS, great multidisciplinary software, which I used throughout this work for simulation studies.

Our research group, the MFDC Lab, deserves special credit. I would like to thank these guys for their patience and understanding of my sometimes stressed out and uncanny behavior. Thank you Alex, Amir, Baris, Haojian, Jake, Josh, Josue, Kamyar, Moataz, Shah, Shigeru, and Ying.

Finally I give my wife a big hug and kisses. I could not thank her enough for the loving support she provided me during the past 3 years!

This research was supported by NASA Dryden Grant (NAG4-175) and Air Force Office of Scientific Research Grant (F49620-01-1-0489).

ABSTRACT

Nonlinear Dynamics and Control for an Aeroservoelastic System Using Neural Networks

by Sang Bum Choi

The high-performance air vehicles of the future are characterized by high-dimensional and highly nonlinear dynamics as they are expected to operate in a wide range of flight and atmospheric conditions. Therefore, conventional methodologies including linear techniques are inadequate to provide satisfactory performance due to the inherent nonlinearity, instability, large maneuverability, and/or extreme velocity and altitude at which these vehicles fly. Future combat aircraft will be expected to operate outside the currently achievable flight envelopes pushing their performance beyond current performance limits. Furthermore, they are expected to maintain their flight control properties in the presence of large uncertainties. During aggressive maneuvers the nonlinear nature of the aircraft dynamics becomes crucial. These nonlinearities can no longer be neglected or approximated by linear systems. Because these nonlinearity cannot be analytically solved, a powerful approach is to use neural networks and adaptive techniques to estimate and accommodate these nonlinearities. In this approach appropriate neural networks whose parameters or weights are continuously updated online using robust adaptive laws approximate the unknown nonlinearities. In this thesis we propose to develop control algorithms based on neural networks techniques for high-

$$\ddot{x}_1 = \frac{x_1 x_2}{1+x_1^2+x_2^2} + 3\sin x_1^2 \cos x_2 + 8e^{1-\cos \dot{x}_1^2} u_1 + \sin(\dot{x}_1^3 + 2x_1)\cos(e^{\dot{x}_2 x_2})u_2$$
$$\ddot{x}_2 = 6(1-\cos \dot{x}_1)x_2 + \{e^{1/(x_2^2+3)} \sin x_1 + \sin \dot{x}_2^3 \cos \dot{x}_1\}u_1 + \{-5.2 + \sin x_2^2 \cos x_2 + 0.2\sin(100t)\cos(10\dot{x}_2)\}u_2 \quad (92)$$

where the all nonlinear functions are assumed unknown. The output of subsystem 1, $y_1(t) = x_1(t)$, is required to track the desired trajectory $y_{d_1}(t) = -0.5 + \sin(2\pi t)$, and the output of subsystem 2, $y_2(t) = x_2(t)$, is required to track the desired trajectory $y_{d_1}(t) = 0.5 + (1-e^{-t})\cos(\pi t)$. The upper bounds of the tracking errors at steady state are required by:

$$|e_1(t)| = |y_1(t) - y_{d_1}(t)| \le 0.02$$
$$|e_2(t)| = |y_2(t) - y_{d_2}(t)| \le 0.01 \quad (93)$$

One hidden layer radial Gaussian networks are used to approximate the unknown nonlinear functions $f_1(x_1, x_2)$ on the compact set $\Omega_1 = \{x_1, x_2 \mid x_1 \in (-3,3), x_2 \in (-2,2)\}$ with 2400 nodes; $f_2(\dot{x}_1, x_2)$ on the compact set $\Omega_2 = \{\dot{x}_1, x_2 \mid x_1 \in (-20,20), x_2 \in (-2,2)\}$ with 4000 nodes; $b_{11}(\dot{x}_1)$ on the compact set $\Omega_3 = \{\dot{x}_1 \mid \dot{x}_1 \in (-20,20)\}$ with 200 nodes; $b_{22}(x_2, \dot{x}_2, t)$ on the compact set $\Omega_4 = \{x_2 \mid x_2 \in (-2,2)\}$ with 80 nodes, where $0.2\sin(100t)\cos(10\dot{x}_2)$ is treated as unmodeled disturbance which is not estimated. In this example the lower bounds, $g_1(\boldsymbol{x}) = g_1^* = 8$, $g_2(\boldsymbol{x}) = g_2^* = 4$, are assumed to be known *a priori*. The upper bounds of the approximation errors, $\psi_{f_1} < 0.2$, $\psi_{f_2} < 0.4$, $\psi_{b_1} < 0.075$, $\psi_{b_2} < 0.1$, are estimated by using off-line back-propagation training method. The interconnection strength in this example is $\max\{|b_{21}|/|b_{11}|, |b_{12}|/|b_{22}|\} \le (\delta_0 = 0.3)$. Following the design parameter procedure, first the condition

$$2\max(\psi_{b_1}, \psi_{b_2}) + \sqrt{2}\delta_0 = 0.63 < 1 \quad (94)$$

is checked. Then $\Delta_1 = 0.05$, $\Delta_2 = 0.05$ are chosen such that

$$2\max(\psi_{b_1}, \psi_{b_2}) + \sqrt{2}\delta_0 + \max(\Delta_1, \Delta_2) = 0.68 < 1 \quad (95)$$

is satisfied. The constants, $\delta_{b_1} = 0.4$, $\delta_{b_2} = 0.2$, are chosen to satisfy the following conditions

$$(\delta_{b_1} = 0.4) < (1 - 2\psi_{b_1} - \delta_0 - \Delta_1)[(1 - \psi_{b_1} - \Delta_1)g_1^*]^2 / (\psi_{b_1} + \delta_0) = 65.3$$
$$(\delta_{b_2} = 0.2) < (1 - 2\psi_{b_2} - \delta_0 - \Delta_2)[(1 - \psi_{b_2} - \Delta_2)g_2^*]^2 / (\psi_{b_2} + \delta_0) = 13.0 \quad (96)$$

Second the design parameters, $\lambda_1 = 1$, $\lambda_2 = 2$, $\Phi$=0.02, are selected such that the desired upper bounds of the tracking errors at steady state are satisfied, i.e., $|e_1| \le \Phi/\lambda_1 = 0.02$ and $|e_2| \le \Phi/\lambda_2 = 0.01$. In the next step, using (54a-e),

nonlinearities, several decentralized adaptive control schmes based on fuzzy systems or neural networks have been proposed by (Spooner and Passino 1999, Da 2000). Most of these studies assume that the interconnections among the subsystems are bounded by a first order or an *n*th order polynomial (Jain and Khorrami 1997, Spooner and Passino 1999, Da 2000, Liu and Li 2002). The polynomial-type interconnections are relaxed to more general nonlinear interconnections in (Jiang 2000). All above decentralized control schemes however cannot be applied to the class of large scale systems with control input interconnections. In fact, in most practical systems the control inputs are interconnected through an input matrix $\boldsymbol{B}(\boldsymbol{x})$, i.e., control inputs through the $\boldsymbol{B}(\boldsymbol{x})\boldsymbol{u}$ structure injecting into the overall system. In the case of centralized control design using feedback linearization, $\boldsymbol{u}$ is calculated based on the estimated plant and requires calculation of $\hat{\boldsymbol{B}}^{-1}(\boldsymbol{x},t)$, where $\hat{\boldsymbol{B}}(\boldsymbol{x},t)$ is the estimate of $\boldsymbol{B}(\boldsymbol{x})$. There are several problems associated with this adaptive centralized methodology. First, we need to estimate every nonlinear element in $\boldsymbol{B}(\boldsymbol{x})$ in order to obtain $\hat{\boldsymbol{B}}(\boldsymbol{x},t)$. If $\boldsymbol{B}(\boldsymbol{x})$ is completely unknown, we may need to model every element in $\boldsymbol{B}(\boldsymbol{x})$ using neural networks or other universal approximators, and then develop adaptive laws to update the unknown weights. For a large-scale system, the computational burden is therefore heavy. Second, we need to calculate the inverse of $\hat{\boldsymbol{B}}(\boldsymbol{x},t)$. The calculation of the inverse of a high dimensional matrix at each time point $t$ is impractical if at all possible. Finally, for the control law to exist it is required that $\underline{\sigma}(\hat{\boldsymbol{B}}(\boldsymbol{x},t)) > 0$ for all $\boldsymbol{x},t$, where $\underline{\sigma}(\hat{\boldsymbol{B}}(\boldsymbol{x},t))$ denotes the minimum singular value of $\hat{\boldsymbol{B}}(\boldsymbol{x},t)$. The on-line estimators that generate $\hat{\boldsymbol{B}}(\boldsymbol{x},t)$ have to guarantee that $\underline{\sigma}(\hat{\boldsymbol{B}}(\boldsymbol{x},t)) > 0$, $\forall \boldsymbol{x},t$. In fact, for computational purposes and uniform boundedness it is required that $\underline{\sigma}(\hat{\boldsymbol{B}}(\boldsymbol{x},t)) > \varepsilon > 0$, $\forall \boldsymbol{x},t$, where $\varepsilon$ is a small constant. This requirement is not guaranteed by the usual estimators resulting in the loss of controllability which has to be dealt with in order to establish stability and uniform boundedness. Several centralized adaptive control schemes have been proposed to deal with this so called "stabilizability problem" for linear as well as nonlinear case (Ioannou and Sun 1996). In (Johansen 1994), the stabilizability problem was discussed without any stability analysis. In (Liu and Chen 1993) each element of $\boldsymbol{B}(\boldsymbol{x})$ is approximated by neural networks of the form $b_{ij}(\boldsymbol{x}) = b_{ij}^a(\boldsymbol{x},\Theta_{ij}) + d_{ij}(\boldsymbol{x})$ where $b_{ij}^a$ represents an approximated function constructed by neural networks, $\Theta_{ij}$, $i,j$=1,2, ,$m$, is a constant parameter vector corresponding to the unknown weights of the neural network, and $d_{ij}$ denotes the approximation error. The weights $\Theta_{ij}$ are estimated on line generating $\hat{\Theta}_{ij}(t)$, the estimate of $\Theta_{ij}$ at time $t$, which in turn is used to generate $b_{ij}^a(\boldsymbol{x},\hat{\Theta}_{ij})$ and therefore $\hat{\boldsymbol{B}}^a$, the estimate of $\boldsymbol{B}^a = \left[b_{ij}^a(\boldsymbol{x},\Theta_{ij})\right]_{m\times m}$. It is assumed that $\hat{\Theta}_{ij}(0)$ is close to the actual value $\Theta_{ij}$ and then $\hat{\Theta}_{ij}(t)$ is updated slowly by choosing small adaptive gains. Based on this condition it

TABLE OF CONTENTS

performance air vehicles. The model is obtained from NASA Dryden Flight Research Center. This work is supported by a grant from the US Air Force and a grant from NASA Dryden Flight Research Center.

The cutting edge research in aeroelasticity is presently being applied to the analysis of modern high performance aerospace vehicles. These vehicles operate over a wide range of speeds and are often designed to be extremely lightweight for their size. This light weight makes them extremely susceptible to aeroelastic phenomena such as wing flutter. In addition aeroservoelastic instabilities may result from the interaction between the flight control systems and the aircraft structural modes. Hence, the accurate prediction of these instabilities is necessary before flight testing the vehicle and establishing its flight envelope.

LIST OF TABLES

LIST OF FIGURES

# CHAPTER 1

# INTRODUCTION

Computational aeroelasticity, or Computational Fluid Dynamic (CFD) – based aeroelasticity is one of the emerging areas of active research in applied flight dynamics and control. Aeroelasticity is the interaction of aerodynamic forces with the flexible aircraft structure and vehicle inertia. Aeroservoelasticity refers to interaction of active control with the aeroelastic structure via the movement of control surfaces. A major concern in aeroelastic analysis is the potential instability, phenomena such as flutter and divergence. Instability occurs as the result of these dynamics interacting over a wide range of altitudes and Mach numbers, nonlinear flight load régimes. Predicting these instabilities is highly important in the design of modern high-performance air vehicles which are required to operate over a wide envelope and perform extreme maneuvers. The design of the vehicle as well as subsequent testing is dependent on novel simulation tools and methods that can provide timely and accurate account of general flight characteristics of the vehicle and flight loads [1]. This has motivated significant research activity to develop tools to rapidly capture aeroelastic phenomena with full airframe geometry.

In a typical static CFD-based aeroelastic analysis a finite element model of the vehicle structure is obtained and solved yielding frequencies and mode shapes. A steady-state rigid vehicle Euler solution is next performed to obtain aerodynamic pressure distribution

on the vehicle surface. The equation of motion is then written in terms of generalized coordinates and the associated generalized forces, which can subsequently be cast into state space format in terms generalized coordinates and their derivatives [2-4]. The next step involves determination of aerodynamic loads as the flexible structure deforms as the result of application of these loads. This step, which involves repeated unsteady CFD solutions at each discrete time interval, is the most difficult and computationally intensive phase of aeroelastic analysis. As seen in Figure 1, taken from [4], it is the unsteady CFD solution at each time step which requires the overwhelming proportion of CPU time. It is not therefore surprising that many researchers have focused on developing more practical procedures for aeroelastic analysis with the aim of alleviating the unsteady CFD computational burden.

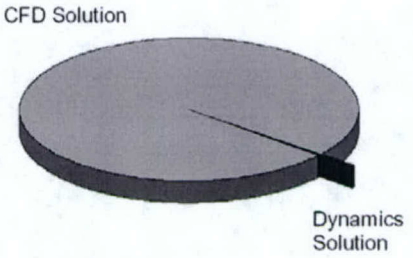


Figure 1 CFD Unsteady Solution CPU usage

Historically, linear static aeroelastic solutions have been acquired for each nonlinear aerodynamics using aerodynamic panel methods. Most recently, a novel system identification procedure has been developed, [3] and [4], that allows one to closely approximate the aerodynamics predicted by the unsteady CFD with a linear state space

formulation. The system identification makes the assumption that the aerodynamics behave linearly about potentially nonlinear steady-state flow in each discrete iteration step associated with a flexible frame. As such the dynamics of the air flow and the associated pressure can be identified as a linear dynamic system using a set of appropriate input and output data generated by selected unsteady CFD solutions in a procedure called Auto Regressive Moving Average (ARMA). This results in a second set of state space equations describing the aerodynamics part of the aeroelastic system. The main advantage in this type of approach is that the aerodynamic model is independent of the structural parameters and can be varied as parameters to search for aeroelastic instabilities.

However, linear methods fail to capture nonlinear phenomenon such as flow separation and moving shock waves during the critical loads flight régimes which is needed in the design and analysis of control systems for high-performance air vehicles. In addition to the inherent nonlinearity, the design of control systems for these vehicles is carried out with a high degree of model uncertainty and with the need to accommodate possible failure or battle damage. This set of stringent requirements makes the aeroelastic analysis an ideal candidate for application of artificial neural networks (ANN). Neural networks are known to be capable of addressing complex dynamic systems which are characterized by high levels of nonlinearity and uncertainty. Their capability to approximate any complex dynamic system and adapting online to account for system uncertainties has made them the method of choice in analysis of dynamic systems in recent years. In this

respect neural networks can be used for system identification by training off line, and/or for providing augmentation to improve dynamic response by training on line to compensate for uncertainties and accommodate for failures.

This thesis is devoted to demonstrating the application of neural networks in aeroelastic analysis. Neural networks are used for identification and control of a cantilever flexible wing, the "Y-Wing." Neural networks are used for development of forward and inverse dynamics modeling the aerodynamics and the combined aerodynamics and structural dynamics. The use of neural network for augmentation for compensation of uncertainty or failure is the subject of future research by the author. This thesis is organized in six chapters. CFD-based aeroelasticity is presented in chapter 2. In chapter 3 the system development of its structural and aerodynamic model is presented. System Identification using ARMA modeling and generation of input output data for off line neural network training is presented in Chapter 4. In Chapter 5 Multi Layer Perceptron Neural Networks is introduced and used for system identification of the "Y-wing". Chapter 6 presents dynamic inversion using neural networks for control. Chapter 7 is discussion of results.

# CHAPTER 2

# COMPUTATIONAL AEROELASTIC ANALYSIS

The aeroelastic analysis used in this thesis is based the algorithm used in *STARS*, a multidisciplinary software developed at NASA Dryden Flight Research Center. *STARS* is one of the modules used in the Multidisciplinary Flight Dynamics and Control laboratory (MFDCLab) testbed. The testbed is an integrated computational environment where a number of commercially available tools, including *STARS, I-DEAS,* and *Matlab* have been linked via a common broker architecture. This allows automated communication and transport of data between different modules. The testbed is used for performing Multidisciplinary Optimization design and analysis of aerospace structures.

The process for an aeroelastic analysis starts with the finite element modeling of the air vehicle structure. This is conducted in FEA software such as *I-DEAS*, or directly in *STARS.* The result of this analysis is the undamped equations of motion for $q$, displacement vector:

$$M\ddot{q} + Kq = 0 \tag{1}$$

In which $M$ and $K$ are the mass and stiffness matrices, respectively, and which can be solved to yield the natural frequencies, $(\varpi)$, and mode shapes, $(\phi)$ that consists of rigid body, elastic and control surface motions. Arbitrary motions of the vehicle structure can

then be formulated by a linear combination of mode shapes multiplied by a generalized displacement:

The matrix equations of motion for an arbitrary structure in terms of generalized coordinates is

$$\hat{M}\ddot{\hat{q}} + \hat{K}\hat{q} + \hat{C}\dot{\hat{q}} + f(t) = 0 \tag{2}$$

where

| | | | |
|---|---|---|---|
| $\hat{M}$ | = | $\Phi^T M \Phi$ | (inertia matrix) |
| $\hat{K}$ | = | $\Phi^T K \Phi$ | (stiffness matrix) |
| $\hat{C}$ | = | $\Phi^T C \Phi$ | (damping matrix) |
| $\hat{q}$ | = | $\Phi^T q$ | (displacement vector) |
| $f$ | = | $f_a + f_I$ | |
| $f_a$ | = | $\Phi_a^T p A$ | (aerodynamic load vector, where $p$ is the Euler pressure, $A$ is surface area, $\Phi_a$ is the modal vector interpolated for structural nodes) |
| $f_I$ | | | (user input, impulse force vector) |

and $f(t)$ is a generic forcing function.

In the aeroelastic analysis presented here $f$ is comprised of two forces; the aerodynamic force, $f_a$, and a user defined force, $f_I$, usually impulsive, that excites the structure and initiates the aeroelastic interaction. In *STARS* the unsteady CFD solution is performed on an unstructured mesh and using the transpiration method to simulate structural

deformation. The transpiration method is a technique in which the direction of the normal vectors to the structural surface is changed at every time step rather than re-meshing the CFD volume. This saves tremendous computational resources.

A complete aeroelastic analysis is accomplished as shown in Figure 2. As seen in the diagram of Figure 2, the unsteady CFD solution is carried out using data from the solution of a steady-state rigid body CFD solution and the modal analysis data provided by the FE solution. These two sets of data are combined, in a module called the dynamic solver to furnish the unsteady CFD boundary conditions at every time step. The FE analysis and the steady CFD are conducted only once.

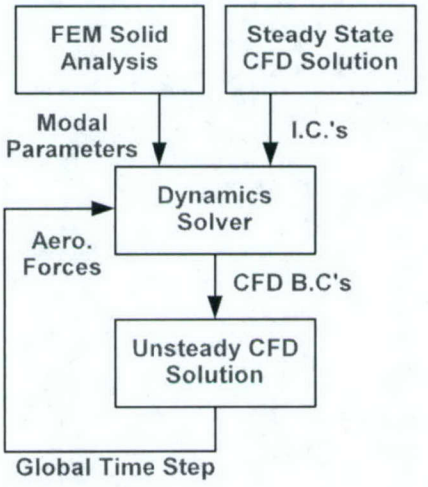


Figure 2 Aeroelastic Analysis Block Diagram

As mentioned in the introduction, it is the unsteady CFD solution that occupies the overwhelming computational time of the aeroelastic solution and needs to be addressed if

this type of analysis is to be useful in an operational environment. Specifically, to search for and to identify points of instability, an aeroelastic analysis must be conducted for many densities and Mach numbers within the flight envelop. This can become a formidable task. In addition, the judgment that a cross-over from stability to instability has occurred must be determined based on evaluation of the time response, which as pointed out in [1] is often difficult to pin down. A system identification method was used by Cowan, Arena, and Gupta [4] where a multi input, multi output (MIMO) discrete time linear dynamic system replaces the unsteady CFD solver in the block diagram of Figure 2. The system identification is based on the well-known autoregressive moving average (ARMA) described in the next chapter.

The objective of this thesis was to use neural networks (NN) to model the aerodynamics and replace the solution of the unsteady CFD in the diagram of Figure 2 with these NN. This study was conducted using a wing model obtained from NASA Dryden Flight Research Center. The wing, called the "Y-Wing" is a cantilever plate. The wing has a moving control surface attached to it at its trailing edge. In addition, this thesis studied the use of NN for control of the aeroelastic wing. The developments of the NN for forward and inverse dynamics are presented in Chapter 4 and 5, and Chapter 6, respectively.

# CHAPTER 3

## AEROELASTIC SYSTEM IDENTIFICATION

In order for the computational aeroelastic analysis to be useful in an operational environment, the repeated solution of the unsteady CFD must be replaced with a more efficient, but at the same time accurate, method. The ARMA system identification method is exactly such an attempt. It is well known from linear system theory that the current output of a MIMO observable system can be determined from knowledge of past inputs and outputs. Assuming that the aerodynamics respond linearly to small perturbations about a nonlinear steady-state mean flow, it can be approximated with a linear dynamic system. Then the corresponding IO representation for the aerodynamics at time $k$ can be written in the format of an ARMA model as

$$f_a(k) = \sum_{i=1}^{na} [A_i] f_a(k-i) + \sum_{j=0}^{nb-1} [B_j] \hat{q}(k-j) \tag{3}$$

The ARMA model of Equation (3) relates the current generalized aerodynamic force output to $na$ past outputs and $nb$ past inputs of the unsteady CFD solver, with matrices $\boldsymbol{A's}$ and $\boldsymbol{B's}$ to be determined by fitting the model to an appropriately generated set of "training" IO data and employing an optimized fitting technique such as the least squares method.

## 3.1 Training Data Generation

The success of the identification method described here and the NN technique described in CHAPTER 4 is critically dependent on the amount and quality of data generated for "training". The data must contain enough information about system dynamics in order for the identification procedure to succeed and for the NN to represent an accurate model of the actual system. The data for identification and NN training are generated by exciting the system with a prescribed input signal and solving the unsteady CFD to obtain an aerodynamic force output. It is therefore critical that the input signal be selected carefully.

In general an input signal that contains a broad spectrum of frequencies needs to be selected so that it can excite all the modes. In addition, the procedure requires application of two signals: one representing generalized displacements, and one representing generalized velocities. Furthermore, these two signals must be consistent. That is, integrating the velocity input must yield the displacement input, and differentiating the displacement signal must result in the velocity signal. One such example, which packs broad frequency content in a short signal, is shown in Figure 3. The signal called the 3211 multi-step has been widely utilized in flight testing application of system identification. In this thesis a variation of the 3211, called variable amplitude velocity and its integrated pair displacement, shown in Figure 3 was used.

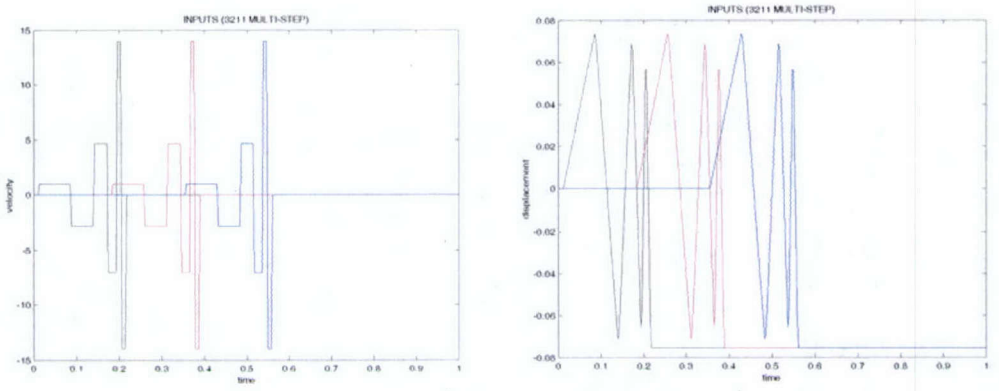


Figure 3 3211 Multi-Step Inputs

## 3.2 State Space Representation

Once system identification of aerodynamic forces is accomplished, both the structural equations of motion, Equation (2), and the ARMA model of Equation (3) can be cast into state space representations and be connected in a linear feedback loop as shown in the diagram in Figure 4. The diagram represents the complete aeroelastic system.

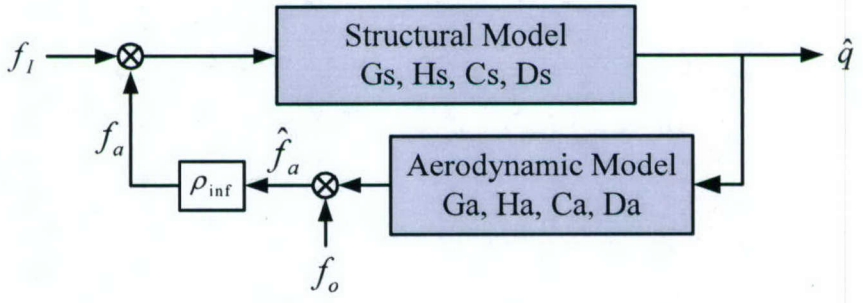


Figure 4 Aeroelastic System

The combined aerodynamics and structural discrete time state space equation can be written as

$$
\begin{aligned}
x_s(k+1) &= G_s x_s(k) + H_s f_a(k) \\
\hat{q}(k) &= C_s x_s(k) + D_s f_a(k)
\end{aligned}
$$

$$
\begin{aligned}
x_a(k+1) &= G_a x_a(k) + H_a \hat{q}(k) \\
\hat{f}_a(k) &= C_a x_a(k) + D_a \hat{q}(k)
\end{aligned}
\tag{4}
$$

where

$$x_s = \left[ \hat{q}_1 \cdots \hat{q}_n \; \hat{q}_{dc_1} \cdots \hat{q}_{dc_m} \; \dot{\hat{q}}_1 \cdots \dot{\hat{q}}_n \; \dot{\hat{q}}_{dc_1} \cdots \dot{\hat{q}}_{dc_m} \right]^T$$

$$f_a = \rho_{\inf} \hat{f}_a = \left[ f_1 \cdots f_n \; f_{dc_1} \cdots f_{dc_m} \right]^T$$

$$\hat{q} = \left[ \hat{q}_1 \cdots \hat{q}_n \; \hat{q}_{dc_1} \cdots \hat{q}_{dc_m} \right]^T$$

$$x_a(k) = \begin{bmatrix} \hat{f}_a(k-1) \\ \vdots \\ \hat{f}_a(k-na) \\ \hat{q}(k) \\ \vdots \\ \hat{q}(k-nb+1) \end{bmatrix}$$

$$\hat{f}_a = \left[ \hat{f}_1 \cdots \hat{f}_n \; \hat{f}_{\delta c_1} \cdots \hat{f}_{\delta c_m} \right]^T$$

n: number of elastic modes
m: number of control modes
n+m: total number of modes
na: number of past outputs
nb: number of past inputs

For detail derivation of the above aeroelastic state space equation refer to [5].

# CHAPTER 4

# UNSTEADY AERODYNAMIC SYSTEM IDENTIFICATION USING NEURAL NETWORK

The unsteady aerodynamics in an aeroelastic system can be considered as a nonlinear dynamic system. In Chapter 3 a linear identification model, ARMA was presented on the assumption that the aerodynamics respond linearly to small perturbation about a steady-state mean flow. Therefore ARMA in this case essentially provides local information about the nonlinear system.

In this chapter, a system identification method for nonlinear dynamic systems, which is globally invertible, will be introduced. The nonlinear system identification, NARMA, will be applied for identification of unsteady aerodynamics utilizing Multi Layer Perceptron (MLP) neural network architecture.

## 4.1 The NARMA Model

For linear time-invariant systems there is an IO representation for every state space representation and vise versa. For nonlinear systems, this dual representation is much harder to establish. However, if certain smoothness conditions are satisfied, the output of an $n$th order single input/single output SISO nonlinear system at time $k$, $y(k)$, can be represented in terms of its past $n$ inputs and outputs:

$$y(k+1)=\Phi(u(k),u(k-1),\ldots,u(k-n+1),y(k),y(k-1),\ldots,y(k-n+1)) \quad (5)$$

This equation is called the nonlinear autoregressive moving average (NARMA) representation of the system with a relative degree of one [6]. In a system with a relative degree one, as it is seen from Equation (5), the current input is affected by the input and output immediately before to the current time step and those prior to it. For a system of relative degree $d$, the current output can be influenced only by the input and output of $d$ times steps before and those prior to it as described by Equation (6):

$$y(k+d)=\Phi(u(k),u(k-1),\ldots,u(k-n+1),y(k),y(k-1),\ldots,y(k-n+1)) \quad (6)$$

Equation (6) can be used for identification of nonlinear dynamical systems using neural networks. Since Equation (6) is known to exist, neural networks can be used to approximate it using IO data. Figure 5 shows a block diagram representation of the NARMA identification scheme represented by Equation (6).

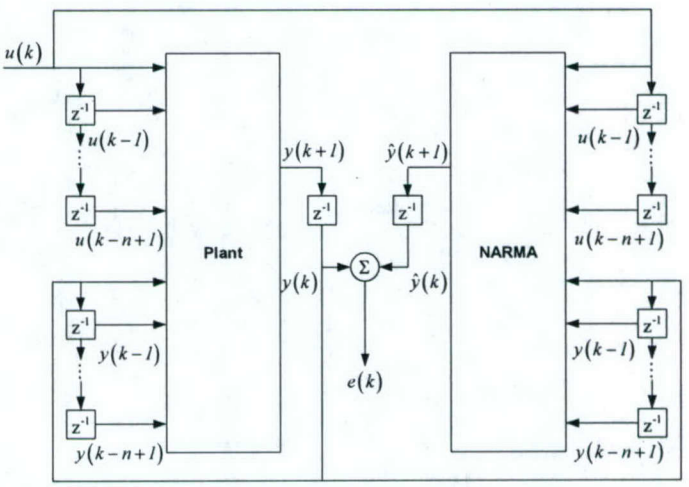


Figure 5 NARMA Identification using IO data

Equation (6) is derived assuming that the linear approximation to the nonlinear dynamic system is observable. Hence, the IO representation by Equation (6) is local in nature. Thus the question arises as under what conditions the above NARMA model can be used for global approximation to the nonlinear dynamic system by NN. The answer is provided by the conditions for the existence of an "extended" NARMA Model. It has been shown [6] that for a state invertible dynamic system of order $n$, $2n + 1$ past values of inputs and outputs are adequate to determine the current output. This is the extended NARMA which is globally valid. For the purpose of this research we assume without proof that the nonlinear dynamic system representing the unsteady aerodynamics does satisfy the conditions of the extended NARMA. Rigorous investigation of this assumption is left to author's future research.

The above NARMA model can be extended to a MIMO system with $t$ inputs and $s$ outputs as in Equation (7), which is the basis of the NN modeling and simulations in this thesis.

$$Y(k+1)=\begin{bmatrix} y_1(k+1) \\ y_2(k+1) \\ \vdots \\ y_s(k+1) \end{bmatrix}=\begin{bmatrix} \Phi_1\left(U(k),\ \ldots, U(k-n+1); Y(k),\ \ldots, Y(k-n+1)\right) \\ \Phi_2\left(U(k),\ \ldots, U(k-n+1); Y(k),\ \ldots, Y(k-n+1)\right) \\ \vdots \\ \Phi_s\left(U(k),\ \ldots, U(k-n+1); Y(k),\ \ldots, Y(k-n+1)\right) \end{bmatrix} \tag{7}$$

where

$$Y = [y_1\ y_2 \ldots y_s]^T$$
$$U = [u_1\ u_2 \ldots u_t]^T$$

## 4.2 Multi Layer Perceptron (MLP) Neural Network

A multilayer Perceptron (MLP) neural network is built up using a simple single-input neuron which is shown in Figure (6). In this simple structure, the input to the neuron p is multiplied by scalar *weight* w, and then sent to the summer. The other input to the neuron is 1, which is multiplied by a *bias* b and then passed to the summer. The summer output n, referred to as the *net input*, is applied to a second block with a *transfer function f,* which produces the output of the neuron, *a*. The neuron output is therefore given by the functional relationship:

$$a = f(wp + b) \tag{8}$$

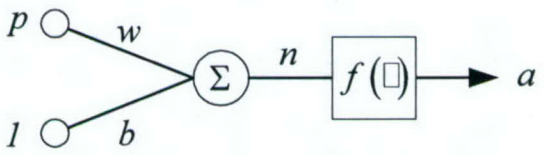


Figure 6 Simple single-input neuron networks

Both the weight and the bias are *adjustable* parameters of the neuron. The transfer function of the neuron may be linear or nonlinear and is chosen by the designer. Next, the parameters *w* and *b* are adjusted applying some learning rule, which is designed for the specific task on hand. The learning rule in most cases is derived by optimizing an

objective function. One of the most commonly used transfer functions is the *log-sigmoid transfer function* shown in Figure 7 with an expression:

$$f(x)=\frac{1}{1+e^{x}} \tag{9}$$

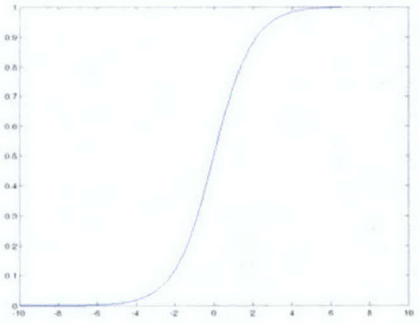

Figure 7 Log-sigmoid transfer function

In most applications multiple layers of $S$ neurons with multiple inputs per layer are needed to produce multiple outputs in order to achieve accurate approximation of dynamic systems. Figure 8, Figure 9, and Figure 10 depict a neuron with $I$ inputs and one output, a layer of $J$ neurons with multiple inputs, and a three-layer multi-input neural network as well as their matrix function representations, respectively. In case of a multilayer neural network vectors of weights $w$, and biases $b$ must be adjusted.

It has been proven that given enough hidden layer neurons, there exists a network of the structure presented above that can approximate any continuous function to any given accuracy [6].

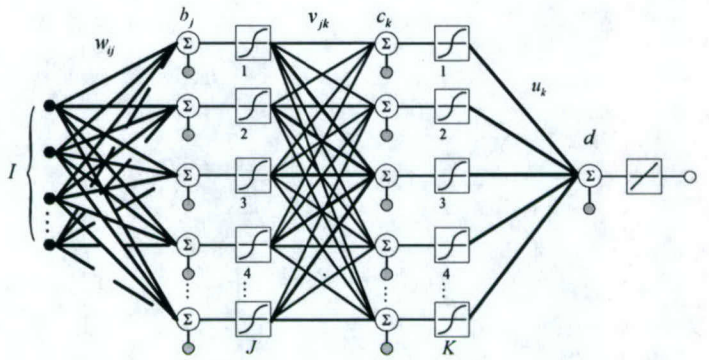


Figure 8 Structure of 3 layer Perceptron Network

In this thesis the structure of multilayer perceptrons (MLP) shown in Figure 10 was used. The network has M inputs, N *sigmoidal* units implementing the hyperbolic tangent function in the hidden layer, and a linear output layer. Each unit in the hidden layer is connected to every input as well as the output. Every connection between neurons in the input layer and the hidden layer has an associated weight described by $w_{ij}$, likewise every connection between the hidden layer and the output layer has a weight, $v_j$. The biases of the neurons in the hidden layer are described by $b_j$ and $c$ as an output layer bias. Thus, the network can be written as:

$$\hat{y} = \sum_{j=1}^{N} v_j \sigma\left(\sum_{i=1}^{M} w_{ij} u_i + b_j\right) + c, \quad \sigma(\cdot): \textit{activation function} \tag{10}$$

An MLP such as the one just presented above can be trained using the back-propagation (BP) algorithm with the cost function defined below:

$$J = \frac{1}{2}(\hat{y} - y)^2 \tag{11}$$

where $J$ is the difference between the actual output, $\hat{y}$, and the desired output, $y$.

The weights are updated using Equation (11) and the learning rate, $\alpha$.

$$w_{ij} = w_{ij} - \alpha \frac{\partial J}{\partial w_{ij}}$$

$$b_j = b_j - \alpha \frac{\partial J}{\partial b_j}$$

$$v_j = v_j - \alpha \frac{\partial J}{\partial v_j}$$

$$c = c - \alpha \frac{\partial J}{\partial c}$$

Specifically, three channels with one hidden layer network and hyperbolic tangent function as an activation function was used for the aeroelastic system identification shown as Figure 9 and Figure 10.

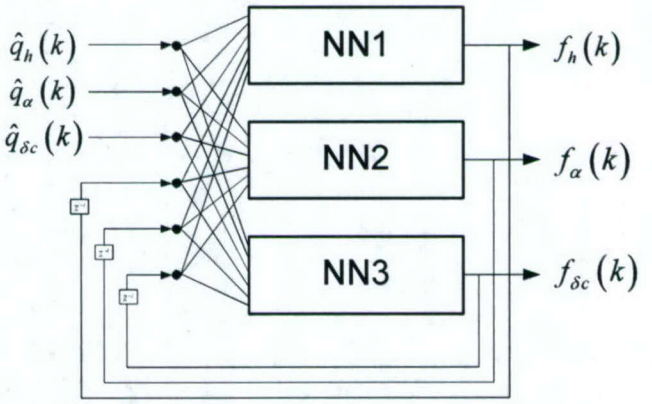


Figure 9 MLP Network Structure with Three Channels

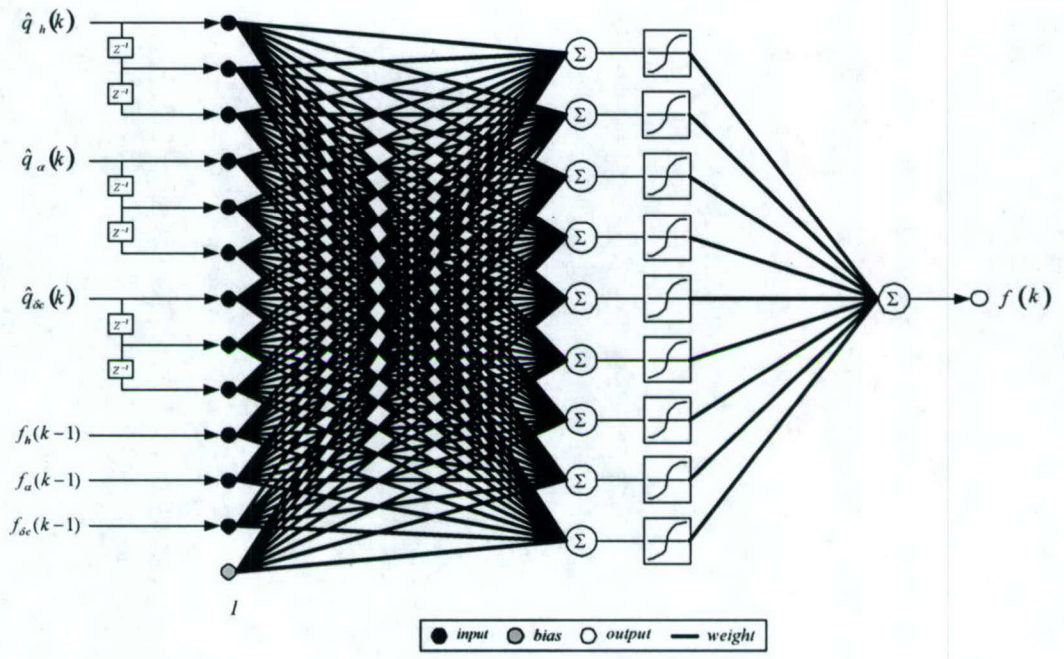


Figure 10 Neural Network Structure for Aeroelastic System Identification

The overall structure of the MLP is depicted in Figure 9. There are three parallel NNs, NN1, NN2, and NN3 used for identification of aerodynamic forces each having a detailed structure shown in Figure 10. The use of three parallel networks is consistent with the fact that the aeroelastic system of the cantilever wing has three degrees of freedom (DOF), pitch, plunge, and control surface angle. The output of the network is the three generalized forces ($f_h(k), f_\alpha(k), f_{\delta c}(k)$), which are the intent of the identification process. However, the input to the network, in addition to the past values of the outputs ($f_h(k-1), f_\alpha(k-1), f_{\delta c}(k-1)$), includes the structural data. (i.e. the current values of

the generalized displacements $(\hat{q}_h(k), \hat{q}_\alpha(k), \hat{q}_{\delta c}(k))$ The training process using the Back Propagation optimization technique is shown in the diagram in Figure 11.

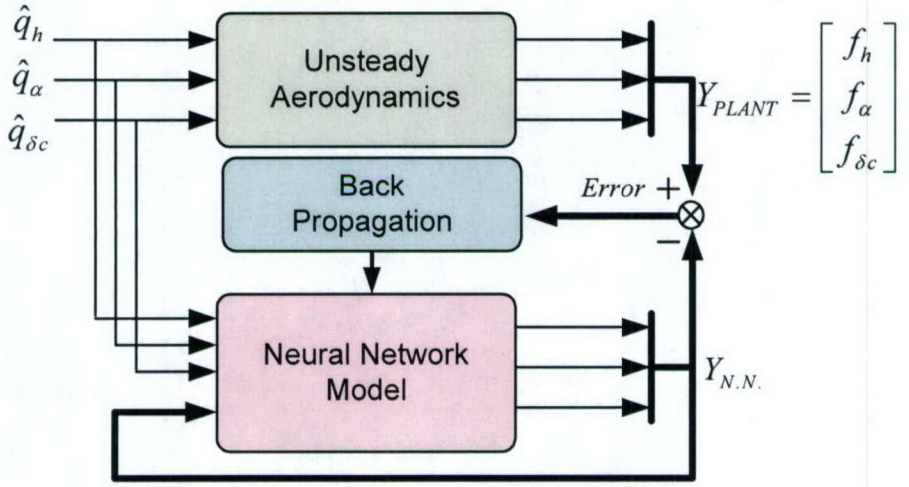


Figure 11 Back Propagation Training Diagram

# CHAPTER 5

# IDENTIFICATION OF AN AEROELASTIC WING USING NARMA MODELING

## 5.1 Structural Dynamics Model

The NARMA identification technique described in Chapter 4 was applied to an aeroelastic wing model. The model, shown in Figure 12, was obtained from NASA Dryden Flight Research Center. It is a cantilever wing that utilizes a NACA 0012 airfoil. The wing has a 2.0178 m span and a 1.0089 m chord length. The control surface, an aileron, attached to the trailing edge of the wing has a 0.6053 m span and a 0.2522 m chord. It is centered at 1.22 m from the wingspan.

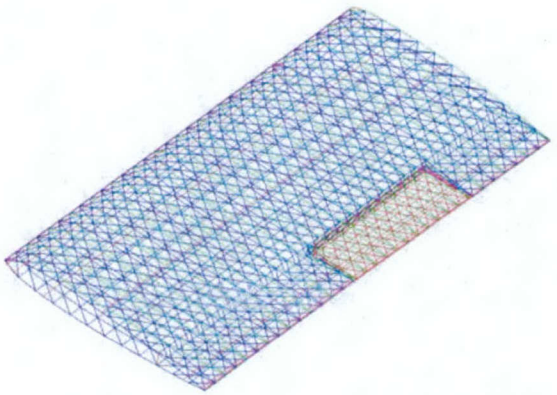

Figure 12 Structural FEA Model of a Cantilever wing with NACA 0012 airfoil

The flight conditions assumed in this study are described in Table 1. Although this wing is not designed for the supersonic speeds that are related to the purpose of this thesis, it can be used to demonstrate the feasibility of using NN in aeroelastic analysis.

| | |
|---|---|
| Mach number | 2.0 |
| Angle of attack | 0° |
| Speed of sound at infinity | 340.29 m/s |

Table 1 Flight Condition

As a first step in conducting the standard aeroelastic analysis supported by *STARS,* an FEA model of the wing was created in I-DEAS and a normal mode analysis was performed to obtain eigenvectors and the associated eigenvalues. Because the wing is a simple structure, only two fundamental modes (the first bending and the first tensional) and the first mode related to the motion of the control surface ($\delta c$) were retained. The first bending mode simulates the plunge ($h$) and the first twisting mode simulates changes in the angle of attack ($\alpha$). These mode shapes and the associated frequencies are shown in Table 2.

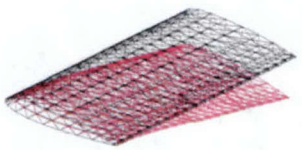

1st Bending Mode ($h$)
3.521 Hz

1st Twisting Mode ($\alpha$)
14.819 Hz

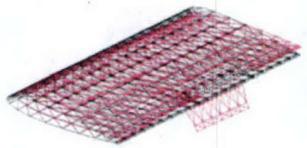

1st Bending Mode ($\delta c$)
59.797 Hz

Table 2 Normal Modes and Frequencies, Reduced Ordered Model

Once mode shapes and the associated frequencies were obtained a discrete-time state space model for the structure, Equation (10), was obtained following the procedure outlined in 3.2.

$$x_s(k+1) = G_s x_s(k) + H_s f_a(k)$$
$$\hat{q}(k) = C_s x_s(k) + D_s f_a(k) \tag{12}$$

The state (including the generalized displacements and their derivatives), the input, the generalized aerodynamic forces, and the output, the pitch, plunge and aileron deflection, are:

$$x_s = \left[h \;\; \alpha \;\; \delta c \;\; \dot{h} \;\; \dot{\alpha} \;\; \dot{\delta c}\right]^T$$
$$f_a = \rho_{\inf} \hat{f}_a = \left[f_h \;\; f_\alpha \;\; f_{\delta c}\right]^T$$
$$\hat{q} = \left[h \;\; \alpha \;\; \delta c\right]^T$$

The numerical values for matrices $(G_s, H_s, C_s, D_s)$ are given in the Appendix. The state space model obtained was used to generate input data for the steady CFD in the next step in the aeroelastic analysis as described below.

## 5.2 Training Data for Aerodynamics Model

The complete aeroelastic model was shown in the block diagram of Figure 4. The aerodynamics module is depicted in Figure 11 which shows $\hat{q} = [h \;\; \alpha \;\; \delta c]^T$ as the input vector and $f_a = \left[f_h \;\; f_\alpha \;\; f_{\delta c}\right]^T$ as the output vector. However, for the purpose of generating IO data for identification in *STARS*, both the displacements and their derivatives have to be applied as input to the block. Once the input and output were substituted in Equation (7), the NARMA Equation for the wing was obtained as:

$$\begin{bmatrix} f_h \\ f_\alpha \\ f_{\delta c} \end{bmatrix} = \begin{bmatrix} N_1\left(f_a(k), f_a(k-1), f_a(k-2), \hat{q}(k), \hat{q}(k-1), \hat{q}(k-2)\right) \\ N_2\left(f_a(k), f_a(k-1), f_a(k-2), \hat{q}(k), \hat{q}(k-1), \hat{q}(k-2)\right) \\ N_3\left(f_a(k), f_a(k-1), f_a(k-2), \hat{q}(k), \hat{q}(k-1), \hat{q}(k-2)\right) \end{bmatrix} \tag{13}$$

where

$$f_a = \left[f_h \; f_\alpha \; f_{\delta c}\right]^T$$
$$\hat{q} = [h \;\; \alpha \;\; \delta c]^T$$

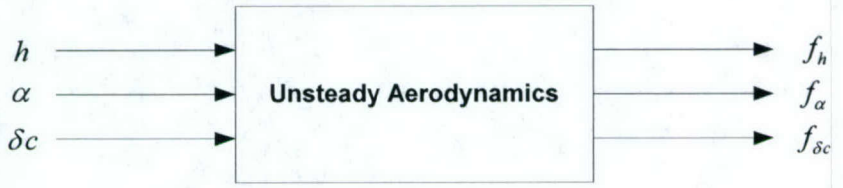


Figure 13 Unsteady Aerodynamic IO

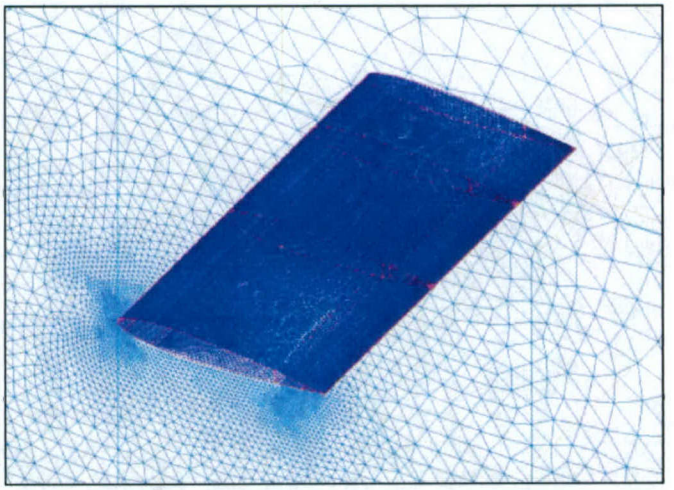

Figure 14 CFD Model of Y-WING for Unsteady CFD

Neural networks were used for identification of the unsteady aerodynamics as described in 4.2. Equation (11) provides the NARMA algorithm for calculating the output of the aerodynamic block in terms of the present input, and the three immediate past inputs and

outputs assuming a system with relative degree of three. At this stage, a set of IO data were obtained by running unsteady CFD analysis for the wing in *STARS*. The process of generating IO data began by first running the steady CFD for the rigid wing to obtain the initial aerodynamic. From this pressure distribution, the initial values of the generalized forces ($f_h, f_\alpha, f_{\delta c}$) were computed and used as initial conditions for the subsequent unsteady CFD runs as described in the flow chart of Figure 2. Next, the 3211 multi-step displacement input shown in Figure 3 was applied and the resulting generalized forces that are shown in Figure 15 were obtained. Once an adequate number of IO data sets were obtained, they were applied to train the MLP NN as described in Chapter 4. The NN simulations were carried out using the NN module of Matlab. Using learning rates, 0.1, 0.01, and 0.03 for $f_h$, $f_\alpha$, and $f_{\delta c}$ respectively, reasonable results reached at 1000, 1500, 1400 iterations for $f_h$, $f_\alpha$, and $f_{\delta c}$ respectively. Figure 16 shows different stages of the training process. The figures show how the output of the NN matches the output of the unsteady CFD for the same input. In addition, in order to validate the results of the NN identification, the response of the NARMA model to the excitation input 3211 were compared with those obtained via the ARMA model for the same system as shown in Figure 17.

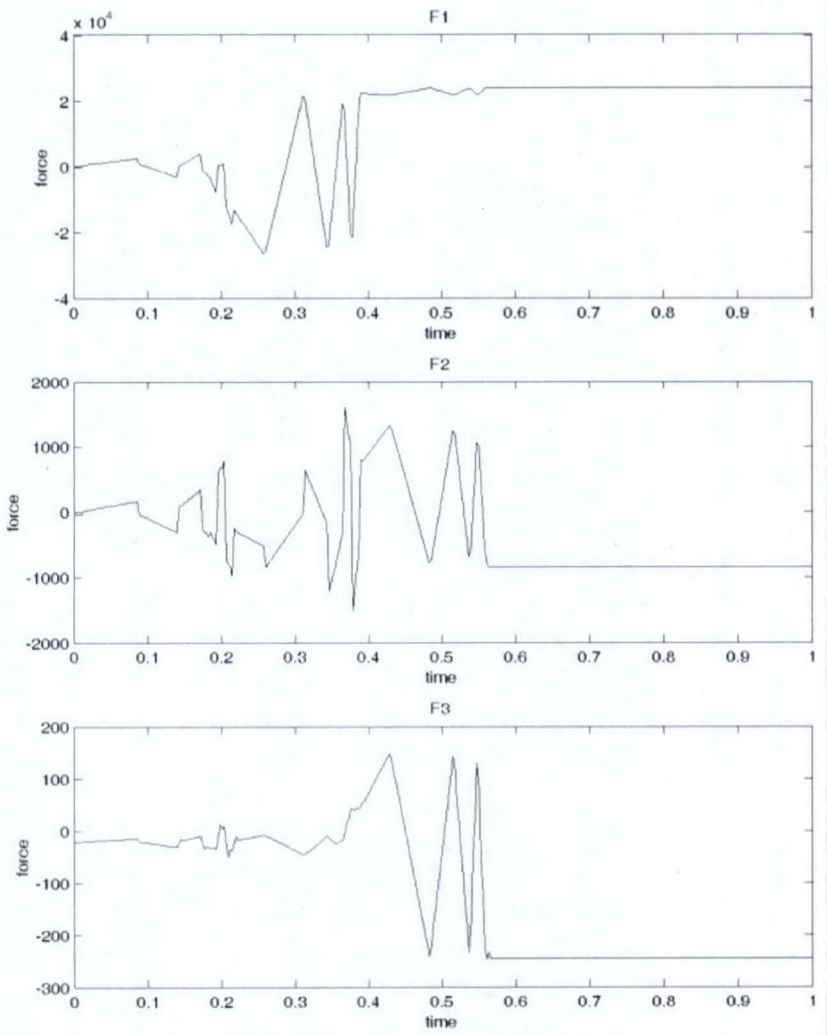


Figure 15 Unsteady Aerodynamic System Responses of 3211 Multi-Step Inputs $(F1(f_h), F2(f_\alpha), F3(f_{\delta c}))$

| it. | F1 | F2 | F3 |
|---|---|---|---|
| 100 | 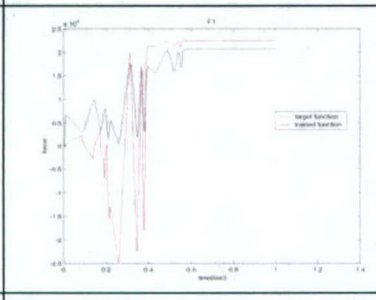 | 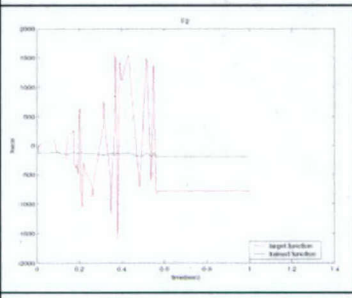 | 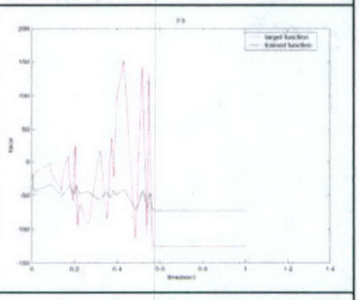 |
| 300 | 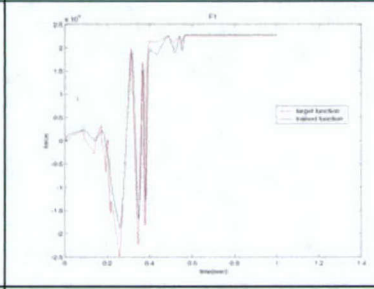 | 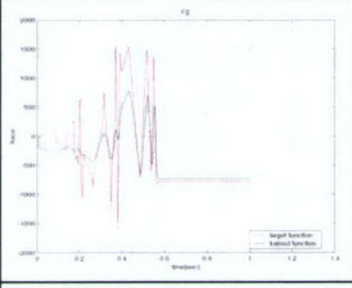 | 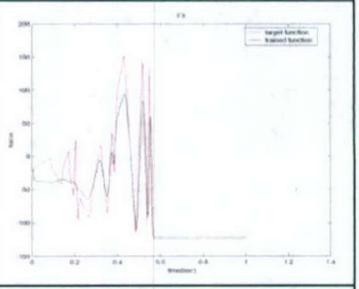 |
| 500 | 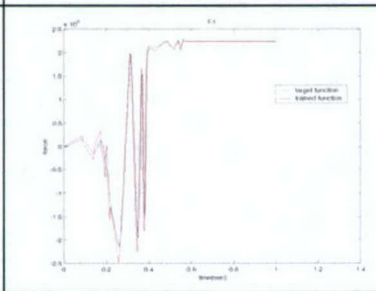 | 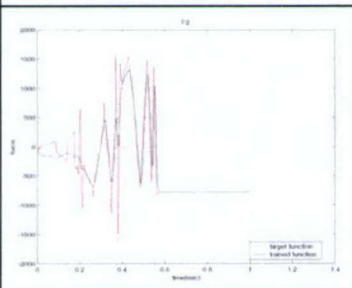 | 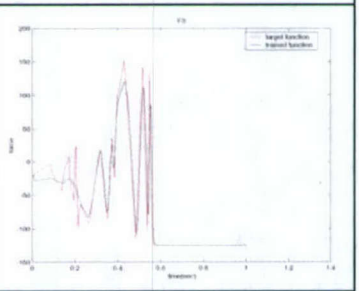 |
| 1000 | 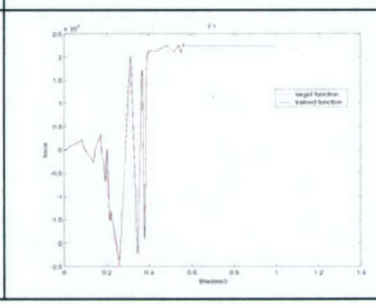 | 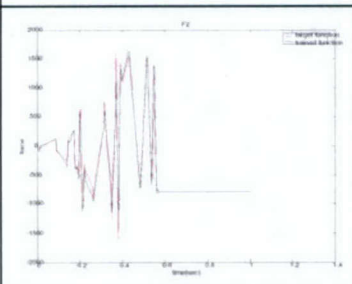 | 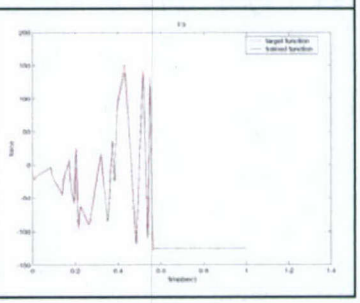 |

Figure 16 Training Progress vs. iterations ( $F1(f_h), F2(f_\alpha), F3(f_{\delta c})$ )

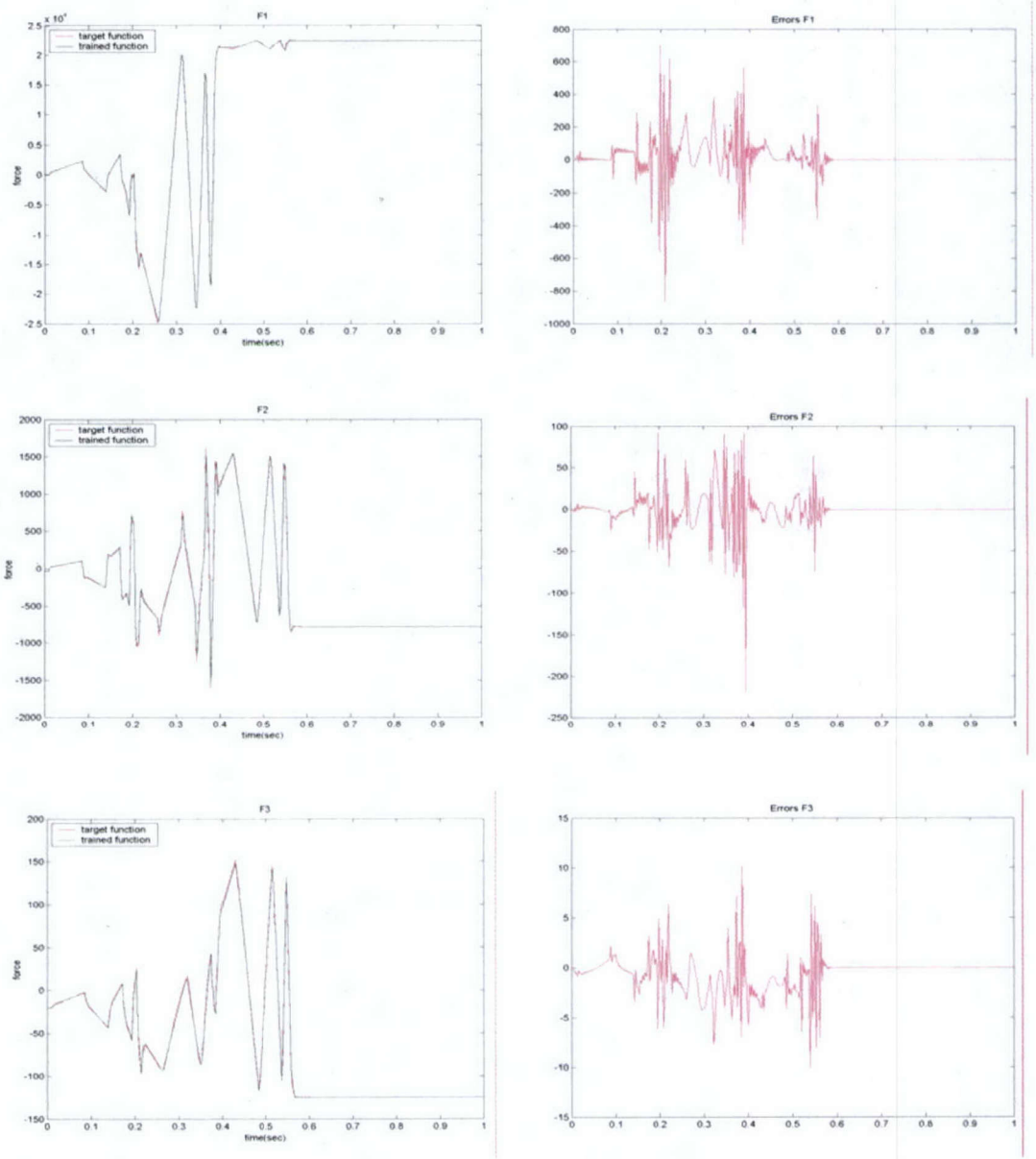


Figure 17 Final Training Results of the Unsteady Aerodynamic Model $(F1(f_h), F2(f_\alpha), F3(f_{\delta c}))$

# CHAPTER 6

# CONTROLLER DESIGN FOR AEROELASTIC SYSTEM

Neural networks were used in the previous chapter for identification of generalized aerodynamic forces. In this chapter neural networks will be used for control. There are several neural network architectures used for control of dynamic systems, including model predictive control, NARMA-L2 control, and model reference control [8-9]. In a more general sense, neural controllers can be categorized as direct and indirect controllers [10]. In a direct control scheme, the parameters of a neural controller are adjusted using the input and output to the plant. In the indirect control, a neural identification model of the plant generates estimates of the plant output. These estimates of the plant output and the input to the plant are used in another neural network. This other neural network is used as the controller for flutter suppression.

The model predictive scheme is a simple type of indirect control since it uses a neural network identification model for control. The controller uses the neural network model of the plant, trained off-line to predict plant response over a certain time horizon. Control input is then generated by an optimization module which is part of the neural controller in a manner that minimizes a quadratic performance index consisting of the square of errors (between the neural model and the plant inputs) and the square of control increments in each time steps over a specified horizon.

When either the plant model or its approximation can be feedback linearized, direct neural control can be implemented. In a NARMA-L2 architecture, it is assumed that the NARMA identification model of the plant takes a certain form which allows control input can be calculated directly in terms of the reference input, past plant outputs and input at each time step. This process is called feedback linearization. Feedback linearization is a form of dynamic inversion which is the method used for control in this thesis.

In the first step of utilizing "model reference control scheme", a neural network plant model is developed. This model of the plant is then used to train a neural controller that forces the output of the plant to follow the output of a reference model. The reference model is chosen in a manner that it possesses the desired dynamics. The advantage of the model reference technique is that it does not require a certain structure for the plant. However, this type of controller requires dynamic backpropagation for training the controller. This process is more time consuming than the standard static backpropagation.

In this thesis a neural controller has been developed by direct mathematical inversion of the neural network plan model. The reference input for pitch and plunge is taken as zero. Therefore, there is no reference model in the forward loop. Because exact mathematical inversion is used, there is no need for training by dynamic backpropagation. However, because the mapping from the input space (control surface deflection) to output spaces

(pitch, plunge, and control surface deflection) is not unique, a neural network optimizer algorithm is used that minimizes the mapping errors.

## 6.1 The Neural Network Inverse Controller

The inversion of the aeroelastic system was obtained from the identified neural network model using Equation (14). Figure 18 describes in block diagram how the inversion of the neural network is optimized. First, it must be noted that because of the interaction between the aerodynamics and the structure, the discrete-time dynamics of the plant can be written in the format of Equation (12). The right-hand-side of the equation is separated into two nonlinear functions $f(\square)$ and $g(\square)$. The physical input to the inverse block is $u_{\delta c}$, which represents the angle of control surface deflection. The other two, $h$ and $\alpha$ represent aeroelastic interaction.

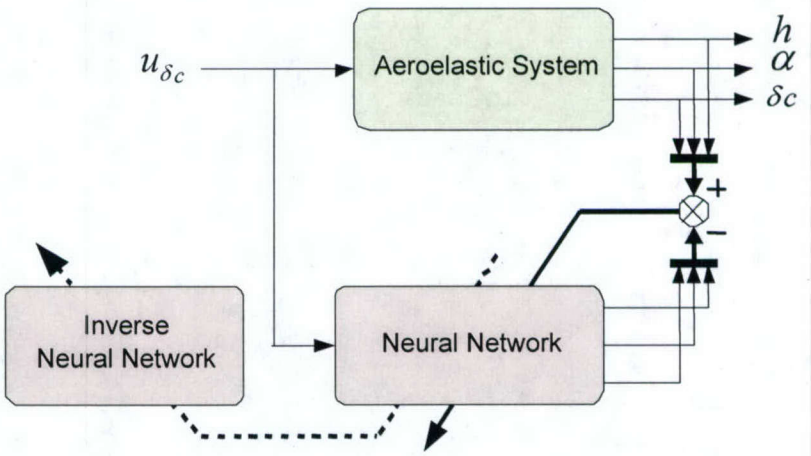


Figure 18 Training the inversion of the aeroelastic system using neural network

$$y^{nr}(k+1) = f^{nr}(x,u,u_{\delta c}) + g^{nr}(x,u), \quad f^{nr}(\cdot), g^{nr}(\cdot): \textit{nonlinear functions of nr channel} \tag{14}$$

Substituting the aeroelastic neural network model of the aeroelastic wing, (Equation (13), Chapter 5) into Equation (15) yields:

$$\begin{aligned}
&f^{nr}\left(x(k), x(k-1), \cdots, x(k-na+1), u(k), u(k-1), \cdots, u(k-nb)\right) \\
&\quad = v^{nr}{}_1 \sigma\left( w^{nr}{}_{11} u_{\delta c}(k) + \sum_{i=1}^{nb} w^{nr}{}_{1i} u(k-i) + \sum_{i=0}^{na+1} w^{nr}{}_{1(i+nb+1)} x(k-i) + b^{nr}{}_1 \right) \\
&g^{nr}\left(x(k), x(k-1), \cdots, x(k-na+1), u(k-1), \cdots, u(k-nb)\right) \\
&\quad = \sum_{j=2}^{N} v^{nr}{}_j \sigma\left( \sum_{i=2}^{nb} w^{nr}{}_{ji} u(k-i) + \sum_{i=0}^{na} w^{nr}{}_{1(i+nb+1)} x(k-i) + b^{nr}{}_j \right) \\
&\sigma(\cdot): \textit{sigmoidal function}
\end{aligned} \tag{15}$$

The inverse of Equation (15) was obtained:

$$u^{nr}{}_{\delta c}(k) = \frac{1}{w^{nr}{}_{11}} \left( \sigma^{-1}\left( \frac{y^{nr}(k+1) - g^{nr}(x,u)}{v^{nr}{}_1} \right) - \left( \sum_{i=1}^{nb} w^{nr}{}_{1i} u(k-i) + \sum_{i=0}^{na+1} w^{nr}{}_{1(i+nb+1)} x(k-i) + b^{nr}{}_1 \right) \right) \tag{16}$$

Equation (14) does not produce a perfect inversion of the aeroelastic system. Therefore a neural network-based optimization algorithm was applied as shown in the block diagram of Figure 19. The optimizer algorithm was trained by minimizing the square of the differences between the outputs of the neural network identification model and the aeroelastic plant off-line. The structure of the overall neural network controller is shown in Figure 15.

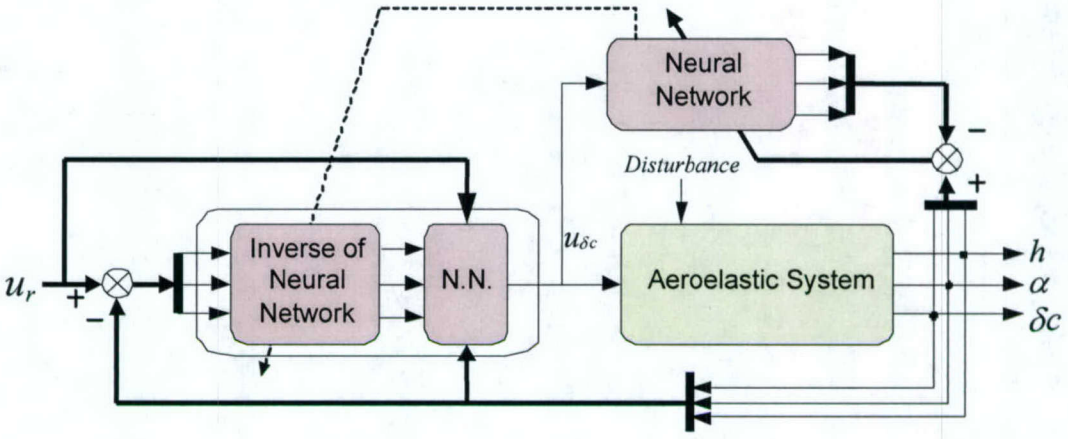


Figure 19 Aeroelastic neural controller architecture

## 6.2 Simulation Results

Simulation studies were conducted using SIMULINK to prove the flutter suppression ability of the neural controller. The aeroelastic model of the "Y-wing" was used and flutter conditions were induced by increasing dynamic pressure. Figure 20 shows the time histories of the outputs, pitch and plunge, and the control surface movement. The thin-line curves show that the unstable self excited oscillations growing quickly in the open-loop mode. The thick-line curves show quick suppression of flutter when the neural controller is placed in the loop.

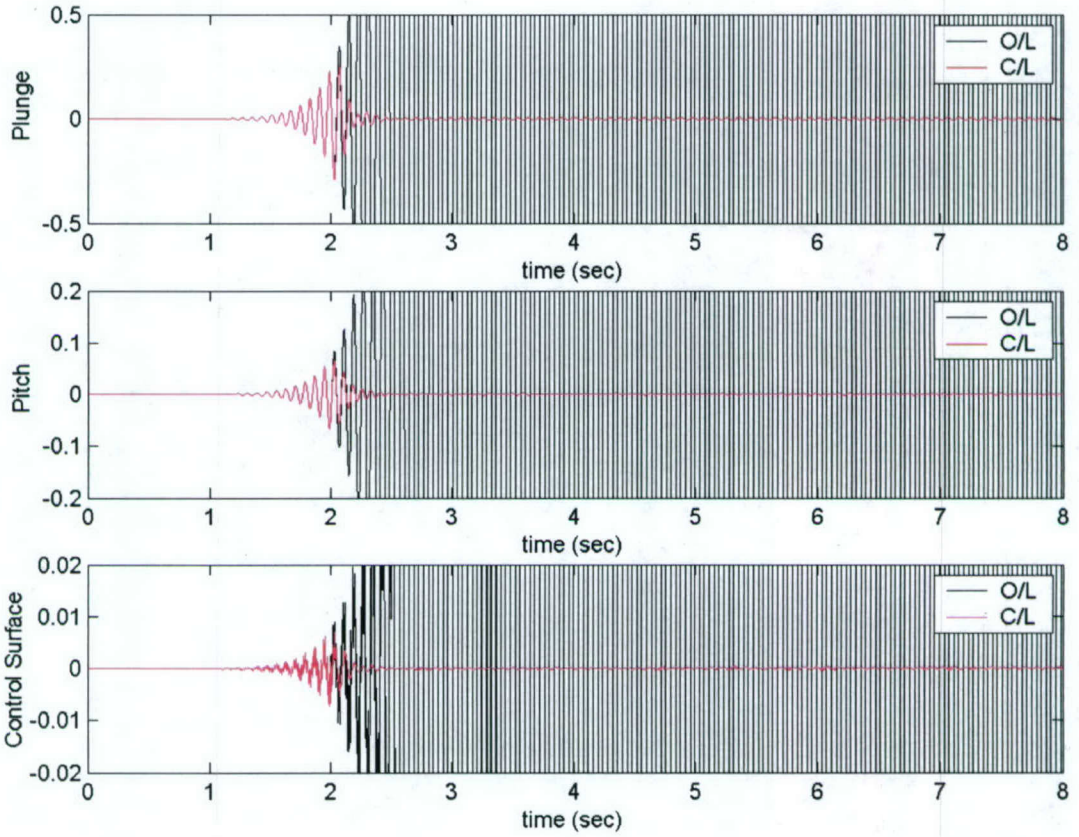


Figure 20 Simulation Result

# CHAPTER 7

# CONCLUSION

Identification and control of aeroelastic instabilities are crucial in design, flight test and certification of new aircraft. Obtaining data through experimentation is expensive, and computational methods based on repeated unsteady CFD solutions are computationally intensive. In both cases, there is strong motivation for methods to reduce time and cost for flutter speed identification. Traditionally, whether using test data or using data generated by computation aeroelasticity, identification of flutter speed is accomplished by extrapolating the estimated damping ratios to clear or/and expand the flight envelope. This procedure however is susceptible to erroneous conclusions especially at points near the flutter speed and in cases where elastic modes are highly coupled. Near flutter, a small change in speed about changes in system behavior can occur resulting in great uncertainty. In the case of strong coupling between the modes, the determination of the damping ratio based on the time history of the response could be misleading.

In this thesis, neural networks as universal approximators where used to identify the generalized aerodynamic forces in one case and the coupled aerodynamic and structural dynamics in another. The neural network identification models were trained using input output data obtained for a flexible wing, called "Y-wing" by using steady and unsteady CFD solver of *STARS*. Time domain simulation studies conducted using the typical 3211 input proved that in both cases the neural identification model predicted system behavior

accurately in a wide frequency range. Developing efficient search methods in frequency domain using describing function method will be the subject of future research.

A dynamic inversion architecture for neural control of the aeroelastic wing was proposed and implemented. The neural controller exploits the specific form of the aeroelastic dynamics to obtain the mathematical inverse of the neural identification model of the aeroelastic plant. Because the inverse dynamic is not exact, a neural network is trained using CFD generated input output data to augment the inverse dynamic controller.

# REFERENCES


[1] K. K. Gupta and J. L. Meek, "Finite Element Multidisciplinary Analysis", AIAA Education Series, 2000.

[2] C. H. Stephens and A. S. Arena, "Application of the Transpiration Method for Aeroservoelastic Prediction using CFD", AIAA-98-2071, 1998.

[3] T. J. Cowan, A. S. Arena, and K. K. Gupta, "Accelerating CFD-Based Aeroelastic Predictions Using System Identification", AIAA-98-4152, January 1998.

[4] T. J. Cowan, A. S. Arena, and K. K. Gupta, "Development of a Discrete-Time Aerodynamic Model for CFD-Based Aeroelastic Analysis", AIAA-99-0765, January 1999.

[5] W. A. Silva, "A Methodology for Using Nonlinear Aerodynamics in Aeroservoelastic Analysis and Design", NASA TM 104087, May 1991.

[6] G. Cybenko, "Approximation by Superposition of a Sigmoidal Function", Mathematics of Control, Signals, and Systems, 2, pp. 303–314, 1989.

[7] J. T. Connor and R. D. Martin, "Recurrent neural networks and robust time series prediction", IEEE Transactions of Neural Networks, 2(5): pp. 240–253, 1994.

[8] K. S. Narendra, "Neural Networks for Control: Theory and Practice", IEEE Proceedings, 84(10), pp. 1385–1406, October 1996.

[9] K. S. Narendra and K. Parthasarathy, "Identification and control of dynamical systems using neural networks", IEEE Transactions on Neural Networks, 1(1), pp. 4–27, March 1990.

[10] M. T. Hagan and H. B. Demuth, "Neural Networks for Control"

[11] A. Pinkus, "Approximation theory of the MLP model in neural networks", Acta Numerica, pp. 143-195, 1999

[12] K. J. Hunt and D. Sbarbaro, "Neural networks for nonlinear internal model control", IEEE Proceedings-D, 138(5), pp. 431–438, September 1991.

[13] D. H. Nguyen and B. Widrow, "Neural Networks for Self-Learning Control Systems", IEEE Control Systems Magazine, 10(4), pp. 18–23, April 1990.

[14] D. Psaltis, A. Sideri., and A. A. Yamamura, "A Multilayered Neural Network Controller", IEEE Control Systems Magazine, 8(4), pp. 17–20, April 1988.

[15] L. George and M Karl, "Efficient Numerical Inversion Using Multilayer Feedforward Neural Networks", The World Congress on Neural Networks, 1996, San Diego, California

[16] A. Yesildirek and F. L. Lewis, "Feedback Linearization using Neural Networks", Automatica, 31(11), pp. 1659-1664, 1995.

[17] L. Praly and Z. P. Jiang, "Stabilization by output feedback for systems with ISS inverse dynamics", Systems and Control Letters, 21, pp. 19-33, 1993

[18] K. Warwick, G. W. Irwin, and K. J. Hunt, "Neural Networks for Control and Systems." Stevenage, U.K.: Peregrinus, 1992.

[19] T. Poggio and F. Girosi, "Networks for approximation and learning," IEEE Proceedings, 78, pp. 1481–1497, September 1990.

[20] H. D. Patino and D. Liu, "Neural Network-Based Model Reference Adaptive Control System", IEEE Transactions, Cybernetics, 30(1), February 2000.

[21] J. J. Slotine, "Applied Nonlinear Control", Prentice Hall, 1991

[22] B. S. Kim and A. J. Calise, "Nonlinear Flight Control Using Neural Networks", AIAA, Journal of Guidance, Control, and Dynamics, 20(1), pp. 26-33, January-February 1997.

2004 International Mechanical Engineering Congress & Exposition
November 13 - 19, 2004, Anaheim, California at the Anaheim Hilton

IMECE2004-61311

# CFD-BASED AEROELASTICITY ANALYSIS IN TRANSONIC FLOW REGIME

**Chunlei He †**
**Maj. D. Mirmirani ‡‡**

**Sangbum Choi ‡**
**Chivey Wu ‡‡**

***California State University, Los Angeles, Los Angeles, 90032***

## ABSTRACT

The aeroelastic instability behavior of the AGARD445.6 wing at transonic flight speed is investigated by using Finite Element-based unsteady CFD simulations and automated three-dimensional unstructured meshing. A general-purpose multidisciplinary computer program called STARS (*Structural Analysis RoutineS*), developed at NASA Dryden Flight Research Center is employed as the tool for this study. The computational results on flutter boundaries of the wing structure are compared with wind tunnel data, and have been found to be satisfactory.

## INTRODUCTION

Aerodynamics analysis is generally considered with the assumption of the rigid body of the test model while the elasticity analysis is considered just under the static force load. However, the performance of an aircraft in actual flight condition usually involves combined features of fluid mechanics and elastic structure, which cannot be studied in any of the two domains independently. That is why aeroelasticity has such a significant role in modern aircraft design.

Aeroelastic analysis of the flight structure is the study of the potential instability of structures under the interaction of aerodynamic forces and the deformation of elastic bodies. For a given geometry, the aerodynamic forces depend on the shape of the structure and flight conditions as well as the deformation of the wing surfaces, which is affected by the aerodynamic forces as its external loads. Since the aerodynamic forces increase with the speed of the air while the structure stiffness remains independent of it, a critical condition might exist at which the structure transfers to be unstable resulting in possible catastrophic structural damage Ref. [2]. The *flutter* of wings is an unsteady aeroelastic instability phenomenon where a small disturbance would excite a self-sustained oscillation of the wing.

It is believed that flutter occurs because the speed of the flow affects the damping ratio and the phase shifts among the motions in different degrees of freedoms. The energy needed for the flutter is absorbed by the wing structure defined by the airfoil section from the upstream of air when it passes by. It is noteworthy that, fluttering does not response linearly to the change of flow speed within a wide Mach number range, especially in the transonic regime. Most of the experimental flutter tests of the sweptback wings show a sharp drop of the flutter speed between the subsonic and supersonic region (M:0.7~1.0), which is the well-known "Transonic Dip" phenomenon. Several factors might cause this phenomenon. One is the large negative out-of-phase component caused by the phase lag of the shock wave motion. Another is the effect from the thickness distribution of the airfoil on the unsteady aerodynamic flow, which was obtained in the Farmer and Hanson's experience Ref. [3].

Interest in flutter instability prediction of flight structures in the transonic regime has intensified in recent years because of the critical role it plays during the design of modern aircraft. However, the traditional wing tunnel testing is tedious, expensive making the sole use of this process impractical. During the past decade, tanks to the availability of inexpensive computational resources and development of efficient numerical methods and tools such as Computational Fluid Dynamics (CFD) and Computational Structure Dynamics (CSD) the use of computational aeroelasticity during the preliminary design phase and flight test has become more widely accepted. Still, to accurately predict the aeroelastic behavior of modern aircraft which operate over a wide range of speed, altitude and maneuvering conditions is a subject of

†: Graduate student, Department of Mechanical Engineering
‡: Research Associate, Multidisciplinary Flight Dynamics & Control Laboratory
‡‡ Professor, Mechanical Engineering Department

current research. The onset of flutter in transonic flight for example involves nonlinear phenomena with the mixed influence from the flow viscosity and shock waves introducing more complexity to the solution of the flutter problem Ref. [4]. Searching for flutter condition point-by-point within the flight envelop involves running a large number of CFD computational time and cost. Hence the motivation for methods to reduce the number of CFD runs to obtain the time dependent response of the aerodynamic forces since it is the unsteady CFD solver that generally requires the overwhelming CPU time. As a result, for the purpose of generating an accurate time marching solution of the unsteady aeroelastic problems, a highly integrated computational tool is need to efficiently synthesize the interaction between aerodynamics, structures, as well as controls to characterize the general dynamics system of a model aircraft.

The multidisciplinary computational program STARS is such an analysis tool employed in this research for the flutter boundary prediction. Its Direct Aeroelasticity Analysis Module utilizes Finite Element (FE) methodology for both CFD solver with unstructured tetrahedral meshes and CSD solver with modal superposition. A full set of Navier-Stoke governing equations is applied for the steady and unsteady CFD solutions because it can predict complex shock induced influences for transonic and supersonic flows and simulates viscosity effects. By coupling the solutions from the CFD unsteady solver with the modal vectors from the CSD solver, the dynamic equations of aeroelastic system can be cast in state-space form. "Transpiration" method is employed at each time step in unsteady solution to simulate the deformation of surface by modifying the normal vector of each surface tetrahedral element instead of re-meshing it Ref. [5].

In addition to the Direct Aeroelastic module STARS is equipped with another system approach to perform computational of aeroelasticity using system identification technique in accelerating the analysis of aeroelasticity. Auto Regressive Moving Average (ARMA) is used to model the input-output relationship between aerodynamic forces and the surface deformation. This ARMA modeling method is proved to reduce the amount of unsteady CFD calculation without affecting the accuracy of the whole aeroelasticity solutions Ref. [6].

AGARD 445.6 Wing was used for this study because it is a well-know structure and in addition to NASA generated wind tunnel data there is at least one set of previously published computational results, in all providing ample data for comparison and validation tests. The main objective of this paper is to identify the various differences and inaccuracies of computational-based flutter behavior in transonic regime by comparing them against each other and against experimental data. The results of flutter behavior of the wing in transonic regime using four sets of data based on a) the ARMA identification model; b) two different versions of Direct Aerlelasticity solvers, STARS Inviscid Ref.[1] and STARS-Viscous; c) the wind tunnel test, are compared.

## NOMENCLATURE

| | | | |
|---|---|---|---|
| CFD | = | Computational Fluid Dynamics | |
| CSD | = | Computational Structure Dynamics | |
| FE | = | Finite Element | |
| A | = | Surface area | |
| P | = | Upstream static pressure | |
| $\rho_{air}$ | = | Density of air in infinity | |
| a | = | Sound speed | |
| $M$ | = | Mach number | |
| [u] | = | Displacement vector | |
| $[q]$ | = | Generalized displacement vector | $\Phi^T[u]$ |
| $[\hat{K}]$ | = | Generalized stiffness matrix | $\Phi^T[K]\Phi$ |
| $[\hat{M}]$ | = | Generalized inertia matrix | $\Phi^T[M]\Phi$ |
| $[\hat{C}]$ | = | Generalized damping matrix | $\Phi^T[C]\Phi$ |
| $\Phi a$ | = | Aerodynamic modal vector, interpolated for structure | |
| $fa$ | = | Generalized aerodynamic force | $\Phi_a^T p A$ |
| $f_I$ | = | Impulse force vector (user input) | |
| $\overline{m}$ | = | Mass of unit length of chord | |
| $\mu$ | = | Mass Ratio | $\overline{m}/\rho_{air}$ |
| $b_{ref}$ | = | Reference length, semi chord | |
| $\omega$ | = | Damping frequency | |
| $\omega a$ | = | Natural frequency | |
| $\zeta$ | = | Flutter Speed Index | $M\frac{1}{\sqrt{\mu}}\frac{a_0}{b\omega_\alpha}\sqrt{\frac{T}{T_0}}$ |

## METHODOLOGY

The computational analyses were conducted using STARS - a program developed at NASA Dryden Flight Research Center. STARS is an high level integrated, finite-element program for Multi-disciplinary Analysis of flight structures, which covers static, dynamic structure analysis, fluid dynamic analysis, heat transfer and aeroelasticity analysis. All the analyses are based on the unstructured tetrahedral mesh.

### Aerodynamics Model

Because both the flow viscosity and shock induced influence need to be accounted for as significant effects during transonic flow, a full set of Navier-stoke equations is employed by the steady and unsteady CFD solvers. Based on the conservation of mass, momentum and energy of the control volume, the Navier-Stoke governing equations of a viscous, compressible fluid could be represented as a series of partial differential equations:

$$\frac{\partial V}{\partial t}+\sum_{i=1}^{3}\frac{\partial F_i}{\partial x_i}=f_b \qquad Eq.(1)$$

The flux $F_i$ consists of two parts: the convection item $f_j$ and the viscosity item $g_j$ . Also, Eq.1 can be expressed as:

$$\frac{\partial V}{\partial t}+\sum_{i=1}^{3}\frac{\partial f_i}{\partial x_i}+\sum_{i=1}^{3}\frac{\partial g_i}{\partial x_i}=f_b \qquad Eq.(2)$$

where each term in this equation is can be expanded as:
the flow variable vectors:

$$\frac{\partial V}{\partial t}=\frac{\partial}{\partial t}(\rho \quad \rho u \quad \rho v \quad \rho w \quad \rho E)^T;$$

the body forces vector:

$$f_b=\begin{pmatrix}0 & f_{b1} & f_{b2} & f_{b3} & \sum_{j=1}^{3}u_j f_{bj}\end{pmatrix}^T;$$

the convection vectors:

$$\sum_{i=1}^{3}\frac{\partial f_i}{\partial x_i}=\frac{\partial}{\partial x}(\rho\cdot\begin{pmatrix}u\\ u^2+\frac{p}{\rho}\\ vu\\ wu\\ u(E+\frac{p}{\rho})\end{pmatrix})+\frac{\partial}{\partial y}(\rho\cdot\begin{pmatrix}v\\ uv\\ v^2+\frac{p}{\rho}\\ wv\\ v(E+\frac{p}{\rho})\end{pmatrix})+\frac{\partial}{\partial z}(\rho\cdot\begin{pmatrix}w\\ uw\\ vw\\ w^2+\frac{p}{\rho}\\ w(E+\frac{p}{\rho})\end{pmatrix}) \qquad Eq.(3)$$

the viscosity flux vector:

$$\sum_{i=1}^{3}\frac{\partial g_i}{\partial x_i}=\frac{\partial}{\partial x}\begin{pmatrix}0\\ \sigma_{11}\\ \sigma_{21}\\ \sigma_{31}\\ u+k\frac{\partial T}{\partial x})\end{pmatrix}+\frac{\partial}{\partial y}\begin{pmatrix}0\\ \sigma_{12}\\ \sigma_{22}\\ \sigma_{32}\\ v+k\frac{\partial T}{\partial y})\end{pmatrix}+\frac{\partial}{\partial z}\begin{pmatrix}0\\ \sigma_{13}\\ \sigma_{23}\\ \sigma_{33}\\ w+k\frac{\partial T}{\partial z})\end{pmatrix} \qquad Eq.(4)$$

and the viscous stress tensor is:

$$\sigma_{ij}=\mu(\frac{\partial u_i}{\partial x_j}+\frac{\partial u_j}{\partial x_i})-\frac{2}{3}\mu\frac{\partial u_k}{\partial x_k}\delta_{ij}.$$

The aerodynamics model is based on the assumption of ideal compressible gas, whose state equation can be written as:

$$p=(\gamma-1)\rho[E-\frac{1}{2}(u_i u_j)] \qquad Eq.(5)$$

$$T=(E-\frac{1}{2}u_i u_j)c_v \qquad Eq.(6)$$

The partial differential equation relating the density and the pressure of the isentropic flow is:

$$\frac{\partial \rho}{\partial t}=\frac{1}{c^2}\frac{\partial p}{\partial t} \qquad Eq.(7)$$

## CFD Mesh Generation

STARS uses an advancing front algorithm in generating the automated three-dimensional unstructured mesh This algorithm has two main advantages. One is its flexibility in describing arbitrary shape and adjusting the grid density through the computational domain. The other is its adaptive meshing associated with solution convergence tendency. In the procedure of surface meshing, the generation front is continuously updated at each step when a new element is created and the nodes and triangles are generated simultaneously on each boundary surface. The followed volume meshing fills the whole computational domain with tetrahedral elements. The appropriated source parameters of the background meshing helps to define the node density, stretching tension and the direction of gradient.

The 3D automated unstructured mesh scheme combined with advancing front technique has proved to be versatile for the modeling of the complex computational domain. However, due to the extensive time spent in searching nodes and faces on the front meshing, a simple modification method is employ by STARS to accelerate the whole meshing processing. In the procedure of surface meshing, an initial coarse mesh is created at the starting sources defined by user input. Then the size of each cell is reduced linearly half of the previous one to reach the desired size. Such new four sub-triangles are created by connecting the midpoint of each edge of the previous triangle with line segments. Similarly, eight new cells replace one big tetrahedral element by introducing six new nodes at the midpoint of each edge.

## Boundary Transformation for Unsteady Calculation

In unsteady CFD/CSD solver, since the structure, in this case the AGARD wing is considered as an elastic body, the boundary condition of the wing surfaces will need to be updated in each time step due to the deformation of surface undergoing the aerodynamic loads.

Instead of using moving mesh to simulate surface deformation, STARS uses the transpiration method adapting the normal to the surface element at each FE node appropriately to reflect its deformation. If the changes in the normal directions of the nodes in a surface element are known, the CFD grid is modified accordingly.

With the transpiration method, CFD solver can account for the surface deformation even without the real mesh deflection at that location. At the same time, it has been proved in Ref [5] that this application has ignorable effect on the accuracy of the CFD solutions.

## FE Structural Model

A finite element model of AGARD 445.6 is constructed to calculate the eigenvalues and eigenvectors that describe the elastic modes for the structure. Any arbitrary motion of the structure can be expressed as the superposition of the eigenvector and the generalized displacements. The matrix equations of motion in terms of generalized coordinates

describing the deformation of the structure under the aerodynamic forces is:

$$\ddot{q}_i + 2\xi_i\omega_i\dot{q}_i + \omega_i^2 q_i = F_a \qquad Eq.(8)$$

where $q_i$ is the generalized modal displacement ($[q_i] = \phi^T[u_i]$), $\xi_i$ is the generalized damping, $\omega_i$ is the generalized modal frequency and $F_a$ is the generalized aerodynamic forces ($[F_a] = \hat{M}^{-1}\phi_a^T p \cdot S$)determined by the aerodynamic static pressure $p$ at the relative surface area $A$ of CFD grid nodes. $\Phi_a$ is the aerodynamic modal vector, which helps transferring the aerodynamic loads $\hat{f}_a(t)$ from the CFD unstructured grid to FE structure grid by interpolation. In this procedure, the triangle CFD element around an FE structure node is first identified. Then the aerodynamic forces of this FE structure node are obtained by interpolating the contribution of the aerodynamic forces from the CFD nodes to the structure nodes. The process is repeated to cover all the structural nodes to derive $\hat{f}_a(t)$ .

This module can effectively perform the static stability and dynamic analyses for linear and nonlinear structures.

## Direct Aeroelasticity Analysis Module and the Flutter Analysis

The complete integrated process for Direct Aeroelastic Analysis in STARS code is shown in the flow chart shown in Figure.1:

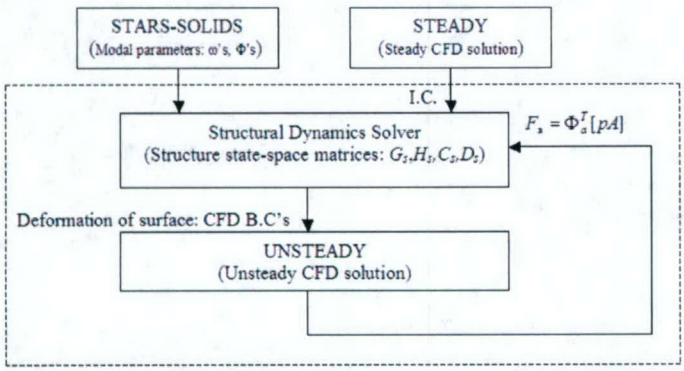


Fig.1 Procedure for Direct CFD-Based Aeroelastic Analysis

At any given flight condition, a steady-state Navier-Stoke solution is first accomplished through an explicit, global time-stepping steady CFD solver associated with the residual smoothing strategy. This steady-state solution is utilized as the initial condition to the following Aeroelastic analysis procedure. Meanwhile, STARS-SOLIDS computes the natural frequencies $\omega$ and modes $\Phi$ of the structure by solving the free vibration motion equation:

$$M\ddot{u} + Ku = 0 \qquad Eq.(9)$$

where $M$ and $K$ are the inertial and stiffness matrices, respectively. And $u$ is the displacement vector.

The Structural Dynamics Solver utilizes the results from SOLIDS and CFD STEADY solver to assemble the equations of motion in the frequency domain repeated here as:

$$\hat{M}\ddot{q} + \hat{C}\dot{q} + \hat{K}q = \hat{f}_a(t) + \hat{f}_I(t) \qquad Eq.(10)$$

STARS then assembles the matrix state-space equation as:

$$\begin{bmatrix}\dot{q}\\ \ddot{q}\end{bmatrix} = \underbrace{\begin{bmatrix}0 & I\\ -\hat{M}^{-1}\hat{K} & -\hat{M}^{-1}\hat{C}\end{bmatrix}}_{A}\begin{bmatrix}q\\ \dot{q}\end{bmatrix} + \underbrace{\begin{bmatrix}0\\ -\hat{M}^{-1}\hat{f}_a(n)\end{bmatrix}}_{B_a(n)} + \underbrace{\begin{bmatrix}0\\ -\hat{M}^{-1}\hat{f}_I(n)\end{bmatrix}}_{B_I(n)} \qquad Eq.(11)$$

The discrete time model response $[q \quad \dot{q}]^T$ within an increment $\Delta t$ step is:

$$\begin{bmatrix}q\\ \dot{q}\end{bmatrix}_{n+1} = e^{A\Delta t}\begin{bmatrix}q\\ \dot{q}\end{bmatrix}_n + A^{-1}[e^{A\Delta t} - I][B_a(n) + B_I(n)] \qquad Eq.(12)$$

Equation (12) shows that the time response solution of $[q,\dot{q}]^T$ comes from two parts: The last output of $[q,\dot{q}]^T$ solution, and the new force load based on the last boundary condition.

On the other hand, the aerodynamic force from STEADY solution is taken as the initial force load $\hat{f}_a(1)$. At an arbitrary time step $n$, the structure deformation $[u,\dot{u}]_n^T$ obtained from $\phi^T[q,\dot{q}]_n^T$ is inputted into the CFD UNSTEADY Solver to update the boundary conditions of the solid surface. This CFD solution follows to produce a new aerodynamic force load $\hat{f}_a(n)$. The Dynamic Solver next utilizes $[q,\dot{q}]_n^T$ and $\hat{f}_a(n)$ to compute the output $[q,\dot{q}]_{n+1}^T$ of n+1st -time step. The entire procedure is repeated until the desired last cycle step is reached. Enough number of the cycles would show either a fully developed convergent or divergent trend. The damping ratio $\varsigma$ and flutter frequency $\omega$ is extracted from $[q,\dot{q}]^T$ in the FFT form:

$$q = \sum_{m=1}^{r} e^{\varsigma m t}(a_m \cos\omega_m t + b_m \sin\omega_m t) \qquad Eq.(13)$$

## Aeroelastic System Identification (ARMA)

The ARMA system identification module of STARS converts the CFD Unsteady part in the Direct Aeroelastic Analysis module with a series of linear equations in state space form, as shown in figure 2.

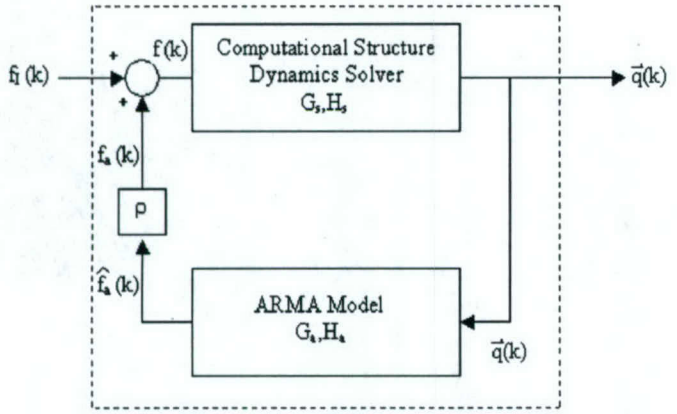


Fig. 2 Coupled ARMA Aeroelasticity Model

It is well known from linear system theory that the current output of a MIMO observable system can be determined from knowledge of past inputs and outputs. Assuming that the aerodynamic responds linearly to small perturbations about a nonlinear steady mean flow, it can be approximated with a linear dynamic system. Then the corresponding IO representation for the aerodynamics at time $k$ can be written in the format of an ARMA model as:

$$f_a(k) = \sum_{i=1}^{na} [A_i] f_a(k-i) + \sum_{j=0}^{nb-1} [B_j] \hat{q}(k-j) \qquad Eq.(14)$$

The ARMA model of equation (14) relates the current generalized aerodynamic force output to $na$ past outputs and $nb$ past inputs of the unsteady CFD solver, with matrices $\boldsymbol{A's}$ and $\boldsymbol{B's}$ to be determined by fitting the model to an appropriately generated set of "training" IO data and employing an optimized fitting technique such as the least squares method.

Once the aerodynamics model is established for a given Mach number by ARMA identification, one aeroelastic calculation can be finished within 60 seconds. Therefore, the critical flutter point at this Mach number can be identified through simply changing the value of the air density in a fraction of time possible using the Direct Aeroelastic module of STARS.

## AGARD 445.6 SWEPTBACK WING

The AGARD 445.6 Wing is a well-defined test case under the AGARD Standard aeroelastic configuration. The wing is structural deformation is defined by the first four vibration modes-first torsion, first bending, second torsion and second bending. A Finite Element model of the AGARD 445.6 Wing conducted in Ref [1] showed similar natural frequencies and mode shapes as those of the wind tunnel model. The characteristic parameters used at each flight point are presented in Table.1:

| | | |
|---|---|---|
| Geometry | Airfoil section | NACA 65A004 |
| | Aspect Ratio $AR$ | 1.65 |
| | Taper Ratio $c_{tip}/c_{root}$ | 0.66 |
| | Swept Angle $\Lambda$ | 45 ° |
| | Semi-Root Chord $b$ | 0.965 *ft* |
| Structure Model | Material mass in unit length $\overline{m}$ | 0.12764 *slug/ft* |
| | 1st torsion frequency $\omega_{\alpha 1}$ | 38.2 Hz |
| | 1st bending frequency $\omega_{\alpha 2}$ | 9.60 Hz |
| | 2nd torsion frequency $\omega_{\alpha 2}$ | 91.54 Hz |
| | 2nd bending frequency $\omega_{\alpha 2}$ | 48.35 Hz |
| CFD Solver | Number of elements | 235000 |
| | Number of nodes | 44648 |
| | STEADY CPU time | 3.96 hr |
| | UNSTEADY CPU time | 48.93 hr/case |
| | | 3~4 cases/ Mach |
| | ARMA Identification | 21.56 hr/Mach |
| | Number of cycles for UNSTEADY | 3000 |

Table .1 Characteristic parameters for Aeroelasticity Analysis of AGARD445.6 Wing

The wind tunnel test for the flutter analysis usually fixes the Mach number and decreases or increases the density of flow until the flutter boundary is reached. In order to obtain an effective comparison with those experimental wind tunnel data, the computational flutter analyses are processed at five Mach numbers: 0.678, 0.901, 0.96, 1.072, 1.141, independently. Since most of the flight conditions are within the transonic regime, the shock wave occurring around the leading edge and the expansion wave occurring around the training edge induce large aerodynamic changes. Therefore, extremely fine meshes around these two regions are required, as shown in Figure (4). The mesh on the symmetric plane shown in Figure (3) also needs to satisfy this requirement. Figure (5) presents a CFD steady solution example of the Pressure Distribution on the wing surface at Mach 1.141, which is used as the initial condition of following unsteady calculation.

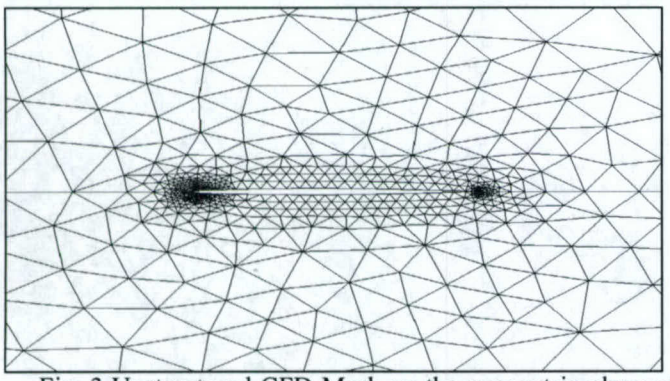

Fig. 3 Unstructured CFD Mesh on the symmetric plane of computational domain

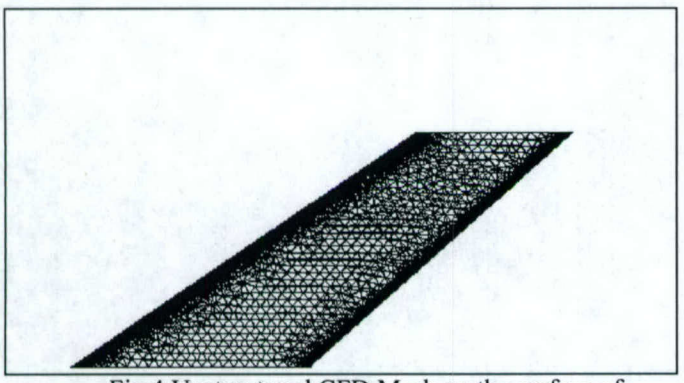

Fig.4 Unstructured CFD Mesh on the surface of AGARD445.6 wing

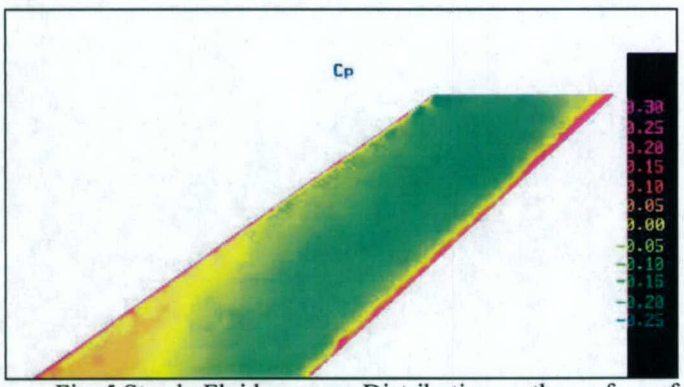


Fig. 5 Steady Fluid pressure Distribution on the surface of AGARD 445.6 Wing at Mach 1.141

Due to the high instability of transonic flow, more than 3000 cycles are required for the UNSTEADY calculation to obtain a fully developed result. The time historic response of the generalized displacement vectors at critical flutter point and the relative unsteady Aerodynamic forces are shown in Figure (6) and Figure (7), respectively:

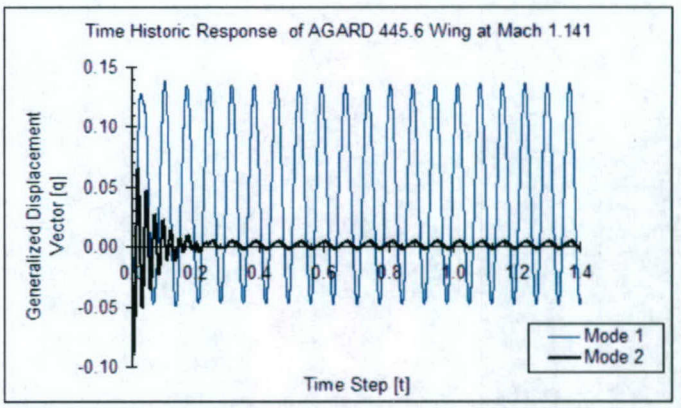


Fig.6 Time History Response of the Generalized Displacement Vectors at the critical flutter condition

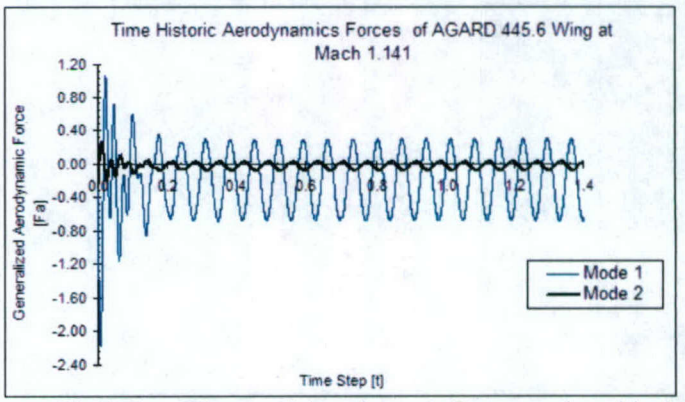


Fig.7 Time History of Aerodynamic Forces at the critical flutter condition

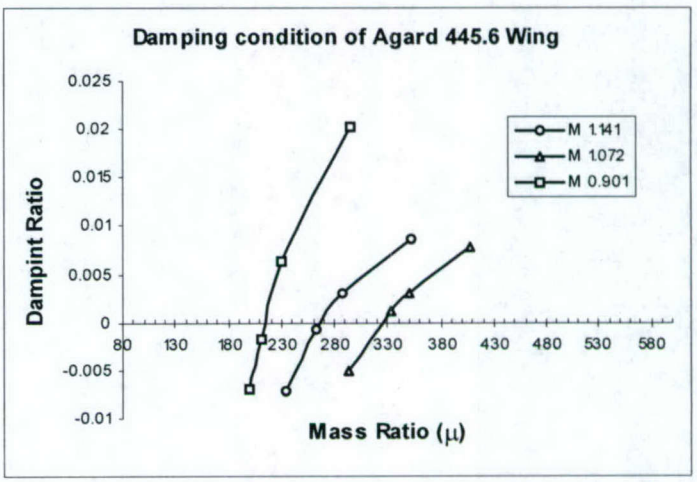


Fig.8 Damping Condition of AGARD445.6 Wing at different Mach numbers

For a given Mach number, the flutter oscillations of AGARD 445.6 Wing occur with different damping ratios and frequency at different flight altitudes. A graph of the damping ratio against the mass ratio $\mu(=\frac{\overline{m}}{\pi\rho_{air}b^2})$ reveals the instabilities of the structure for a given Mach. As shown in Fig.8, as the mass ratio grows, the damping ratio reduces and

ultimately cross the zero point from positive to negative and indication that the flutter oscillations change from convergent to divergent . At the exact cross-over point of zero damping the magnitude of oscillations is constant - the so-called *Critical Flutter Point*. The density of air at this point is defined as *critical flutter density*. The structural behavior of the wing is thus related to the flight altitude (indicated by density of air $\rho_{air}$) and the flight speed by a non-dimensional variable, the *Flutter Speed Index* $\zeta$, defined as:

$$\xi = \frac{V_\infty}{a_\infty}\sqrt{\frac{\pi\rho_{air}b^2}{\overline{m}}}\frac{a_\infty}{b\omega_\alpha} = M\frac{1}{\sqrt{\mu}}\frac{a_0}{b\omega_\alpha}\sqrt{\frac{T}{T_0}} \qquad Eq.(19)$$

$\omega_\alpha$ is the natural frequency of the wing. Since the temperature $T_0$, sound speed $a_0$ and the density of free stream air $\rho_\infty$ dependent on the flight altitude $h$, for an isentropic perfect flow ($\sqrt{T/T_0}$ = *function(M)*), *Flutter Speed Index* $\zeta$ could be regarded as a function of Mach number and the flight Altitude only:

$$\zeta = f(M,h)$$

| Mach | Flutter Speed Index $\zeta$ | | | |
|---|---|---|---|---|
| | STARS-Viscous | ARMA | STARS-Inviscid | Experiment |
| 0.678 | 0.444 | 0.429 | 0.380 | 0.417 |
| 0.901 | 0.380 | 0.376 | 0.341 | 0.370 |
| 0.96 | 0.334 | 0.322 | 0.280 | 0.306 |
| 1.072 | 0.359 | 0.350 | 0.302 | 0.306 |
| 1.141 | 0.418 | 0.402 | 0.410 | 0.308 |

Table.2 Comparison of Critical Flutter Speed Index of AGARD445.6 Wing around the transonic regime

| Mach | Flutter Frequency Ratio $\frac{\omega}{\omega_\alpha}$ | | | |
|---|---|---|---|---|
| | STARS-Viscous | ARMA | STARS-Inviscid | Experiment |
| 0.678 | 0.490 | 0.463 | 0.428 | 0.471 |
| 0.901 | 0.411 | 0.414 | 0.397 | 0.421 |
| 0.96 | 0.387 | 0.366 | 0.364 | 0.380 |
| 1.072 | 0.380 | 0.380 | 0.363 | 0.366 |
| 1.141 | 0.428 | 0.415 | 0.435 | 0.364 |

Table.3 Comparison of Flutter Frequency Ratio of AGARD445.6 Wing around the transonic regime

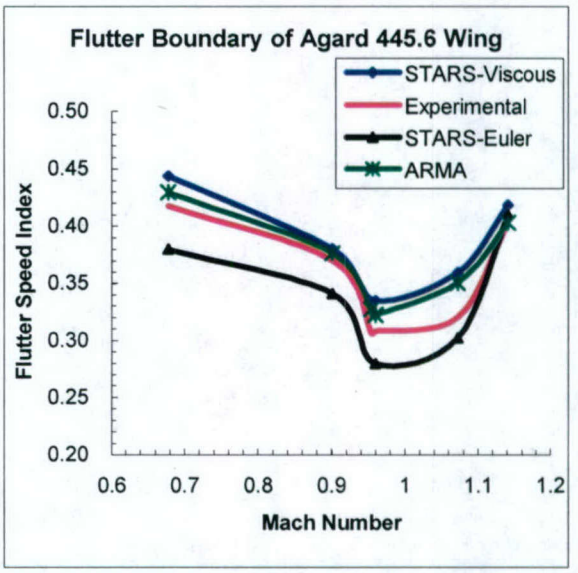


Fig.9 Flutter Boundary of AGARD445.6 Wing around the transonic regime

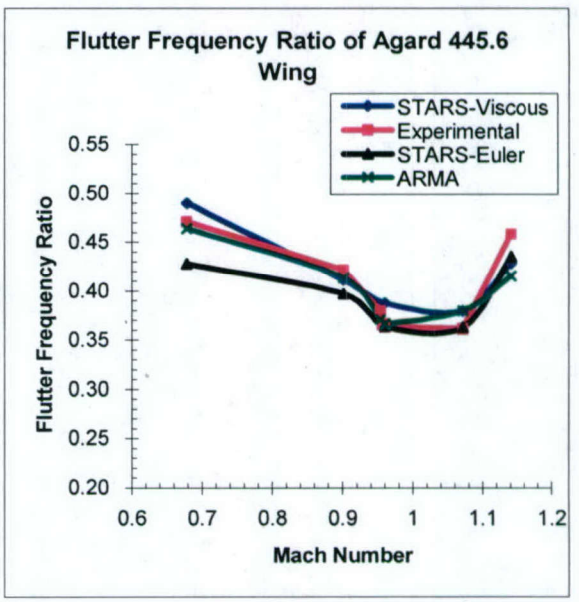


Fig.10 Flutter Frequency Ratio of AGARD445.6 Wing around the transonic regime

The *Critical flutter speed index* are plotted against Mach number for four sets of data: three obtained using CFD and one obtained using wind tunnel tests as shown in Figure (9). These graphs help predict the critical flutter boundary within a wide flight regime. Table.2, as well as Figure (9), presents the Critical Flutter Speed Index comparison among the STARS aeroelastic solutions from Viscous CFD model, ARMA identification model and the experimental data from the wind tunnel test launched by Langley Research Center. Meanwhile, a previous STARS aeroelastic solution based on the inviscid (Euler) CFD model is provided as a reference. The relative comparison of the damping flutter frequency $\omega$ and the natural flutter frequency $\omega_\alpha$ is presented in Table.3 as well as in Figure.10.

Flutter analysis of AGARD445.6 Wing shows close matching between the computational and wind tunnel data with reasonable disagreements in some areas. The 'Transonic Dip' is well predicted by both computational models at the same Mach range as the experiment data. In the region of 0.9< Mach < 1.2, a sudden decreasing of critical flutter speed is observed in wind tunnel tests representing the "*Transonic Dip*". Both models of STARS-Viscous and STARS-Inviscous predict the results closely to the wind tunnel tests with a clear sharp drop within the same Mach range. Disagreements between the computational solution and the experimental data grows for low Mach numbers. This discrepancy could be due to two main reasons:

a. The combined influences from the shock wave and Viscous effects on the drag;

b. The viscous effects on the boundary layer of wing surface;

c. The shock induced flow separation on the wing surface.

The viscosity induced drag dominates the total drag in the subsonic regime while the shock wave induced drag dominates the supersonic regime. However, within the transonic regime, both of these two mechanisms have significant effects on the drag. The viscosity effects are not accounted for in the STARS-Inviscid (Euler) model. This is the main reason why the solution of STARS-Inviscid model under-estimates the flutter boundary as compared with the experimental as well as the STARS-Viscous model data. The latter is shown to over-estimate the experimental data. In addition, viscosity increases the boundary layer around the wing surface, which effectively changes the 'thickness' of airfoil as perceived by the flow. The thicker airfoil causes a shift of flutter boundary curve to higher flutter speed index level at a given Mach.

Within the transonic regime, shock flow separation occurs around the maximum thickness point of the wing. Therefore, besides the leading and training edges, the mesh generated around the region of the maximum thickness should also be refined to capture the flow mechanism and produce accurate results.

## REMARKS

An integrated programs code- STARS employs the Finite Element modeling and numerical methods to process a complete and effective aeroelasticity analysis of aerial structure in a wide flight condition. Utilizing the common advantages of FE modeling it is possible to effectively commutes the interaction between the fluid and structure domains, facilitating simulation of aeroelastic instability in time domain.

With respect to CPU time the transpiration boundary method used in STARS in the UNSTEADY procedure largely saves the time required for updating the CFD mesh at each time step. The ARMA identification procedure is the most time efficient method that accelerates the UNSTEADY procedure with acceptable accuracy of solutions. However, this method can be applied for each Mach number at the time and is valid only for small structural deformation and when the unsteady aerodynamics can be approximated by a linear dynamic system. CFD-based aeroelasticity is useful to cut down the design cycle time and save the cost of preliminary analysis before launching the wing tunnel test

All computational aeroelasticity analyses conducted in this study were performed using the STARS program. Common PS computer was the only required hardware. It helps to shorten the design period.

## ACKNOWLEDGMENTS

The authors would like to thank Drs. Kajal Gupta and Shun Lung of NASA Dryden Flight Research Center for providing invaluable comments and suggestions during the performance of this research. This research is funded by NASA Grant (URC-NCC4-00158 ) and Air Force Office of Scientific Research Grant (F49620-01-1-0489).

## REFERENCES

[1] "Development of a Finite Element Aeroelastic Analysis Capability", K.K. Gupta, Journal of Aircraft, Volume 33, No.5. Pages 995-1002.

[2] "An introduction to the Theory of Aeroelasticty", Fung, Y.C., Chapter 5, 6.

[3] "Fully-Implicit Time-Marching Aeroelastic Solutions", Alonso, J. J., Jameson, Anthony, 32nd AIAA Aerospace Sciences Meeting & Exhibit, Jan 10-13, 1994, Reno, NV.

[4] "Improved Understanding of Transonic Flutter: a three Parameter Flutter Surface", Kholodar, D.B., Dpwell, E.H., Thomas, J.P., Hall, K.C..

[5] "Application of The Transpiration Method for Aeroelastic Prediction Using CFD", Stephens, H.C., Areno, Jr S.A., Gupta, K.K., AIAA-98-2071.

[6] "Development of a Discrete-Time Aerodynamic Model for CFD-Based Aeroelasticity Analysis", Cowan, T.J. , Areno, Jr S.A., and Gupta, K.K., AIAA-99-0765.

## Appendix IV


1. S. Keshmiri, M. Mirmirani, and R. Colgren, "Six-DOF Modeling and Simulation of a Generic Hypersonic Vehicle for Conceptual Design Studies," AIAA Modeling and Simulation Technologies Conference, Providence, Rhode Island, August 2004
2. B. Fidan, M. Mirmirani, and P. Ioannou, "Flight Dynamics and Control of Air-Breathing Hypersonic Vehicles: Review and New Directions," 12th AIAA International Space Planes and Hypersonic Systems and Technologies Conference, Norfolk, Virginia, December 2003

**AIAA Modeling and Simulation Technologies Conference**
**Providence, Rhode Island**

**Paper Number: AIAA-2004-4805**

# Six-DOF Modeling and Simulation of a Generic Hypersonic Vehicle for Conceptual Design Studies

Shahriar Keshmiri and Maj D. Mirmirani Ph. D.
College of Engineering, Computer Science, and Technology
California State University, Los Angeles
5151 State University Dr. Los Angeles, CA 90032
Skeshmi@calstatela.edu and mmirmir@calstatela.edu
Richard D. Colgren Ph. D.
University of Kansas
Lawrence, KS 66045
rcolgren@ku.edu

## Abstract

This paper covers the development of a CFD-based Six Degrees of Freedom simulation of a generic hypersonic vehicle [1]. The model and simulation are being developed to support conceptual design studies of hypersonic vehicles with multiple cycle engines. This includes both air breathing and rocket propulsion models. This work is supported by the NASA grant # NCC4-158, in support of their emphasis on new aerospace vehicle concepts and hypersonic technologies. A description of the aerodynamic and propulsion system models developed is included in this paper.

## Nomenclature

| Symbol | Definition |
|---|---|
| h | Altitude, ft |
| b | lateral-directional reference length, span, ft |
| B | Body coordinate frame |
| c | longitudinal reference length, mean aerodynamic chord, ft |
| $C_D$ | total drag coefficient |
| $C_{Da}$ | drag increment coefficient for basic vehicle |
| $C_{D,\delta_a}$ | drag increment coefficient for right elevon |
| $C_{D,\delta_e}$ | drag increment coefficient for left elevon |
| $C_{D,\delta_r}$ | drag increment coefficient for rudder |
| $C_{D,\delta_c}$ | drag increment coefficient for canard |
| $C_L$ | total lift coefficient for basic vehicle |
| $C_{La}$ | lift increment coefficient for basic vehicle |
| $C_{L,\delta_a}$ | lift increment coefficient for right elevon |
| $C_{L,\delta_e}$ | lift increment coefficient for left elevon |
| $C_{L,\delta_r}$ | lift increment coefficient for rudder |
| $C_{L,\delta_c}$ | lift increment coefficient for canard |
| $C_Y$ | total side force |
| $C_{Y\beta}$ | side force with sideslip derivative for basic vehicle |
| $C_{Y,\delta_a}$ | side force increment coefficient for right elevon |
| $C_{Y,\delta_e}$ | side force, increment coefficient for left elevon |
| $C_{Y,\delta_r}$ | side force, increment coefficient for rudder |
| $C_l$ | total rolling moment coefficient |
| $C_{l\beta}$ | rolling moment with sideslip derivative for basic vehicle |
| $C_{l,\delta_a}$ | rolling moment increment for right elevon |
| $C_{l,\delta_e}$ | rolling moment increment for left elevon |
| $C_{l,\delta_r}$ | rolling moment increment for rudder |
| $C_{lp}$ | rolling moment with roll rate dynamic derivative |
| $C_{lr}$ | rolling moment with yaw rate dynamic derivative |
| $C_m$ | total pitching moment coefficient |

| | |
|---|---|
| $C_{ma}$ | pitching moment increment coefficient for basic vehicle |
| $C_{m,\delta_a}$ | pitching moment increment coefficient for right elevon |
| $C_{m,\delta_e}$ | pitching moment increment coefficient for left elevon |
| $C_{m,\delta_r}$ | pitching moment increment coefficient for rudder |
| $C_{m,\delta_c}$ | pitching moment increment coefficient for canard |
| $C_{mq}$ | pitching moment pitch rate dynamic derivative |
| $C_n$ | total yawing moment coefficient |
| $C_{n\beta}$ | yawing moment with sideslip derivative for basic vehicle |
| $C_{n,\delta_a}$ | yawing moment increment coefficient for right elevon |
| $C_{n,\delta_e}$ | yawing moment increment coefficient for left elevon |
| $C_{n,\delta_r}$ | yawing moment increment coefficient for rudder |
| $C_{np}$ | yawing moment roll rate dynamic derivative |
| $C_{nr}$ | yawing moment yaw rate dynamic derivative |
| E | inertial coordinate frame |
| ISP | engine specific impulse, sec |
| $\alpha$ | Angle of attack, degree |
| $\beta$ | Sideslip angle, red. |
| $\phi$ | Engine fuel ratio |
| M | Mach number |
| $\bar{q}$ | dynamic pressure |
| $S_{ref.}$ | Reference area, theoretical wing area, $ft^2$ |
| T | engine net thrust, lb |
| X, Y, Z | total aerodynamic forces (in body coordinate x, y, and z) |
| V | vehicle free stream velocity (ft/sec) |
| $\dot{W}$ | Fuel flow rate, lb/sec |
| $W_0$ | initial value of vehicle weight, lb |
| $W_{con}$ | weight of fuel consume |
| $X_{cg.}$ | Longitudinal distance from momentum reference to vehicle c.g., positive aft, ft |
| $I_{XX}$, $I_{YY}$, $I_{ZZ}$ | roll, pitch, and yaw moments of inertia respectively, slg-$ft^2$ |
| n.d. | Non-dimensional |
| c.g. | Vehicle center of gravity |
| SSTO | Single-Stage-To-Orbit |
| DOF | degrees of freedom |
| {q} | The rotation quaternion |
| $\{Q^{BE}\}$ | the rotational tensor of body frame wrt the Earth frame |
| $\{\Omega^{BE}\}$ | Angular velocity quaternion of body frame wrt the Earth |
| [I] | Identity matrix |
| p | roll rate |
| q | Pitch rate |
| r | yaw rate |
| A.O.A | Angle of attack, degree |
| PLA | pilot lever angle, (%0~%100) |
| Thr. | Throttle angle |
| $F_{a,p}$ | Aerodynamic and Propulsive forces |
| $[M_B]^B$ | Momentum in Body coordinate |

## Introduction

The objective of this paper is to present a CFD-based Six Degrees of Freedom (DOF) simulation model for a generic hypersonic vehicle (GHV), the "Winged-Cone." It was developed to support NASA funded conceptual design studies of hypersonic flight vehicles at the Multidisciplinary Flight Dynamics and Control Laboratory at California State University, Los Angeles (see www.calstatela.edu/centers/mfdclab). The aerodynamic characteristics of the vehicle were developed using a CFD-based study conducted jointly at NASA Langley and Rockwell International. The Aerodynamic Preliminary Analysis System (APAS) CFD results in reference [1] were digitized and organized in more than 60 lookup tables for this simulation. In addition, analytical expressions up to seventh order polynomials were developed [9], [10] based on the values of Sum of Squares due to Error (SSE). A multiple cycle engine model was developed which includes both air breathing and rocket propulsion modes to cover subsonic, supersonic and hypersonic speed ranges. A FORTRAN code was developed as the implementation of the nonlinear simulation. Results from straight and level flight, ascending and descent flight, are presented.

## Vehicle Description

The three-view drawing of the Generic Hypersonic Vehicle (GHV) is given in Figure 1. The geometric characteristics of the vehicle are given in Table 1. Deflections of the elevons are measured with respect to the hinge line, which is perpendicular to the fuselage centerline. A fuselage, centerline-mounted vertical tail has a full span rudder with its hinge line at 25 percent of the chord from the trailing edge. Deflections of the rudder are measured with respect to its hinge line. Positive deflections are tailing edge left. Small canards (65 A series airfoil) are deployed at subsonic speeds for improved longitudinal stability and control [1]. A sizing analysis of the vehicle

yielded an estimated full-scale gross weight of 300,000 lbs. The equations of motion account for the time varying center of mass, center of gravity, and moments of inertia as experienced during flight. It is assumed that c.g moves only along the body x-axis as fuel is consumed, vertical changes are not modeled Fuel slosh is not considered, and products of inertia are assumed negligible.

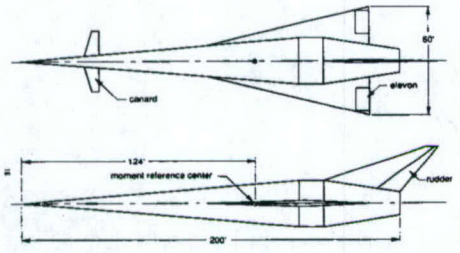


Figure 1: Three View of Generic Hypersonic Vehicle

Table 1: Geometric Characteristics of Generic Hypersonic Vehicle

| Wing | Unit | |
|---|---|---|
| Reference area | $ft^2$ | 3603.00 |
| Aspect ratio | | 1.00 |
| Span | ft | 60.00 |
| Leading edge sweep angle | deg. | 75.97 |
| Trailing edge sweep angle | deg. | 0.00 |
| Mean aerodynamic chord | ft | 80.00 |
| Airfoil section | - | Diamond |
| Airfoil thickness to chord ratio | % | 4.00 |
| Induced angle | deg. | 0.00 |
| Dihedral | deg. | 0.00 |
| Wing flap (elevon) | Unit | |
| Area each | $ft^2$ | 92.30 |
| Chord (constant) | ft | 7.22 |
| Inboard section span location | ft | 15.00 |
| Outboard section span location | ft | 27.78 |
| Vertical tail, body centerline | Unit | |
| Exposed area | $ft^2$ | 645.70 |
| Theoretical area | $ft^2$ | 1248.80 |
| Span | | 32.48 |
| Leading edge sweep angle | deg. | 70.00 |
| Trailing edge sweep angle | deg. | 38.13 |
| Airfoil section | - | Diamond |
| Airfoil thickness to chord ratio | % | 4.00 |
| Rudder | Unit | |
| Area | $ft^2$ | 161.40 |
| Span | ft | 22.80 |
| Chord of vertical tail chord ratio | % | 25.00 |
| Canard | Unit | |
| Exposed area | $ft^2$ | 154.30 |
| Theoretical area | $ft^2$ | 5.48 |
| Span | ft | 33.60 |
| Leading edge sweep angle | deg. | 16.00 |
| Trailing edge sweep angle | deg. | 0.00 |
| Airfoil section | - | NACA 65A006 |
| Induced angle | deg. | 0.00 |
| Dihedral | deg. | 0.00 |
| Axisymmetric fuselage | Unit | |
| Theoretical length | ft | 200.00 |
| Cone half angle | deg. | 5.00 |
| Cylinder radius (maximum) | ft | 12.87 |
| Cylinder length | ft | 12.88 |
| Boat tail half angle | deg. | 9.00 |
| Boat tail length | ft | 40.00 |
| Momentum reference center | ft | 124.01 |

## Flat-Earth Equations of Motion

The translational equations of motion subjected to aerodynamic and thrust forces $f_{a,p}$, along with the gravitational acceleration g under the approximations of a "flat-Earth," are presented in this section. The time rate of change of linear momentum in the inertial frame [I] equals the externally applied forces [2].

$$mD^E v_B^E = f_{a,p} + mg \quad (1)$$

$$mD^E v_B^E = m\left[D^B v_B^E + \Omega^{BE} v_B^E\right] \quad (2)$$

The same equation can be written in the Body Coordinate Frame as:

$$m\left[D^B v_B^E + \Omega^{BE} v_B^E\right] = f_{a,p} + mg \quad \text{Airfoil section} \quad (3)$$

To generate the ordinary time derivative, the rotational derivative must be expressed in the coordinate system $]^B$ associated with the frame B. The aerodynamic and propulsive forces, the linear velocity of vehicle with, and angular velocity of vehicle with respect to the Earth are expressed in the body axis coordinate system. In the flat Earth approximation the gravity vector simplifies to $\left[\overline{g}\right]^t = [0 \quad 0 \quad g]$ [2].

The transitional equation of motion in matrix format is written as:

$$m\left[\frac{d v_B^E}{dt}\right] + m[\Omega^{BE}]^B [v_B^E]^B = [f_{a,p}]^B + m[T]^{BL}[g]^L \quad (4)$$

Or in the matrix form

$$m\left\{\begin{bmatrix} du/dt \\ dv/dt \\ dw/dt \end{bmatrix}^B + \begin{bmatrix} 0 & -r & q \\ r & 0 & -p \\ -q & p & 0 \end{bmatrix}^B \begin{bmatrix} u \\ v \\ w \end{bmatrix}^B\right\} = \begin{bmatrix} f_{a,p1} \\ f_{a,p2} \\ f_{a,p3} \end{bmatrix}^B + [T]^{BL}\begin{bmatrix} 0 \\ 0 \\ mg \end{bmatrix}^L$$

Where

$$[T]^{BL} = \begin{bmatrix} t_{11} & t_{12} & t_{13} \\ t_{21} & t_{22} & t_{23} \\ t_{31} & t_{32} & t_{33} \end{bmatrix}^{BL} \quad (5)$$

Equivalently the three scalar equations for translational motion of the vehicle are [2]:

$$\frac{du}{dt} = rv - qw + \frac{f_{a,p1}}{m} + t_{13}\, g \quad (6-1)$$

$$\frac{dv}{dt} = pw - ru + \frac{f_{a,p2}}{m} + t_{23}\, g \quad (6-2)$$

$$\frac{dw}{dt} = qu - pv + \frac{f_{a,p3}}{m} + t_{33} g \quad (6-3)$$

Two successive integrations of these equations will yield the velocity vector and the location of the air vehicle c.g. with respect to an Earth reference point. However, since the integration is carried out in the local-level coordinate system a transformation from the Body Frame to the Local-Level coordinate frame is required:

$$[D^E S_{BE}]^L = [\overline{T}]^{BL}[v_B^E]^B \quad (7)$$

The translational equations of motion for the vehicle are nonlinear. They are coupled with the rotational equations of motion through the body rates p, q, and r and the directional cosine matrix $[T]^{BL}$. Euler's law is used for modeling the rotational degrees of freedom. Euler's law states that the time rate of change of angular momentum equals the externally applied moments. The rotational equations of motion in the inertial coordinate frame, E, and its transformation to the body coordinate frame, B, are written below (9-10&11)[2]:

$$D^E I_B^B \omega^{BE} = M_B \quad (9)$$

$$D^B I_B^B \omega^{BE} + \Omega^{BE} I_B^B \omega^{BE} = M_B \quad (10)$$

$$D^B(I_B^B \omega^{BE}) = I_B^B D^B \omega^{BE} + \omega^{BE} D^B I_B^B \quad (11)$$

For a rigid body term $D^B I_B^B$ is zero and equation (11) reduces to:

$$\left[\frac{dw^{BE}}{dt}\right]^B = \left([I_B^B]^B\right)^{-1}\left(-[\Omega^{BE}]^B [I_B^B]^B [\omega^{BE}]^B + [M_B]^B\right) \quad (12)$$

The above set of equations represents the three rotational degrees of freedom. This set is coupled with the translational equations through the aerodynamic moments $[M_B]^B$ [2].To determine the orientation of the vehicle with respect to an inertial Earth centered frame from motions described by the body rates $[w^{BI}]^B$, Hamilton's quaternion method is applied. The rotation quaternion {q}, the rotational tensor of body frame with respect to E {QBE}, and angular velocity quaternion of body frame with respect to frame E $\{\Omega^{BE}\}$, are used to develop the quaternion differential equations. The quaternion formulation has the advantage that the singularities at angles of ninety degrees encountered in the Euler formulation are avoided.

Define the Quaternion vector as [3]:

$$\{q\} = \begin{Bmatrix} q_0 \\ [q] \end{Bmatrix} \quad (13-1) \qquad [q] = \begin{bmatrix} q_1 \\ q_2 \\ q_3 \end{bmatrix} \quad (13-2)$$

The four-quaternion elements of $\{q\}$: $q_0, q_1, q_2, q_3$

$q_0$ : a scalar part(rotation angle)

[q]: a three-dimensional vector

$$\{Q^{BE}\} = \begin{Bmatrix} q_0 & [\overline{q}] \\ -[q] & q_0[E] + [Q] \end{Bmatrix}$$

$$\{\Omega^{BE}\}^L = \begin{Bmatrix} 0 & -[\overline{\omega^{BE}}]^L \\ [w^{BE}]^L & -[\Omega^{BE}]^L \end{Bmatrix}$$

With substitution of the values for $\{\Omega^{BE}\}^L$ & $[\overline{\omega}^{BE}]^L$, the desired quaternion linear differential are.

$$\begin{Bmatrix} \dot{q}_0 \\ \dot{q}_1 \\ \dot{q}_2 \\ \dot{q}_3 \end{Bmatrix} = \frac{1}{2}\begin{bmatrix} 0 & -p & -q & -r \\ p & 0 & r & -q \\ q & -r & 0 & p \\ r & q & -p & 0 \end{bmatrix}\begin{Bmatrix} q_0 \\ q_1 \\ q_2 \\ q_3 \end{Bmatrix} \quad (14)$$

Combining $q(\psi),\ q(\theta), q(\phi)$ leads to following equations:

$$q_0 = \cos(\frac{\psi}{2})\cos(\frac{\theta}{2})\cos(\frac{\phi}{2}) + \sin(\frac{\psi}{2})\sin(\frac{\theta}{2})\sin(\frac{\phi}{2}) \quad (15-1)$$

$$q_1 = \cos(\frac{\psi}{2})\cos(\frac{\theta}{2})\sin(\frac{\phi}{2}) - \sin(\frac{\psi}{2})\sin(\frac{\theta}{2})\cos(\frac{\phi}{2}) \quad (15-2)$$

$$q_1 = \cos(\frac{\psi}{2})\sin(\frac{\theta}{2})\cos(\frac{\phi}{2}) + \sin(\frac{\psi}{2})\cos(\frac{\theta}{2})\sin(\frac{\phi}{2}) \quad (15-3)$$

$$q_1 = \sin(\frac{\psi}{2})\cos(\frac{\theta}{2})\cos(\frac{\phi}{2}) - \cos(\frac{\psi}{2})\sin(\frac{\theta}{2})\sin(\frac{\phi}{2}) \quad (15-4)$$

The above equations can be solved to give the Euler angles in terms of the Quaternion elements as follows:

$$\tan\psi = \frac{2(q_1q_2 + q_0q_3)}{q_0^2 + q_1^2 + q_2^2 + q_3^2} \quad (16-1)$$

$$\sin\theta = -2(q_1q_3 + q_0q_2) \quad (16-2)$$

$$\tan\phi = \frac{2(q_2q_3 + q_0q_1)}{q_0^2 - q_1^2 - q_2^2 - q_3^2} \quad (16-3)$$

The matrix $[T]^{BL}$ also can be written in terms of quaternion variables too:

$$[T]^{BL} = \begin{bmatrix} q_0^2+q_1^2-q_2^2-q_3^2 & 2(q_1q_2+q_0q_3) & 2(q_1q_3-q_0q_2) \\ 2(q_1q_2-q_0q_3) & q_0^2-q_1^2+q_2^2-q_3^2 & (q_2q_3+q_0q_1) \\ 2(q_1q_3+q_0q_2) & (q_2q_3-q_0q_1) & q_0^2-q_1^2-q_2^2+q_3^2 \end{bmatrix} \quad (17)$$

## The Propulsion and Aerodynamic Forces & Moments

For the simulation, using the flat-Earth approximation, the aerodynamic and thrust forces and momentums are written in the body coordinate system as follows [2]:

$$[F_{A,P}] = \begin{bmatrix} \bar{q}SCx + f_p \\ \bar{q}SC_Y \\ \bar{q}SC_Z \end{bmatrix} \quad (18)$$

$$[M_B]^B = \begin{bmatrix} \bar{q}SbC_l \\ \bar{q}ScC_m \\ \bar{q}SbC_n \end{bmatrix} \quad (19)$$

The CFD-based code developed jointly by NASA Langley and Rockwell International Inc. was used for developing the aerodynamic model for the GHV [1]. Data was computed for the following Mach numbers 0.3, 0.7, 4.0, 6.0, 10.0, 15.0, 20.0, and 24.2 and angles of attack -1.0°, 0.0°, 2.0°, 4.0°, 6.0°, 8.0°, 10.0°, and 12.0°. Coefficients were generated for a range of deflections of the right elevon, the left elevon, and the rudder at each Mach number and angle of attack combination, each taken separately. Rudder deflections of -20.0°, -10.0°, 0.0°, 10.0°, and 20.0° were used for each surface. At two subsonic Mach numbers, 0.3, 0.7, and eight angles of attack, -1.0°, 0.0°, 2.0°, 4.0°, 6.0°, 8.0°, 10.0°, and 12.0°, coefficients were estimated for canard deflections of -10.0°, -5.0°, 0.0°, 5.0°, and 10.0°.
The lift, drag, and sideslip force, as well as the rolling, pitching, and yawing moment increment coefficients and derivatives are determined as functions of angle of attack and Mach number. The increment coefficients caused by control surface deflections are determined as functions of angle of attack, surface deflection, and Mach number. They are added to the basic vehicle increments to form total aerodynamic force and moment coefficients [1]. MATLAB code was developed and was used to obtain coefficients of the polynomials describing the aerodynamic coefficients, (CD, CL, Cl, CY, Cm, and Cn)

### Drag Force Computation

The total drag coefficient is described by he expression:
CD= CDa+ CD, δe+ CD, δa+ CD, δr+ CD, δc Where
CD = $f(M, \alpha, \delta_a, \delta_e, \delta_r, \delta_c)$
Using a MATLAB routine called FITTER, analytical expressions for the components of $C_D$ are obtained for subsonic, supersonic, and hypersonic speeds:

Subsonic

$C_{Da}$ =+5.810E-03-7.000E-04* α
$C_{Da}$ =+ 5.800E-03 -7.000E-04*α
+ 3.400E-03*(M) + 3.000E-04*(α) ^3
-6.4E-05*(α) ^4 +5.998E-06*(α) ^5
-2.032E-07*(α) ^6+5.235E-10 * (α) ^7
$C_{D,\delta a}$ =- 5.184E-04+1.100E-03*α
+3.38E-07*(α*δa)-1.36E-03 *(α*M)
-2.79E-04*(M*δa)-1.53E-04 *(α*M)*δa
+1.29E-03*M^2-1.02E-04 *α^2+9.39E-08*δa^2
-5.69E-07*((α*M)*δa) ^2+4.14E-07 *(α*δa) ^2
+ 1.81E-04*(α*M) ^2-1.68E-05*(M*δa) ^2
-1.84E-06*δa^3+6.40E-08*α^4+5.76E-08*δa^4
+5.71E-09*δa^5 - 8.93E-15*((α*M) *δa) ^5
-7.58E-12*((α*M)*δa) ^4- 3.94E-10*((α*M) *δa) ^3

$C_{D,\delta_e}$ =- 5.184E-04+1.100E-03*α
+3.38E-07*(α*δe)-1.36E-03 *(α*M)
-2.79E-04*(M*δe)-1.53E-04*(α*M)*δe
+1.29E-03*M^2-1.02E-04*α^2
+9.39E-08*δe^2-5.69E-07*((α*M)*δe) ^2
+4.14E-07*(α*δe) ^2+1.81E-04*(α*M) ^2
-1.68E-05*(M*δe) ^2-1.84E-06*δe^3
-3.94E-10*((α*M)*δe) ^3+6.40E-08*α^4
+5.76E-08*δe^4-7.58E-12*((α*M)*δe) ^4
+ 5.71E-09*δe^5 - 8.93E-15*((α*M)*δe) ^5
$C_{D,\delta_r}$ =+2.47E-04-1.93E-04 *α+7.27E-05*(α*M)
+4.73E-05*M^2 +1.50E-05*α^2+5.03E-06*δr^2
-1.30E-07*((α*M)*δr) ^2-3.50E-08*(αa*δr) ^2
- 1.68E-06*(α*M) ^2+4.53E-06*(M*δr) ^2
-1.98E-11 *α^3-2.63E-08*α^4+7.54E-09*δr^4
+ 3.12E-12*((α*M)*δr) ^4
$C_{D,\delta_c}$ =-5.334E-04+5.548E-04*M+9.3E-05*α
+4.660E-05*(α*δc) -6.330E-05*(α*M)
+1.900E-05*(M*δc) +1.270E-05*(α*M)*δc
+3.100E-05*α^2+1.550E-05*δc^2
+2.000E-07*((α*M)*δc) ^2 + 2.000E-07*(α*δc) ^2
+3.000E-06*(α*M) ^2+2.230E-05*(M*δc) ^2
-7.900E-06*α^3+9.000E-07*δc^3+5.000E-07*α^4
-1.01E-08*α^5-1.00E-08*δc^5
-3.08E13*((α*M)* δc) ^5+8.71E-08*δc^4
-4.44E-11*((α*M)*δc) ^4+3.02E-09*((α*M)*δc)^3

Supersonic/ Hypersonic

$C_{Da}$ =+8.717E-02-3.307E-02*M
+3.179E-03*α-1.250E-04*(α*M)
+ 5.036E-03*M^2- 0.100E-03*α^2
+1.405E-07*(α*M) ^2-3.658E-04*M^3
+3.175E-04*α^3+1.274E-05*M^4-2.985E-05*α^4
- 1.705E-07 *M^5 + 9.766E-07*α^5
$C_{D,\delta_a}$ =+4.02E-04+2.34E-05 *α-1.02E-04 *M
-3.46E-05*δa-5.38E-07*(α*M)*δa+3.08E-06*α^2
+2.61E-06*M^2+6.84E-06*δa^2
+5.28E-12*((α*M)*δa)^2
$C_{D,\delta_e}$ =+4.02E-04+2.34E-05 *α-1.02E-04 *M
-3.46E-05*δe-5.38E-07*(α*M)*δe+3.08E-06*α^2
+ 2.61E-06*M^2+6.84E-06*δe^2
+5.28E-12*((α*M)*δe) ^2
$C_{D,\delta_r}$ = + 7.50E-04-2.29E-05*α 9.69E-05*M
-1.83E-06*δr+9.13E-09*(α*M)*δr+8.76E-07*α^2
+2.70E-06*M^2+1.97E-06*δr^2+...
...-1.77E-11*((α*M)* δr) ^2

The drag force is given by:

$$D = \bar{q} S_{ref} C_D$$

## Lift Force Computation

The total lift coefficient is obtained as:

CL= CLa+ CL, δa+ CL, δe+ CL, δc Where

CL= $f(M, \alpha, \delta_a, \delta_e, \delta_c)$

Using a MATLAB routine called FITTER, analytical expressions for the components of CL are obtained for subsonic, supersonic, and hypersonic speeds:

Subsonic

$C_{La}$ =-0.001576+1.800E-02*α
+0.001944*(α*M)-0.000308*M^2
+0.0013622*α^2+0.0001992*(α*M) ^2
+6.46E-05*α^3+2.29E-05*α^4+1.06E-06*α^5
$C_{L,\delta_a}$ =-5.119E-04+1.000E-03*α
-1.406E-04*(α*δa)+1.313E-03*(α*M)
-8.584E-04*(M*δa)+8.879E-05*(α*M)*δa
-1.604E-04*M^2-3.477E-04*α^2
- 9.788E-05*(α*M)^2-1.703E-06*(M*δa)^2
+2.532E-05*α^3-3.727E-05*δa^3
+1.781E-07*δa ^2+7.912E-07*((α*M)* δa) ^2
+2.465E-08*(α*δa) ^2-9.788E-05*(α*M) ^2
-5.942E-09 *((α*M)*δa) ^3-7.377E-08*α^4
+2.672E-08*δa ^4-1.610E-11*((α*M)* δa) ^4
-3.273E-08*α^5+7.624E-08*δa ^5
+1.388E-13*((α*M)* δa)^5
$C_{L,\delta_e}$ =-5.119E-04+1.000E-03*α
-1.406E-04*(α*δe)+1.313E-03 *(α*M)
-8.584E-04*(M*δe)+8.879E-05*(α*M)* δe
-1.604E-04*M^2- .477E-04*α^2
-9.788E-05*(α*M)^2-1.703E-06*(M*δe)^2
+2.532E-05*α^3-3.727E-05*δe^3+1.781E-07*δe ^2
+7.912E-07*((α*M)* δe) ^2+2.465E-08*(α*δe)^2
-9.788E-05*(α*M) ^2-5.942E-09 *((α*M)* δe) ^3
-7.377E-08*α^4+2.672E-08*δe ^4
-1.610E-11*((α*M)* δe) ^4-3.273E-08*α^5
+7.624E-08*δe^5+1.388E-13*((α*M)* δe) ^5
$C_{L,\delta_c}$ =-1.022E-03+7.000E-04*M
+8.33E-04*α+1.96E-05*(α*δc)-3.93E-04*(α*M)
-3.40E-04*(M*δc)+1.85E-05*(α*M)*δc
+1.04E-05*α^2+1.77E-05*δc^2
+1.08E-06*((α*M)* δc)^2+2.70E-07*(α*δc)^2
+1.92E-05*(α*M)^2-1.51E-05*(M*δc)^2
-2.46E-05*α^3+3.91E-07*δc^3
+3.63E-09*((α*M)* δc) ^3+2.43E-06*α^4
-2.56E-09*δc ^4-1.29E-10*((α*M)* δc) ^4
-7.29E-08*α^5-2.04E-08*δc ^5
- 2.27E-13 *((α*M)* δc) ^5

Supersonic/ Hypersonic

$C_{La}$ =-8.19E-02+4.70E-02*M
+1.86E-02*α-4.73E-04*(α*M)
-9.19E-03*M^2-1.52E-04*α^2
+5.99E-07*(α*M)^2+7.74E-04*M^3
+4.08E-06 *α^3-2.93E-05*M^4
-3.91E-07*α^4+4.12E-07*M^5 +1.30E-08*α^5
$C_{L,\delta_a}$ =-1.45E-05+1.01E-04*α+7.10E-06 *M
-4.14E-04*δa -3.51E-06 *(α*δa)+4.70E-06*(α*M)
+8.72E-06*(M*δa)-1.70E-07*(α*M)* δa
$C_{L,\delta_e}$ =- 1.45E-05+1.01E-04*α+7.10E-06 *M

-4.14E-04*δe -3.51E-06 *(α*δe)
+4.70E-06*(α*M)+8.72E-06*(M*δe)
-1.70E-07*(α*M)* δe

The lift force is given by:

$$L = \bar{q} S_{ref.} C_L$$

## Rolling Moment Computation

The total rolling moment coefficient is obtained as:

$$Cl = Cl\,\beta + Cl,\delta a + Cl,\delta e + Cl,\delta r + C_{lr}\left(\frac{r\,b}{2\,V}\right) + C_{lp}\left(\frac{p\,b}{2\,V}\right)$$

Where β is in radians, and the terms $\left(\frac{p\,b}{2\,V}\right)$ and $\left(\frac{r\,b}{2\,V}\right)$ are the computed nondimensional roll and yaw rates

$C_l = f(M, \alpha, \beta, \delta_e, \delta_a, \delta_r)$ . Using a MATLAB routine called FITTER, analytical expressions for the components of Cl are obtained for subsonic, supersonic, and hypersonic speeds:

Subsonic

$C_{lB}$ =- 9.380E-02-1.250E-02*M
$C_{l,\delta_a}$ = + 5.310E-05-5.272E-04*α
+3.690E-05*(α* δa)+2.680E-05*(α*M)
+1.926E-04*(M* δ a)-8.500E-06*(α*M)* δ a
-4.097E-04*M^2+1.258E-04*α^2
+3.762E-06* δa^2-5.302E-08*((α*M)*δ a) ^2
+5.100E-06*(α*M) ^2+2.100E06*(M* δ a) ^2
- 8.700E-06*α^3+8.400E-06* δ a ^3
+1.153E-09*((α*M)* δ a) ^3
-3.576E-08*(α* δ a) ^2+1.384E-08*α^4
-1.137E-08* δ a ^4+1.011E-12*((α*M)* δa)
^4+1.381E-08*α^5-1.676E-08* δ a ^5
-2.984E-14*((α*M)* δ a) ^5
$C_{l,\delta_e}$ = - (+ 5.310E-05-5.272E-04*α
+3.690E-05*(α*δe)+2.680E-05*(α*M)
+1.926E-04*(M*δe)-8.500E-06*((α*M)*δe)
-4.097E-04*M^2+1.258E-04*α^2+3.762E-06* δ e
^2 -5.302E-08*((α*M)*δe) ^2+5.100E-06*(α*M) ^2
+2.100E-06*(M*δe) ^2-8.700E-06*α^3
+8.400E-06*δe ^3+1.153E-09*((α*M)*δe) ^3
-3.576E-08*(α*δe) ^2+1.384E-08*α^4
-1.137E-08*δe ^4
+1.011E-12*((α*M)*δe) ^4+1.381E-08*α^5
- 1.676E-08*δe ^5-2.984E-14*((α*M)*δe) ^5)
$C_{l,\delta_r}$ =+7.000000E-04*δr
$C_{lr}$ =+2.625000E-01+2.50E-02*(M)
$C_{lp}$ =-1.337500E-01-1.250000E-02*(M)

Supersonic/ Hypersonic

$C_{lB}$ =-1.402E-01+3.326E-02*M-7.590E-04*α
+8.596E-06*(α*M)-3.794E-03*M^2
+2.354E-06*α^2-1.044E-08*(α*M) ^2
+2.219E-04*M^3-8.964E-18*α^3-6.462E-06*M^4
+3.803E-19*α^4+7.419E-08*M^5-3.353E-21*α^5
$C_{l,\delta_a}$ =+3.570E-04-9.569E-05*α-3.598E-05*M
+1.170E-04* δ a+2.794E-08*(α*M)*δa
+4.950E-06*α^2+1.411E-06*M^2-1.160E-06*δa ^2
-4.641E-11*((α*M)*δa) ^2
$C_{l,\delta_e}$ =- (+3.570E-04-9.569E-05*α-3.598E-05*M
+1.170E-04*δe+2.794E-08*(α*M)*δe
+4.950E-06*α^2+1.411E-06*M^2-1.160E-06*δe^2
-4.641E-11*((α*M)*δe) ^2)
$C_{l,\delta_r}$ =-5.0103E-19+6.2723E-20*α
+2.3418E-20*M+0.00011441*δr-2.6824E-06*(α*δr)
-3.4201E-21*(α*M)-3.5496E-06*(M*δr)
+5.5547E-08*(α*M)*δ r
$C_{lr}$ =+3.82E-01-1.06E-01*M+1.94E-03*α
-8.15E-05*(α*M)+1.45E-02*M^2-9.76E-06*α^2
+4.49E-08*(α*M)^2+1.02E-03*M^3-2.70E-07*α^3
+3.56E-05*M^4+3.19E-08*α^4-4.81E-07*M^5
-1.06E-09*α^5
$C_{lp}$ =-2.99E-01+7.47E-02*M+1.38E-03*α
-8.78E-05*(α*M)-9.13E-03*M^2-2.04E-04*α^2
-1.52E-07*(α*M)^2+5.73E-04*M^3-3.86E-05*α^3
-1.79E-05*M^4+4.21E-06*α^4+2.20E-07*M^5
-1.15E-07*α^5

The rolling moment is given by:

$$l = \bar{q} b S_{ref.} C_l$$

## Pitching Momentum Computation

The total pitching moment coefficient is obtained as:

$$Cm = Cma + Cm,\delta\alpha + Cm,de + Cm,dr + Cm,dc + C_{mq}\left(\frac{q\,c}{2\,V}\right)$$

, Where $\left(\frac{q\,c}{2\,V}\right)$ is the computed non-dimensional If pitching moment about the c.g. is required, then is computed using the following:

$$\overline{M} = \overline{M}_{mrc} - x_{cg} Z$$

where Z - axis force is given by

Z = - D sin α - L cos α

Using a MATLAB routine called FITTER, analytical expressions for the components of Cm are obtained for subsonic, supersonic, and hypersonic speeds:

Subsonic

$C_{ma}$ =+ 1.600E-03+1.371E-03*α
+1.041E-03*(α*M) + 4.464E-04*M^2
+1.969E-04*α^2 - 5.475E-05*(α*m) ^2
-6.047E-05*α^3+4.018E-06*α^4
-1.007E-07 * α^05
$C_{m,\delta_a}$ =+ 2.880E-04-5.351E-04*α
+4.550E-05*(α*δa) +3.3790E-04*(α*M)
+6.665E-04*(M*δa) -2.770E-05*(α*M)* δa
-6.027E-04*M^2 +2.660E-05*α^2-1.600E-06*δa^2
-1.000E-07*((α*M)*δa) ^2-1.910E-05*(α*M) ^2

+2.300E-06*(M*δa) ^2+1.300E-05*α^3
+1.920E-05*δa ^3 +1.90E-09 *((α*M)* δa) ^3
-1.861200E-06*α^4-4.69E-10*δa ^4
+1.29E-12*((α*M)* δa) ^4+7.29E-08*α^5
-3.87E-08*δa ^5-4.67E-14*((α*M)* δa) ^5
$C_{m,\delta_e}$ =+ 2.880E-04-5.351E-04*α
+4.550E-05*(α*δe) +3.379E-04*(α*M)
+6.665E-04*(M*δe) -2.770E-05*(α*M)* δe
-6.027E-04*M^2+2.660E-05*α^2-1.600E-06*δe ^2
-1.000E-07*((α*M)* δe) ^2-1.910E-05*(α*M) ^2
+2.300E-06*(M*δe) ^2+1.300E-05*α^3
+1.920E-05*δe ^3+1.90E-09*(( α*M)* δe) ^3
- .8612E-06*α^4-4.69E-10*δe ^4
+1.29E-12*((α*M)*δe) ^4+7.29E-08*α^5
-3.87E-08*δe ^5-4.67E-14*((α*m)* δe) ^5
$C_{m,\delta_r}$ =-1.841E-04+3.5E-06*α+2.762E-04*M
-1.0E-07*δr-4.0E-07*α^2+5.8E-06*δr ^2
+6.482E-09 *((α*M)* δr) ^2
$C_{m,\delta_c}$ =+7.0E-04 +1.0E-04*α-5.1469e-004*M
+3.0E-03*δc+1.0E-04*(α*δc) +1.0E-04*(α*M)
+1.4E-03*(M*δc) +2.922E-06* (α*M)* δc
$C_{mq}$ =-1.0313-3.125000E-01*M
Cm, δe =+2.880E-04-5.351E-04*α
+4.550E-05*(α*δe) +3.379E-04*(α*M)
+6.665E-04*(M*δe)-2.770E-05*(α*M)*δe
-6.027E-04*M^2+2.660E-05*α^2-1.600E-06*δe^2
-1.000E-07*((α*M)*δe) ^2-1.910E-05*(α*M) ^2
+2.300E-06*(M*δe) ^2+1.300E-05*α^3+1.920E-05*δe^3
+1.90E-09*((α*M)* δe)^3-1.8612E-06*α^4
-4.69E-10*δe ^4+1.29E-12*((α*M)* δe)^4
+7.29E-08*α^5-3.87E-08*δe ^5
-4.67E-14*((α*M)* δe) ^5
Cm, δr =-1.841E-04+3.5E-06*α+2.762E-04*M
-1.0E-07*δr -4.0E-07*α^2+5.8E-06*δr^2
+6.482E-09*((α*M)* δr) ^2
Cm, δc =+7.0E-04+1.0E-04*α-5.1469e-004*M
+3.0E-03*δc+1.0E-04*(α*δc) +1.0E-04*(α*M)
+ 1.4E-03*(M*δc) +2.922E-06* (α*M)* δc
Cmq = 1.0313-3.125000E-01*M

Supersonic/ Hypersonic

C ma =-5.67E-05-6.59E-05*α-1.51E-06*M
+2.89E-04*δa+4.48E-06*(α*δa)-4.46E-06*(α*M
-5.87E-06*(M*δa) +9.72E-08*(α*M)* δa
Cm, δa =-5.67E-05 - 6.59E-05*α -1.51E-06*M
+2.89E-04*δa+4.48E-06*(α*δa)-4.46E-06*(α*M)
-5.87E-06*(M*δa) +9.72E-08*(α*M)* δa
Cm, δe =-5.67E-05-6.59E-05*α-1.51E-06*M
+2.89E-04*δe+4.48E-06*(α*δe) -4.46E-06*(α*M)
-5.87E-06*(M*δe) +9.72E-08*(α*M)* δe
Cm, δr =-2.79E-05*α-5.89E-08*(α) ^2
+1.58E-03*(M) ^2+6.42E-08*(α) ^3
-6.69E-04*(M) ^3-2.10E-08*(α) ^4
+1.05E-04*(M) ^4 +1.43E-07*(δr) ^4
+3.14E-09*(α) ^5-7.74E-06*(M) ^5
-4.77E-22*(δr) ^5-2.18E-10*(α) ^6
+2.70E-07*(M) ^6-3.38E-10*(δr) ^6
+5.74E-12*(α) ^7-3.58E-09*(M) ^7
+2.63E-24*(δr) ^7
Cm, δc = 0.00
Cmq =-1.36E+00+3.86E-01*M+7.85E-04*α
+1.40E-04*(α*M)-5.42E-02 *M^2+2.36E-03*α^2
-1.95E-06*(α*M) ^2+3.80E-03*M^3-1.48E-03 *α^3
-1.30E-04 *M^4+1.69E-04*α^4+1.71E-06*M^5
-5.93E-06 *α^5

The pitching moment relative to the moment reference center is given by:

$$\overline{M}_{pitching\ moment} = \bar{q}cS_{ref}C_m$$

## Yawing Moment Computation

The total yawing moment coefficient is obtained as:

$$Cn = C_{n\beta} + Cn,\ \delta a + Cn,\ \delta e + Cn,\ \delta r + C_{np}\left(\frac{p\,b}{2\,V}\right) + C_{nr}\left(\frac{r\,b}{2\,V}\right)$$

Where β is in radian, and the terms $\left(\frac{p\,b}{2\,V}\right)$ and $\left(\frac{r\,b}{2\,V}\right)$ are the computed non-dimensional roll and yaw rates. $C_n = f(M, \alpha, \beta, \delta_e, \delta_a, \delta_r)$

Using a MATLAB routine called FITTER, analytical expressions for the components of Cn are obtained for subsonic, supersonic, and hypersonic speeds:

Subsonic

CnB =+1.062E-01+6.250E-02*M
Cn, δa =-2.700E-07*(α*δa)-1.008E-05*(M*δa)
+3.564E-07*(α*M)*δa+1.11E-07* δa ^3
-9.32E-12*((α*M)* δa) ^3- 1.9910e-021* α^4
+2.89E-25*δa ^4+1.82E-28*((α*M)* δa ^4
+6.95E-23*α^5-2.2046e-010*δa ^5
+2.22E-16*((α*M)* δa) ^5
Cn, δe =-(-0.00000027*(α*δe)-1.008E-05*(M*δe)
+3.564E-07*(α*M)*δe+1.11E-07*δe ^3
-9.32E-12*((α*M)* δe) ^3-1.9910e-021* α^4
+2.89E-25*δe ^4+1.82E-28*((α*M)*δe) ^4
+6.95E-23*α^5 - 2.2046e-010*δe ^5
+2.22E-16*((α*M)* δe) ^5)
Cn, δr =-3.000E-03*δr
Cnp =+1.790E-01+2.000E-02*M
Cnr =- 1.2787-1.375e-001*M

Supersonic/ Hypersonic

$C_{nB}$ =+3.68E-01+6.03E-16*(α) -9.79E-02*(M)
-3.84E-16*(α) ^2+1.24E-02*(M) ^2
+8.58E-17*(α) ^3-8.05E-04 *(M) ^3
-7.75E-18 *(α) ^4+2.57E-05*(M) ^4
+2.42E-19*(α) ^5-3.20E-07*(M) ^5
$C_{n,\delta_a}$ =+2.10E-04+1.83E-05*α-3.56E-05*M
-1.30E-05*δa-8.93E-08*(α*M)* δa-6.39E-07*α^2

+8.16E-07*M^2+1.97E-06*δa^2
+1.41E-11*((α*M)* δa) ^2
$C_{n,\delta_e}$ =- (+2.10E-04+1.83E-05*α-3.56E-05*M
-1.30E-05*δe-8.93E-08*(α*M)*δe-6.39E-07*α^2
+8.16E-07*M^2+1.97E-06*δe^2
+1.41E-11*((α*M)* δe)^2)
$C_{n,\delta_r}$ =+2.85E-18-3.59E-19*α -1.26E-19*M
-5.28E-04*δr+1.39E-05*(α*δr) +1.57E-20*(α*M)
+1.65E-05*(M*δr)-3.13E-07*(α*M)* δr
$C_{np}$ =+ 3.68E-01-9.79E-02*M+9.55E-16*α
-2.79E-17*(α*M) +1.24E-02*M^ -4.26E-16*α^2
+7.00E-20*(α*M) ^2 -8.05E-04*M^3+9.40E-
17*α^3 +2.57E-05*M^4-8.90E-18*α^4-3.20E-07*
M^5
+2.99E-19*α^5
$C_{nr}$ =-2.41E+00+5.96E-01*M-2.74E-03*α
+2.09E-04*(α*M)-7.57E-02*M^2+1.15E-03*α^2
-6.53E-08*(α*M) ^2+4.90E-03*M^3-3.87E-04*α^3
-1.57E-04*M^4+3.60E-05*α^4+1.96E-06*M^5
- .18E-06*α^5

The yawing moment relative to the moment reference center is given by

$$\overline{N_{mrc}} = \bar{q}bS_{ref}C_n$$

If pitching moment about the c.g. is required then it is computed as follows: $\overline{M} = \overline{M}_{mrc} - x_{cg}Y$

Where the y-axis aerodynamic force is given in the following equations:

## Side Force Computation

The total side force coefficient is obtained as:

$C_Y = C_{Y\beta} + C_{Y,\delta a} + C_{Y,\delta e} + C_{Y,\delta r}$ where β is in radian. $C_Y = f(M, \alpha, \beta, \delta_e, \delta_a, \delta_r)$

Using a MATLAB routine called FITTER, analytical expressions for the components of CY are obtained for subsonic, supersonic, and hypersonic speeds:

Subsonic

$C_{Y\beta}$ =-4.750E-01-5.000E-02*M
CY, δa =-1.845E-04*M-2.13E-07*(α*δa)
+3.740E-05*(α*M) +1.990E-05*(M*δa)
+6.17E-08*(α*M)* δa+3.39E-06*α^2
+1.37E-07*δa ^2-2.14E-06*(α*M)^2-1.11E-06*α^3
-3.40E-07*δa ^3+1.09E-07*α^4
+3.53E-09*((α*M)* δa)^2 - 2.66E-09*(α*δa)^2
+ 3.92E-08* (M*δa)^2 + 5.42E-11*((α*M)* δa)^3
-4.73E-10*δa^4+7.35E-14*((α*M)* δa) ^4
-3.45E-09*alpha^5+6.53E-10*δa^5
-1.11E-15*((α*M)* δa) ^5
$C_{Y,\delta e}$ =-(-1.845E-04*M-2.13E-07*(α*δe)
+3.740E-05*(α*M)+1.990E-05*(M*δe)
+6.17E08*(α*M)*δe+3.39E-06*α^2
+1.37E-07*δe^2-2.14E-06*(α*M) ^2-1.11E-06*α^3
-3.40E-07*δe^3+1.09E-07*α^4
+3.53E-09*((α*M)*δe) ^2
-2.66E-09*(α*δe) ^2+3.92E-08*(M*δe) ^2
+5.42E-11*((α*M)* δe) ^3-4.73E-10*δe^4
+7.35E-14*((α*M)* δe) ^4-3.45E-09*α^5
+6.53E-10*δe^5-1.11E-15*((α*M)* δe) ^5)
$C_{Y,\delta r}$ =+2.440E-03*δr

Supersonic/ Hypersonic

$C_{Y\beta}$=1.76E+00+4.58E-01*M-3.26E-03*α
+3.80E-05*(α*M)-6.36E-02*M^2
+2.36E-03*α^2+3.45E-07*(α*M) ^2
+4.44E-03*M^3-6.03E-04*α^3
-1.51E-04*M^4+4.52E-05*α^4 +1.98E-06*M^5
-1.09E-06*α^5
$C_{Y,\delta a}$ =-1.02E-06-1.12E-07*α + 4.48E-07*M +
2.27E-07*δa+ 4.11E-09 *(α*M)*δa+2.82E-09*α^2
-2.36E-08*M^2-5.04E-08*δa^2
+4.50E-14*((α*M)* δa) ^2
$C_{Y,\delta e}$ =- (-1.02E-06-1.12E-07*α
+4.48E-07*M+2.27E-07*δe
+4.11E-09*(α*M)* δe+2.82E-09*α^2
-2.36E-08*M^2-5.04E-08*δe^2
+4.50E-14*((α*M)* δe) ^2)
CY, δr=-1.43E-18+4.86E-20*α+1.86E-19*M
+3.84E-04*δr-1.17E-05*(α*δr)
-1.07E-05*(M*δr) +2.60E-07*(α*M)* δr

The side force is given by

$$Y = \bar{q}S_{ref}C_Y$$

## The Engine Model

In order to accelerate through all Mach regimes, a combined-cycle propulsion system has been developed for the GHV. This engine is a combination of a hypothetical turbojet, ramjet, and rocket motor. Turbojets are particularly suited for the low-speed portions of the mission and have adequate performance up to Mach 3.00[4]. These engine designs tend to operate with low overall pressure ratios and low rotor speeds at takeoff.

Ramjets have no rotor machinery and only start to operate efficiently at speeds above Mach 2.00.The internal flow of the traditional ramjet engine is subsonic. Ramjet engines can be used to reach speeds up to Mach 6. Scramjets are similar to ramjets; expect that their combustion occur at supersonic speeds. They become efficient only above Mach 6.00 [6]. The designed engine deck generates a maximum 330,000 lb thrust at 100% PLA [see Figures 2 and 3].

Assuming a fuel flow rate, $\dot{m}$ , and the exhaust stream velocity, $\eta$ , the thrust generated by the engine is:

Thrust= $\dot{m} \times \eta$

In this study the specific impulse $I_{SP}$ was used instead of the exhaust velocity for the calculation of the thrust. ISP is defined as the ratio of thrust to $W_{con.}$

$$I_{SP.} = \frac{\text{Thrust}}{W_{Con.}} \quad or \quad \text{Thrust} = I_{SP.} \times W_{Con.}$$

Where

$$W_{Con.} = \frac{\text{Thrust} \times thr}{I_{SP.}} \qquad (20)$$

## Engine Simulation

Using data available in the open literature, analytical expressions for the discussed three engine cycles were developed. For the turbojet and ramjet engines, the thrust force was simulated as a function of Mach number and PLA as in the following two equations, respectively:

Thrust = PLA*(2.99E+05-1.00E+01*(h)
+1.33E-04*(h) ^2-6.48E-10*(h) ^3
+3.75E+03* (AMACH) ^3)
*(Max. Mach 3.25)*

Thrust = PLA*(396.103*m-703.1*m^2+816.19*m^3
-442.48*m^4+118.28*m^5-15.34*m^6+ 0772*m^7)
*(Max. Mach 6)*

For the hypothetical rocket engine, the thrust force was simulated as a function of Mach number and altitude (h), or dynamic pressure as follows:

Thrust =-79.7204 + 1.9927 * h + 316.2086*PLA
-0.0126*(h) ^2+19.4536 *(PLA) ^2
*(h: 30k ft~ 100k ft) & (PLA= %0~%100)*

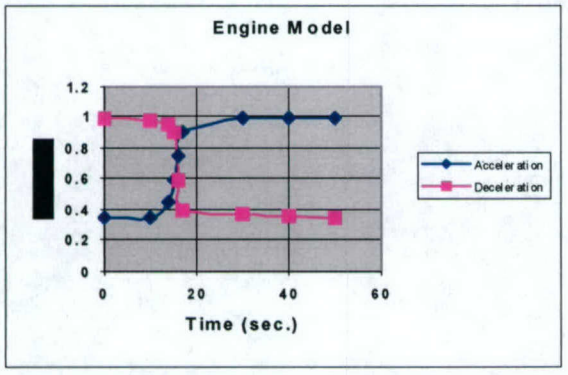


Figure 2: Time Response of Effective PLA due to Step Acceleration and Deceleration Commands

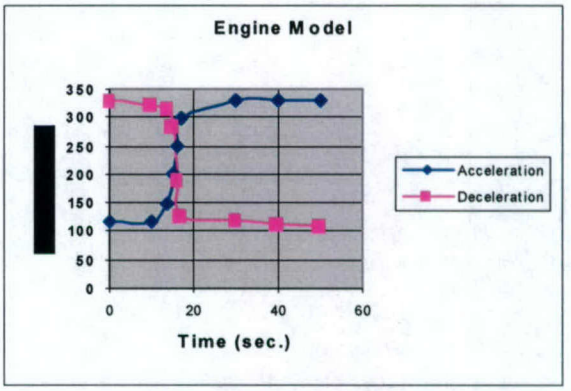


Figure 3: Time Response of Thrust due to Step Acceleration and Deceleration Commands

## Simulation - Flight Trajectory

After take-off, subsonic flight is maintained below 20,000 ft (1780-psf dynamic pressure). The vehicle then ascends and accelerates to 50,000 ft (944-psf) and Mach 3. In the third phase of the flight the vehicle ascends to 100,000 ft and accelerates to Mach 20. During descent, the vehicle's speed is reduced to Mach 4, and vehicle lands after slowing down to low subsonic speeds. The ascent and descent flight trajectories are shown in Figure4 [7].

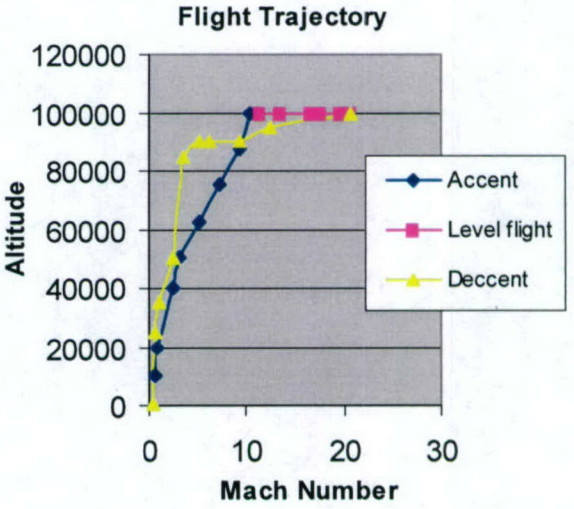


Figure 4: Vehicle Flight Trajectory

## Flight Trim Condition

Using the previously discussed equations of motion, the simulation of the aerodynamic and propulsion forces and moments was accomplished. The simulation was implemented in visual FORTRAN. It

was also been implemented in MATLAB. Using a Jacobian technique, we generated the steady-state models at the desired flight conditions. The steady-state flight conditions were determined by solving the nonlinear state equations for the state and control vectors using the following additional constraints according to the flight condition(s) [3], [8].

$$\textit{Steady Wing-Level Flight} \quad \phi, \dot{\phi}, \dot{\theta}, \dot{\psi} \equiv 0 \ (\because P, Q, R \equiv 0)$$

$$\textit{Steady Pull-up} \quad \phi, \dot{\phi}, \dot{\psi} \equiv 0 \ (\dot{\theta} \equiv \textit{Pull-up Rate})$$

## Summary

This paper covered the development of a Six Degrees of Freedom simulation of a generic hypersonic vehicle. The model and simulation were developed to support NASA's conceptual design studies of hypersonic vehicles with multiple cycle engines. The models were implemented in a combination of MATLAB and FORTRAN coded subroutines. The simulation includes both air breathing and rocket propulsion models. This work was supported under NASA grant # NCC4-158.

## References


[1] Hypersonic Vehicle Simulation Model, Winged-Cone Configuration by John D. Shaughnessy, S. Zane Pinckney, John D. McMinn, Christopher I. Cruz, and Marie-Louise Kelley.

[2] Peter H. Zipfel, Modeling and Simulation of Aerospace Vehicle Dynamics, AIAA Educational series, 2000.

[3] Frank L. Lewis and Brian L. Stevens, Aircraft Control and Simulation, Wiley, 1992.

[4] Jan Roskam, Airplane Flight Dynamics and Automatic Flight Control part I, DARCORPORATION, 1997.

[5] NASA Hypersonic Research at the Edge of Space, http://www.hq.nasa.gov/office/pao/History/x15/cover.html.

[6] E. T. Curran and S. N. B. Murthy, Scramjet Propulsion, Department of the Air Force (Editor), Purdue University.

[7] Conceptual design of the OREAD EXPRESS: TransAtmospheric Cargo (TAC) Vehicle. The University of Kansas Propulsion Design Team June-1992 (1991/ 1992 AIAA/ AIR BREATHING PROPULSION competition).

[8] John H. Blakelock, Automatic Control of Aircraft and Missiles, Wiley, 1991.

[9] Paul Dierckx, Curve and surface fitting with splines, Oxford University, 1995.

[10] Philip George, Numerical methods of curve fitting, Cambridge [Eng.] University Press, 1961.

# FLIGHT DYNAMICS AND CONTROL OF AIR-BREATHING HYPERSONIC VEHICLES: REVIEW AND NEW DIRECTIONS*

Barış Fidan[†¶], Maj Mirmirani[‡#], and Petros A. Ioannou[§¶]
[¶] *University of Southern California* Los Angeles, CA 90089
[#] *California State University*, Los Angeles, CA 90032

**Abstract**

The current air-breathing hypersonic flight (AHF) technology programs focus on development of flight test vehicles and operational vehicle prototypes that utilize airframe-integrated scramjet engines. A key issue in making AHF feasible and efficient is the control design. The non-standard dynamic characteristics of air-breathing hypersonic flight vehicles (AHFVs) together with the aerodynamic effects of hypersonic flight make the system modeling and controller design highly challenging. Moreover the wide range of speed during operation and the lack of a broad flight dynamics database add significant plant parameter variations and uncertainties to the AHF modeling and control problem. In this paper, first, different approaches to this challenging problem presented in the literature are reviewed. Basic dynamic characteristics of AHFVs are described and various mathematical models developed for the flight dynamics of AHFVs are presented. Major nonlinearity and uncertainty sources in the AHF dynamics are explained. The theoretical and practical AHF control designs in the literature, including the control schemes in use at NASA research centers, are examined and compared. The review is supported by a brief history of the scramjet and AHF research in order to give a perspective of the AHF technology. Next, the existing gaps in AHF control and the emerging trends in the air-breathing hypersonic transportation are discussed. Potential control design directions to fill these gaps and meet the trends are addressed. The major problem in AHF control is the handling of the various coupling effects, nonlinearities, uncertainties, and plant parameter variations. As a potential solution, the use of integrated robust (adaptive) nonlinear controllers based on time varying decentralized/triangular models is proposed. This specific approach is motivated by the promise of novel techniques in control theory developed in recent years.

*This work was supported in parts by Air Force Office of Scientific Research under Grant #F49620-01-1-0489 and by NASA under grant URC Grant #NCC4-158.

[†]Student Member AIAA, graduate student, Electrical Engineering Department.

[‡]Member AIAA, professor, Mechanical Engineering Department.

[§]Professor, Electrical Engineering Department

**Nomenclature** The following notation is used throughout the paper, unless otherwise stated.

| | | |
|---|---|---|
| $a_\infty$ | : | free stream velocity of sound |
| $\bar{A}_D$ | : | diffuser exit/inlet (area) ratio |
| $\bar{c}$ | : | reference length |
| $C_D$ | : | drag coefficient |
| $C_L$ | : | lift coefficient |
| $C_m$ | : | pitching moment coefficient (pmc) |
| $C_m(q)$ | : | pmc due to pitch rate |
| $C_m(\alpha)$ | : | pmc angle of attack |
| $C_{m_\alpha}$ | : | $\partial C_m/\partial\alpha$ |
| $C_m(\delta_e)$ | : | pmc due to $\delta_e$ |
| $C_T$ | : | thrust coefficient |
| $f_s$ | : | stoichiometric ratio for hydrogen, 0.029 |
| $h$ | : | vehicle altitude |
| $I$ ($I_n$) | : | the $(n \times n)$ identity matrix |
| $I_{yy}$ | : | vehicle $y$-axis inertia per unit width |
| $m$ | : | vehicle mass |
| $\bar{m}$ | : | vehicle mass per unit width |
| $\dot{m}_{air}$ | : | air mass flow rate |
| $\dot{m}_f$ | : | fuel mass flow rate |
| $M$ | : | pitching moment |
| $M_\infty$ | : | vehicle flight Mach Number |
| $n_x$ | : | acceleration along the vehicle $x$-axis |
| $n_z$ | : | acceleration along the vehicle $z$-axis |
| $P$ | : | pressure |
| $q$ | : | pitch rate |
| $Q$ | : | generalized elastic force |
| $r_e$ | : | radial distance from Earth's center |
| $R_e$ | : | radius of the Earth, 20,903,500 ft |
| $S$ | : | reference area |
| $T_0$ | : | temperature across the combustor |
| Th | : | thrust |
| $u$ | : | speed along the vehicle $x$-axis |
| $V$ | : | vehicle velocity |
| $X$ | : | force along the vehicle $x$-axis |
| $Z$ | : | force along the vehicle $z$-axis |
| $\alpha$ | : | angle of attack |
| $\gamma$ | : | flight path angle ($\gamma = \theta - \alpha$) |
| $\delta_e$ | : | pitch control surface deflection |
| $\delta_t$ | : | throttle setting |
| $\Delta\tau_1$ | : | fore-body elastic mode shape |
| $\Delta\tau_2$ | : | after-body elastic mode shape |
| $\zeta_1$ | : | damping ratio of the first vibration mode |
| $\eta$ | : | generalized elastic coordinate |

$\eta_f$ : fuel equivalence ratio, $\frac{\dot{m}_f}{f_s \dot{m}_{air}}$
$\theta$ : pitch angle
$\mu_g$ : gravitational constant
$\rho$ : density of air
$\omega_1$ : natural frequency of the first vibration mode
$0_{n\times m}$: the $n \times m$ zero matrix

*Subscripts*
$A$ : due to aerodynamics
$E$ : due to external nozzle
$T$ : due to engine thrust
$0$ : trim condition
$\infty$ : free stream condition

## 1 INTRODUCTION

A recent multi-year research program of NASA, Hyper-X, focuses on one of the greatest aeronautical research challenges, air-breathing hypersonic flight (AHF).[1–5] The main task is to design and build vehicles that will fly at speeds of Mach 7 and 10 without using any rocket noting that the world's fastest air-breathing aircraft for the time being, the SR-71, cruises slightly above Mach 3 and the highest speed attained by NASA's rocket-powered X-15 was Mach 6.7, back in 1967. The prototype (X-43A) developed for this task is depicted in Figure 1. Based on this prototype, the first goal of the Hyper-X Program, which is conducted by the Dryden and Langley Research Centers of NASA, is to demonstrate and flight validate key propulsion and related technologies for air-breathing hypersonic aircraft.

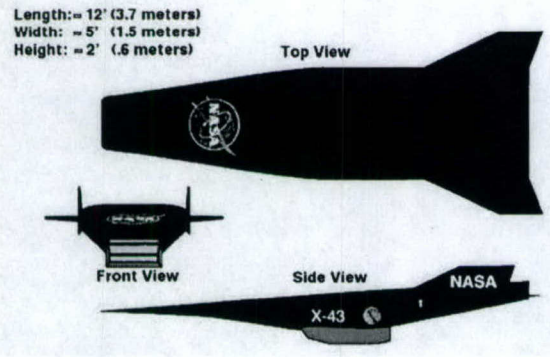


**Figure 1:** X-43A (NASA LRC archive).

The interest in AHF is based on the advantages it offers, namely increase in payload capacity and propulsion efficiency, expansion of launch windows, and reduction in construction and operation costs.[1,2,4] The key technology behind AHF and its benefits is usage of the so-called scramjet (supersonic-combustion ramjet) engines.[6] Scramjet technology is an enhanced version of the ramjet technology, in which the engines operate by subsonic combustion of fuel in an air stream compressed by the aircraft's forward speed. In conventional turbojet engines, the compressor fans compress the air. Scramjets are basically ramjet engines in which the airflow through the engine is kept supersonic. Using hydrogen as the basic fuel for combustion, the air-breathing scramjet engines burn oxygen scooped from the atmosphere. Obtaining the oxygen from air rather than carrying it on-board, air-breathing hypersonic flight vehicles (AHFVs) can carry more payload than equivalent rocket-powered systems.

Since testing via ground facilities gives limited information about the behavior of the air-breathing scramjet technology, flight tests at hypersonic conditions are needed for a broader understanding. For this purpose, several flights at Mach 7 and Mach 10 have been planned. For each flight, the profile (see Figure 2) has a ground track of 400 miles. X-43A rides on the first stage of a Pegasus booster rocket, which is launched by

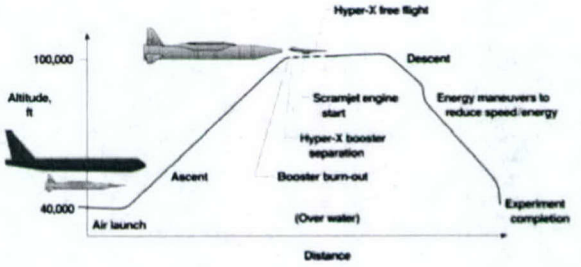


**Figure 2:** Hyper-X flight trajectory (NASA LRC archive).

Once separated from the booster, the control system of X-43A is required to regulate a strict flight condition for the duration of the test flight and to perform a series of maneuvers to identify hypersonic flight characteristics. The Dynamics and Control Branch of NASA Langley Research Center (LRC) is responsible for development of the X-43A control system. The non-standard dynamic characteristics of X-43A together with the aerodynamic effects of hypersonic flight make the control system design very challenging. Moreover, the wide speed range of operation and the lack of a broad flight dynamics database suggest that plant parameter variations and uncertainties are the main issues to deal with in the controller design.

Although there have been other research programs re-

lated to or independent of NASA, (see, e.g.,[7–12]), the current Hyper-X Program of NASA, described briefly above, gives an adequate perspective of the current state of the hypersonic flight technology. As can be understood from the above, there are several aspects of the research on hypersonic flight. In this work, we concentrate on flight dynamics, modeling, and control issues.

After presenting a brief history of the AHF technologies in Section 2, we describe the basic dynamic characteristics of air-breathing hypersonic aircraft in Section 3. Section 4 is devoted to the existing mathematical models in the literature for the flight dynamics of AHFVs. In this paper, we make a distinction between approaches by academicians and those used in industry. In Section 5, we review approaches proposed for the AHF control design problem in academia. The approaches to the same problem adopted by NASA centers and the corresponding control laws are presented in Section 6. The paper is concluded with a discussion of the future trends in the air-breathing hypersonic transportation and possible control design directions to meet these trends, which can be found in Section 7. Some final remarks are made in Section 8.

## 2 A BRIEF HISTORY

Hypersonic air-breathing propulsion has been studied by NASA for more than sixty years, since the evolvement of the hydrocarbon-fueled conventional ramjet (CRJ) engine concept.[1,9] Reviews of the early works on CRJ development and the early design approaches to achieving increased flight speeds can be found in.[6,13,14] In the late 1940s, the feasibility of developing a scramjet engine was attracting attention as well. It had been proposed to add heat directly to a supersonic stream, by means of a standing wave, as early as 1946.[9,15] The generic problems needed to be addressed in scramjet, such as the technical hurdles about fuel injection and mixing, wall cooling and frictional losses, and nozzle performance, were outlined in early 1960s. Meanwhile, performances of CRJ and scramjet engines were compared, and it was concluded that the performance of the scramjet engine would exceed that of the CRJ somewhere in the speed range of Mach 6–8 and would be superior at higher speeds.[9,16,17] The studies on comparison of CRJ and scramjet engines continued, however these studies could not produce substantive results due to the lack of demonstrated scramjet component performance and the lack of test data on hypersonic CRJ engines. Subsequently, the later studies on high-speed engine development were concentrated on the scramjet engine.

The scramjet engine programs conducted in Aerodynamics Laboratory of the Polytechnic Institute of Brooklyn (PIBAL) and General Applied Science Laboratories (GASL) under supervision of Ferri[9,18,19] focused on the development of fixed geometry scramjet engines that have good performance over a wide speed range, e.g., Mach 3–12. The key ideas that enable wide speed ranges of operation in these programs are thermal compression and variable aerodynamic contraction ratios. The design of high performance wide speed range scramjets was approached by other research groups, mainly in the United States, the former Soviet Union, and France, using different techniques such as using dual-mode engines and utilizing mechanically variable geometry engines as well.[9,10,20–23]

The promising high-speed performance of the hydrogen-fueled scramjet engines led to increasing attention on hypersonic cruise missions. The PIBAL and GASL scramjet engine programs inspired the U.S. Air Force funded Scramjet Incremental Flight Test Vehicle (IFTV) program, which was initiated in April 1965.[9] The purpose of the program was to demonstrate the vehicle acceleration from boosted speed of 5400 ft/s to at least 6000 ft/s using four hydrogen-fueled scramjet modules located around the central vehicle body. Although a non-powered flight test vehicle was launched in January 1967, the IFTV program was cancelled in August 1967 due to technical difficulties such as considerable problems and delays encountered in the ground test program due to inlet–combustor interactions.

Another major test program was the NASA Hypersonic Research Engine (HRE) program which began in 1964 aiming to flight test a complete, regeneratively cooled, flight weight scramjet research engine on the X-15 rocket-powered research plane.[6,24–26] X-15 flew several times with a dummy test ramjet attached to it and reached a record-making speed of 6.72 M in 1967. However, this program was terminated without reaching its main goal due to financial problems in 1968.

After the cancellation of the IFTV and HRE flight test programs, the emphasis of NASA research shifted to developing and ground testing new engine models for a while. A structural full-scale HRE model known as the structures assembly model (SAM) was tested at NASA LRC and the original model was enhanced by using new techniques and developing new structures such as a flight-weight hydrogen-cooled structure. Simultaneously, another model known as the aerothermodynamic integration model (AIM) was ground tested and analyzed in the NASA John H. Glenn Research Center. The AIM ground tests conducted from September 1972 to April 1974 produced a comprehensive database

on inlet and combustor performance at Mach 5–7.[9] Moreover the AIM program demonstrated high internal thrust performance, smooth transition from supersonic to subsonic mode of combustion, strong interactions between fuel injector stages, and combustor design approaches. A review of the HRE program is presented in.[27]

The axisymmetric configuration of the HRE used in the SAM and AIM programs has been popular, and has been utilized by the French ESOPE engine and several Russian engines[9,28–30] as well. Later the Russian Central Institute of Aviation Motors (CIAM) performed four major flight tests on axisymmetric hydrogen-fueled engines utilizing a Hypersonic Flying Laboratory (HFL) in November 1991, November 1992, March 1995, and February 1998. The second and third of these tests were supported by the French aerospace institute ONERA, and the fourth was a joint project with NASA. Although the third test was not successful due to HFL system problems, the other three tests were completed successfully producing data for both the subsonic and the supersonic combustion modes.[30–32]

Another concept NASA started to focus on in 1970s is the rectangular airframe-integrated engine configuration.[6,9,25,33–36] Superior to the axisymmetric HRE configuration, this concept utilizes the inlet sidewalls to produce extra horizontal compression in addition to the vertical forebody compression and uses in-stream struts as housings for distributed fuel injectors. The early works on the airframe-integrated scramjet concept can be seen in.[33] Some of the later developments and the corresponding research at NASA LRC are presented in.[35,36] The airframe-integrated engine concept has also been studied extensively in Russia and Japan, and has become a preferred configuration in recent years.

The newly developed scramjet engine technologies of 1970s and early 1980s, specifically the development of the airframe-integrated engine concept, and the need for flight testing and flight demonstrating these technologies led the U.S. Air Force and NASA to initiate a major hypersonic flight research program including flight tests, the National Aerospace Plane (NASP) program, in 1986, eighteen years after the cancellation of the IFTV program.[6,9,37–40] The focus of the NASP program was to build an air-breathing single-stage-to-orbit (SSTO) experimental aircraft, the X-30, which would be used for hypersonic flight testing and demonstration. During the NASP program, there had been extensive development in the rectangular airframe-integrated scramjet technology. A large number of newly developed modular experimental engines were tested at NASA LRC in the Mach 4–7 regime.[9,37,41] The NASP program led to extensive studies on dynamic modeling and control of the AHFVs as well. In,[42,43] the dynamic characteristics of AHFVs with airframe-integrated engines were brought into picture with emphasis on the interactions between the airframe, engine, and structural dynamics. Shortly, based on the X-30 configuration, a few mathematical models were developed, some guidance and control schemes were designed, and certain performance and stability issues were analyzed.[44–51] In spite of the enormous amount of effort and achievement in many aspects, the NASP program was first reduced in scope to the Hypersonic Systems Technology Program (HySTP) in 1993 and then completely terminated in January 1995 without conducting any flight test due to funding problems. The aim of HySTP was building up and testing a Mach 10-15 scramjet propulsion in a test project called the Hypersonic Flight Test Experiment (HyFLITE).[9,37,38] In the first two of the three phases of HyFLITE, which were all cancelled, a rocket powered vehicle would be used to bring the scramjet system to hypersonic conditions similar to the HRE program with X-15. Integration of the scramjet and a test AHFV would be performed at the last stage. The original NASP program on the other hand was an attempt for a full-scale operational prototype vehicle system development rather than an incremental technology program. It was realized with the NASP program that further development in scramjet propulsion systems, materials, other systems, and thermal management are needed before building an operational vehicle similar to X-30.

In 1996, NASA started a similar but more extensive and incremental hypersonic technology program, the Hyper-X program, which is currently underway.[1–5,9] The exclusive Hyper-X program, which is considered as the last stage preceding prototype development for AHF, is currently foreseen to be completed by 2017. During the program, four small scale (X-43A, X-43B, X-43C, X-43D) and one full scale demonstrator vehicles are planned to be constructed and flight tested.[4]

X-43A is a 12 foot-long hydrogen-powered experimental vehicle with a wing span of 5 feet (see Figure 1) which is "smart scaled" from a 200 foot operational concept. It is planned to be used in scramjet powered and un-powered flight tests at Mach 7 and Mach 10. X-43B is a 35'–45' reusable demonstrator vehicle with a combined cycle engine to be tested in all the propulsion modes from subsonic flight through full scramjet operation (Mach 0.7–7). X-43C is a 16 foot-long hydrocarbon-powered vehicle utilizing a three-module engine which will be used to accelerate the vehicle from Mach 5 to Mach 7 during the flight test. X-43D is a concept to be used for flight testing hydrogen fueled

scramjet engines at velocities of Mach 15 or greater. Finally a large-scale reusable demonstrator (LSRD) vehicle, whose architecture is the same as that of the operational vehicle and whose size is large enough to operate over all air-breathing propulsion speeds, is planned to be built and flight tested. Among these flight vehicle projects, however, only X-43A and X-43C are currently funded. X-43B and LSRD projects are scheduled around 2006 and 2010, respectively, with the first flight tests to be conducted in 2010 and 2016. X-43D project is in a formulation stage.

The X-43C project started only at low level in 2001 and will continue through 2007. The X-43A project, on the other hand, is highly active, with the major ground tests performed and the flight tests underway. The ground tests, engine designs, propulsion system airframe integration issues, computational fluid dynamics (CFD) analysis, aerodynamic database development, and simulation studies for the Hyper-X program are presented in.[52–61]

The X-43A flight test profiles are shown in Figure 2. After accelerating to the test conditions (Mach 7 or Mach 10 at about 100,000 feet) on the first stage of a Pegasus booster rocket, X-43A vehicles are planned to perform powered and un-powered flight tests using its scramjet engine and gaseous hydrogen fuel for 5–10 seconds. The first X-43A flight test on June 2, 2001 was unsuccessfully terminated after a booster failure 13.5 seconds into the mission. The second flight test is planned to be performed in 2003.

U.S Air Force currently conducts another scramjet development program, the Air Force Hydrocarbon Scramjet Engine Technology (HyTech) program.[4,9,62] Although the HyTech program is currently missile oriented, it is expected to be incorporated with the hypersonic transportation and, in particular, the X-43B and X-43C projects of the Hyper-X program.

Outside the U.S., the only current exclusive hypersonic flight technology program including ground and flight tests is the Russian IGLA program.[9,63–65] IGLA is a winged scramjet powered gliding vehicle. In the flight tests, it is accelerated to Mach 16 using a large booster rocket and then is let to glide down to scramjet operation speeds at which the engine tests are performed. Successful attempts with IGLA are reported at low hypersonic velocities.[64] The other major recent/current hypersonic flight technology programs are the French PREPHA and PROMETHEE programs,[66,67] the French–German JAPHAR project,[68] and the extensive series of engine ground tests performed using the very capable facilities in the Japanese National Aerospace Laboratory, Kakuda Research Center.[69] The PREPHA program, which ended in 1999 focused on development and testing of hydrogen-fueled scramjets. In this program, CFD was extensively used in design and analysis of scramjet engines and several prototypes were developed including a Mach 3–12 wide range ramjet. The current PROMETHEE program focuses on usage of hydrocarbon fueled scramjets in air-launched missiles rather than hypersonic transportation. The JAPHAR program, on the other hand, is an ongoing program similar to PREPHA that aims to develop enhanced wide range scramjets for AHFVs.

Above, we presented a brief history of the air breathing hypersonic flight technologies in an attempt to show the big picture in as many aspects as possible in a limited space. More detail can be found in the works cited above and the references therein. In the rest of this paper, we focus on flight dynamics, modeling, and control.

## 3 FLIGHT DYNAMICS OF AIR-BREATHING HYPERSONIC VEHICLES

Before the 1990s, the hypersonic research was almost solely focused on development of engines that would provide hypersonic flight speeds or wide speed ranges in subsonic, supersonic, and hypersonic regimes. However, the studies that pursued, especially the NASP and the Hyper-X programs, have all shown that in order to make hypersonic transportation feasible and efficient there are other key technologies that need to be addressed. Amongst them is flight controller design. In order to design reliable and effective controllers for AHFVs, it is essential to consider the unique dynamic characteristics of these vehicles carefully since they differ in major ways from those of a typical aircraft. In this section, we review the basic dynamic characteristics of air-breathing hypersonic aircraft with integrated scramjet engines addressed in the literature. We consider generic hypersonic aircraft configurations with airframe-integrated scramjet engines similar to X-30 or X-43A.[40,43,47] For these configurations, the primary lift generating surface is the body itself due to inefficiency of using a thin wing. It is worth noting that there is no major difference between the dynamics of X-30 and X-43A since the X-43A model is obtained by photographically scaling each part of an operational configuration which is very similar to X-30 except the engine. For the engine, a scaling that would keep the propulsion effectiveness the same and make the flight tests results for X-43A valid for the operational vehicle is preferred.

Beside the aerodynamic effects of the hypersonic speed, the strong interactions between the elastic airframe, the propulsion system, and the structural dynamics make the explicit characterization of flight dynamics of AHFVs highly challenging.[40,43,70] The dynamic characteristics of the hypersonic vehicle vary more significantly over the flight envelope than other aircraft due to its extreme range of operating conditions and rapid change of mass distribution. Moreover, many aerodynamic and propulsion characteristics still remain uncertain and are hard to predict due to lack of sufficiently many flight tests and inadequacy of the ground test facilities. Below, we analyze the major issues characterizing the AHFV flight dynamics in more detail.

### 3.1 Effects of the Hypersonic Speed

"Real gas" and viscous effects become important at hypersonic speeds.[43,70–72] Here, "real gas" effects denote the deviations of the aerothermodynamic properties of the air from the ideal gas behavior. These effects become significant at Mach numbers $M > 6$ due to the increase in the temperatures behind the normal shock waves with increasing Mach number. Two of the main impacts of the "real gas" effects are the increase in loading on certain aircraft surfaces and the increase in pitching moment coefficient.[43,73,74]

Viscous effects, on the other hand, are basically due to the thickening of the boundary layer around the aerofoil by the large temperature gradients across this boundary layer at hypersonic flow regimes. With the viscous effects, the effective aerodynamic surface is not the aerofoil itself but the boundary layer together with the aerofoil. Hence the viscous behavior in terms of pressure distribution, shock waves, and drag differs significantly from the results of the inviscid analysis for the aerofoil. The difference is not only due to the thickening but because of the skin frictions caused by non-smoothness of the boundary layer as well.

In order to reach hypersonic speeds, the scramjet engine needs to be operated at a high dynamic pressure, which causes an increase in aerodynamic heating and drag.[43] This may cause violation of temperature and structural constraints. In order to counteract the high operating temperatures, which are estimated to be in the range of 2000°F–4000°F, temperature resistant materials and active structural cooling must be utilized.[40,43,70,72,75] The most essential parts of the AHFV to be considered for the high temperature issues are the combustor wall, the fore-body inlet ramp, and the control surfaces. Temperature of the combustor wall is directly related to the engine operation. Increase in the inlet ramp temperature makes the aerodynamic boundary layer thicker, and hence increases the drag. High temperatures on the control surfaces, on the other hand, put constraints on the deflections applied by the controller to these surfaces.

At hypersonic speeds, the speed of the flight condition variations on a specific path is faster than the lower velocity regimes. Considering this fact in addition to the variations due to wide speed ranges of a complete flight and the sensitivity of the AHF dynamics to the flight conditions, which will be explained in detail in the following section, the guidance scheme and the flight control system need to be highly integrated in order to provide a robust stable high performance flight. On the other hand, hypersonic speeds cause the so-called "path-attitude decoupling" phenomenon which can be basically described as the resistance of the high momentum of the AHFV to the changes in the desired flight path.[76–78] Hence the actual flight path significantly lags the changes in the pitch attitude at hypersonic speeds.

### 3.2 Variations due to Wide Speed Ranges

The effect of hypersonic speed on flight stability of vehicles similar to X-30 and X-43A configurations was extensively studied as early as 1970s. In,[43,79] it is concluded that the static stability margins of such AHFVs generally decrease as Mach number increases. Hence there exists a trade off between having reasonable static margins by allowing high static stability margins, large control deflections, and decreased maneuverability at lower speeds and keeping the low speed static stability margins in the conventional range and accepting unstable configurations at hypersonic speeds.

The dynamic characteristics of the AHFVs vary much more over the flight envelope than other aircraft due to extremely wide range of operating conditions and mass distributions.

The hypersonic configuration needed for efficient AHF also affects the landing/take off performance and increases the transonic drag. It has been recorded during the ground tests at NASA LRC that examined the subsonic AHFV behavior close to the ground plane that turning the power off causes a sharp increase in the lift while turning the power on causes negative lift effect together with a large increase in the pitching moment. These effects have been concluded to be due to the diverging angle between the nozzle and the ground plane.[80] The external nozzle configuration for good hypersonic performance causes flow separation at lower speeds and a steep increase in the drag while passing from the subsonic to supersonic regime as well. Several flow energizing mechanisms have been developed to overcome the latter effect.[43,80]

### 3.3 Scramjet Engine Dynamics

Since our focus is on hypersonic aircraft configurations with airframe-integrated scramjet engines similar to X-30 or X-43A, it is essential to understand the basic features of the scramjet engines in order to model and control flight dynamics of these configurations reliably. As stated in Section 2, the airframe-integrated scramjet engine concept has been studied extensively in the U.S., Russia, and Japan, and has become a preferred configuration in recent years. The preference is based on the potential performance at hypersonic speeds (M $>$ 6). Aside from the airframe-integration issue, the preference of scramjet engines to ramjets and the other conventional engines at hypersonic speeds is due to the fact that slowing the high-velocity airstream to subsonic speeds reduces the performance significantly.

The scramjet engines operate by supersonic combustion of fuel in an air stream compressed by the aircraft's forward speed. Using hydrogen as the basic fuel for combustion, the air-breathing scramjet engines burn oxygen scooped from the atmosphere. Since the hydrogen and the scooped oxygen have less time to mix and react in supersonic combustion, the combustor needs to be longer. Moreover, in order to produce sufficient thrust for hypersonic flight, the engine inlet needs to capture as much of the airflow under the AHFV surface as possible. This is provided by integration of the engine with the airframe so that the inlet area is contiguous with the vehicle undersurface.[6,9,34,43] The inlet sidewalls produce extra horizontal compression in addition to the vertical fore-body compression.

Beside the fore-body inlet, the internal modules and the exhaust nozzle are the main components of the engine. Figure 1 illustrates these components. The grey section under the AHFV body in the front and side views contains the internal modules. The front part of this section and the lower boundary of the fore-body constitute the inlet, while the exhaust nozzle constitutes the back part of the grey section together with the lower boundary of the after-body. The internal modules are located symmetrically with respect to the AFHV plane of symmetry. Each module diverges a few degrees from the adjacent modules for better alignment with the fore-body flow. In the minimum-area section of each of the internal modules there exist a number of wedge shaped in-stream struts that are used as final compressors as well as housings for distributed fuel injectors. Injector distribution relaxes the constraint on the mixing time due to supersonic combustion and shortens the required combustor length.

Similar to the inlet, the integration of the exhaust nozzle with the airframe provides larger net thrust, i.e., increase in the gross thrust without significantly increasing the drag that much.[6,34,43] It is worthwhile to note here that the net thrust in AHF is usually a small fraction of the gross thrust, hence any additional drag source can affect flight performance significantly. In addition to increasing the net thrust, the airframe integrated exhaust nozzle configuration generates propulsive lift and increases the lift-to-drag ratio. Because of this two-fold contribution to the flight performance, use of this configuration is essential in AHF.[6,43,73]

### 3.4 Airframe/Propulsion/Strucural Dynamics Interactions

In X-30 and X-43A, the elastic airframe, propulsion system, and structural dynamics are highly interactive; hence the control tasks for flight and propulsion systems cannot be separated clearly. Because of the engine-airframe integration issues explained in Section 3.3, there is significant interaction between the propulsion system and the vehicle aerodynamics.[40,42,43,80] Considering the longitudinal dynamics, the inlet flow pressure acting on the fore-body generates a nose-up pitching moment while the external nozzle flow generates a nose-down pitching moment. These flows may also affect the lateral dynamics if they are laterally non-uniform.

Similarly, the aerodynamics of the AHFV effects the propulsion system in several ways. The capture and compression of the flow through the inlet is determined by the properties of the bow shock wave under the vehicle fore-body, which are determined by the angle of attack (AOA) and the dynamic pressure as well as the free stream characteristics.[43,81] The AOA and the dynamic pressure also effect the combustion kinetics and the exhaust flow/free stream shear layer. The sensitivity of the performance to the AOA and the dynamic pressure is small at high Mach numbers and increases as the speed decreases. At low speeds, the AOA and the dynamic pressure need to be greater than certain values in order to provide acceptable performance.

The dynamic coupling among the AHFV aerodynamics, the airframe, and the propulsion system is demonstrated via the results of a frequency domain numerical analysis in.[43] This analysis shows that the thrust and the pressure at the engine inlet are significantly effected by pitching control surface, e.g., elevon deflections over a wide frequency range. The analysis indicates a similar effect of the fuel flow rate and diffuser area ratio changes on the AHFV pitch rate.

Another major source of dynamic coupling in the AHFVs is the structural aeroelastic modes. Bending of the fore-body and after-body together with propagations throughout the entire airframe affect the flows

through the inlet and the exhaust and hence the aerodynamic performance. Elastic-rigid body interactions are also significant in AHFVs due to the low structural vibration frequencies which appear as a result of the requirement for very low structural weight mass fraction.[43,82] Accurate determination of the structural elastic modes is critical for flight control, especially for precise control of the AOA. However the non-uniform aerodynamic heating in AHF, unconventional composite materials used in building the airframe, and the shell type structure of AHFVs cause significant variations and uncertainties in the shapes and natural frequencies of the elastic modes. Further information on aeroelastic effects and mode shapes of AHFVs can be found in.[47,83–88] The interactions among the flight dynamics, the engine, and the structural dynamics are illustrated in Figure 3.

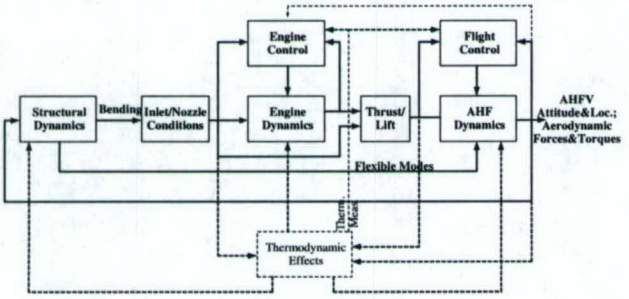


**Figure 3:** AHFV dynamics.

### 3.5 Databases and Uncertainties

Despite the unprecedented capabilities of the powerful CFD codes available today, the development of conventional aircraft and the design of their control systems depends on the use of empirical estimates of aerodynamic and engine data obtained from sources such as U.S. Air Force DATCOM, wind tunnel data, and flight test data. Design and development of hypersonic aircraft, however, must proceed without the benefit of a vast statistical database of actual flight test data. As a result, there are many aerodynamic and propulsion uncertainties that are a result of insufficient flight test data and inadequacy of the ground test facilities.

Unpredictable aerodynamic and thermodynamic behaviors due to hypersonic speed and airframe/ propulsion/structural dynamics interactions constitute another uncertainty source.[43,51,82] The propulsion system perturbations that indirectly impact the longitudinal dynamics, the elastic mode variations, nonuniform pressure distribution, and uncertainties explained in Section 3.4 are some of these unpredictable behaviors. The mass property variations discussed in Section 3.2 can also be considered as uncertainties in modeling. In general, many of the critical aerodynamic characteristics are very hard to predict while the ability to experimentally determine them is limited. Hence, conventional control methodologies that depend on relatively accurate models and a reliable aerodynamic database may not be applied and the corresponding uncertainties need to be dealt with during the flight using intelligent, adaptive, or robust control.

## 4 MODELING THE HYPERSONIC FLIGHT DYNAMICS

The dynamic characteristics of AHF described in Section 3 make the modeling and control of AHFVs very challenging. Due to the strong coupling between the aerodynamics, the airframe, and the propulsion system, the modeling and control techniques used for conventional aircraft are inadequate if feasible at all. Mathematical models incorporating the interactions within the AHFV as well as an integrated airframe-engine control system are needed.[43,47,89] Furthermore the large variations and uncertainties associated with the dynamic characteristics over the flight envelope and the corresponding robustness issues need to be taken into account.[43,51] Even if dynamic interactions are ignored and parameter variations and modeling uncertainties are assumed to be negligible — an invalid assumption as demonstrated in[51]—, the unique aerothermodynamic characteristics of hypersonic flight explained in Section 3.1 need to be considered. Although a number of studies on the control of AHFVs do consider all of the challenges above, most of the works in the AHF control literature have ignored the coupling effects, have assumed parameter variations and uncertainties to be small, and have considered only some of the aerothermodynamic characteristics due to hypersonic speed. Even in these cases, significant nonlinearities had to be introduced making them distinctly different from the conventional flight control problems. In this section we review the AHF literature where the distinct characteristics of hypersonic flight have been incorporated in the modeling process.

The majority of the AHF dynamic models in the literature consider only the longitudinal motion. The nominal longitudinal models, in general, are described in state space by equations of the form

$$\begin{aligned} \dot{\mathbf{x}} &= \bar{\mathbf{f}}(\mathbf{x},\mathbf{u}) \\ \mathbf{y} &= \bar{\mathbf{h}}(\mathbf{x},\mathbf{u}) \end{aligned} \tag{4.1}$$

where $\mathbf{x}$, $\mathbf{u}$, and $\mathbf{y}$ denote, respectively, the state, the input, and the output of the AHF system. Typically, $\mathbf{x}$ is a vector of dimension 5–9 which contains information about velocity, AOA, pitch rate, pitch attitude, and altitude. The input $\mathbf{u}$ is 2–3 dimensional vector whose entries are adjustable control coefficients, such

as elevon angle and fuel equivalence ratio, that determine the aerodynamic and propulsive power supplied to the system and/or fuel and air flow rates in the integrated engine. The output $\mathbf{y}$ can be the state $\mathbf{x}$ itself —if the state $\mathbf{x}$ is fully measurable or can be acceptably estimated—, measurable entries of $\mathbf{x}$, or some measurements giving information about $\mathbf{x}$. It typically carries information about the altitude and the velocity of the AHFV. The nominal system functions $\bar{\mathbf{f}}$ and $\bar{\mathbf{h}}$ can be linear or nonlinear, and their domain can be extended to include uncertainties and external disturbances.

A widely used longitudinal model in the literature is the rigid-body model of[90,91] for the winged-cone accelerator configuration. Several different formulations of this model are available in the literature. They differ in the method used for modeling and linearization—if the model is a linear one—, and the aerodynamics, mass, environment, and propulsion properties assumed. In[91] the linear model

$$\dot{\mathbf{x}} = \mathbf{A}\mathbf{x} + \mathbf{B}\mathbf{u} \tag{4.2}$$

where $\mathbf{A}$ and $\mathbf{B}$ are system matrices that depend on the flight condition —the Mach number and the altitude— and

$$\begin{aligned} \mathbf{x} &= [V(\text{ft/s}) \quad \alpha(\text{deg}) \quad q(\text{deg/s}) \quad \theta(\text{deg}) \quad h(\text{ft})]^T, \\ \mathbf{u} &= [\delta_e(\text{deg}) \quad \eta_f]^T \end{aligned}$$

is developed and studied. Numerical values of $\mathbf{A}$ and $\mathbf{B}$ for certain flight conditions are derived from a 6-degree of freedom (DOF) nonlinear rigid-body simulation of the conical accelerator vehicle using a software program to optimize simulated trajectories(POST).[92] In,[91] the atmospheric affects such as turbulence are included and the model (4.2) is generalized to

$$\dot{\mathbf{x}} = \mathbf{A}\mathbf{x} + \mathbf{B}\mathbf{u} + \mathbf{E}_x\mathbf{d} \tag{4.3}$$

where $\mathbf{d}$ is a vector of dimension 2 which represents the atmospheric disturbances and $\mathbf{E}_x$ is a $5 \times 2$ system matrix depending on the flight conditions.

The winged-cone configuration considered in deriving the dynamic model of[90,91] is significantly different from the rectangular airframe-integrated engine configuration in that the forebody is axisymmetric and conical, the nozzle section is a cone frustum, and the engine modules are placed cylindrically all around the body. Moreover the model is derived assuming that the body is rigid the coupling effects among aerodynamics, propulsion, and structural dynamics of the vehicle are negligible. The coupling effects for the linear model (4.2) are later considered in.[82] They are formulated as uncertainties and incorporated into the model (4.2) as

$$\dot{\mathbf{x}} = (\mathbf{A} + \Delta_A)\mathbf{x} + (\mathbf{B} + \Delta_B)\mathbf{u} \tag{4.4}$$

where $\Delta_A$ and $\Delta_B$ are additive uncertainties respectively. In,[82] the impact of the propulsive perturbations on the pitching moment is focused among the coupling effects and this effect is addressed as parametric uncertainty in $C_{m_\alpha}$. In this direction, further analysis has been performed for the special case of (4.4) where $\Delta_A = \nu[0 \quad 0 \quad 1 \quad 0 \quad 0]^T[0 \quad 1 \quad 0 \quad 0 \quad 0]$, $\Delta_B = 0_{5\times 2}$ and $\nu$ is an uncertain parameter. For this case study, (4.4) is scaled so that $\nu \in \{0, 1\}$. Later in,[82] the coupling between elastic and rigid structure modes is included in the frequency domain equivalent of (4.4) by defining a cover function carrying information about the flexible modes.

A drawback of the linear approaches above is that the capability of the model to represent the dynamics and the coupling effects realistically is limited. One way to eliminate this drawback is introducing nonlinear models that carry more information instead of linear ones. Although using a nonlinear model puts limitations on the designs that can be used to control the system in general, recent and ongoing developments in nonlinear control would relieve this burden. A nonlinear longitudinal model for a specific flight condition based on[90,91] is presented in.[93,94] In this model the coupling effects and other possible variations from the nominal system are also considered. These effects and variations, however, are represented by a set of random variables in the context of stochastic robustness[95–97] as an alternative to the classical (linear) robustness theory,[98,99] without elaborating their behavior. In this context, the system model, in its most general form, is described by

$$\begin{aligned} \dot{\mathbf{x}}(t) &= \mathbf{f}(\mathbf{x}(t), \mathbf{u}(t), \mathbf{v}) \\ \mathbf{y}(t) &= \mathbf{h}(\mathbf{x}(t), \mathbf{v}) \end{aligned} \tag{4.5}$$

where $\mathbf{f}$ and $\mathbf{h}$ are smooth nonlinear (vector) functions, and $\mathbf{v}$ is a random vector with normal probability density function representing the uncertainties in the parameters of the dynamics. $\mathbf{v}$ is assumed to be constant throughout an individual process. More specifically, in,[93,94] the system variables are defined to be

$$\begin{aligned} \mathbf{x} &= [V(\text{ft/s}) \quad \gamma(\text{rad}) \quad h(\text{ft}) \quad \alpha(\text{rad}) \quad q(\text{rad/s})]^T, \\ \mathbf{u} &= [\delta_t \quad \delta_e(\text{rad})]^T \end{aligned}$$

and $\mathbf{v}$ a random vector of dimension 28 following a normal distribution with mean 1 and standard deviation 0.1. The longitudinal dynamics are explicitly given by

$$\dot{V} = \frac{T\cos\alpha - D}{m} - \frac{\mu_g \sin\gamma}{r_e^2} \tag{4.6}$$

$$\dot{\gamma} = \frac{L + T\sin\alpha}{mV} - \frac{(\mu_g - V^2 r_e)\cos\gamma}{V r_e^2} \tag{4.7}$$

$$\dot{h} = V\sin\gamma \tag{4.8}$$

$$\dot{\alpha} = q - \dot{\gamma} \quad (4.9)$$
$$\dot{q} = M/\mathrm{I}_{yy} \quad (4.10)$$

where the lift $L$, the drag $D$, the thrust $T$, the pitching moment $M$, and the radius $r_e$ from the Earth's center are modeled as

$$\begin{aligned} L &= \frac{1}{2}\rho V^2 S C_L \\ D &= \frac{1}{2}\rho V^2 S C_D \\ T &= \frac{1}{2}\rho V^2 S C_T \\ M &= \frac{1}{2}\rho V^2 S \bar{c}\,(C_m(\alpha) + C_m(\delta_e) + C_m(q)) \\ r_e &= h + R_e \end{aligned}$$

In,[93,94] the model parameters $m$, $\mathrm{I}_{yy}$, $S$, $\bar{c}$, $\rho$, $a_\infty$, $C_L$, $C_D$, $C_T$, $C_m(\alpha)$, $C_m(\delta_e)$, and $C_m(q)$ are explicitly formulated as functions of the system parameters they depend on as well as some of the entries of the random uncertainty vector $\mathbf{v}$. For the definition of the above symbols, see Nomenclature at the beginning of the paper.

The nonlinear model (4.5) is too general to form a basis for control design. A more practical model is the so-called triangular form, which is suitable for a large set of control design procedures in the literature as well as being general enough to describe many physical systems. In this form, the system equations (4.5) can be rewritten as

$$\begin{aligned} \dot{\mathbf{x}}_1 &= \mathbf{f}_1(\mathbf{x}_1, \mathbf{x}_2, \mathbf{v}) \\ \dot{\mathbf{x}}_2 &= \mathbf{f}_2(\mathbf{x}_1, \mathbf{x}_2, \mathbf{x}_3, \mathbf{v}) \\ &\vdots \\ \dot{\mathbf{x}}_k &= \mathbf{f}_k(\mathbf{x}_1, \mathbf{x}_2, \ldots, \mathbf{x}_k, \mathbf{v}) + \mathbf{g}(\mathbf{x}_1, \mathbf{x}_2, \ldots, \mathbf{x}_k, \mathbf{v})\mathbf{u} \\ \mathbf{x} &= [\,\mathbf{x}_1^T \;\; \mathbf{x}_2^T \;\; \cdots \;\; \mathbf{x}_k^T\,]^T \\ \mathbf{y} &= \mathbf{h}(\mathbf{x}, \mathbf{v}) \end{aligned} \quad (4.11)$$

where $\mathbf{f}_i$, $\mathbf{g}$, and $\mathbf{h}$ are smooth nonlinear vector and matrix functions, respectively. In,[94] considering the engine throttle dynamics to be of the form

$$\ddot{\delta}_t = \delta_{tcom}$$

where $\delta_{tcom}$ is the throttle setting command signal, instead of assuming perfect desired setting tracking and defining

$$V_I(t) = \int_0^t (V(\tau) - V_d)d\tau \quad (4.12)$$
$$h_I(t) = \int_0^t (h(\tau) - h_d)d\tau \quad (4.13)$$

where the subscript $d$ stands for the desired value, the longitudinal dynamics (4.6)–(4.10) are expressed in the triangular form as

$$\begin{aligned} \dot{\mathbf{x}}_1 &= \mathbf{f}_1(\mathbf{x}_1, \mathbf{x}_2, \mathbf{v}) \\ \dot{\mathbf{x}}_2 &= \mathbf{f}_2(\mathbf{x}_1, \mathbf{x}_2, \mathbf{x}_3, \mathbf{v}) \\ \dot{\mathbf{x}}_3 &= \mathbf{f}_3(\mathbf{x}_1, \mathbf{x}_2, \mathbf{x}_3, \mathbf{v}) + \mathbf{g}(\mathbf{x}_1, \mathbf{x}_2, \mathbf{x}_3, \mathbf{v})\mathbf{u} \end{aligned} \quad (4.14)$$

where

$$\begin{aligned} \mathbf{x}_1 &= [\,V_I \;\; V \;\; \gamma\,]^T \\ \mathbf{x}_2 &= [\,\delta_t \;\; h_I \;\; h \;\; \alpha\,]^T \\ \mathbf{x}_3 &= [\,\dot{\delta}_t \;\; q\,]^T \\ \mathbf{u} &= [\,\delta_{tcom} \;\; \delta_e\,]^T \end{aligned}$$

and the random uncertainty vector $\mathbf{v}$ is defined the same as before. The use of the models (4.5) and (4.14) as well as the stochastic robustness context will be more clear with presentation of the robust control designs based on these models in Section 5.

Although the models above are simple and suitable for developing control design techniques, they do not describe the AHF dynamics detailed enough. A more exclusive and more realistic mathematical model in the literature is the analytical aeropropulsive/aeroelastic hypersonic-vehicle model derived for the X-30 configuration in.[46,47] The focus of this model is dynamic couplings and control system integration. The corresponding approach involves a two-dimensional Newtonian aerodynamic analysis, a one-dimensional aero/thermo flow analysis of the propulsion system, and simple lumped-mass model characterization of the vibration modes in the airframe structural dynamics. The elastic motion is characterized by a single body bending mode. The control effectors considered are the pitch-control surfaces for the aerodynamic system and the fuel flow and diffuser area ratio adjusters for the engine. The mathematical model derived incorporates most of the issues covered in Section 3 and summarized in Figure 3. The derived force and moment equations in[46,47] are summarized as follows:

$$\begin{aligned} X &= \dot{X}_A + X_T + X_E \\ Z &= Z_A + Z_T + Z_E \\ M &= M_A + M_T + M_E \\ Q &= Q_A + Q_T + Q_E \end{aligned}$$

$$\begin{bmatrix} \Delta X_A \\ \Delta Z_A \\ \Delta M_A \\ \Delta Q_A \end{bmatrix} = A \begin{bmatrix} \Delta \mathrm{M}_\infty \\ \Delta\alpha \\ \Delta q \\ \Delta\eta \\ \Delta\dot{\eta} \end{bmatrix} + A_c \Delta\delta_e$$

$$\begin{bmatrix} \Delta X_T \\ \Delta Z_T \\ \Delta M_T \\ \Delta Q_T \end{bmatrix} = T \begin{bmatrix} \Delta \mathrm{M}_\infty \\ \Delta\alpha \\ \Delta q \\ \Delta\eta \\ \Delta\dot{\eta} \end{bmatrix} + T_c \begin{bmatrix} \Delta\bar{A}_D \\ \Delta T_0 \end{bmatrix}$$

$$\begin{bmatrix} \Delta X_E \\ \Delta Z_E \\ \Delta M_E \\ \Delta Q_E \end{bmatrix} = E \begin{bmatrix} \Delta \mathrm{M}_\infty \\ \Delta\alpha \\ \Delta q \\ \Delta\eta \\ \Delta\dot{\eta} \end{bmatrix} + E_c \begin{bmatrix} \Delta\bar{A}_D \\ \Delta T_0 \end{bmatrix}$$

where the notation given in the nomenclature is used. $A$, $T$, and $E$ are $4 \times 5$ system matrices whose elements are the stability derivatives of aerodynamics, engine-thrust, and external nozzle, respectively. $A_C$ is a $4 \times 1$ vector whose elements are the aerodynamic control derivatives. $T_C$ and $E_C$ are $4 \times 2$ and contain engine-thrust and external nozzle control derivatives, respectively. All the elements in the second and the forth rows of $T$ and $T_C$ are zero. Detailed analytic expressions for all these system matrices, i.e., the stability and control derivatives can be found in.[46,47] These expressions are basically nonlinear functions of vehicle geometry and mass properties, atmospheric conditions, structural vibration mode shapes, and Mach number.

Based on the force and moment equations summarized above the AHFV longitudinal equations of motion were derived and expressed in the state space form as well as

$$\dot{\mathbf{x}} = \mathbf{A}\mathbf{x} + \mathbf{B}\mathbf{u} \tag{4.15}$$

where

$$\mathbf{x} = \begin{bmatrix} \Delta h \ \text{(ft)} \\ \Delta u \ \text{(ft/s)} \\ \Delta\alpha \ \text{(rad)} \\ \Delta\theta \ \text{(rad)} \\ \Delta q \ \text{(rad/s)} \\ \Delta\tau_1\eta \ \text{(rad)} \\ \Delta\tau_1\dot{\eta} \ \text{(rad/s)} \end{bmatrix}, \quad \mathbf{u} = \begin{bmatrix} \Delta\delta_e \ \text{(rad)} \\ \Delta\bar{A}_D \\ \Delta T_0 \ (^\circ\text{R}) \end{bmatrix}$$

$$\mathbf{A} = T_1 + T_2 \begin{bmatrix} c_1\mathbf{S}_{11} & & \\ c_1\mathbf{S}_{21} & & \\ c_1\mathbf{S}_{31} & \mathbf{S} & \\ c_1\mathbf{S}_{41} & & \end{bmatrix} T_3$$

$$\mathbf{B} = T_2 \begin{bmatrix} A_c & T_c + E_c \end{bmatrix}$$

$$\mathbf{S} = A + T + E$$

$$c_1 = \frac{\mathrm{M}_\infty}{2P_\infty}\frac{dP_\infty}{dh}$$

$$T_1 = \begin{bmatrix} 0 & 0 & -u_0 & u_0 & 0 & 0 & 0 \\ 0 & 0 & -g & 0 & 0 & 0 & 0 \\ 0 & 0 & 0 & 0 & 1 & 0 & 0 \\ 0 & 0 & 0 & 0 & 1 & 0 & 0 \\ 0 & 0 & 0 & 0 & 0 & 0 & 0 \\ 0 & 0 & 0 & 0 & 0 & 0 & 1 \\ 0 & 0 & 0 & 0 & 0 & -\omega_1^2 & -2\zeta_1\omega_1 \end{bmatrix}$$

$$T_2 = \begin{bmatrix} 0 & 0 & 0 & 0 \\ 1/\bar{m} & 0 & 0 & 0 \\ 0 & 1/\bar{m}u_0 & 0 & 0 \\ 0 & 0 & 0 & 0 \\ 0 & 0 & 1/\mathrm{I}_{yy} & 0 \\ 0 & 0 & 0 & 0 \\ 0 & 0 & 0 & \Delta\tau_1/\bar{m} \end{bmatrix}$$

$$T_3 = \begin{bmatrix} 1 & 0 & 0 & 0 & 0 & 0 & 0 \\ 0 & 1/\mathrm{a}_\infty & 0 & 0 & 0 & 0 & 0 \\ 0 & 0 & 1 & 0 & 0 & 0 & 0 \\ 0 & 0 & 0 & 0 & 1 & 0 & 0 \\ 0 & 0 & 0 & 0 & 0 & 1/\Delta\tau_1 & 0 \\ 0 & 0 & 0 & 0 & 0 & 0 & 1/\Delta\tau_1 \end{bmatrix}$$

The longitudinal dynamic model for the X-30 configuration in[46,47] can be extended to include some other relatively minor dynamic effects using the equations of motion, kinematic equations, and 3-DOF point-mass-model derived for generic elastic hypersonic flight vehicles in.[89] The equations derived in[89] include the effects of rigid-body motion, elastic deformation, fluid flow, rotating machinery, wind, and Earth rotation together with the couplings among them. The derivation is based on a Lagrangian approach and the significance of selected terms in the derived equations are discussed.

Although the integrated scramjet engine dynamics and the hypersonic aerodynamics are modeled to some extent, and the coupling issues in AHF dynamics are analytically elaborated in,[46,47,89] the parameter variations and the modeling uncertainties are neglected. These latter issues are considered in detail in modeling in.[51] The focus of[51] is determination of the sources and the extents of uncertainties, and development of uncertainty models for AHFVs, specifically for the X-30 configuration, which can be used in robust multivariable control designs, and checking whether these models satisfy the usual assumptions in robust control theory. The uncertainty sources have already been discussed in Section 3.5. Elaborating on some of these sources, the following generic model is considered in:[51]

$$\dot{\mathbf{x}} = \mathbf{A}\mathbf{x} + \mathbf{B}\mathbf{u}, \quad \mathbf{y} = \mathbf{C}\mathbf{x} + \mathbf{D}\mathbf{u}, \tag{4.16}$$

$$\mathbf{A} = \bar{\mathbf{A}} + \sum_{i=1}^{n_p} \delta p_i \mathbf{A}_i, \quad \mathbf{B} = \bar{\mathbf{B}} + \sum_{i=1}^{n_p} \delta p_i \mathbf{B}_i,$$

$$\mathbf{C} = \bar{\mathbf{C}} + \sum_{i=1}^{n_p} \delta p_i \mathbf{C}_i, \quad \mathbf{D} = \bar{\mathbf{D}} + \sum_{i=1}^{n_p} \delta p_i \mathbf{D}_i,$$

where

$$\mathbf{x} = \begin{bmatrix} h(\text{ft}) \\ u(\text{ft/s}) \\ \alpha(\text{rad}) \\ \theta(\text{rad}) \\ q(\text{rad/s}) \\ \eta(\text{rad}) \\ \dot{\eta}(\text{rad/s}) \end{bmatrix}, \mathbf{u} = \begin{bmatrix} \delta_e(\text{rad}) \\ \Delta\bar{A}_D \\ \dot{m}_f(\text{slug/s}) \end{bmatrix}, \mathbf{y} = \begin{bmatrix} \alpha_m(\text{rad}) \\ q_f(\text{rad/s}) \\ q_t(\text{rad/s}) \\ P_2(\text{atm}) \\ \mathrm{M} \\ \mathrm{Th}_e(\text{lb/ft}) \\ n_x(\text{g}) \\ n_z(\text{g}) \end{bmatrix}$$

$\mathbf{A}$ and $\mathbf{B}$ are the system matrices carrying the stability and control derivative information. They are similar to the system matrices of (4.15), noting the similarity between the state and input vectors of (4.15) and

(4.16). The other two system matrices, $\mathbf{C}$ and $\mathbf{D}$ have the sensor structure information. $\bar{\mathbf{A}}$, $\bar{\mathbf{B}}$, $\bar{\mathbf{C}}$, $\bar{\mathbf{D}}$ are the nominal values of $\mathbf{A}$, $\mathbf{B}$, $\mathbf{C}$, $\mathbf{D}$. $p_i$, $i = 1, \ldots, n_p$ denote the uncertain parameters in the system. $\delta p_i$ are the corresponding fractional variations and $\mathbf{A}_i = \frac{\partial \mathbf{A}}{\partial \delta p_i}$, $\mathbf{B}_i = \frac{\partial \mathbf{B}}{\partial \delta p_i}$, $\mathbf{C}_i = \frac{\partial \mathbf{C}}{\partial \delta p_i}$, $\mathbf{D}_i = \frac{\partial \mathbf{D}}{\partial \delta p_i}$.

In,[51] the case with $n_p = 5$,

$$p_1 = P_\infty,\ p_2 = \omega_1,\ p_3 = \zeta,\ p_4 = \Delta\tau_1,\ p_5 = \Delta\tau_2$$
$$\delta p_1 = \frac{P_\infty - \bar{P}_\infty}{\bar{P}_\infty},\ \delta p_2 = \frac{\omega_1 - \bar{\omega}_1}{\bar{\omega}_1},\ \delta p_3 = \frac{\zeta - \bar{\zeta}}{\bar{\zeta}},$$
$$\delta p_4 = \frac{\Delta\tau_1 - \bar{\Delta}\tau_1}{\bar{\Delta}\tau_1},\ \delta p_5 = \frac{\Delta\tau_2 - \bar{\Delta}\tau_2}{\bar{\Delta}\tau_2}$$

where the over-bar indicates nominal values, is analyzed further and, as an example, the effects of $\delta p_1$ and $\delta p_2$ in the frequency domain are demonstrated via numerical analysis results. Based on these results, it is concluded in[51] that some of the general assumptions on uncertainties in robust control theory are violated. Specifically, the additive plant uncertainty

$$\Delta_a = \left(\mathbf{C}(sI - \mathbf{A})^{-1}\mathbf{B} + \mathbf{D}\right) - \left(\bar{\mathbf{C}}(sI - \bar{\mathbf{A}})^{-1}\bar{\mathbf{B}} + \bar{\mathbf{D}}\right)$$

is shown to be unstable which violates the frequently made stability assumptions although the limited numerical results do not violate the less conservative assumption of invariance of the number of unstable poles.[98] Moreover, derivation of the model (4.16) is based on the assumption that the uncertain parameters are mutually independent and the dynamic uncertainties can be represented by a set of uncertain parameters which does not need to hold at all. It is also remarked in[51] that the uncertainties appear to be so large over a wide frequency range robustness conditions on their magnitudes are hard to satisfy. This leads to the corollary that rigid body assumptions ignoring the aeroelastic modes will result in greater and unacceptable uncertainties.

Beside the analytical AHF models above, it is worth to mention the Generic Hypersonic Aerodynamic Model Example (GHAME),[40,100] an extensive computational model. GHAME is composed of five data sets: Two aerodynamic models one of which is based on several empirical data sources and the other based on analytical programs, two aerothermodynamic models first of which is a simple convection-radiation heat flux and equilibrium model and the second a model obtained using analytical programs, and a simplified switching turbojet-ramjet-scramjet engine model. The aerodynamic models are based on a rigid body configuration with a geometry similar to that of the conic accelerator.[90,91] The engine modules are assumed to be wrapped around the lower surface of the fuselage. The engine mode switches to turbojet for $V < 2$ M, ramjet for $2\ \text{M} \leq V < 6$ M, and scramjet for $V \geq 6$ M. The effects of AOA and Mach number on the propulsion are considered in the engine model. In terms of control, GHAME is suitable for simulation and numerical intelligent controller synthesis rather than analytical design methods.

Having covered all the main models for AHFVs in the literature above, we see that a comprehensive analytical model expressing all the dynamic characteristics of AHF presented in Section 3 in detail is still not available. Nonetheless each of the models (4.2), (4.3), (4.4), (4.5), (4.14), (4.15), (4.16) addresses a portion of issues in longitudinal AHF dynamics. Especially, (4.16) covers almost all significant characteristics of longitudinal AHF dynamics, although the concerns in[51] about the uncertainties need to be clarified. The validity and use of the models above will be more apparent in the next section where we review the AHF control designs based on these models.

## 5 HYPERSONIC FLIGHT CONTROL: THEORY AND SIMULATIONS

In this section, we review the attempts in the literature to solve the AHF control problem, which can be defined as computation of the command signals to be applied to the control effectors of an AHFV in order to make certain flight condition parameters to track desired trajectories during a time interval of interest. The available theoretical studies in the AHF control literature focus on the longitudinal dynamics ignoring its lateral-directional counterpart. This is basically due to the lack of full 6-DOF models which are simple enough to form a basis for control design purposes. Moreover the modeling and control of longitudinal AHF dynamics itself is complicated enough as demonstrated in Section 4, and the control problem is expected to become more complex considering the lateral-directional characteristics. Nevertheless, the existing control design attempts can be thought as the initial steps in solving the integrated AHF control problem.

The main models for longitudinal AHF dynamics that appear in the literature have been presented in Section 4. The goal of the control design based on anyone of these models is to force the system outputs (entries of $\mathbf{y}$) to follow desired time-trajectories by adjusting a set of control coefficients (entries of $\mathbf{u}$). Similar to any other control problem, there are three main concerns in reaching this goal: Stability, performance, and robustness. The time-trajectories of the actual system outputs are required to be close enough to the desired ones while guaranteeing the system parameters

to be bounded within allowable margins irrespective of the modeling uncertainties and external disturbances. There is always a trade-off between performance and robustness in control design for systems with uncertainties and disturbances. However, this trade-off is much more significant in AHF control due to the fast time varying nature of the system and the large size of anticipated uncertainties and disturbances.

Among different approaches in the AHF control literature, robust control approaches are more realistic since they take into account modeling uncertainties. We can divide the available robust AHF control approaches into two subcategories as linear model based and nonlinear model based. In the linear model based approaches, classical techniques of robust control,[98,99] such as $\mathcal{H}_\infty$ techniques and $\mu$-synthesis, are applied to the AHFV models with structured and unstructured uncertainties. The resultant controllers have the common property of being highly conservative in terms of robustness with undesirable side effects on performance.

The robust control design for the rigid conic accelerator configuration in[91] is a milestone among the linear model based approaches. In that paper, based on the linear model (4.3) with the assumption that $\mathbf{y} \cong \mathbf{x}$, i.e., all the states are available for measurement with some small corruption due to sensor noises, the control problem is defined as stabilizing the vehicle and tracking the velocity ($V$) and altitude ($h$) commands highly accurately while keeping the magnitude of the AOA ($\alpha$) deviation from nominal less than 0.5° and minimizing the control power use. The limit on the AOA minimizes the perturbations in the integrated engine inlet and nozzle conditions discussed in Section 3 which affect the propulsion performance. The nominal flight condition is assumed to be $V = 8$ M and $h = 85,700$ ft. The control problem is reformulated in the robust control context in order to apply design controllers that would provide $\mathcal{H}_\infty$-stability and $\mu$-optimality.[99] The detailed scheme of the reformulation can be found in.[91] In this formulation, system uncertainty due to parameter variations from vehicle acceleration are represented as a $2 \times 2$ diagonal 20 % multiplicative input uncertainty. The tracking and stability performance requirements are converted to weighting function conditions for the state $\mathbf{x}$ and the input $\mathbf{u}$. Frequency varying weighting is used for $V$ and $h$, which are required to track certain desired values, while constant weighting is used for other state and input entries.

The robust control problem is approached by both direct $\mathcal{H}_\infty$ loop shaping techniques and $\mu$-synthesis with $DK$-iteration in.[91] The design has produced three controllers: An $\mathcal{H}_\infty$ controller for the nominal plant—ignoring the 20 % input uncertainty in the design—, an $\mathcal{H}_\infty$ controller for the uncertain plant—considering the 20 % input uncertainty in the design procedure—, and a $\mu$-optimal controller obtained using $DK$-iteration. Each of the three controllers is of the form

$$\begin{aligned} \dot{\mathbf{x}}_c &= \mathbf{A}_c\mathbf{x}_c + \mathbf{B}_c \begin{bmatrix} \mathbf{y} \\ V_c \\ h_c \end{bmatrix}, \\ \mathbf{u} &= \mathbf{C}_c\mathbf{x}_c \end{aligned} \tag{5.1}$$

where $V_c$ and $h_c$ are command signals for $V$ and $h$, respectively. Dimension of $\mathbf{x}_c$ is 12 for the $\mathcal{H}_\infty$ controllers and 13 for the $\mu$-optimal controller, which is obtained by truncating the 18-dimensional result of the $DK$-iteration using residue and Hankel norm approximation methods.

In,[91] the designed controllers are numerically analyzed and compared in both frequency domain and time domain. For the time domain analysis, a linear simulation of the system is used and the entries of the external disturbance $\mathbf{d}$ in (4.3) due to turbulence are implemented as outputs of Dryden turbulence filters fed with white noises. The simulation results demonstrate that the $\mu$-optimal controller is successful in satisfying all the robustness and performance requirements while the $\mathcal{H}_\infty$ controllers are not. The use of the $\mathcal{H}_\infty$ controller for the nominal plant results in significant sensitivity to external disturbances even in the absence of the input modeling uncertainty. The $\mathcal{H}_\infty$ controller for the uncertain plant, however, satisfies the requirements provided that the input uncertainty is reduced to 17 %.

A similar robust control approach to the same control problem is conducted in[82] based on the uncertainty model (4.4). The focus of this work is use of a special technique for designing fixed low order controllers,[101] which do not have implementation problems caused by high system dimensionality. In this technique, rather than performing the $DK$-iteration and then reducing the order of the resulting controller, the controller dimension is fixed a priori and a fixed-order $\mu$-synthesis procedure is used. The procedure employs a mixed $\mu$-synthesis method called $DGK$-iteration[102] in order to reduce the robustness conservatism. Although it promises a controller with very desirable properties, the procedure itself is hard to implement due to some requirements such as knowledge of an initial stabilizing controller of fixed order.

In,[82] the $DK$-iteration without any dimension constraint is used first to design a $\mu$-optimal controller. Using model reduction methods similar to those used in,[91] this controller —of order 47— is truncated to

5th–9th stabilizing controllers. Later, a fixed fifth-order controller is obtained using the special technique of[101] together with the truncated fifth order controller as the initial stabilizing controller of the $DGK$-iteration. Performance of the full order controller, the truncated controllers, and the fixed fifth-order controller are illustrated and compared via simulation results as well in.[82] The simulation results demonstrate the superiority of the fixed order controller to the truncated controllers as well as its successful performance and robustness properties which are close to those of the full order controller.

Another $\mathcal{H}_\infty$ based approach to control of the linear model of[90,91] is presented in.[103] However, this approach is based on the simple form (4.2), which does not take into account the disturbances and modeling uncertainties, and the $\mathcal{H}_\infty$ techniques are used to develop an alternative to the Shapiro eigenstructure assignment design. The focus of the approach is decoupling the phugoid and short-period modes of (4.2) using this alternative design. The simulation results in[103] demonstrate the effectiveness of the new $\mathcal{H}_\infty$ based eigenstructure assignment design compared to the traditional Shapiro design.

It has already been mentioned in Section 4 that it is better to use nonlinear models instead of linear ones in order to represent the dynamics and the coupling effects in detail. Since the classical robustness theory has been developed for linear systems and does not fit well to nonlinear models the context of stochastic robustness[95–97] has been introduced as an alternative to the classical robustness theory. In this context, all the modeling uncertainties are assumed to be parametric in contrary to the classical robustness theory where the modeling uncertainties are preferred to be expressed in terms of uncertainty transfer functions and matrices. All the uncertainty information is collected in a random vector $\mathbf{v}$ and inserted in to the nonlinear model as already shown in (4.5).

For a fixed uncertainty vector $\mathbf{v}$, let us denote the plant with dynamics (4.5) by $\mathcal{G}_\mathbf{v}$. The acceptability of using a certain controller $\mathcal{K}$ to control $\mathcal{G}_\mathbf{v}$ is quantified via a binary indicator function $J$ that is defined as follows: $J(\mathcal{G}_\mathbf{v}, \mathcal{K})$ is equal to 0 if the closed loop system $(\mathcal{G}_\mathbf{v}, \mathcal{K})$ is acceptable —in terms of stability and performance requirements— and 1 otherwise. The robustness of the controller $\mathcal{K}$ over the set $\mathcal{V}$ of all possible uncertainty vectors $\mathbf{v}$ is measured as

$$P_\mathcal{V}(\mathcal{K}) = \int_{\mathbf{v}\in\mathcal{V}} J\left(\mathcal{G}_\mathbf{v}, \mathcal{K}\right) \mathrm{pr}(\mathbf{v}) d\mathbf{v} \qquad (5.2)$$

where , $\mathrm{pr}(\mathbf{v})$ is the probability density function of $\mathbf{v}$ satisfying $\int_{\mathbf{v}\in\mathcal{V}} \mathrm{pr}(\mathbf{v})d\mathbf{v} = 1$. Note that the smaller $P_\mathcal{V}(\mathcal{K})$ is the more robust $\mathcal{K}$ is. In the cases where (5.2) cannot be computed analytically, a random sample set $\{\mathbf{v}_1, \mathbf{v}_2, \ldots, \mathbf{v}_{N_v}\}$, where $N_v$ is large enough for sampling, is selected from $\mathcal{V}$ and the probability estimate

$$\hat{P}_\mathcal{V}(\mathcal{K}) = \frac{1}{N_v} \sum_{i=1}^{N_v} J\left(\mathcal{G}_{\mathbf{v}_i}, \mathcal{K}\right) \qquad (5.3)$$

is used as a practical alternative to $P_\mathcal{V}(\mathcal{K})$.

Nonlinear model based (stochastically) robust control techniques have the benefit of being less conservative in terms of robustness in addition to taking into account the system dynamics and the design requirements in detail. Their drawback is the difficulty of parameterizing the uncertainties and forming the uncertainty vector $\mathbf{v}$ reliably. These techniques are applied to the longitudinal AHF models (4.5) and (4.14) in[93] and,[94] respectively. In,[93] the state equation in (4.5) is approximated using Taylor's series expansion about the trim state $\mathbf{x}_0$ as

$$\dot{\mathbf{x}} = F_x(\mathbf{v})\Delta\mathbf{x} + F_u(\mathbf{v})\Delta\mathbf{u} \qquad (5.4)$$

where $F_x(\mathbf{v}) = \partial f/\partial x$, $F_u(\mathbf{v}) = \partial f/\partial u$, $\mathbf{x} = \mathbf{x}_0 + \Delta\mathbf{x}$, $\mathbf{u} = \mathbf{u}_0 + \Delta\mathbf{u}$, and $\mathbf{u}_0$ is the nominal trim value of the control signal that is assumed to be available. $\Delta\mathbf{u}$ is further composed as

$$\Delta\mathbf{u} = \Delta\mathbf{u}_d + \Delta\mathbf{u}_s$$

where $\Delta\mathbf{u}_d$ is the increment needed to bring the system to a new desired trim condition and $\Delta\mathbf{u}_s$ is a dynamic signal to ensure stability and desired shape of transition. $\Delta\mathbf{u}_d$ is computed algebraically in terms of nominal values of the system parameters of the model (5.4) and the command-actuator dynamics, and the desired increment in the trim state.

The essential part of control design and analysis in[93] is the design and analysis of the component $\Delta\mathbf{u}_s$. This component is designed as a robust LQ optimal controller of the form

$$\Delta\mathbf{u}_s = -k_R K_{LQ} \Delta\mathbf{x}_c \qquad (5.5)$$

where $K_{LQ}$ is the LQ optimal gain matrix obtained by minimizing a LQ cost function, $k_R$ is a scalar constant used for robustness purposes,

$$\Delta\mathbf{x}_c = \left[\, (\Delta\mathbf{x})^T \quad V_I \quad h_I \,\right]^T,$$

and $V_I$, $h_I$ are defined in (4.12), (4.13). A genetic algorithm is used to select the robustness coefficient $k_R$ and the design parameters determining the LQ cost function to be solved to obtain $K_{LQ}$ based on performance and stability metrics defined using the stochastic robustness notions (5.2) and (5.3). The designed controller is tested in[93] using numerical stability analysis

and simulations for the nominal flight condition with $V = 15$ M, $h = 110,000$ ft, $\gamma = 0$ deg, $q = 0$ deg/sec.

The LQ design of[93] is improved in[94] using the triangular model (4.14) instead of the general model (4.5) and imposing nonlinear dynamic inversion techniques[104] into the control design. The improvement is illustrated in[94] via numerical analysis and simulation results.

A recent alternative to the nonlinear controller of[94] is the adaptive sliding mode control approach of.[105,106] In this work, a new adaptive sliding mode technique is developed for a class of MIMO nonlinear systems including the nonlinear models (4.5)–(4.14). The adaptive scheme is based on the inverse dynamics of the original system. The common controllability issues faced at the instants when the gain matrices become (almost) singular is circumvented in[105,106] using a switching technique. Furthermore some specific form of $\sigma$-modification[107] is used to preserve stability at such instants. The adaptive structure makes the controller efficient in dealing with the parametric uncertainties. The states that are not available for measurement are estimated using a nonlinear sliding mode observer. Simulation results demonstrate that the controller structure proposed in[105,106] is successful in general under a mild assumption about some of the system parameters.

In all the above designs, the designed controller applies to a certain flight condition and hence a supervisor such as a gain scheduling scheme is needed in order to run the controller during the complete flight envelop. In the design of the supervisor, the significant variations in the AHF system due to wide speed ranges (see Section 3.2) should be taken into account. To this point, time and/or parameter varying approaches appear as alternatives to the gain scheduling schemes. The design issues in constructing a supervisor for the complete flight envelop and the use of time varying approaches will be elaborated in Section 7.

Various other efforts to control hypersonic flight are presented in the literature. However these works pay less attention to the airframe/engine/elastic coupling in the hypersonic flight dynamics of air-breathing aeroelastic vehicles and characteristics of the modeling uncertainties. They concentrate on application of specific techniques to the existing hypersonic flight dynamic models. Main categories of these approaches are model reference adaptive control approach for linear models,[108] optimal and sub-optimal control approaches,[109–111] genetic algorithm based approaches,[112] fuzzy control approaches,[113] and neural network approaches.[114,115]

## 6 FLIGHT CONTROL LAWS IN USE

Although a significant number of control schemes for AHFVs have been designed and tested via simulations as presented in Section 5, none of these schemes has been completely implemented in a real AHFV. One obvious reason for this is that the AHF technology is in the development and testing phase. There is still no operational AHFV and the aim of flight tests conducted or planned up to now was to analyze the newly developed AHFV components and quantifying the AHF dynamics rather than performing a complete guided flight. Nonetheless, one of the key technologies for flight demonstration of the scramjet powered hypersonic aircraft is use of an efficient flight controller. In the Hyper-X program, such an efficient controller is required to enable a successful separation from the booster rocket, to achieve and maintain the design condition during the engine test, and to provide a controlled descent at the end.[5] The control laws to perform these tasks are being developed by a Boeing/NASA partnership. It is demonstrated via flight simulations and stability margin analyses that the control laws developed so far meet the flight test requirements.

The basic goal of the flight control system in Hyper-X is to maintain the desired AOA and bank angle to within $\pm 0.5$ degrees during the test flights, and to follow steering commands from the guidance system to maintain a desired descent trajectory after the tests are completed. The tools to accomplish this task are the aerodynamic control surfaces, which are basically symmetric and differential deflection of the all-moving wings (AMW) and twin rudders, the pitch rate, yaw rate, roll rate, and bank angle measurement units, and the control mechanism which generates the aerodynamic surface commands by processing guidance commands and sensor feedbacks. Conventional AOA measurement devices can not be used due to aerodynamic heating. Several techniques to estimate an accurate measure of AOA are developed and used.[5]

In the design of the Hyper-X flight control scheme, which is illustrated in Figure 4, classical linear control techniques[116] are preferred to advanced techniques such as the ones in Section 5. The control design is based on a linear model including rigid-body modes, second order actuation modes, and dynamics or certain filters. Lead-lag compensators are used to improve stability margins. Elastic mode effects are circumvented in the controller design as a part of the gain margin requirements avoiding use of a separate structural filter. The affect of propulsion system and dynamic pressure variations on the AHFV aerodynamics are suppressed using a feedforward compensator. The controller parameters are gain scheduled with AOA

and Mach number.

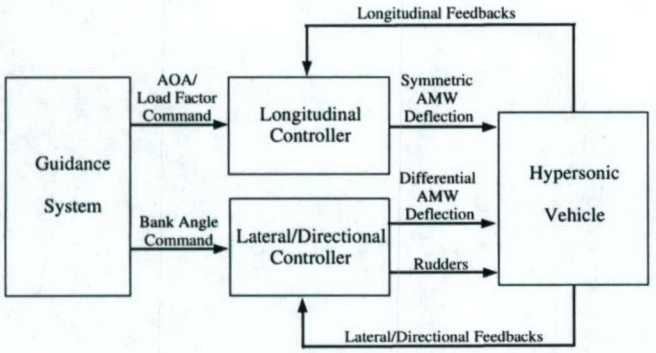


**Figure 4:** Overview of the flight control scheme for X-43A designed by Langley and Dryden Research Centers of NASA.

The continuous-time dynamic equations are discretized using Tustin (bilinear) transformation for implementation and simulation purposes. In simulations, nonlinear models of the dynamics are used to uncover the possible effects of linearization and variations of the system parameters. Simulation and stability analysis results demonstrate that the flight test requirements are met.[5]

The controller design issues in the HRE test flights with X-15 were slightly different from those in the Hyper-X program, since the hypersonic research with X-15 was terminated without performing a AHF test. All the 199 flights of X-15 with or without a dummy non-operated scramjet were performed with rocket power.[24,26] For flight in the atmosphere, conventional aerodynamic control systems such as the yaw motion controlling rudder surfaces on the vertical stabilizers and the pitch and roll motion controlling horizontal surfaces on the tail were used. Outside the atmosphere hydrogen peroxide thrust rockets on the nose and wings were used as a reaction augmentation system. Therefore the air-breathing propulsion, and the interactions and structural constraints brought thereby were not dealt in the control design. However the control techniques developed to enable guided hypersonic flight with X-15s were unique in the supersonic and hypersonic flight control in many aspects.[24]

In the NASP and the HySTP, test flights could not be performed at all. Hence, although a number of control schemes were developed based on the configurations used in these programs as stated in Section 2, they remained in the theory and simulation level. The control tools planned to be used in scramjet operated X-30s and HyFLITE vehicles were similar to the ones designed for X-43s —described above. In addition, a set of engine control effectors were desired to be developed in order to control fuel flow, inlet/diffuser area ratio, exit area of the internal nozzle.[43]

Beside the control laws in use for hypersonic flight tests, it is also worth to mention the ones applied on subsonic flights of some testbeds with geometries optimized for hypersonic flight. The X-43A-LS and the LoFLYTE® test aircraft are two such actively used testbeds.[7,8] Both of these two test aircraft are turbojet powered, remotely piloted, and designed for subsonic flights. The former aircraft is specially designed to collect subsonic flight data for the AHFV X-43A. A series of test flights with these two testbeds have been planned and a number of them have already been performed successfully. Unlike the hypersonic wind tunnel and flight tests, experimentation with many advanced control schemes such as adaptive neural and robust flight controllers, adaptive engine controllers, neural actuator controllers have been included in these subsonic flight tests.[7,8,114,115] All these techniques have been implemented via software installed in the so-called advanced airborne data acquisition and control system (AADACS) hardware.

## 7 FUTURE TRENDS AND DIRECTIONS FOR NEW CONTROL DESIGNS

As can be deducted from the previous sections, flight of an AHFV operated by an air-breathing engine has not been performed yet. One of the main goals of the current AHF programs is to perform such a flight. The next step will be guided AHFs that follow certain prescribed paths. The final goal can be thought as to use AHFVs efficiently to follow arbitrary paths similar to conventional aircraft in a wide speed span including hypersonic ranges. This goal can be widened to include the original SSTO space access task of NASP. Development of new technologies in various areas including controls will be vital in reaching all these future goals. In this section, first, we present the major emerging trends and necessities in AHF technologies briefly keeping the focus on control issues. Then we summarize the gaps in the current AHF control schemes and propose a set of recently developed techniques to fill some of these gaps.

For the current and foreseen AHF technology programs the airframe integrated scramjet engine concept forms the basis. This configuration is widely accepted in all major AHF research centers of the world.[4,9,117,118] Having the airframe integrated engine configuration fixed, an essential task is to enhance and optimize the propulsion systems developed for this configuration. To this point, some discussions on new combustor designs and the ideas on us-

ing hydrocarbons as fuel instead of hydrogen can be found in.[4,6,9,117] Due to aerothermodynamic issues discussed in Section 3, new materials and active cooling techniques need to be developed and used widely in many structural components of the AHFVs.[9,40,117] The new combustion ideas mentioned above are basically performance related. However, use of passive and active heat resistant devices will reduce the uncertainties due to aerothermodynamic effects in modeling and control as well as increasing the overall flight performance. Note from Section 4 that the uncertainties in the existing models are too large to meet certain assumptions in robust control theory and they need to be reduced as much as possible in order to build robust high performance flight controllers.

The most dominant two among the uncertainty sources mentioned in Sections 3 and 4 are the lack of sufficient data on hypersonic flight dynamics and ignorance of coupling effects in modeling. The former of these sources can only be suppressed in time via a number of ground and flight tests which have been in progress since the early stages of the AHF research and which will inevitably continue till maturation of the AHF technology if not forever. An anticipated option to speed up the data broadening process is performing simulations and numerical analysis techniques such as CFD methods on dependable models of various elements of a AHF system in parallel with the ongoing ground and flight experiments. Ongoing studies and discussions on data collection via experiments and numerical techniques can be found in.[54,55,57–60,83,117]

The ignorance of coupling effects in modeling as an uncertainty source was already discussed in Section 4 and the integrated longitudinal aeropropulsive/aeroelastic models derived and elaborated in[46,47,51] were presented as more dependable alternatives to the simpler conventional models. These models may be enhanced to a more comprehensive model combining lateral and directional modes of the aerodynamics with the longitudinal mode. Thereby, the significant longitudinal-lateral-directional and lateral-directional-propulsive interactions would be addressed. To this point, it is worth mentioning the trade off between comprehensiveness of a model and the complexity of designing/implenting a controller for this model. More comprehensive models will have larger numbers of states, inputs, outputs, and nonlinearities. Hence it can be argued that a controller satisfying certain performance, stability, and robustness requirements would be hard. However, a set of techniques recently developed for certain classes of nonlinear and multivariable systems diminish this burden provided the model can be formulated in certain triangular forms similar to (4.11).[119–124]

In order to implement the control designs based on the integrated models, the aerodynamic and propulsive control laws to be applied need to be interactive. Engine control effectors controlling fuel flow, inlet/diffuser area ratio, exit area of the internal nozzle should be in use as well as the aerodynamic control surfaces. These control effectors should be commanded via an integrated mechanism that processes the information signals coming from the aerodynamic and propulsive measurement units together instead of using them as separate feedbacks to the corresponding controller units. It is worth noting that the use of the system integration approach is not limited to modeling and control. In,[118] for example, the integration approach is used to optimize configuration variables of a scramjet-powered hypersonic cruise missile for maximizing the air-breathing range.

Another major issue to be addressed in order to perform a fully guided AHF is design of a supervisor to handle the variations in the complete flight envelop as mentioned at the end of Section 5. Each of the control designs presented in Section 5 applies to a certain flight condition and therefore, in order to extend the applicability of the design to the entire flight envelop, the design procedure needs to be repeated for a sufficient number of flight conditions and a supervisory scheme is required to perform the transitions between these flight conditions. The conventional supervision methodology in aerospace applications is gain scheduling. However, in spite of the wide use of this methodology and the increase of interest of the academic research community in it for the last fifteen years, there is still a lack of tests to guarantee global stability of gain scheduled systems in general.[125–128] Furthermore, slow plant parameter variations and sufficient number of flight conditions at which the dynamics are completely quantified are generic assumptions for applicability of the gain scheduling schemes. Taking the significant and fast variations in the AHF system due to dominant hypersonic regime during the entire flight as well as wide operation ranges and the lack of broad flight data (see Section 3), designing a gain scheduling scheme for AHFVs will be extremely hard if possible. Leaving the discussions on use of gain scheduling to the references,[125–128] we concentrate on use of time and parameter varying approaches as alternatives to gain scheduling next.

For the parameter varying approaches, the flight condition specific models (4.3), (4.5), (4.11) are respectively replaced with

$$\dot{\mathbf{x}} = \mathbf{A}_p(p)\mathbf{x} + \mathbf{B}_p(p)\mathbf{u} + \mathbf{E}_{xp}(p)\mathbf{d} \tag{7.1}$$

$$\begin{aligned} \dot{\mathbf{x}} &= \mathbf{f}_p(\mathbf{x}, \mathbf{u}, \mathbf{v}, p) \\ \mathbf{y} &= \mathbf{h}_p(\mathbf{x}, \mathbf{v}, p) \end{aligned} \tag{7.2}$$

$$
\begin{aligned}
\dot{\mathbf{x}}_1 &= \mathbf{f}_{1p}(\mathbf{x}_1, \mathbf{x}_2, \mathbf{v}, p) \\
\dot{\mathbf{x}}_2 &= \mathbf{f}_{2p}(\mathbf{x}_1, \mathbf{x}_2, \mathbf{x}_3, \mathbf{v}, p) \\
&\vdots \\
\dot{\mathbf{x}}_k &= \mathbf{f}_{kp}(\mathbf{x}_1, \ldots, \mathbf{x}_k, \mathbf{v}, p) + \mathbf{g}_p(\mathbf{x}_1, \ldots, \mathbf{x}_k, \mathbf{v}, p)\mathbf{u} \\
\mathbf{x} &= [\mathbf{x}_1^T \quad \mathbf{x}_2^T \quad \cdots \quad \mathbf{x}_k^T]^T \\
\mathbf{y} &= \mathbf{h}_p(\mathbf{x}, \mathbf{v}, p)
\end{aligned} \tag{7.3}
$$

where $\mathbf{A}_p$, $\mathbf{B}_p$, $\mathbf{E}_{xp}$, $\mathbf{f}_p$, $\mathbf{f}_{ip}$, $\mathbf{h}_p$, $\mathbf{g}_p$ are smooth nonlinear functions and $p$ is a lumped time varying parameter vector defining the flight conditions, i.e., $p(t)$ defines the flight condition of the AHFV at time $t$. Since $p$ is basically a vector function of time, we can treat the dependance of the system functions in (7.1), (7.2), (7.3) as dependance of them on time and further rewrite the model equations as

$$
\dot{\mathbf{x}} = \mathbf{A}_t(t)\mathbf{x} + \mathbf{B}_t(t)\mathbf{u} + \mathbf{E}_{xt}(t)\mathbf{d} \tag{7.4}
$$

$$
\begin{aligned}
\dot{\mathbf{x}} &= \mathbf{f}_t(\mathbf{x}, \mathbf{u}, \mathbf{v}, t) \\
\mathbf{y} &= \mathbf{h}_t(\mathbf{x}, \mathbf{v}, t)
\end{aligned} \tag{7.5}
$$

$$
\begin{aligned}
\dot{\mathbf{x}}_1 &= \mathbf{f}_{1t}(\mathbf{x}_1, \mathbf{x}_2, \mathbf{v}, t) \\
\dot{\mathbf{x}}_2 &= \mathbf{f}_{2t}(\mathbf{x}_1, \mathbf{x}_2, \mathbf{x}_3, \mathbf{v}, t) \\
&\vdots \\
\dot{\mathbf{x}}_k &= \mathbf{f}_{kt}(\mathbf{x}_1, \ldots, \mathbf{x}_k, \mathbf{v}, t) + \mathbf{g}_t(\mathbf{x}_1, \ldots, \mathbf{x}_k, \mathbf{v}, t)\mathbf{u} \\
\mathbf{x} &= [\mathbf{x}_1^T \quad \mathbf{x}_2^T \quad \cdots \quad \mathbf{x}_k^T]^T \\
\mathbf{y} &= \mathbf{h}_t(\mathbf{x}, \mathbf{v}, t)
\end{aligned} \tag{7.6}
$$

where $\mathbf{A}_t$, $\mathbf{B}_t$, $\mathbf{E}_{xt}$, $\mathbf{f}_t$, $\mathbf{f}_{it}$, $\mathbf{h}_t$, $\mathbf{g}_t$ are smooth functions. The information about these functions that can be used for control design purposes is determined by the guidance scheme of the complete flight and the flight condition data base. Due to lack of a perfect data base, the difference between the desired (guided) and actual flight trajectories, and unmodeled disturbances and uncertainties, the system parameters defining $\mathbf{A}_t$, $\mathbf{B}_t$, $\mathbf{E}_{xt}$, $\mathbf{f}_t$, $\mathbf{f}_{it}$, $\mathbf{h}_t$, $\mathbf{g}_t$ are not expected to be fully known. Hence adaptive laws to estimate these parameters online will be required in the control design.

Time varying and parameter varying methods have already been used in designing controllers for various aerospace systems.[129–131] These control designs, however, are in general based on the assumption that the variations are slow in some sense and they do not exploit the a priori information about the variation structures. A method to exploit the a priori information about system parameter in designing controllers for time varying systems is presented in.[132] This method is used to design effective adaptive controllers for linear time varying systems in.[132–135] Moreover the control scheme of[135] can be extended to a class of nonlinear systems including (7.6). The extended scheme will be a potential candidate for controlling AHFVs.

As a final issue to be addressed in AHF control design, we consider estimation and observer schemes. This issue is partially circumvented in output feedback designs such as the ones in,[119,132,135] in which among the plant signals, only the plant output is required to be measured in order to generate the control signal. Even with these controllers, some estimation may be needed if the output signal can not be measured accurately. Such a case is the AOA measurement issue that occurred in the control law development for the X-43A.[5] In hypersonic operation of the X-43A conventional AOA measurement devices can not be used due to aerodynamic heating. Several techniques to estimate an accurate measure of AOA have already been developed and used in the Hyper-X program.[5] The estimation techniques to be used, however, need to guarantee no harm to the stability performance of the control scheme. Using linear model based estimators together with nonlinear controllers, for example, may not be efficient. Newly developed nonlinear observers and estimators[119,136–138] can be used with possible nonlinear AHF controllers.

## 8 CONCLUSIONS

In this paper, we have reviewed the literature on characterizing, modeling, and controlling the AHF dynamics. The review demonstrates that despite the significant progress in various aspects of the hypersonic flight in the last sixty years, the AHF technology is still in the development and testing phase. Flight of an AHFV operated by an air-breathing engine has not been performed yet. Lack of an operational AHFV and the focus of the flight tests on analyzing new AHFV components and quantifying the AHF dynamics rather than performing a complete guided flight delay complete implementation and experimental testing of the recently developed AHF control schemes.

Majority of the mathematical models and control schemes presented in the AHF literature consider only the dynamic characteristics of the AHFV that are due to hypersonic speed while some pay attention to all major characteristics including the system integration and interaction issues. The airframe integrated scramjet engine configuration is widely accepted as a basis in all major AHF research centers of the world. Aerodynamic/propulsive/structural interactions in this configuration are at a non-negligible level. Hence the dynamic couplings due to these interactions need to be addressed in addition to effects of hypersonic speed in any affective AHF model or control scheme. The other

main issues to be addressed in designing an effective AHF controller are variations due to wide speed ranges in complete flights, compensation of measurement inaccuracies, fast variations of system parameters, system nonlinearities, and modeling uncertainties. A potential approach that could address all these issues is the use of integrated robust adaptive nonlinear controllers based on time varying models. Such approach has been used to control plants with time varying parameters of the same class as the AHFV models.

## ACKNOWLEDGEMENT

The authors would like to acknowledge Dr. David B. Doman of the Air Force Research Laboratory for various discussions and for his suggestions in improvement of the paper.

## References

[1] Freeman, D. C., Reubush, D. E., McClinton, C. R., Rausch, V. L., and Crawford, J. L., "The NASA Hyper–X program," *48th International Astronautical Congress*, Oct. 1997.

[2] Rausch, V. L., McClinton, C. R., and Crawford, J. L., "Hyper–X: Flight validation of hypersonic airbreathing technology," *XIII ISABE*, ISABE 97-7024, Sept. 1997.

[3] McClinton, C. R., Rausch, V. L., Sitz, J., and Reukauf, P., "Hyper–X program status," *10th AIAA/NAL/NASD-ISAS International Space Planes and Hypersonic Systems and Technologies Conference*, AIAA 2001-1910, Apr. 2001.

[4] Hueter, U. and McClinton, C. R., "NASA's advanced space transportation hypersonic program," *11th AIAA/AAAF International Conference*, AIAA 2002-5175, 2002.

[5] Davidson, J., Lallman, F. J., McMinn, J. D., Martin, J., Pahle, J., Stephenson, M., Selmon, J., and Bose, D., "Flight control laws for NASA's Hyper–X research vehicle," AIAA Paper 99-4124, 1999.

[6] Heiser, W. H., Pratt, D. T., Daley, D. H., and Mehta, U. B., editors, *Hypersonic Airbreathing Propulsion*, AIAA, Washington, DC, 1994.

[7] Gibson, C., Neidhoefer, J., Cooper, S., Carlton, L., Cox, C., and Jorgensen, C., "Development and Flight Test of the X-43A-LS Hypersonic Configuration UAV," AIAA Paper 2002-3462, 2002.

[8] Neidhoefer, J., Gibson, C., Saeks, R., Cox, C., Kocher, M., and Hunt, L., "Accurate Automation Corporation's LoFLYTE® Program," AIAA Paper 2002-3502, 2002.

[9] Curran, E. T., "Scramjet Engines: The first forty years," *AIAA Journal of Propulsion and Power*, Vol. 17, No. 6, Nov. 2001, pp. 1138–1148.

[10] Bouchez, M., Falempin, F., Levine, V., Avrashkov, V., and Davidenko, D., "French-Russian partnership on hypersonic wide-range ramjets," *AIAA Journal of Propulsion and Power*, Vol. 17, No. 6, Nov. 2001, pp. 1177–1183.

[11] Grallert, H., "Synthesis of a FESTIP airbreathing TSTO space transportation system," *AIAA Journal of Propulsion and Power*, Vol. 17, No. 6, Nov. 2001, pp. 1191–1198.

[12] Sakurai, H., Kobayasi, M., Yamazaki, I., Shirouzu, M., and Yamamoto, M., "Development of the hypersonic flight experimental vehicle," *Acta Astronautica*, Vol. 40, No. 2-8, 1997, pp. 105–112.

[13] *High Mach Number Airbreathing Engines*, Oxford, U.K., 1961, Pergamon.

[14] Dugger, G. L., *Ramjets*, Vol. 6, AIAA Selected Reprint Series, New York, NY, 1969.

[15] Roy, M. M., "Moteurs thermiques," *Comptes rendus de l' Academie des Sciences*, Vol. 222, No. 1, 1946, See also Aircraft+Establishment Library Translation 112.

[16] Weber, R. J. and Mackay, J. S., "An Analysis of Ramjet Engines Using Supersonic Combustion," NACA TN 4386, Sep. 1958.

[17] Dugger, G. L., "Comparison of hypersonic ramjet engines with subsonic and supersonic combustion," *High Mach Number Airbreathing Engines*, Pergamon, Oxford, U.K., 1961.

[18] Ferri, A., "Review of problems in application of supersonic combustion," *Journal of the Royal Aeronautical Society*, Vol. 68, No. 645, 1964, pp. 575–597.

[19] Ferri, A., "Mixing controlled supersonic combustion," *Annual Review of Fluid Dynamics*, Vol. 5, 1973, pp. 301–338.

[20] Waltrup, P. J., Stull, F. D., and Anderson, G. Y., "Supersonic combustion ramjet(scramjet) engine development in the United States," *Proc. of the Third International Symposium on Air Braething Engines*, March 1976, pp. 835–862.

[21] Marguet, R. and Huet, C., "Research of an optimum solution for a fized geometry ramjet, in the Mach 3-7 range, with successively subsonic and supersonic combustion," ONERA TP 656E, 1968.

[22] Tretyakov, P. K., *Experimentation, Modeling, and Computaion in Flow, Turbulence, and Combustion*, Vol. 1, chap. The Study of Supersonic Combustion for a Scramjet, Wiley, New York, NY, 1996, pp. 319–336.

[23] Tretjakov, P., Golovitchev, V. I., and Bruno, C., "Supersonic combustion: A Russian view, 1967-1993,"

*Proc. Joint Meeting of the Italian and Spanish Sections of the Combustion Institute*, June–July 1993, pp. VIII–1.1–VIII–1.4.

[24] Hallion, R. P., editor, *The Hypersonic Revolution*, Vol. Vol. I: From Max Valier to Project PRIME (1924–1967), Air Force History and Museums Program, Bolling AFB, DC, 1998.

[25] Hallion, R. P., editor, *The Hypersonic Revolution*, Vol. Vol. II: From Scramjet to National Aero-Space Plane, (1964–1986), Air Force History and Museums Program, Bolling AFB, DC, 1998.

[26] Thompson, M. O., *At the Edge of Space: The X-15 Flight Program*, Smithsonian Institution Press, Washington, DC, 1992.

[27] Andrews, E. H. and Mackley, E. A., "Review of NASA's Hypersonic Research Engine Project," AIAA Paper 93-2323, 1999.

[28] Contensou, P., Marguet, R., and Huet, C., "Etude theorique et experimentale d'un Statoreacteur a combustion mixte (domaine de vol Mach 3/7)," International Council of the Aeronautical Sciences, ICAS Paper 72-74, 1972.

[29] Albegov, R. V., Vinogradov, V. A., Zhadan, G. G., and Kobyzhskii, S. A., "Experimental investigation of hydrogen combustion and supersonic cooling in an annular chanel," *Fizika Goreniya i Vzryva*, Vol. 27, No. 6, 1991, pp. 24–29.

[30] Roudakov, A., Schickhman, Y., Semenov, V., Novelli, P., and Fourt, O., "Flight testing an axisymmetric scramjet: Russian recent advances," International Astronautical Federation, IAF Paper 93-S.4.485.44th, Oct. 1993.

[31] McClinton, C., Roudakov, A., Semenov, V., and Kopchenov, V., "Comperative flow path analysis and design assessment of an axisymmetric hydrogen fueled scramjet flight test engine at a Mach number of 6.5," AIAA Paper 96-4571, 1996.

[32] Voland, R. T., Auslander, A. H., Smart, A. H., Roudakov, A. S., Semenov, V. L., and Kopchenov, V. I., "CIAM/NASA Mach 6.5 scramjet flight and ground test," AIAA Paper 99-4848, 1999.

[33] Henry, J. R. and Anderson, G. Y., "Design considerations for the airframe-integrated scramjet," NASA TM X-2895, 1973.

[34] Weidner, J. P., Small, W. J., and Penland, J. A., "Scramjet Integration on Hypersonic Airplane Concepts," *AIAA Journal of Aircraft*, Vol. 14, No. 5, May 1977, pp. 460–466.

[35] Northam, G. B. and Anderson, G. Y., "Supersonic combustion research at Langley," AIAA Paper 86-0159, Jan. 1986.

[36] Rogers, R. C., Capriotti, D. P., and Guy, R. W., "Experimental supersonic combustion research at NASA Langley," AIAA Paper 98-2506, June 1998.

[37] Schweikart, L., editor, *The Hypersonic Revolution*, Vol. Volume III: The Quest for the Orbital Jet: The National Aero-Space Plane Program (1983–1995), Air Force History and Museums Program, Bolling AFB, DC, 1998.

[38] Chase, R. L. and Tang, M. H., "A historty of the NASP program from the formation of the Joint Program Ofiice to the termination of the HySTP scramjet performance demonstration program," AIAA Paper 95-6051, 1995.

[39] Hicks, J. W. and Trippensee, G., "NASA hypersonic X-plane development of technologies and capabilities for 21st Century access to space," *AGARD Future Aerospace Technology in Service to the Alliance*, April 1997, pp. 12–1–12–10.

[40] White, D. A., Bowers, A., Iliff, K., and Menousek, J., *Handbook of Intelligent Control: Neural, Fuzzy, and Adaptive Approaches*, chap. Flight, Propulsion, and Thermal Control of Advanced Aircraft and Hypersonic Vehicles, Van Nostrand Reinhold, New York, NY, 1992, pp. 357–465.

[41] Voland, R. and Rock, K., "NASP concept demonstration engine and subscale parametric engine tests," AIAA Paper 95-6055, April 1995.

[42] McRuer, D., "Design and modeling issues for integrated airframe/propulsion control of hypersonic flight vehicles," *Proc. American Control Conference*, 1991, pp. 729–734.

[43] Schmidt, D. K., Mamich, H., and Chavez, F., "Dynamics and control of hypersonic vehicles The integration challenge for the 1990s," AIAA Paper 91-5057, Dec. 1991.

[44] Schmidt, D. K., "Dynamics and control of hypersonic aeropropulsive/aeroelastic vehicles," AIAA paper 92-4326, Aug. 1992.

[45] Schmidt, D. K., "Integrated control of hypersonic vehicles," AIAA paper 93-5091, Dec. 1993.

[46] Chavez, F. R. and Schmidt, D. K., "An Integrated Analytical Aeropropulsive/Aeroelastic for Dynamic Analysis of Hypersonic Vehicles," NASA ARC 92-2, June 1992.

[47] Chavez, F. R. and Schmidt, D. K., "Analytical aeropropulsive/aeroelastic hypersonic-vehicle model with dynamic analysis," *AIAA Journal of Guidance, Control, and Dynamics*, Vol. 17, No. 6, Nov. 1994, pp. 1308–1319.

[48] Schmidt, D. K. and Lovell, T. A., "Mission performance and design sensitivities of air-breathing hypersonic launch vehicles," *AIAA Journal of Spacecraft and Rockets*, Vol. 34, No. 2, March 1997, pp. 158–164.

[49] Schmidt, D. K., "Optimum mission performance and multivariable flight guidance for airbreathing launch vehicles," *AIAA Journal of Guidance, Control,*

*and Dynamics*, Vol. 20, No. 6, Nov. 1997, pp. 1157–1164.

[50] Schmidt, D. K. and Hermann, J. A., "Use of energy-state analysis on a generic air-breathing hypersonic vehicle," *AIAA Journal of Guidance, Control, and Dynamics*, Vol. 21, No. 1, Jan. 1998, pp. 71–76.

[51] Chavez, F. R. and Schmidt, D. K., "Uncertainty modeling for multivariable-control robustness analysis of elastic high-speed vehicles," *AIAA Journal of Guidance, Control, and Dynamics*, Vol. 22, No. 1, Jan. 1999, pp. 87–95.

[52] Rock, K. E., Voland, R. T., Rogers, R. C., and Huebner, L. D., "NASA's Hyper-X Scramjet Engine Ground Test Program," ISABE 99-7214, Sept. 1999.

[53] Engelund, W. C., Holland, S. D., Cockrell Jr., C. E., and Bittner, R. D., "Propulsion System Airframe Integration Issues and Aerodynamic Database Development for the Hyper-X Flight Research Vehicle," ISOABE Paper 99-7215, 1999.

[54] Engelund, W. C., "Hyper-X Aerodynamics: The X-43A Airframe-Integrated Scramjet Propulsion Flight-Test Experiments," *AIAA Journal of Spacecraft and Rockets*, Vol. 38, No. 6, Nov. 2001, pp. 801–802.

[55] Engelund, W. C., Holland, S. D., Cockrell Jr., C. E., and Bittner, R. D., "Aerodynamic Database Development for the Hyper-X Airframe-Integrated Scramjet Propulsion Experiments," *AIAA Journal of Spacecraft and Rockets*, Vol. 38, No. 6, Nov. 2001, pp. 803–810.

[56] Woods, W. C., Holland, S. D., and DiFulvio, M., "Hyper-X Stage Separation Wind-Tunnel Test Program," *AIAA Journal of Spacecraft and Rockets*, Vol. 38, No. 6, Nov. 2001, pp. 811–819.

[57] Buning, P. G., Wong, T. C., Dilley, A. D., and Pao, J. L., "Computational Fluid Dynamics Prediction of Hyper-X Stage Separation Aerodynamics," *AIAA Journal of Spacecraft and Rockets*, Vol. 38, No. 6, Nov. 2001, pp. 820–827.

[58] Holland, S. D., Woods, W. C., and Engelund, W. C., "Hyper-X Research Vehicle Experimental Aerodynamics Test Program Overview," *AIAA Journal of Spacecraft and Rockets*, Vol. 38, No. 6, Nov. 2001, pp. 828–835.

[59] Cockrell Jr., C. E., Engelund, W. C., Bittner, R. D., Jentink, T. N., Dilley, A. D., and Frendi, A., "Integrated Aeropropulsive Computational Fluid Dynamics Methodology for the Hyper-X Flight Experiment," *AIAA Journal of Spacecraft and Rockets*, Vol. 38, No. 6, Nov. 2001, pp. 836–843.

[60] Huebner, L. D., Rock, K. E., Ruf, E. G., Witte, D. W., and Andrews Jr., E. H., "Hyper-X Flight Engine Ground Testing for Flight Risk Reduction," *AIAA Journal of Spacecraft and Rockets*, Vol. 38, No. 6, Nov. 2001, pp. 844–852.

[61] Reubush, D. E., Martin, J. G., Robinson, J. S., Bose, D. M., and Strovers, B. K., "Hyper–X Stage Separation—Simulation Development and Results," AIAA 2001-1802, April 2001.

[62] Faulkner, R. F. and Weber, J. W., "Hydrocarbon Scramjet Propulsion System Development, Demonstration, and Application," AIAA Paper 99-4922, 1999.

[63] Sosounov, V. A., Roudakov, A. S., Semenov, V. S., Kopchenov, V. I., Lanshin, V. I., and Romankov, O. N., "Two Generations of Russian Scram Flying Test Beds. The Oriel Programme," *Proc. the 12th International Symposium on Air Breathing Engines*, Sept. 1995.

[64] Goldfeld, M. A., Nestoulia, R. V., Starov, A. V., and Vinodragov, V. A., "Experimental Study of Scramjet Modules," *Proc. the 14th International Symposium on Air Breathing Engines*, ISABE Paper 99-7052, Sept. 1999.

[65] Curran, E. T. and Murthy, S. N. B., editors, *Scramjet Propulsion*, Progress in Astronautics and Aeronautics, AIAA, Washington, DC, 2001.

[66] Sancho, M., Colin, Y., and Johnson, C., "Program Overview: The French Hypersonic Research Program PREPHA," *Proc. the 7th AIAA International Space Planes and Hypersonic Systems and Technologies Conference*, Nov. 1996.

[67] Falempin, F. and Serre, L., "The French PROMETHEE Program: Main Goals and Status in 1999," AIAA Paper 99-4814, 1999.

[68] Novelli, P. and Koschel, W., "JAPHAR—A Joint ONERA–DLR Research Project on High Speed Airbreathing Propulsion," *Proc. the 14th International Symposium on Air Breathing Engines*, ISABE Paper 99-7091, Sept. 1999.

[69] Yatsuyanagi, N. and Chinzei, N., "Status of Scramjet Research at NAL," *Proc. the 20th International Symposium on Space Technology and Science*, Paper 96-a-2-10, May 1996.

[70] Bertin, J. J., Periaux, J., and Ballmann, J., editors, *Advances in Hypersonics*, Birkhäuser, Boston, MA, 1992.

[71] Anderson, Jr., J. D., *Hypersonic and High Temperature Gas Dynamics*, McGraw-Hill, 1989.

[72] Bertin, J. J., *Hypersonic Aerothermodynamics*, AIAA, Washington, DC, 1994.

[73] Johnson, P. J., Whitehead, Jr., A. H., and Chapman, G. T., "Fitting Aerodynamics and Propulsion in to the Puzzle," *AIAA Aerospace America*, Sept. 1987, pp. 32–34.

[74] Maus, J. R., Giffith, B. J., Szema, K. Y., and Best, J. T., "Hypersonic Mach Number and Real

Gas Effects on Space Shuttle Orbiter Aerodynamics," *AIAA Journal of Spacecraft and Rockets*, Vol. 21, No. 2, Nov. 1984, pp. 132–141.

[75] Schindel, L., "Design of High Prformance Ramjet or Scramjet Powered Vehicles," AIAA paper 89-0379, 1989.

[76] Raney, D. L., Phillips, M. R., and Person, L. H., "Investigation of Piloting Aids for Manual Control of Hypersonic Maneuvers," NASA Technical Paper 3525, October 1995.

[77] Chalk, C. R., "Flying Qualities Criteria Review, Assesment and Recommendations for NASP," NASP CR-1065, NASP JPO, Wright-Patterson AFB, 1989.

[78] McRuer, D. T. and Myers, T. T., "Considerations for the Development of NASP Flying Qualities Specifications," WL-TR-92-3042, U.S. Air Force, 1992.

[79] Penland, J. A., Dinlon, J. L., and Pittman, J. L., "An Aero Dynamic Analysis of Several Hypersonic Research Airplane Concepts from M=0.2 to 6.0," *AIAA Journal of Aircraft*, Vol. 15, No. 11, Nov. 1978, pp. 716–723.

[80] Whitehead, Jr., A. H., "NASP Aerodynamics," AIAA Paper 89-5013, 1989.

[81] Walton, J. T., "Performance Sensitivity of Hypersonic Vehicles to Change Angle of Attack and Dynamic Pressure," AIAA Paper 89-2463, 1989.

[82] Bushcek, H. and Calise, A. J., "Uncertainty modeling and fixed-order controller design for a hypersonic vehicle model," *AIAA Journal of Guidance, Control, and Dynamics*, Vol. 20, No. 1, Jan. 1997, pp. 42–48.

[83] Gupta, K. K., Voelker, L. S., Bach, C., Doyle, T., and Hahn, E., "CFD-Based Aeroelastic Analysis of the X-43 Hypersonic Flight Vehicle," AIAA Paper 01-0712, 2001.

[84] Cowan, J. C., Arena, Jr., A. S., and Gupta, K. K., "Development of a Discrete-Time Aerodynamic Model for CFD-Based Aeroelastic Analysis," AIAA Paper 99-0765, 1999.

[85] Gupta, K. K. and Petersen, K. L., "Multidisciplinary Aeroelastic Analysis of a Generic Hypersonic Vehicle," AIAA Paper 93-5028, Dec. 1993.

[86] Thuruthimattam, B., Friedmann, P., Powell, K., and McNamara, J., "Aeroelasticity of a Generic Hypersonic Vehicle," AIAA Paper 2002-1209, 2002.

[87] Raney, D. L., Pototzky, A. S., and McMinn, J. D., "Impact of Aero-Propulsive-Elastic Interactions on Longitudinal Flight Dynamics of a Hypersonic Vehicle," *AIAA Journal of Aircraft*, Vol. 32, March 1995.

[88] Lind, R., Buffington, J., and Sparks, A., "Multi-Loop Aeroservoelastic Control of a Hypersonic Vehicle," AIAA Paper 99-4123, August 1999.

[89] Bilimoria, K. D. and Schmidt, D. K., "Integrated Development of the Equations of Motion for Elastic Hypersonic Flight Vehicles," *AIAA Journal of Guidance, Control, and Dynamics*, Vol. 18, No. 1, Jan. 1995, pp. 73–81.

[90] Shaughnessy, J. D., Pinckney, S. Z., McMinn, J. D., Cruz, C. I., and Kelley, M. L., "Hypersonic Vehicle Simulation Model: Winged-Cone Configuration," NASA TM-102610, 1990.

[91] Gregory, I. M., Chowdhry, R. S., McMinn, J. D., and Shaughnessy, J. D., "Hypersonic vehicle model and control law development using $\mathcal{H}_\infty$ and $\mu$-synthesis," NASA TM-4562, 1994.

[92] Brauer, G. L., Cornick, D. E., and Stevenson, R., "Capabilities and Applications of the Program to Optimize Simulated Trajectories(POST)—Program Summary Document," NASA CR-2770, 1977.

[93] Marrison, C. I. and Stengel, R. F., "Design of robust control systems for a hypersonic aircraft," *AIAA Journal of Guidance, Control, and Dynamics*, Vol. 21, No. 1, Jan. 1998, pp. 58–63.

[94] Wang, Q. and Stengel, R. F., "Robust nonlinear control of a hypersonic aircraft," *AIAA Journal of Guidance, Control, and Dynamics*, Vol. 23, No. 4, July 2000, pp. 577–585.

[95] Stengel, R. F., *Optimal Control and Estimation*, Dover, New York, NY, 1994.

[96] Ray, L. R. and Stengel, R. F., "Stochastic Robustness of Linear-Time-Invariant Control Systems," *IEEE Transactions on Automatic Control*, Vol. 36, No. 1, January 1991, pp. 82–87.

[97] Ray, L. R. and Stengel, R. F., "A Monte Carlo Approach to the Analysis of Control System Robustness," *Automatica*, Vol. 29, No. 1, January 1993, pp. 229–236.

[98] Maciejowski, J. M., *Multivariable Feedback Design*, Addison-Wesley, New York, NY, 1989.

[99] Zhou, K. and Doyle, J. C., *Essentials of Robust Control*, Prentice-Hall, Upper Saddle River, NJ, 1998.

[100] Bowers, A. H. and Iliff, K. W., "Generic Hypersonic Aerodynamic Model Example (GHAME) for computer simulation," NASA TM, NASA Ames-Dryden, Edwards, CA, 1987.

[101] Bushcek, H. and Calise, A. J., "$\mu$ Controllers: Mixed and Fixed," *AIAA Journal of Guidance, Control, and Dynamics*, Vol. 20, No. 1, Jan. 1997, pp. 34–41.

[102] Young, P. M., "Controller Design with Mixed Unceratinties," *Proc. American Control Conference*, 1994, pp. 2333–2337.

[103] Lohsoonthorn, P., Jonckheere, E., and Dalzell, S., "Eigenstructure vs constrained $\mathcal{H}^\infty$ design for hypersonic winged cone," *AIAA Journal of Guidance,*

*Control, and Dynamics*, Vol. 24, No. 4, July 2001, pp. 648–658.

[104] Isidori, A., *Nonlinear Control Systems*, Springer-Verlag, 1997.

[105] Xu, H. and Mirmirani, M., "Robust adaptive sliding control for a class of MIMO nonlinear systems," AIAA Paper 2001-4168, 2001.

[106] Xu, H., Leung, P., Mirmirani, M., Boussalis, H., and Ioannou, P., "Adaptive sliding mode control of a hypersonic flight vehicle," *Advances in Astronautical Sciences* 108, Part 2, 2001, pp. 1947–1962.

[107] Ioannou, P. A. and Sun, J., *Robust Adaptive Control*, Prentice-Hall, Upper Saddle River, NJ, 1996.

[108] Mooij, E., "Numerical investigation of model reference adaptive control for hypersonic aircraft," *AIAA Journal of Guidance, Control, and Dynamics*, Vol. 24, No. 2, March 2001, pp. 315–323.

[109] Dewell, L. D. and Speyer, J. L., "Fuel-optimal periodic control and regulation in constrained hypersonic flight," *AIAA Journal of Guidance, Control, and Dynamics*, Vol. 20, No. 5, Sep. 1997, pp. 923–932.

[110] Chuang, C. H. and Morimoto, H., "Sub-optimal and optimal periodic solutions for hypersonic transport," *Proc. American Control Conference*, June 1995, pp. 1186–1190.

[111] Naidu, D. S., Banda, S. S., and Buffington, J. L., "Unified approach to $\mathcal{H}_2$ and $\mathcal{H}_\infty$ optimal control of a hypersonic vehicle," *Proc. American Control Conference*, June 1999, pp. 2737–2741.

[112] Austin, K. J. and Jacobs, P. A., "Application of genetic algorithms to hypersonic flight control," *Proc. IFSA World Congress and 20th NAFIPS International Conference*, Vol. 4, July 2001, pp. 2428–2433.

[113] Zhou, Z. and Lin, C. F., "Fuzzy logic based flight control system for hypersonic transporter," *Proc. Conference on Decision and Control*, Dec 1997, pp. 2730–2735.

[114] Cox, C., Neidhoefer, J., Saeks, R., and Lendaris, G., "Neural adaptive control of the LoFLYTE®," *Proc. American Control Conference*, Vol. 4, 2001, pp. 2913–2917.

[115] Saeks, R., Neidhoefer, J., Cox, C., and Pap, R., "Neural control of the LoFLYTE® aircraft," *Proc. IEEE Int. Conference on Systems, Man, and Cybernetics*, Vol. 4, Oct. 1998, pp. 3112–3117.

[116] Ogata, K., *Modern Control Engineering*, Prentice-Hall, Upper Saddle River, NJ, 2002.

[117] Marren, D., Lewis, M., and Maurice, L. Q., "Experimentation, test, and evaluation requirements for future airbreathing hypersonic systems," *AIAA Journal of Propulsion and Power*, Vol. 17, No. 6, Nov. 2001, pp. 1361–1365.

[118] Bowcutt, K. G., "Multidisciplinary optimization of airbreathing hypersonic vehicles," *AIAA Journal of Propulsion and Power*, Vol. 17, No. 6, Nov. 2001, pp. 1184–1190.

[119] Krstić, M., Kanellakopoulos, I., and Kokotović, P. V., *Nonlinear and Adaptive Control Design*, Wiley, New York, NY, 1995.

[120] Krstić, M. and Deng, H., *Stabilization of Nonlinear Unceratin Systems*, Springer-Verlag, 1998.

[121] Marino, R. and Tomei, P., *Nonlinear Control Design — Geometric, Adaptive, and Robust*, Prentice-Hall, London, UK, 1995.

[122] Qu, Z., *Robust Control of Nonlinear Unceratin Systems*, Wiley, New York, NY, 1998.

[123] Isidori, A., Lamnabhi-Lagarrigue, F., and Respondek, W., editors, *Nonlinear Control in the Year 2000*, Springer-Verlag, 2001.

[124] Fidan, B., Kosmatopoulos, E. B., and Ioannou, P. A., "A Switching Controller for Multivariable LTI Systems with Known and Unknown Parameters," *Proc. 41st IEEE Conference on Decision and Control*, Vol. 4, 2002, pp. 4688–4693.

[125] Hyde, R. A., editor, $\mathcal{H}_\infty$ *Aerospace Control Design: A VSTOL Flight Application*, Springer-Verlag, 1995.

[126] Shamma, J. S. and Athans, M., "Analysis of Gain Scheduled Control for Nonlinear Plants," *IEEE Transactions on Automatic Control*, Vol. 35, No. 8, August 1990, pp. 898–907.

[127] Shamma, J. S. and Athans, M., "Gain Scheduling: Potential Hazards and Possible Remedies," *IEEE Control Systems Magazine*, June 1992, pp. 101–107.

[128] Rugh, W. J. and Shamma, J. S., "Research on Gain Sceduling," *Automatica*, Vol. 36, No. 10, October 2000, pp. 1401–1425.

[129] Wiśniewski, R., "Linear Time-Varying Approach to Satellite Attitude Control Using Only Electromagnetic Actuation," *AIAA Journal of Guidance, Control, and Dynamics*, Vol. 23, No. 4, July-Aug. 2000.

[130] Zhu, J. J. and Mickle, M. C., "Missile Autopilot Design Using a New Linear Time-Varying Control Technique," *AIAA Journal of Guidance, Control, and Dynamics*, Vol. 20, No. 1, Jan.-Feb. 1997.

[131] Biannic, J. M., Apkarian, P., and Garrard, W. L., "Parameter Varying Control of a High-Performance Aircraft," *AIAA Journal of Guidance, Control, and Dynamics*, Vol. 20, No. 2, March-April 1997.

[132] Tsakalis, K. S. and Ioannou, P. A., *Linear Time Varying Systems: Control and Adaptation*, Prentice-Hall, Englewood Cliffs, NJ, 1993.

[133] Limanond, S. and Tsakalis, K., "Model reference adaptive and nonadaptive control of linear time-varying plants," *IEEE Trans. on Automatic Control*, Vol. 45, 2000, pp. 1290–1300.

[134] Limanond, S. and Tsakalis, K. S., "Adaptive and nonadaptive pole-placement control of multivariable linear time-varying plants," *Int. J. of Control*, Vol. 74, 2001, pp. 507–523.

[135] Zhang, Y., Fidan, B., and Ioannou, P. A., "Backstepping Control of Linear Time Varying Systems with Known and Unknown Parameters," to appear in *IEEE Trans. on Automatic Control*, 2003.

[136] Nijmeijer, H. and Fossen, T. I., editors, *New Directions in Nonlinear Observer Design*, Springer-Verlag, 1999.

[137] Kokotović, P. and Arcak, M., "Constructive nonlinear control: A historical perspective," *Automatica*, Vol. 37, No. 5, 2001, pp. 637–662.

[138] Arcak, M. and Kokotović, P., "Nonlinear observers: A circle criterion design and robustness analysis," *Automatica*, Vol. 37, No. 12, December 2001, pp. 1923–1930.